Contents of issue 2 vol. XLVII

Polish Academy of Sciences

Institute of Fundamental Technological Research

Archives of Mechanics

Archiwum Mechaniki Stosowanej

volume 47 issue 2

Polish Scientific Publishers PWN

Warszawa 1995

ARCHIVES OF MECHANICS IS DEVOTED TO
Theory of elasticity and plasticity • Theory of nonclassical continua • Physics of continuous media • Mechanics of discrete media • Nonlinear mechanics • Rheology • Fluid gas-mechanics • Rarefied gas • Thermodynamics

---

Printed in Poland, Editorial Office: Świętokrzyska 21,
00-049 Warszawa (Poland)

Arkuszy wydawniczych 19,5. Arkuszy drukarskich 17.
Papier offset. kl. III 70 g. B1. Oddano do składania w marcu 1995 r.
Druk ukończono w czerwcu 1995 r.
Druk i oprawa: Drukarnia Braci Grodzickich, Żabieniec ul. Przelotowa 7

Arch. Mech., 47, 2, pp. 147–148, Warszawa 1995

Preface

Polish Solid Mechanics Conferences have a long tradition going back to the first conference in 1953 at Karpacz. At the beginning, those conferences were of the summer school type, lasted 2 weeks and concentrated on classical problems of elasticity and structural mechanics. Until 1969 all conferences were organised by the late Professor Wacław Olszak. Afterwards, they turned into Polish Solid Mechanics Conferences held every year, and later every other year. Polish Solid Mechanics Conferences have always been organised by the Institute of Fundamental Technological Research of the Polish Academy of Sciences in co-operation with the Committee of Mechanics of the Academy of Sciences.

30th Polish Solid Mechanics Conference held in Zakopane, September 5–9, 1994, was organised by the Centre of Mechanics of the Institute of Fundamental Technological Research. Among 255 participants there were 147 scientists from Polish universities and research institutions and 78 participants from other countries. The conference scientific program included 11 invited general lectures, 4 sectional lectures, 113 oral presentations and 72 contributions presented during a poster session.

The main subject of the Conference concentrated on mechanics of materials and on the structural mechanics. Specific topics of the sessions were as follows:

- foundations of mechanics,
- mechanics of phase transformations,
- strain localisation and instability,
- mechanics of porous media and composites,
- fracture mechanics, damage and fatigue,
- inelastic materials and structures,
- dynamics of solids and structures,
- structural mechanics and optimisation,
- numerical methods.

The Conference provided the forum for presentation of new scientific results and ideas in all major areas of contemporary mechanics of solids and structures. The participants have enriched the Conference with excellent scientific contributions and with stimulating discussions during various sessions. High level of the presented papers and friendly atmosphere created by the participants certainly contributed to the success of the conference.

Though no conference proceedings volume was planned, all participants were encouraged to submit their contributions as full-length papers for publication in the Archives of Mechanics or Engineering Transactions. This proposal has evoked

a great response and resulted in submission of more than 60 papers. A great majority of them, after a regular reviewing procedure, have been accepted for publication and they are now printed in this and the forthcoming issues of the journal.

March 1995

W. K. Nowacki
Conference Chairman

Arch. Mech., 47, 2, pp. 149–171, Warszawa 1995

Unconventional approach to linear elasticity (*)

J. RYCHLEWSKI (WARSZAWA)

In memoriam Jack Pipkin

A CONCISE OVERVIEW of a series of papers following [9] has been presented; their principal feature consists in spectral decomposition of the stiffness and compliance tensors: the stiffness tensor is determined by six stiffness moduli and six mutually orthogonal stress-strain states, called proper elastic states. Numerous consequences of such a description have been analyzed.

1. Introduction

OVER TEN YEARS ago I became attracted by the idea of describing elastic and plastic anisotropy in an unconventional manner, i.e. by means of eigenvalues and eigenelements of tensors of the fourth order. I was enchanted by the freshness of the idea even more so because it concerned an area both vital and seemingly totally exploited. After the first statements were send to print [9, 10, 11], it occured to me, however, that such a simple and reccuring idea, strongly connected with the classical 19th century theory of quadratic forms, could not have possibly been overlooked by the old masters.

I was right. Among the volumes of the Jagiellonian University in Kraków I soon found the work of William Thomson [2] – to become Lord Kelvin – with quite a clear exposition of the heart of the idea. Fortunately, I was able to add an appropriate remark in the proof of my first paper on the subject. Continuing the search, I realized that Kelvin gave a concise summary of his results in Encyclopaedia Britannica [3]. His work was reviewed – unfortunately without proper undestanding – by TODHUNTER and PEARSON [4] and ... was completely forgotten in the years to come. Nevertheless, the very idea of applying eigenvalues and eigenelements of elasticity tensors has sporadically occurred here and there. Of the recent results I came across K.S. ALEKSANDROV [5], P. ANGLES d'AURIAC [6] and most important A.C. PIPKIN [7]. This list can surely be expanded. Taking the risk of roughly assessing the number of important publications on classical elasticity to be $\sim 10^5$, I would rather leave all further investigations in the matter to professional historians. As far as I know, the results of paper [10] have not been preceded.

(*) General Lecture at 30-th Polish Solid Mechanics Conference (Zakopane, Sept. 5–9, 1994); see also J. RYCHLEWSKI, *Anisotropy and proper states of materials*, submitted to the Proc. of the IUTAM Symposium on Anisotropy, Nonhomogeneity and Nonlinearity in Solid Mechanics, Nottingham, August, 29-th September, 3, 1994.

The possibilities created by the research on proper states have been studied in a series of papers [12–17]. In the recent years Kelvin's idea has been independently rediscovered over again by MEHRABADI and COWIN [18] and developed and applied in papers [19–32].

This presentation is a concise overview of all these results.

2. The underlying idea

We are thus discussing the truly classical materials, in which the infinitesimal strain $\boldsymbol{\varepsilon}$ causes the stress $\boldsymbol{\sigma}$ according to *Hooke's law*

$$\boldsymbol{\sigma} = \mathbf{S} \cdot \boldsymbol{\varepsilon}, \qquad \boldsymbol{\varepsilon} = \mathbf{C} \cdot \boldsymbol{\sigma},$$

where $\mathbf{S}$ is the *stiffness tensor* and $\mathbf{C}$ is the *compliance tensor*, $\mathbf{C} \circ \mathbf{S} = \mathbf{S} \circ \mathbf{C} = \mathbb{1}$. Let us assume that stresses are bounded by the *limit condition of Mises type*

$$\boldsymbol{\sigma} \cdot \mathbf{H} \cdot \boldsymbol{\sigma} \leq 1,$$

where $\mathbf{H}$ is the *limit tensor*.

In the entire solid body mechanics, it is difficult to find a simpler and a better known, as well as a more widely applied law than Hooke's law. From the point of view of general theory of materials, this is merely a noteworthy special case of constitutive equation. From the point of view of applicability, it is quite the opposite: the range of Hooke's law has no match. The thing consists in the unrivalled physical universality of Hooke's law. In an appropriate range of stresses, nearly all solid materials – say steel, quartz, glass, rubber, bones and skin, are subject to it, although the physical mechanism of its functioning is completely different for alloy, cristal, supercooled liquid, polymer or biological tissue.

This might sound quite shocking, yet ... one should not assume that all the essential characteristics of elasticity tensors have been described long ago. Let us quote two preliminary examples.

The components S_{ijkl} in an accidental basis do not constitute, of course, material constants. Thus: *do the two samples, described by* S_{ijkl} *and* $S'_{i'j'k'l'}$, *represent the same or two different materials*? We do not have a general answer [1], because we do not have a functional basis of invariants for the fourth order tensors (the more so, neither do we have an integrity basis). It is only clear that the variety of the distinct materials is a manifold of $21 - 3 = 18$ dimensions. A global continuous functional basis of 39 polynomials invariants for some large submanifold was presented recently by J.P. BOEHLER, A.A. KIRILLOV and E.T. ONAT [35]. To this problem we shall return in Sec. 4.

[1] NOVOZHILOV's proposal [33, 34] of applying the so-called principal directions of anisotropy is not general enough.

Let us take another example. The classsification of elastic bodies according to symmetry perfectly done by Love and Voigt, is the lesser in value, the lesser the symmetry.

According to what characteristics one should thus distinguish two materials which have no symmetry? This question is even more important since the number of materials of optimum controlled anisotropy will increase (e.g. in composites), whereas the symmetry is speedily being lost with the increase in complication of the structure.

Let us consider the *extremum of the stored elastic energy* $E(\boldsymbol{\varepsilon})$ on unit sphere in the strain-stress space

$$E(\boldsymbol{\omega}) = \text{ext}, \qquad \boldsymbol{\omega} \cdot \boldsymbol{\omega} = 1.$$

Because of $\boldsymbol{\sigma} = \partial E / \partial \boldsymbol{\varepsilon}$, the Lagrange condition takes the following form: for each $\boldsymbol{\varepsilon} = e\boldsymbol{\omega}$ in the energy extremum direction $\boldsymbol{\omega}$

$$\boldsymbol{\sigma} = \lambda_{\boldsymbol{\omega}}(e)\boldsymbol{\varepsilon}.$$

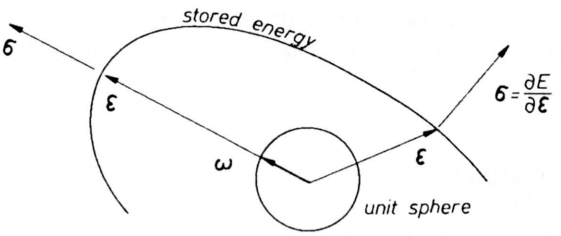

FIG. 1.

We call each energy extremum direction $\boldsymbol{\omega}$ a *proper elastic state* of the material under consideration. The factor $\lambda_{\boldsymbol{\omega}}(e)$ will be called *stiffness modulus* for the proper elastic state $\boldsymbol{\omega}$.

In the case of linear elasticity we have $2E(\boldsymbol{\varepsilon}) = \boldsymbol{\varepsilon} \cdot \mathbf{S} \cdot \boldsymbol{\varepsilon}$ and the necessary condition for local extremum of stored energy takes the form: $\boldsymbol{\varepsilon} = \boldsymbol{\omega}$, where

$$\mathbf{S} \cdot \boldsymbol{\omega} = \lambda \boldsymbol{\omega}, \qquad \boldsymbol{\omega} \cdot \boldsymbol{\omega} = 1.$$

For each strain in direction $\boldsymbol{\omega}$, $\boldsymbol{\varepsilon} = e\boldsymbol{\omega}$, the corresponding stress $\boldsymbol{\sigma} = \mathbf{S} \cdot \boldsymbol{\varepsilon}$ is in direct proportion to the strain

$$\boldsymbol{\sigma} = \lambda_{\boldsymbol{\omega}} \boldsymbol{\varepsilon}.$$

But this is a perfectly adequate formulation of the anagram in whose form Robert Hooke gracefully announced his law

$$c\ e\ i\ i\ i\ n\ o\ s\ s\ s\ t\ t\ u\ v$$

giving the solution after two years: *ut tensio sic vis* [1].

In an exactly identical manner we can examine the *limit stress intensity* $\psi(\boldsymbol{\sigma})$ of a material with a limit condition $\psi(\boldsymbol{\sigma}) \leq 1$,

$$\psi(\boldsymbol{\sigma}) = \text{ext}, \qquad \boldsymbol{\sigma} \cdot \boldsymbol{\sigma} = 1.$$

For the Mises criterion $\psi(\boldsymbol{\sigma}) = \boldsymbol{\sigma} \cdot \mathbf{H} \cdot \boldsymbol{\sigma}$ we obtain the necessary condition of local extremum of limit stress intensity in the form $\boldsymbol{\sigma} = \boldsymbol{\rho}$, where

$$\mathbf{H} \cdot \boldsymbol{\rho} = \frac{1}{\chi^2} \boldsymbol{\rho}, \qquad \boldsymbol{\rho} \cdot \boldsymbol{\rho} = 1.$$

For each stress in direction $\boldsymbol{\rho}$, $\boldsymbol{\sigma} = s\boldsymbol{\rho}$, the limit condition takes the form

$$\boldsymbol{\sigma} \cdot \boldsymbol{\sigma} \leq \chi^2.$$

Each solution $\boldsymbol{\rho}$ will be called the *proper limit state* of the material under consideration. The parameter χ will be called the *limit of elasticity* corresponding to direction $\boldsymbol{\omega}$.

The proper elastic states $\boldsymbol{\omega}$ and the proper limit states $\boldsymbol{\rho}$ can be quite different.

This is my starting point on the grounds of mechanics. The next step belongs to pure mathematics.

3. Mathematical treatment

Mathematical treatment of the presented idea is a well-known part of classical linear algebra.

Let us denote by $\mathcal{E}$ the Euclidean 3-dimensional space with a scalar product $\mathbf{xy}$. The set of symmetric second order tensors $\mathcal{S} = \operatorname{sym} \mathcal{E} \otimes \mathcal{E}$ is (among others) a linear space of dimension $\dim \mathcal{S} = 3^2 - 3 = 6$ with scalar product $\boldsymbol{\alpha} \cdot \boldsymbol{\beta}$. Assuming that the stresses are related to a unit, we may consider $\mathcal{S}$ as a strain-stress space. Elasticity tensor $\mathbf{S} \in \mathcal{T} = \operatorname{sym} \mathcal{S} \otimes \mathcal{S}$ can be considered as (among others) a symmetric linear operator, $\boldsymbol{\alpha} \to \mathbf{S} \cdot \boldsymbol{\alpha}$, $\boldsymbol{\alpha} \cdot \mathbf{S} \cdot \boldsymbol{\beta} = \boldsymbol{\beta} \cdot \mathbf{S} \cdot \boldsymbol{\alpha}$ mapping the strain-stress space $\mathcal{S}$ into itself. Identically one can consider tensor $\mathbf{H}$, although it appears as a quadratic form $\boldsymbol{\sigma} \cdot \mathbf{H} \cdot \boldsymbol{\sigma}$. The necessary extremum conditions $\mathbf{S} \cdot \boldsymbol{\omega} = \lambda \boldsymbol{\omega}$, $\mathbf{H} \cdot \boldsymbol{\rho} = \boldsymbol{\rho}/\chi^2$ define the eigenvalues λ, χ^2 and eigenelements (here being tensors) $\boldsymbol{\omega}$, $\boldsymbol{\rho}$ of those operators. The situation is described by *classical theorem on the spectral decomposition of symmetric linear operator in a space with a scalar product* (see e.g. [36]). When formulated with an adequate precision it assumes, in relation to tensor $\mathbf{S}$, the following form:

THEOREM. *For each stiffness tensor* $\mathbf{S}$ *there exists exactly one orthogonal decomposition of the strain-stress space*

$$(*) \qquad \mathcal{S} = \mathcal{P}_1 \oplus \ldots \oplus \mathcal{P}_r, \qquad r \leq 6,$$

$\mathcal{P}_i \perp \mathcal{P}_j$ for $i \neq j$, and exactly one sequence of stiffness moduli $\lambda_1 < \ldots < \lambda_r$, such that

$$\mathbf{S} = \lambda_1 \mathbf{P}_1 + \ldots + \lambda_r \mathbf{P}_r,$$

where $\mathbf{P}_1, \ldots, \mathbf{P}_r$ are orthogonal projectors which map the space $\mathcal{S}$ onto subspace $\mathcal{P}_1, \ldots, \mathcal{P}_r$, respectively, Fig. 2.

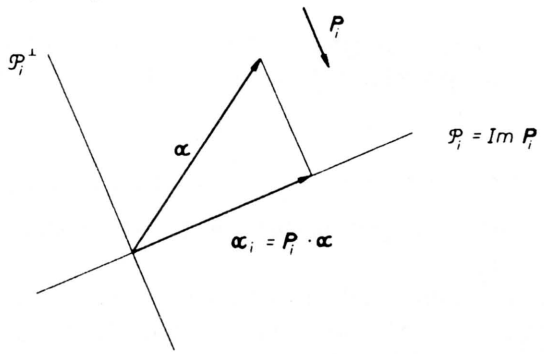

FIG. 2.

The sequence $\mathbf{P}_1, \ldots, \mathbf{P}_r$ constitutes *proper orthogonal decomposition of the unit operator* $\mathbb{1}$, $\mathbb{1} \cdot \boldsymbol{\omega} \equiv \boldsymbol{\omega}$,

$$\mathbb{1} = \mathbf{P}_1 + \ldots + \mathbf{P}_r, \qquad \mathbf{P}_k \circ \mathbf{P}_l = \begin{cases} \mathbf{P}_k, & k = l, \\ \mathbf{0}, & k \neq l. \end{cases}$$

The meaning of the presented proper subspaces of tensor $\mathbf{S}$ is quite clear: subspace $\mathcal{P}_k$ contains all proper elastic states, corresponding to stiffness modulus λ_k

$$\boldsymbol{\sigma} = \mathbf{S} \cdot \boldsymbol{\varepsilon} = \lambda_k \boldsymbol{\varepsilon} \qquad \text{iff} \qquad \boldsymbol{\varepsilon} \in \mathcal{P}_k, \qquad k = 1, \ldots, r.$$

Decomposing the stresses and strains into the parts in proper subspaces $\boldsymbol{\sigma}_k = \mathbf{P}_k \cdot \boldsymbol{\sigma}$, $\boldsymbol{\varepsilon}_k = \mathbf{P}_k \cdot \boldsymbol{\varepsilon}$,

$$\boldsymbol{\sigma} = \boldsymbol{\sigma}_1 + \ldots + \boldsymbol{\sigma}_r, \qquad \boldsymbol{\sigma}_k \cdot \boldsymbol{\sigma}_j = 0 \qquad \text{for} \qquad k \neq j,$$

$$\boldsymbol{\varepsilon} = \boldsymbol{\varepsilon}_1 + \ldots + \boldsymbol{\varepsilon}_r, \qquad \boldsymbol{\varepsilon}_k \cdot \boldsymbol{\varepsilon}_j = 0 \qquad \text{for} \qquad k \neq j,$$

we see that Hooke's law $\boldsymbol{\sigma} = \mathbf{S} \cdot \boldsymbol{\varepsilon}$ can be written in an equivalent form of $r \leq 6$ proportionalities of these parts of stress and strain

$$\boldsymbol{\sigma} = \lambda_1 \boldsymbol{\varepsilon}_1, \qquad \ldots, \qquad \boldsymbol{\sigma}_r = \lambda_r \boldsymbol{\varepsilon}_r.$$

Spectral decomposition of the compliance tensor has the form

$$\mathbf{C} = \frac{1}{\lambda_1} \mathbf{P}_1 + \ldots + \frac{1}{\lambda_r} \mathbf{P}_r$$

with the same projectors $\mathbf{P}_1, \ldots, \mathbf{P}_r$.

The presented spectral decomposition of stiffness tensor **S** (and compliance tensor **C**) I dare call the *main structural formula of linear elasticity*.

Identically, we obtain the spectral decomposition of limit tensor **H**.

4. Elastic constants

For an *extremely complex material* we have $r = 6$, thus the proper subspaces are straight lines $\mathcal{P}$ with projectors $\mathbf{P} = \boldsymbol{\omega} \otimes \boldsymbol{\omega}$, and the spectral decomposition has the form

$$(**) \qquad \mathbf{S} = \lambda_{\mathrm{I}}\boldsymbol{\omega}_{\mathrm{I}} \otimes \boldsymbol{\omega}_{\mathrm{I}} + \ldots + \lambda_{\mathrm{VI}}\boldsymbol{\omega}_{\mathrm{VI}} \otimes \boldsymbol{\omega}_{\mathrm{VI}},$$

where $\boldsymbol{\omega}_{\mathrm{I}}, \ldots, \boldsymbol{\omega}_{\mathrm{VI}}$ is the orthonormal basis in the stress-strain space, $\boldsymbol{\omega}_K \cdot \boldsymbol{\omega}_L = \delta_{KL}$, $K, L = \mathrm{I}, \ldots, \mathrm{VI}$.

It is convenient to assume that in this formula the moduli λ_K can coincide. Then, from the formula $(**)$ we can obtain each of the possible spectral decompositions $(*)$.

It was Kelvin himself who presented the elastic energy in the form

$$2E(\boldsymbol{\varepsilon}) = \boldsymbol{\varepsilon} \cdot \mathbf{S} \cdot \boldsymbol{\varepsilon} = \lambda_{\mathrm{I}} e_{\mathrm{I}}^2 + \ldots + \lambda_{\mathrm{VI}} e_{\mathrm{VI}}^2,$$

where $e_K = \boldsymbol{\varepsilon} \cdot \boldsymbol{\omega}_K$ is the extent of strain in direction $\boldsymbol{\omega}_K$

$$\boldsymbol{\varepsilon} = e_{\mathrm{I}}\boldsymbol{\omega}_{\mathrm{I}} + \ldots + e_{\mathrm{VI}}\boldsymbol{\omega}_{\mathrm{VI}}.$$

I suggested in [9] the stiffness moduli $\lambda_{\mathrm{I}}, \ldots, \lambda_{\mathrm{VI}}$ to be called *Kelvin moduli* and I dare have the hope that this name shall be commonly accepted (as it does in [22]).

It is evident that

$$\lambda_{\mathrm{I}} \geq 0, \quad \ldots, \quad \lambda_{\mathrm{VI}} \geq 0$$

and these are the only limitations imposed by thermodynamics on the stiffness tensor **S**.

The variety of stiffness tensors can, therefore, be locally and continuously described by 21 parameters which constitute the following, quite independent groups: 6 *Kelvin moduli* $\lambda_{\mathrm{I}}, \ldots, \lambda_{\mathrm{VI}}$ defining the global stiffness, 12 invariants describing the orthonormal basis $\boldsymbol{\omega}_{\mathrm{I}}, \ldots, \boldsymbol{\omega}_{\mathrm{VI}}$ which I propose to call *elasticity distributors*, and 3 *orientation angles* placing the tensor **S** against the laboratory, e.g. Euler's angles of the proper basis of a selected tensor $\boldsymbol{\omega}_K$,

$$\underset{\substack{\text{Kelvin}\\\text{moduli}}}{6} + \underset{\substack{\text{elasticity}\\\text{distributors}}}{12} + \underset{\substack{\text{orientation}\\\text{angles}}}{3} = 21.$$

The Kelvin moduli and elasticity distributors constitute *a local functional basis of* $(6 + 12) = 18$ *invariants* on appropriate open neighbourhood of any extremely

complex stiffness tensor. The submanifold of extremely complex stiffness tensors is a dense set in manifold of all stiffness tensors.

For details see KELVIN [2], ANGLES d'AURIAC [6], PIPKIN [7], RYCHLEWSKI [8, 9], COWIN, MEHRABADI and SADEGH [21] and others.

5. Proper states and the symmetry of elastic materials

For an expert on anisotropy, especially for one involved in the physics of crystals, the difference between anisotropic materials comes down to the description of their spatial symmetry.

I strongly oppose that point of view. Nevertheless, symmetry is of a great importance and we have to refer to classical results, wandering for decades in an unaltered form from one textbook to another.

From the uniqueness of spectral decomposition immediately follows the main *theorem on elastic symmetry*:

THEOREM. *The group* $\mathcal{O}(\mathbf{S})$ *of rotational symmetry* ([2]) *of the stiffness tensor* $\mathbf{S}$ *is a symmetry group of orthogonal decomposition of stress-strain space* $\mathcal{S} = \mathcal{P}_1 + \ldots + \mathcal{P}_r$, *which corresponds to* $\mathbf{S}$.

Since the symmetry of the subspace $\mathcal{P}$ is identical with the symmetry of its orthogonal projector $\mathbf{P}$, then the theorem can be expressed as follows: for any rotation $\mathbf{Q} \in \mathcal{O}$

$$\mathbf{Q} * \mathbf{S} = \mathbf{S} \qquad \text{iff} \qquad \mathbf{Q} * \mathbf{P}_1 = \mathbf{P}_1, \ \ldots \ , \mathbf{Q} * \mathbf{P}_r = \mathbf{P}_r$$

(one of the projectors may be omitted), [9].

The mechanical problem of presenting all types of the elastic symmetry comes down to the description of types of symmetry of all possible orthogonal decompositions $\mathcal{S} = \mathcal{P}_1 + \ldots + \mathcal{P}_r$ of the space of the second order tensors. While solving this purely mathematical problem, one might make use of the fairly known Hermann's theorem: if a tensor of the order p has a symmetry axis of the order $q > r$, then it is symmetrical to each rotation around this axis [37]. The above outlined procedure leads to the well-known types of elastic symmetry as well as to all proper states corresponding to them.

From these considerations, it is particularly evident that the division of linearly elastic materials into types of symmetry has, in principle, nothing in common with crystallography. The true causes are the properties of Euclidean tensors of the fourth order and therefore, *exclusively the linearity of Hooke's law*. For instance, the presence of rotation axes of the fifth order in linear elastic materials is excluded by Hermann's theorem (which belongs to pure mathematics), since $5 > 4$, but not by the translation symmetries of crystalline lattices.

([2]) Since we are considering here only the tensors of even orders, we may limit ourselves only to the group of rotations $\mathcal{O}$.

Let us limit ourselves to presenting only two examples: the simplest and the most intricate one.

Isotropy, $\mathcal{O}(\mathbf{S}) = \mathcal{O}$. The only isotropic decomposition of the strain-stress space has the form

$$\mathcal{S} = \mathcal{P} \oplus \mathcal{D}, \qquad 6 = 1 + 5,$$

where $\mathcal{P}$ is a straight line of spherical tensors, and $\mathcal{D}$ is a 5-dimensional deviator space. Therefore the spectral decomposition of stiffness tensor of an isotropic material has a general form

$$\mathbf{S} = \lambda_{\mathcal{P}}\mathbf{P}_{\mathcal{P}} + \lambda_{\mathcal{D}}\mathbf{P}_{\mathcal{D}},$$

where the projectors are $\mathbf{P}_{\mathcal{P}} = \frac{1}{3}\mathbf{1} \otimes \mathbf{1}$, $\mathbf{P}_{\mathcal{D}} = \mathbb{1} - \frac{1}{3}\mathbf{1} \otimes \mathbf{1}$ and Kelvin's moduli are equal to: $\lambda_{\mathcal{P}} = 3K = 2\mu + 3\lambda$, $\lambda_{\mathcal{D}} = 2\mu$, where λ, μ are *Lamé's constants*. Decomposing each tensor $\boldsymbol{\alpha} = \boldsymbol{\alpha}_{\mathcal{P}} + \boldsymbol{\alpha}_{\mathcal{D}}$ into the hydrostatic part $\boldsymbol{\alpha}_{\mathcal{P}} \in \mathcal{P}$ and the deviatoric part $\boldsymbol{\alpha}_{\mathcal{D}} \in \mathcal{D}$, we write Hooke's law in its classical form

$$\boldsymbol{\sigma}_{\mathcal{P}} = 3K\boldsymbol{\varepsilon}_{\mathcal{P}}, \qquad \boldsymbol{\sigma}_{\mathcal{D}} = 2\mu\boldsymbol{\varepsilon}_{\mathcal{D}}.$$

In a general formula we have $\lambda_{\mathrm{I}} = \lambda_{\mathcal{P}}$, $\lambda_{\mathrm{II}} = \ldots = \lambda_{\mathrm{VI}} = \lambda_{\mathcal{D}}$.

Thus, for isotropy we have

$$\underset{\substack{\text{Kelvin}\\ \text{moduli}}}{(\ 2\ } + \underset{\substack{\text{elasticity}\\ \text{distributors}}}{0\ )} + \underset{\substack{\text{orientation}\\ \text{angles}}}{0} = 2.$$

Trigonal symmetry. The decomposition of strain-stress space, invariant under the group of rotations around versor $\mathbf{k}$ by angles $2\pi/3$, $4\pi/3$ has the form

$$\mathcal{S} = (\mathcal{K}_1 \oplus \mathcal{K}_2) \oplus (\mathcal{L}_1 \oplus \mathcal{L}_2), \qquad 6 = (1 + 1) + (2 + 2),$$

where straight lines $\mathcal{K}_1$, $\mathcal{K}_2$ and planes $\mathcal{L}_1$, $\mathcal{L}_2$ are not unique, but plane $\mathcal{K}_1 \oplus \mathcal{K}_2$ and 4-dimensional subspace $\mathcal{L}_1 \oplus \mathcal{L}_2$ are unique. The decomposition is described by proper elastic states

$$\mathcal{K}_1: \quad \boldsymbol{\omega}_{\mathrm{I}} \sim c \begin{pmatrix} \sin\kappa & 0 & 0 \\ 0 & \sin\kappa & 0 \\ 0 & 0 & \sqrt{2}\cos\kappa \end{pmatrix},$$

$$\mathcal{K}_2: \quad \boldsymbol{\omega}_{\mathrm{II}} \sim c \begin{pmatrix} \cos\kappa & 0 & 0 \\ 0 & \cos\kappa & 0 \\ 0 & 0 & -\sqrt{2}\sin\kappa \end{pmatrix},$$

$$\mathcal{L}_1: \quad \boldsymbol{\omega}_{\mathrm{III}} \sim c \begin{pmatrix} 0 & \cos\rho & \sin\rho \\ \cos\rho & 0 & 0 \\ \sin\kappa & 0 & 0 \end{pmatrix}, \qquad \boldsymbol{\omega}_{\mathrm{IV}} \sim c \begin{pmatrix} \cos\rho & 0 & 0 \\ 0 & -\cos\rho & \sin\rho \\ 0 & \sin\rho & 0 \end{pmatrix},$$

$$\mathcal{L}_2: \quad \boldsymbol{\omega}_{\mathrm{V}} \sim c \begin{pmatrix} 0 & -\sin\rho & \cos\rho \\ -\sin\rho & 0 & 0 \\ \cos\rho & 0 & 0 \end{pmatrix}, \qquad \boldsymbol{\omega}_{\mathrm{VI}} \sim c \begin{pmatrix} -\sin\rho & 0 & 0 \\ 0 & \sin\rho & \cos\rho \\ 0 & \cos\rho & 0 \end{pmatrix},$$

where κ, ρ are elasticity distributors, $c \equiv 1/\sqrt{2}$.

Stiffness tensor has the form

$$\mathbf{S} = \lambda_{\mathrm{I}}\mathbf{K}_1(\kappa) + \lambda_2\mathbf{K}_2(\kappa) + \lambda_3\mathbf{L}_1(\rho) + \lambda_4\mathbf{L}_2(\rho),$$

where

$$\mathbf{K}_1 = \boldsymbol{\omega}_{\mathrm{I}} \otimes \boldsymbol{\omega}_{\mathrm{I}}, \qquad \mathbf{K}_2 = \boldsymbol{\omega}_{\mathrm{II}} \otimes \boldsymbol{\omega}_{\mathrm{II}},$$
$$\mathbf{L}_1 = \boldsymbol{\omega}_{\mathrm{III}} \otimes \boldsymbol{\omega}_{\mathrm{III}} + \boldsymbol{\omega}_{\mathrm{IV}} \otimes \boldsymbol{\omega}_{\mathrm{IV}}, \qquad \mathbf{L}_2 = \boldsymbol{\omega}_{\mathrm{V}} \otimes \boldsymbol{\omega}_{\mathrm{V}} + \boldsymbol{\omega}_{\mathrm{VI}} \otimes \boldsymbol{\omega}_{\mathrm{VI}}.$$

We have here

$$\underset{\substack{\text{Kelvin}\\ \text{moduli}}}{4} + \underset{\substack{\text{elasticity}\\ \text{distributors}}}{2} + \underset{\substack{\text{orientation}\\ \text{angles}}}{2} = 8.$$

For $\kappa = \rho = \kappa^0$, $\operatorname{tg}\kappa^0 = \sqrt{2}$, $\lambda_3 = \lambda_4$ the trigonal material turns into a material of *cubic* symmetry.

For $\rho \to 0$ we obtain a general form of *transverse isotropic* material with proper elastic states shown in Fig. 3.

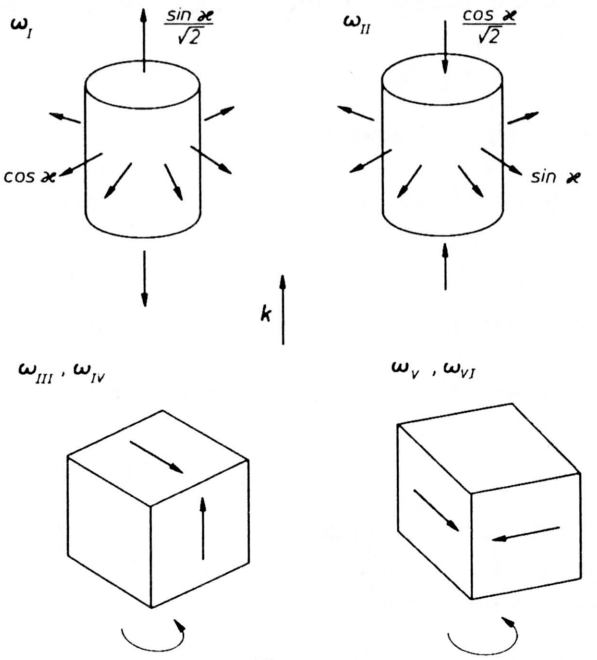

FIG. 3.

The types of decomposition of space $\mathcal{S}$, as well as the number of Kelvin's moduli, elasticity distributors and orientation angles for all types of symmetry are given in Table 1. I found it while preparing the paper [9] and the most important results were included in [8, 9]. They were later defined independently (and in a slightly different manner) in [18, 22, 32]. In S. SUTCLIFFE'S paper [32] Kelvin's moduli and proper states were presented for various crystals: copper, beryl, cobalt, magnesium, pentearythritol, tin, indium, Q-quartz, tourmaline, topaz, gallium, gypsum and copper sulfate $CuSO_4 \cdot 5H_20$.

Table 1.

Elastic symmetry	Spectral decomposition of strain-stress space	Kelvin moduli	elasticity distributors	orientation angles
isotropy	1 + 5	2	0	0
cubic	1 + 2 + 3	3	0	3
transverse isotropy	(1 + 1) + 2 + 2	4	1	2
4-fold symmetry axis	(1 + 1) + 1 + 1 + 2	5	1	3
3-fold symmetry axis	(1 + 1) + (2 + 2)	4	2	3
orthotropy	(1 + 1 + 1) + 1 + 1 + 1	6	3	3
one symmetry plane	(1 + 1 + 1 + 1) + (1 + 1)	6	7	3
full anisotropy	1 + 1 + 1 + 1 + 1 + 1	6	12	3

All that has been said here about the symmetry of tensor **S** refers – *mutatis mutandis* – to the limit tensor **H**.

6. On the optimum design of anisotropy

Let us repeat that the stiffness tensor **S** in a most general situation is described by the formula:

$$\mathbf{S} = \lambda_{\mathrm{I}}\boldsymbol{\omega}_{\mathrm{I}} \otimes \boldsymbol{\omega}_{\mathrm{I}} + \ldots + \lambda_{\mathrm{VI}}\boldsymbol{\omega}_{\mathrm{VI}} \otimes \boldsymbol{\omega}_{\mathrm{VI}}$$

with 6 + 12 invariant parameters and 3 orientation angles.

While the stiffness tensor is *given*, moduli λ and the proper states $\boldsymbol{\omega}$ are available through standard analytical procedures and ready-made computer programs,

$$\mathbf{S} \rightarrow (\lambda_{\mathrm{I}}, \ldots, \lambda_{\mathrm{VI}};\ \boldsymbol{\omega}_{\mathrm{I}}, \ldots, \boldsymbol{\omega}_{\mathrm{VI}}).$$

My view of the essence and usefulness of spectral decomposition is completely different: the sequence $(\lambda_{\mathrm{I}}, \ldots, \lambda_{\mathrm{VI}};\ \boldsymbol{\omega}_{\mathrm{I}}, \ldots, \boldsymbol{\omega}_{\mathrm{VI}})$ should be treated as a set of *decision parameters, defining linearly elastic material*

$$(\lambda_{\mathrm{I}}, \ldots, \lambda_{\mathrm{VI}};\ \boldsymbol{\omega}_{\mathrm{I}}, \ldots, \boldsymbol{\omega}_{\mathrm{VI}}) \rightarrow \mathbf{S}.$$

Taking any non-negative parameters $\lambda_{\mathrm{I}}, \ldots, \lambda_{\mathrm{VI}}$ and any orthonormal bases $\boldsymbol{\omega}_{\mathrm{I}}, \ldots, \boldsymbol{\omega}_{\mathrm{VI}}$ in a stress-strain space we obtain a certain, theoretically possible, linearly elastic material. Its characteristics are as follows:

$$
\begin{aligned}
\operatorname{Tr}\mathbf{S} &\equiv S_{ijij} = \lambda_{\mathrm{I}} + \ldots + \lambda_{\mathrm{VI}}, \\
\mathbf{S}\cdot\mathbf{S} &\equiv S_{ijkl}S_{ijkl} = \lambda_{\mathrm{I}}^2 + \ldots + \lambda_{\mathrm{VI}}^2, \\
\frac{1}{K} &= \frac{(\operatorname{tr}\boldsymbol{\omega}_{\mathrm{I}})^2}{\lambda_{\mathrm{I}}} + \ldots + \frac{(\operatorname{tr}\boldsymbol{\omega}_{\mathrm{VI}})^2}{\lambda_{\mathrm{VI}}}, \\
\frac{1}{E(\mathbf{n})} &= \frac{(\mathbf{n}\boldsymbol{\omega}_{\mathrm{I}}\mathbf{n})^2}{\lambda_{\mathrm{I}}} + \ldots + \frac{(\mathbf{n}\boldsymbol{\omega}_{\mathrm{I}}\mathbf{n})^2}{\lambda_{\mathrm{VI}}}, \\
-\frac{\nu(\mathbf{m},\mathbf{n})}{E(\mathbf{n})} &= \frac{(\mathbf{m}\boldsymbol{\omega}_{\mathrm{I}}\mathbf{m})(\mathbf{n}\boldsymbol{\omega}_{\mathrm{I}}\mathbf{n})}{\lambda_{\mathrm{I}}} + \ldots + \frac{(\mathbf{m}\boldsymbol{\omega}_{\mathrm{VI}}\mathbf{m})(\mathbf{n}\boldsymbol{\omega}_{\mathrm{VI}}\mathbf{n})}{\lambda_{\mathrm{VI}}}, \\
\frac{1}{4G(\mathbf{m},\mathbf{n})} &= \frac{(\mathbf{m}\boldsymbol{\omega}_{\mathrm{I}}\mathbf{n})^2}{\lambda_{\mathrm{I}}} + \ldots + \frac{(\mathbf{m}\boldsymbol{\omega}_{\mathrm{VI}}\mathbf{n})^2}{\lambda_{\mathrm{VI}}},
\end{aligned}
$$

where $\operatorname{Tr}\mathbf{S}/6$ is *mean stiffness modulus*, $\mathbf{S}\cdot\mathbf{S}$ *global stiffness*, $K^{-1} = \mathbf{1}\cdot\mathbf{C}\cdot\mathbf{1}$ the *bulk modulus*, $E(\mathbf{n})$ *Young's modulus* in direction $\mathbf{n}$, $\nu(\mathbf{n},\mathbf{m})$ *Poisson ratio* in direction $\mathbf{m}$ under stretch in direction $\mathbf{n}$, $G(\mathbf{n},\mathbf{m})$, $\mathbf{nm} = 0$ is *shear modulus* in the plane defined by $\mathbf{n}, \mathbf{m}$.

In *conventional language*, $\mathbf{S} \sim S_{ijkl}$, we have an amorphic set of S_{ijkl} components in an accidental base. In the *proposed language* we have decision variables $(\lambda, \boldsymbol{\omega})$, which have quite a clear formal status (eigenvalues and eigenelements) and a fairly good physical meaning (stiffness moduli and directions of energy extrema).

Identically, decision variables which shape the limit properties may be taken in the form

$$(\lambda_{\mathrm{I}}, \ldots, \lambda_{\mathrm{VI}};\ \rho_{\mathrm{I}}, \ldots, \rho_{\mathrm{VI}}) \to \mathbf{H}.$$

7. On types of elastic bodies. A particular role of pure shears

Spectral decompositions open completely new possibilities of comparing elastic materials, not connected with their symmetry at all. Among others, they can be distinguished according to the Kelvin moduli, to the types of proper states and to the orthonormal systems which they form.

Particularly interesting are here the *pure shears* defined by $\operatorname{tr}\boldsymbol{\tau} = 0$, $\det\boldsymbol{\tau} = 0$, Fig. 4. One can show that, for example, *an elastic material is isotropic iff each pure shear is its proper state*. The equality of stiffness moduli for all pure shears is here the result, not the assumption. Similarly by pure shears one may define elastic orthotropy or transverse isotropy.

The question arises: do there exist materials of the form

$$\mathbf{S} = \lambda\mathbf{1}\otimes\mathbf{1} + 2(\mu_1\boldsymbol{\tau}_1\otimes\boldsymbol{\tau}_1 + \ldots + \mu_5\boldsymbol{\tau}_5\otimes\boldsymbol{\tau}_5),$$

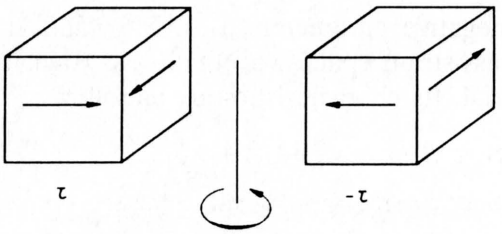

FIG. 4.

where $\mu_i \neq \mu_j$ for $i \neq j$ and all proper states different from the hydrostatic state, $\boldsymbol{\tau}_1, \ldots, \boldsymbol{\tau}_5$ are pure shears? In other words: do there exist in 5-dimensional deviator space $\mathcal{D} \subset \operatorname{sym} \mathcal{E} \otimes \mathcal{E}$, orthonormal bases consisting of pure shears only?

A positive answer to that was found by BLINOWSKI and RYCHLEWSKI [38] ([3]). The presented class of bases is a 2-parameter one. Here is an example for direct verification of equations $\operatorname{tr} \boldsymbol{\tau}_i = 0$, $\det \boldsymbol{\tau}_i = 0$, $\boldsymbol{\tau}_i \cdot \boldsymbol{\tau}_j = 0$, $i, j = 1, \ldots, 5$

$$\boldsymbol{\tau}_1 \sim \frac{1}{2}\begin{pmatrix} \sqrt{2} & 0 & 0 \\ 0 & -\sqrt{2} & 0 \\ 0 & 0 & 0 \end{pmatrix}, \qquad \boldsymbol{\tau}_2 \sim \frac{1}{2}\begin{pmatrix} 0 & 0 & 0 \\ 0 & 0 & \sqrt{2} \\ 0 & \sqrt{2} & 0 \end{pmatrix},$$

$$\boldsymbol{\tau}_3 \sim \frac{1}{6}\begin{pmatrix} 0 & 2\sqrt{2} & -\sqrt{10} \\ 2\sqrt{2} & 0 & 0 \\ -\sqrt{10} & 0 & 0 \end{pmatrix}, \qquad \boldsymbol{\tau}_4 \sim \frac{1}{6}\begin{pmatrix} \sqrt{3} & \sqrt{5} & 2 \\ \sqrt{5} & \sqrt{3} & 0 \\ 2 & 0 & -2\sqrt{3} \end{pmatrix},$$

$$\boldsymbol{\tau}_5 \sim \frac{1}{6}\begin{pmatrix} \sqrt{3} & -\sqrt{5} & -2 \\ -\sqrt{5} & \sqrt{3} & 0 \\ -2 & 0 & -2\sqrt{3} \end{pmatrix}.$$

8. Plane states, plates and shells, [39]

For a quick orientation and to form an intuition in the presented approach, let us examine the simplest case, that is when we deal only with plane tensors,

$$\dim \mathcal{E} = 2, \qquad \dim \mathcal{S} = 2^2 - 1 = 3, \qquad \dim \mathcal{T} = 3^2 - 3 = 6.$$

The results will be applicable to plates and shells.

The space of symmetric plane tensors $\boldsymbol{\alpha}$ will be presented as an orthogonal sum

$$\mathcal{S} = \mathcal{P} \oplus \mathcal{D}, \qquad 3 = 1 + 2,$$

([3]) Josef Matoulek from Prague took part in search of such bases.

where straight line $\mathcal{P}$ consists of plane isotropic tensors and plane $\mathcal{D}$ consists of pure shears, $\boldsymbol{\alpha} = \boldsymbol{\alpha}_{\mathcal{P}} + \boldsymbol{\alpha}_{\mathcal{D}}$,

$$\begin{pmatrix} \alpha_{11} & \alpha_{12} \\ \alpha_{12} & \alpha_{22} \end{pmatrix} = \begin{pmatrix} \alpha & 0 \\ 0 & \alpha \end{pmatrix} + \begin{pmatrix} \beta & \gamma \\ \gamma & -\beta \end{pmatrix}.$$

Stiffness tensors have the form

$$\mathbf{S} = \lambda_{\mathrm{I}}\boldsymbol{\omega}_{\mathrm{I}} \otimes \boldsymbol{\omega}_{\mathrm{I}} + \lambda_{\mathrm{II}}\boldsymbol{\omega}_{\mathrm{II}} \otimes \boldsymbol{\omega}_{\mathrm{II}} + \lambda_{\mathrm{III}}\boldsymbol{\omega}_{\mathrm{III}} \otimes \boldsymbol{\omega}_{\mathrm{III}},$$

where $\boldsymbol{\omega}_{\mathrm{I}}, \boldsymbol{\omega}_{\mathrm{II}}, \boldsymbol{\omega}_{\mathrm{III}}$ is an orthonormal basis in $\mathcal{S}$, $\boldsymbol{\omega}_K \cdot \boldsymbol{\omega}_L = \delta_{KL}$, $K, L = \mathrm{I}, \mathrm{II}, \mathrm{III}$.

It will be convenient to represent the plane tensors of the second order in the following form

$$\boldsymbol{\omega} = \kappa(\cos\chi\mathbf{1} + \sin\chi\mathbf{d}(\vartheta)),$$

where

$$\mathbf{1} \sim \begin{pmatrix} 1 & 0 \\ 0 & 1 \end{pmatrix}, \qquad \mathbf{d}(\vartheta) \sim \begin{pmatrix} \cos\vartheta & \sin\vartheta \\ \sin\vartheta & -\cos\vartheta \end{pmatrix}.$$

Since space $\mathcal{S}$ is here 3-dimensional, we enjoy the privilege of illustrating all our considerations by nice pictures, Fig. 5.

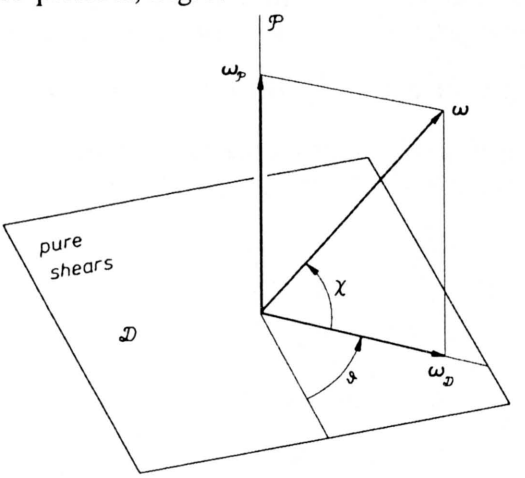

FIG. 5.

A particular role is played by pure shears. 6-dimensional manifolod of stiffness tensors can be divided into disjoint types:

A – no pure shear is a proper state,

B – exactly one pure shear is a proper state,

C – exactly two pure shears are proper states,

D – each pure shear is a proper state.

TYPE A. (Fig. 6). Proper basis $\boldsymbol{\omega}$ is here in a general position and touches neither the plane $\mathcal{D}$ nor the straight line $\mathcal{P}$.

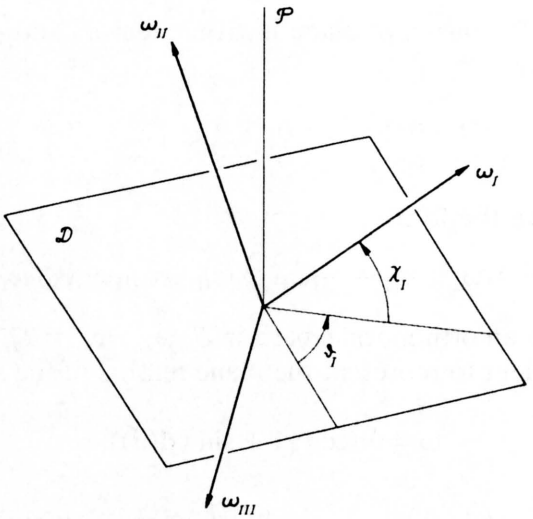

FIG. 6.

Stiffness tensor of this type is described by (3 + 2) + 1 = 6 independent parameters: stiffness moduli $\lambda_{\mathrm{I}}, \lambda_{\mathrm{II}}, \lambda_{\mathrm{III}}$, distributors $\chi_{\mathrm{I}}, \chi_{\mathrm{II}}$, orientation angle ϑ_{I}. The remaining parameters $\chi_{\mathrm{III}}, \vartheta_{\mathrm{II}}, \vartheta_{\mathrm{III}}$ result from the orthogonality conditions

$$\operatorname{tg}\chi_K \operatorname{tg}\chi_L + \cos(\vartheta_K - \vartheta_L) = 0, \qquad K, L = \mathrm{I}, \mathrm{II}, \mathrm{III}.$$

TYPE B. (Fig. 7). If exactly one proper state is a pure shear, say $\boldsymbol{\omega}_{\mathrm{III}} \in \mathcal{D}$, then $\chi_{\mathrm{I}} = \chi$, $\chi_{\mathrm{II}} = \pi/2 - \chi$, $\chi_{\mathrm{III}} = 0$, $\vartheta_{\mathrm{I}} = \vartheta$, $\vartheta_{\mathrm{II}} = \vartheta + \pi$, $\vartheta_{\mathrm{III}} = \vartheta + 3\pi/2$.

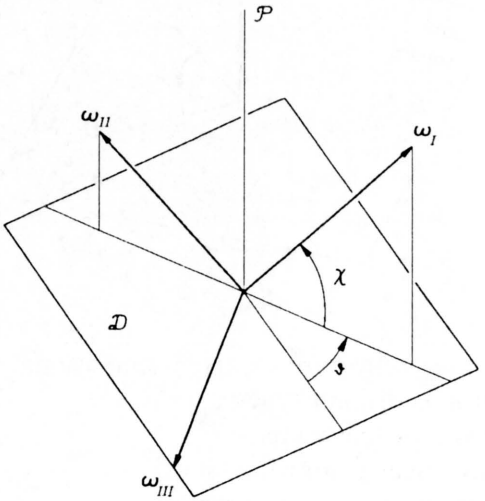

FIG. 7.

Stiffness tensor of this type is described by (3 + 1) + 1 = 5 independent parameters: moduli $\lambda_{\mathrm{I}}, \lambda_{\mathrm{II}}, \lambda_{\mathrm{III}}$, stiffness distributor χ, orientation angle ϑ.

TYPE C (Fig. 8). If exactly two proper states are pure shears, say $\boldsymbol{\omega}_{II}, \boldsymbol{\omega}_{III} \in \mathcal{D}$, then $\chi_I = \pi/2$, $\chi_{II} = \chi_{III} = 0$, $\vartheta_{II} = \vartheta$, $\vartheta_{III} = \vartheta + \pi/2$. Stiffness tensor of this type is described by (3) + 1 = 4 independent parameters: stiffness moduli $\lambda_I, \lambda_{II}, \lambda_{III}$, orientation angle ϑ.

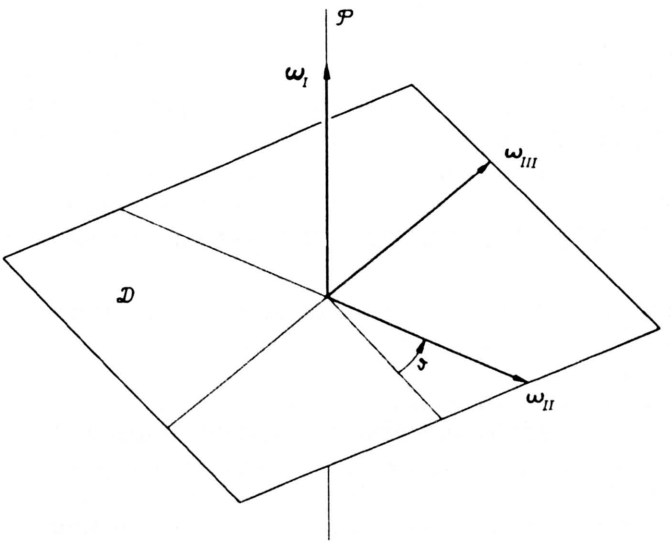

FIG. 8.

TYPE D. If each pure shear $\boldsymbol{\tau} \in \mathcal{D}$ is a proper state, then, according to Fig. 5, the isotropic tensor $\mathbf{1}/\sqrt{2}$ is a proper state as well. Therefore

$$\mathbf{S} = \lambda_{\mathcal{P}}\mathbf{P}_{\mathcal{P}} + \lambda_{\mathcal{D}}\mathbf{P}_{\mathcal{D}},$$

$$\mathbf{P}_{\mathcal{P}} = \frac{1}{2}\mathbf{1} \otimes \mathbf{1}, \qquad \mathbf{P}_{\mathcal{D}} = \mathbb{1} - \frac{1}{2}\mathbf{1} \otimes \mathbf{1}.$$

Quite unexpectedly, the obtained classification of plane stiffness tensors with regard to the types of proper states is, at the same time, their complete classification with regard to symmetry: Type A $\leftrightarrow$ full anisotropy, Type B $\leftrightarrow$ symmetry of a rectangle, Type C $\leftrightarrow$ symmetry of a square, Type D $\leftrightarrow$ isotropy. Climbing the steps of increasing symmetry is accompanied by the increase in the number of pure shears occuring as proper states.

All that we have presented here applies to plane limit tensors $\mathbf{H}$.

9. Locked strains and unsupported stresses, [40, 41]

The language of proper states is an adequate one to describe linearly elastic materials with constraints or/and looses. As to constraints, it was PIPKIN [7] who was the first, as far as I know, who noticed that (see also [8, 9]).

1. Let us first examine a material with such an internal structure (strong fibers or sheets, etc.) that it hinders some modes of strains so strongly that one may regard them as negligibly small,

$$\boldsymbol{\sigma} \neq \mathbf{0} \qquad \text{but} \qquad \boldsymbol{\varepsilon} = \mathbf{0}.$$

We call some stress $\boldsymbol{\sigma}$ *reactive* when it does not cause any strain $\mathbf{C} \cdot \boldsymbol{\sigma} = \mathbf{0}$. The set of all reactive stresses is the kernel of the operator $\operatorname{Ker}\mathbf{C}$. Each strain $\boldsymbol{\varepsilon}$ that is admissible in the material under consideration is orthogonal to this kernel, $\boldsymbol{\varepsilon} \perp \operatorname{Ker}\mathbf{C}$, because of $\boldsymbol{\omega} \cdot \boldsymbol{\varepsilon} = \boldsymbol{\omega} \cdot \mathbf{C} \cdot \boldsymbol{\sigma} = \boldsymbol{\sigma} \cdot \mathbf{C} \cdot \boldsymbol{\omega} = 0$ for each $\boldsymbol{\omega} \in \operatorname{Ker}\mathbf{C}$. We call the kernel $\mathcal{P}_c \equiv \operatorname{Ker}\mathbf{C}$ the *space of locked strains and reactive stresses*. Its orthogonal complement $\mathcal{P}_a$ will be called the space of *admissible strain and active stresses*.

Thus the material with such restrains on strains is described as follows:

$$\mathcal{S} = \underset{\substack{\downarrow \\ \text{admissible strains} \\ \text{and active stresses}}}{\mathcal{P}_a} \oplus \underset{\substack{\downarrow \\ \text{locked strains and} \\ \text{reactive stresses}}}{\mathcal{P}_c}$$

$$\boldsymbol{\varepsilon} = \boldsymbol{\varepsilon}_a + \mathbf{0}, \qquad \boldsymbol{\sigma} = \boldsymbol{\sigma}_a + \boldsymbol{\sigma}_r, \qquad \boldsymbol{\sigma}_r \quad \text{is free.}$$

Hooke's law connects admissible strain with active stress

$$\boldsymbol{\varepsilon}_a = \mathbf{C}_a \cdot \boldsymbol{\sigma}_a,$$

where $\mathbf{C}_a$ is an invertible operator that maps $\mathcal{P}_a$ onto itself.

This situation exactly corresponds to the proper states approach because the kernel $\mathcal{P}_c$ consists of proper states with zero compliance modulus. This corresponds to limit transition $\lambda \to \infty$ in $\mathbf{C} = \ldots + \frac{1}{\lambda}\mathbf{P} + \ldots$ stiffening the material up to rigidity with respect to the strains belonging to $\mathcal{P} = \operatorname{Im}\mathbf{P}$.

PIPKIN [7] examined in detail a particular case $\dim \mathcal{P}_c = 1$, $\dim \mathcal{P}_a = 5$, that is when the constraints have the form $\boldsymbol{\varepsilon} \cdot \boldsymbol{\omega} = 0$ for some tensor $\boldsymbol{\omega}$. When $\boldsymbol{\omega} = \mathbf{1}$ this means *incompressibility*, when $\boldsymbol{\omega} = \mathbf{k} \otimes \mathbf{k}$ – *fiber inextensibility*.

2. In exactly the same way, one can examine a situation where the structure of material enables some modes of strain to appear under negligibly small stresses,

$$\boldsymbol{\varepsilon} \neq \mathbf{0} \qquad \text{but} \qquad \boldsymbol{\sigma} = \mathbf{0}.$$

We call some strain $\boldsymbol{\varepsilon}$ *loose* when it occurs without any stresses, $\mathbf{S} \cdot \boldsymbol{\varepsilon} = \mathbf{0}$. Each stress $\boldsymbol{\sigma}$ that is admissible in the material under consideration is orthogonal to all loose strains, $\boldsymbol{\sigma} \perp \operatorname{Ker}\mathbf{S}$ because of $\boldsymbol{\omega} \cdot \boldsymbol{\sigma} = \boldsymbol{\omega} \cdot \mathbf{S} \cdot \boldsymbol{\varepsilon} = \boldsymbol{\varepsilon} \cdot \mathbf{S} \cdot \boldsymbol{\omega} = 0$ for all $\boldsymbol{\omega} \in \operatorname{Ker}\mathbf{S}$. We call the kernel $\mathcal{P}_l \equiv \operatorname{Ker}\mathbf{S}$ the space of *loose strains and unsupported stresses*. Its orthogonal complement $\mathcal{P}_a$ will be called the space of *active strains and stresses*.

Thus we have

$$\mathcal{S} = \mathcal{P}_a \oplus \mathcal{P}_l,$$

$$\boldsymbol{\sigma} = \boldsymbol{\sigma}_a + \mathbf{0}, \qquad \boldsymbol{\varepsilon} = \boldsymbol{\varepsilon}_a + \boldsymbol{\varepsilon}_l, \qquad \boldsymbol{\varepsilon}_l \quad \text{is free.}$$

This corresponds to limit transition $\lambda \to 0$ in $\mathbf{S} = \ldots + \lambda\mathbf{P} + \ldots$.

3. Finally, one cannot neglect such a possibility when some modes of strains are locked and some others are loose

$$\boldsymbol{\sigma} \neq \mathbf{0} \quad \text{but} \quad \boldsymbol{\varepsilon} = \mathbf{0},$$
$$\boldsymbol{\varepsilon} \neq \mathbf{0} \quad \text{but} \quad \boldsymbol{\sigma} = \mathbf{0}.$$

In this case we have

$$\mathcal{S} = \underset{\substack{\downarrow \\ \text{active stresses} \\ \text{and strains}}}{\mathcal{P}_a} \oplus \underset{\substack{\uparrow \\ \text{locked strains and} \\ \text{reactive stresses}}}{\mathcal{P}_c} \oplus \underset{\substack{\downarrow \\ \text{loose strains and} \\ \text{unsupported stresses}}}{\mathcal{P}_l}$$

$$\boldsymbol{\sigma} = \boldsymbol{\sigma}_a + \boldsymbol{\sigma}_r + \mathbf{0}, \quad \boldsymbol{\sigma}_r \quad \text{is free,}$$
$$\boldsymbol{\varepsilon} = \boldsymbol{\varepsilon}_a + \mathbf{0} + \boldsymbol{\varepsilon}_l, \quad \boldsymbol{\varepsilon}_l \quad \text{is free.}$$

Hooke's law takes the form

$$\boldsymbol{\varepsilon} = \mathbf{C}_a \cdot \boldsymbol{\sigma}_a, \qquad \boldsymbol{\sigma}_a = \mathbf{S}_a \cdot \boldsymbol{\varepsilon}_a,$$

where $\mathbf{C}_a, \mathbf{S}_a$ map active space $\mathcal{P}_a$ onto itself.

As far as I know the theory of bodies made of such materials has not been developed, of course apart from the classical *incompressible inviscid fluids*, when

$$\mathcal{S} = \mathcal{P}_c \oplus \mathcal{P}_l, \qquad \mathcal{P}_c = \mathcal{P}, \qquad \mathcal{P}_l = \mathcal{D},$$

$$\boldsymbol{\sigma} = \boldsymbol{\sigma}_r \in \mathcal{P}, \qquad \boldsymbol{\varepsilon} = \boldsymbol{\varepsilon}_l \in \mathcal{D}.$$

The stresses are reactive and hydrostatic, the strains are loose and purely distortional. Strains are not connected with stresses at all.

The model of material with locked strains was used in the description of multidirectional composites with families of inextensible fibers, RYCHLEWSKI and XIAO HENG [17].

Let us examine s families of fibers directed along unit vectors $\mathbf{k}_1, \ldots, \mathbf{k}_s$. Constraints have the form $\boldsymbol{\varepsilon} \cdot \boldsymbol{\pi}_1 = \ldots = \boldsymbol{\varepsilon} \cdot \boldsymbol{\pi}_s = 0$, $\boldsymbol{\pi}_1 = \mathbf{k}_1 \otimes \mathbf{k}_1, \ldots, \boldsymbol{\pi}_s = \mathbf{k}_s \otimes \mathbf{k}_s$. Locked strain space has the form $\mathcal{P}_r = \text{lin}\,(\boldsymbol{\pi}_1, \ldots, \boldsymbol{\pi}_s)$.

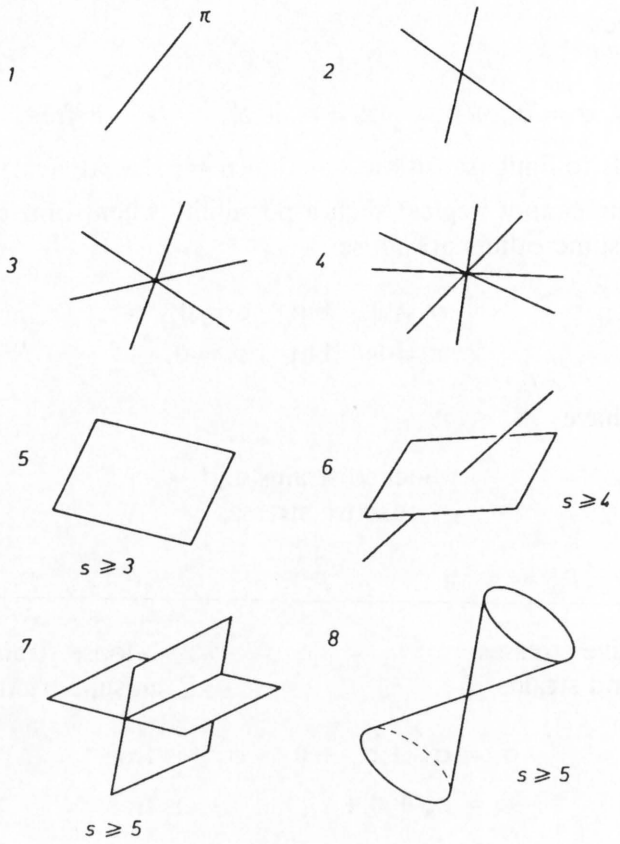

FIG. 9.

Sufficiently large or/and properly directed system of fibers can entirely lock the material, $\mathcal{S} = \mathcal{P}_r$. The following, purely kinematic theorem was proved:

A system of inextensible fibers does not entirely lock the material only in 8 *cases, as shown in Fig.* 9*; the dimensions of active strain spaces for these cases are as follows:* $\dim \mathcal{P}_a = 5,\ 4,\ 3,\ 2,\ 3,\ 2,\ 1,\ 1.$

In the Cases 1, 2, 3, 4 the number of fibers passing through a point is $s = 1, 2, 3, 4$, respectively, and no three fibers belong to one plane. In the Cases 5 we have at least 3 fibers and they all belong to one plane and lock it. In the Case 6 $s \geq 4$. In Case 7 $s \geq 5$ and a least 3 fibers lock a plane, and then at least two fibers lock another one. In Case 8 $s \geq 5$ and all fibers belong to an elliptical cone and lock it.

It is not difficult to establish the stiffness tensor for each case. For example, in the case of isotropic matrix and Case 6 of the system of fibers, we have

$$\mathbf{S} = \left(\lambda \frac{2\cos^2\theta}{1+\cos^2\theta} + 2\mu\right) \boldsymbol{\omega}_1 \otimes \boldsymbol{\omega}_1 + 2\mu \boldsymbol{\omega}_2 \otimes \boldsymbol{\omega}_2,$$

where θ is the slope angle shown in Fig. 10, λ, μ are Lamé's moduli of the matrix and $\boldsymbol{\omega}_1, \boldsymbol{\omega}_2$ are proper states given in [17].

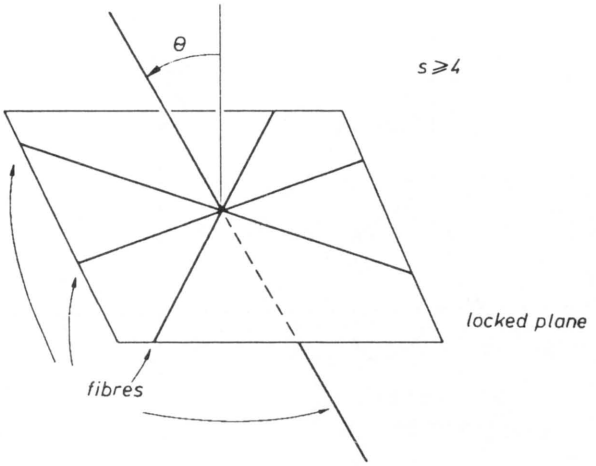

FIG. 10.

10. Safe stresses, energy-orthogonal stresses

All that has been said about elasticity tensors passes – *mutatis mutandis* – onto the limit tensor **H**, describing the range of elastic behaviour $\boldsymbol{\sigma} \cdot \mathbf{H} \cdot \boldsymbol{\sigma} \leq 1$. Spectral decomposition has the form

$$\mathbf{H} = \frac{1}{\chi_1^2}\mathbf{R}_1 + \ldots + \frac{1}{\chi_k^2}\mathbf{R}_k, \qquad k \leq 6,$$

where the sequence $\mathbf{R}_1, \ldots, \mathbf{R}_k$ is an orthogonal decomposition of the unit operator, and the sequence $\chi_1, \ldots, \chi_k$ is constituted by respective elasticity limits. The limit condition takes the form

$$\frac{\boldsymbol{\sigma}_1 \cdot \boldsymbol{\sigma}_1}{\chi_1^2} + \ldots + \frac{\boldsymbol{\sigma}_k \cdot \boldsymbol{\sigma}_k}{\chi_k^2} \leq 1,$$

where $\boldsymbol{\sigma}_i \equiv \mathbf{R}_i \cdot \boldsymbol{\sigma}$, i.e. $\boldsymbol{\sigma} = \boldsymbol{\sigma}_1 + \ldots + \boldsymbol{\sigma}_r$, $\boldsymbol{\sigma}_i \cdot \boldsymbol{\sigma}_j = 0$ for $i \neq j$. It describes the inside of a 6-dimensional ellipsoid in the stress space. If $\chi_l \to \infty$, then $\mathcal{R}_l = \operatorname{Im} \mathbf{R}_l$ becomes the subspace of safe stresses, $\mathcal{S} = \mathcal{R}_s \oplus \mathcal{R}_{\text{uns}}$, Fig. 11.

For isotropic material (see p. 5)

$$\boldsymbol{\sigma} \cdot \mathbf{H} \cdot \boldsymbol{\sigma} = \frac{\boldsymbol{\sigma}_\mathcal{P} \cdot \boldsymbol{\sigma}_\mathcal{P}}{\chi_\mathcal{P}^2} + \frac{\boldsymbol{\sigma}_\mathcal{D} \cdot \boldsymbol{\sigma}_\mathcal{D}}{\chi_\mathcal{D}^2}.$$

If $\chi_\mathcal{P} \to \infty$, then we obtain the classical Maxwell – Huber – Mises – Hencky condition:

$$\boldsymbol{\sigma}_\mathcal{D} \cdot \boldsymbol{\sigma}_\mathcal{D} \leq \chi_\mathcal{D}^2.$$

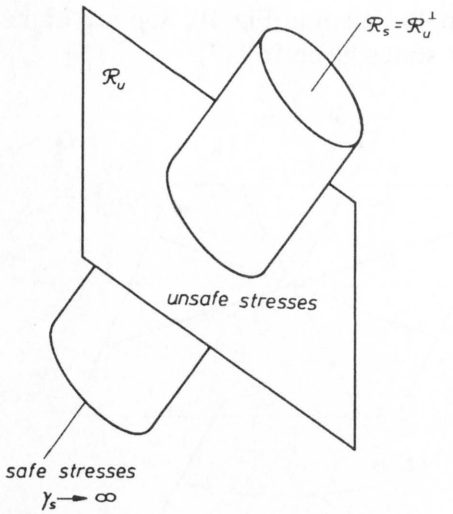

FIG. 11.

Since $\boldsymbol{\sigma}_{\mathcal{D}} \cdot \boldsymbol{\sigma}_{\mathcal{D}}/4\mu$ is the distortion energy, this condition limits this energy. As Maxwell wrote in a letter to KELVIN (1856) "I have strong reasons for believing that when $\boldsymbol{\sigma}_{\mathcal{D}} \cdot \boldsymbol{\sigma}_{\mathcal{D}}/4\mu$ (our notation, J.R.) reaches a certain limit, then the element will begin to give way". HUBER (1904) and HENCKY (1924) recreated this point of view independently (see [10]).

The energy is the most universal physical notion. The idea, that the stored elastic energy, if properly calculated, is an appropriate measure of the hazard of the material giving way appears attractive indeed. A question arises here: *does the Mises condition* $\boldsymbol{\sigma} \cdot \mathbf{H} \cdot \boldsymbol{\sigma} \leq 1$ *have any energy interpretation for any anisotropic material?*

This question was posed in 1956 by my professors W. OLSZAK and W. URBANOWSKI. The customary idea of the exceptional character of hydrostatic stress and dilatational strain precluded the finding of a general answer [42, 43]. I arrived at it only 27 years later using the proper states approach [10].

The crucial point of this answer lies in yet another idea. Two states of stress $\boldsymbol{\alpha}$ and $\boldsymbol{\beta}$ I called *energy-orthogonal* if one of them does not work on the strain caused by the other, i.e. when $\boldsymbol{\alpha} \cdot \mathbf{C} \cdot \boldsymbol{\beta} = 0$. The energy orthogonality will be denoted by $\boldsymbol{\alpha} \dot{\perp} \boldsymbol{\beta}$.

Afterwards, pure mathematics comes into play. The mapping $(\boldsymbol{\alpha}, \boldsymbol{\beta}) \to \boldsymbol{\alpha} \cdot \mathbf{C} \cdot \boldsymbol{\beta} = \boldsymbol{\beta} \cdot \mathbf{C} \cdot \boldsymbol{\alpha}$ is a symmetric and positive definite bilinear form on stress-strain space $\mathcal{S}$ and it can be regarded as a new *energy scalar product*

$$\boldsymbol{\alpha} \bullet \boldsymbol{\beta} \equiv \boldsymbol{\alpha} \cdot \mathbf{C} \cdot \boldsymbol{\beta}.$$

But, then space $\mathcal{S}$ with new scalar product also obeys the general spectral theory!

Applying it we introduce *energy proper states* and *energy proper values*

$$\mathbf{H} \bullet \chi = \mu\chi, \qquad \chi \cdot \chi = 1,$$

where $\mathbf{H}\bullet$ is the symmetric linear operator acting according to the formula $\mathbf{H}\bullet\boldsymbol{\omega} = \mathbf{H} \cdot (\mathbf{C} \cdot \boldsymbol{\omega}) = (\mathbf{H} \circ \mathbf{C}) \cdot \boldsymbol{\omega}$. As a result we obtain the following theorem:

THEOREM. *For each linearly elastic material, described by the compliance tensor* $\mathbf{C}$ *and the limit tensor* $\mathbf{H}$, *there is exactly one energy orthogonal decomposition of the stress space*

$$\mathcal{S} = \mathcal{H}_1 \oplus \ldots \oplus \mathcal{H}_l, \qquad l \leq 6,$$

$\mathcal{H}_i \overset{\cdot}{\perp} \mathcal{H}_j$ *for* $i \neq j$, *and only one sequence of energy limits of elasticity* $\gamma_1 < \ldots < \gamma_l$, *such that*

$$\boldsymbol{\sigma} \cdot \mathbf{H} \cdot \boldsymbol{\sigma} = \frac{1}{\gamma_1} \boldsymbol{\sigma}_1 \cdot \mathbf{C} \cdot \boldsymbol{\sigma}_1 + \ldots + \frac{1}{\gamma_l} \boldsymbol{\sigma}_l \cdot \mathbf{C} \cdot \boldsymbol{\sigma}_l,$$

where

$$\boldsymbol{\sigma} = \boldsymbol{\sigma}_1 + \ldots + \boldsymbol{\sigma}_l, \qquad \boldsymbol{\sigma}_i \in \mathcal{H}_i, \qquad i = 1, \ldots, l.$$

(As a matter of fact this is a certain form of the classical theorem on simultaneous transforming into the diagonal form of two quadratic forms, one of which is positive definite).

But $2E(\boldsymbol{\sigma}) = \boldsymbol{\sigma} \cdot \mathbf{C} \cdot \boldsymbol{\sigma}$ is twice the stored elastic energy of stress $\boldsymbol{\sigma}$. Therefore the Olszak–Urbanowski problem has the *unique solution*:

The Mises limit criterion bounds the weighted sum of stored elastic energies corresponding to uniquely defined, energy-orthogonal parts of stress

$$\frac{1}{\gamma_1} E(\boldsymbol{\sigma}_1) + \ldots + \frac{1}{\gamma_l} E(\boldsymbol{\sigma}_l) \leq 1.$$

If the energy limit of elasticity γ_1 tends to infinity, $\gamma_1 \to \infty$, then the space $\mathcal{H}_1$ consists of safe stresses.

The notion of energy orthogonality was examined later by THEOCARIS and PHILIPPIDES [28, 29].

CONLUDING REMARK. Polishing a few new faces of a precious stone discovered by Robert Hooke was my great honor and pleasure.

NOTATION. With respect to well-known Cartesian index notation we have

$$\boldsymbol{\alpha} \otimes \boldsymbol{\beta} \leftrightarrow \alpha_{ij}\beta_{kl}, \qquad \boldsymbol{\alpha} \cdot \boldsymbol{\beta} \leftrightarrow \alpha_{ij}\beta_{ij}, \qquad \mathbf{1} \leftrightarrow \delta_{ij},$$

$$\mathbf{A} \cdot \boldsymbol{\alpha} \leftrightarrow A_{ijpq}\alpha_{pq}, \qquad \boldsymbol{\alpha} \cdot \mathbf{A} \cdot \boldsymbol{\beta} \leftrightarrow A_{ijkl}\alpha_{ij}\beta_{kl},$$

$$\mathbf{A} \circ \mathbf{B} \leftrightarrow A_{ijpq}B_{pqkl}, \qquad \mathbb{1}_{ijkl} = \frac{1}{2}(\delta_{ik}\delta_{jl} + \delta_{il}\delta_{kj}),$$

$$\mathbf{Q} * (\boldsymbol{\alpha} \otimes \boldsymbol{\beta}) = \mathbf{Q} * \boldsymbol{\alpha} \otimes \mathbf{Q} * \boldsymbol{\beta}, \qquad \mathbf{Q} * \boldsymbol{\alpha} \leftrightarrow Q_{ip} Q_{jq} \alpha_{pq},$$
$$\mathbf{Q} * \mathbf{A} \leftrightarrow Q_{ip} Q_{jq} Q_{kr} Q_{ls} A_{pqrs}.$$

Paper supported by Grant KBN 3 P 404 027 05.

References

1. R. HOOKE, *Lecture de potentia restitutiva or of spring explaining the power of springing bodies to which are added some collections*, London, Martin, p. 56, 1678.
2. W. THOMSON (Lord Kelvin), *On six principal strains of an elastic solid*, Phil. Trans. R. Soc., **166**, 495–498, 1856.
3. W. THOMSON (Lord Kelvin), *Elasticity*, Encyclopaedia Britannica, Adam and Charles Black, Edinburgh 1878.
4. I. TODHUNTER, K. PEARSON, *A history of the theory of elasticity*, Univ. Press, Cambridge 1886.
5. K.S. ALEKSANDROV, *Elastic properties of anisotropic media* [in Russian], Dissertation, Inst. of Crystallography, USSR Acad. Sci., unpublished, 1967.
6. P. ANGLES d'AURIAC, *Etude du tenseur d'anisotropie, basée sur la représentation d'un tenseur symmetrique dans un espace E_3 par un vecteur dans un espace E_6* [in French], C.R. Acad. Sc. Paris, **272**, ser. A, 612–613, 1971.
7. A.C. PIPKIN, *Constraints in linearly elastic materials*, J. Elasticity, **6**, 2, 179–193, 1976.
8. J. RYCHLEWSKI, *CEIIINOSSSTTUV (mathematical structure of elastic materials)* [in Russian], Inst. Mech. Probl. USSR Acad. Sci., Preprint No 217, pp. 113, 1983.
9. J. RYCHLEWSKI, *On Hooke's law*, PMM, **48**, pp. 420–435, 1984 (in Russian; see English translation Prikl. Matem. Mekhan., **48**, 303–314).
10. J. RYCHLEWSKI, *Elastic energy decompositions and limit criteria* [in Russian], Uspekhi Mekh. – Advances in Mech., **7**, 3, 51–80, 1984.
11. J. RYCHLEWSKI, *On thermoelastic constants*, Arch. Mech., **36**, 1, 77–95, 1984.
12. J. RYCHLEWSKI, *On non-collinearity of elastic strain and stress* [in Russian], Mekh. Tverd. Tela, 2, pp. 101–105, 1985.
13. J. RYCHLEWSKI, *Una propriedad notable de los materiales elasticas isotropos* [in Spanish], Acad.Sc. of Cuba, Ciencias téchnicas fizicas y matematicas, 5, pp. 99–104, 1984.
14. J. RYCHLEWSKI, *Mathematical structure of elastic materials*, Parts I, II [in Viet-Namese], Viet-Nam J. Mech., **5**, 4, pp. 1–6, 1983; **6**, 1, pp. 1–4, 1984.
15. J. OSTROWSKA-MACIEJEWSKA and J. RYCHLEWSKI, *Plane elastic and limit states in anisotropic solids*, Arch. Mech., **40**, 4, 379–386, 1988.
16. J. RYCHLEWSKI and ZHANG JIN-MIN, *Anisotropy degree of elastic materials*, Arch. Mech., **41**, pp. 697–715, 1989.
17. J. RYCHLEWSKI and XIAO HENG, *Elasticity models of multidirectional composites with strong fibres*, Uspekhi Mekh. – Advances in Mech., **14**, 1, pp. 41–78, 1991.
18. M.M. MEHRABADI and S.C. COWIN, *Eigentensors of linear anisotropic materials*, Quart. J. Mech. Appl. Math., **43**, pp. 15-41, 1990.
19. A.M. SADEGH and S.C. COWIN, *The proportional elastic invariants for anisotropic material*, J. Appl. Mech., **58**, pp. 50–71, 1991.
20. S.C. COWIN and A.M. SADEGH, *Noninteracting modes for stress strain and energy in hard tissue*, J. Biomechanics, **24**, pp. 859–867, 1991.
21. S.C. COWIN, M.M. MEHRABADI and A.M. SADEGH, *Kelvin formulation of the anisotropic Hooke's law* [in:] Modern theory of Anisotropic Elasticity and Applications, J.J. WU, T.C.T. TING and D.M. BARNET [Eds.], SIAM, Philadelphia, PA, pp. 340–365, 1991.
22. S.C. COWIN and M.M. MEHRABADI, *On the structure of the linear anisotropic elastic symmetries*, J. Mech. Phys. Solids, **40**, 1459–1472, 1992.

23. M.M. MEHRABADI, S.C. COVIN and C.O. HORPAN, *Strain energy bounds for linear anisotropic materials*, J. Elasticity, **30**, pp. 191–196, 1993.
24. M.W. BIEGLER and M. MEHRABADI, *An energy-based failure criterion for anisotropic solids subject to damage* [in:] Damage in Composite Materials, G.Z. VOYIADJIS [Ed.], Elsevier, pp. 23–34, 1993.
25. K.A. LURIE, *Some problems of optimum bending and tension of elastic plates* [in Russian], Mekh. Tv. Tela, **6**, 8, pp. 86–99, 1979.
26. K.A. LURIE and A.V. CHERKAEV, *Effective characteristics of composites and optimum structural design*, Uspekhi Mekh. – Advances in Mech., **9**, 2, 3–81, 1986.
27. T.C.T. TING, *Invariants of anisotropic elastic constants*, Quart. J. Appl. Math., **40**, 3, 431–448, 1987.
28. P.S. THEOCARIS and T.P. PHILIPPIDES, *Variational bounds on the eigenangle of transversely isotropic materials*, Acta Mech., **85**, pp. 13–26, 1990.
29. P.S. THEOCARIS and T.P. PHILIPPIDES, *Spectral decomposition of compliance and stiffness fourth-rank tensors suitable for orthotropic materials*, ZAMM, **71**, pp. 161–171, 1991.
30. A. BERTRAM and J. OLSCHEWSKI, *Formulation of anisotropic linear viscoelastic constitutive laws by a projection method*, MD – Vol. 26/AMD – Vol. 121, High Temperature Constitutive Modeling. Theory and Application, ASME, pp. 129–137, 1991.
31. A. BERTRAM and J. OLSCHEWSKI, *Zur Formulierung anisotroper linear anelastischer Stoffgleichungen mit Hilfe einer Projektion Methode* [in German], ZAMM, **73**, 4–5, pp. 401–403, 1993.
32. S. SUTCLIFFE, *Spectral decomposition of the elasticity tensor*, J. Appl. Mech., **59**, pp. 762–773, 1992.
33. V.V. NOVOZHILOV, *Theory of elasticity* [in Russian], Sudpromgiz, Leningrad 1958.
34. K.F. CHERNYKH, *Introduction to anisotropic elasticity* [in Russian], Nauka, Moscow 1988.
35. J.P. BOEHLER, A.A. KIRILLOV and E.T. ONAT, *On the polynomial invariants on the elasticity tensor*, J. Elasticity, **34**, 2, pp. 97–110, 1994.
36. P. HALMOS, *Finite-dimensional vector spaces*, D. van Nostrand Company, INC., New York 1958.
37. C. HERMANN, *Tensoren und Kristallsymmetric* [in German], Zs. Kristallogr. A., **89**, 32–48, 1934.
38. A. BLINOWSKI and J. RYCHLEWSKI, *Pure shears and elastic behaviour* (in preparation).
39. J. RYCHLEWSKI, *Proper elastic and limit states for plane stress and strain, plates and shells* (in preparation).
40. J. RYCHLEWSKI, *Constraints and looses in linear elasticity* (in preparation).
41. A. BLINOWSKI and J. RYCHLEWSKI, *Elastic waves in materials with constraints and looses* (in preparation).
42. W. OLSZAK and W. URBANOWSKI, *The plastic potential and generalized distortion energy in the theory of non-homogeneous anisotropic elastic-plastic bodies*, Arch. Mech. Stos., **8**, 4, pp. 671–694, 1956.
43. W. OLSZAK and J. OSTROWSKA-MACIEJEWSKA, *The plastic potential in the theory of anisotropic elastic-plastic solids*, Engng. Fracture Mech., **21**, 4, pp. 625–632, 1985.
44. A. BLINOWSKI and J. OSTROWSKA-MACIEJEWSKA, *On the elastic orthotropy*, [submitted to Arch. Mech.].
45. A. BLINOWSKI, J. OSTROWSKA-MACIEJEWSKA and J. RYCHLEWSKI, *Two-dimensional Hooke's tensor-isotropic decomposition effective symmetry criteria*, Arch. Mech., [to be published].
46. J. OSTROWSKA-MACIEJEWSKA, *Mechanics of deformable bodies* [in Polish], PWN, Warszawa 1994.

POLISH ACADEMY OF SCIENCES
INSTITUTE OF FUNDAMENTAL TECHNOLOGICAL RESEARCH, WARSZAWA.

Received October 12, 1994.

Arch. Mech., 47, 2, pp. 173–202, Warszawa 1995

Integral equations of thermoelasticity and thermoconductivity for cracked isotropic or anisotropic multiply connected bodies with reinforcement (*)

D. BARDZOKAS (ATHENS) and G. EXADAKTYLOS (CHANIA)

BY APPLYING the complex functions theory and the theory of singular integral equations, a general method has been developed for the solution of plane thermoconductivity and thermoelasticity problems for isotropic or anisotropic multiply connected bodies with cracks, containing also rectilinear and curvilinear stringers. The proposed general method can be applied effectively for the study of many difficult problems of engineering applications such as the interaction of weakened regions (cracks, holes) of a material with linear or curvilinear stringers under the influence of stress and thermal fields. Furthermore, based on the above method, the behaviour of existing singularities in these fields can be examined. Two specific examples are analyzed, one concerning an infinite cracked isotropic plate with holes and straight and curvilinear thin strip inclusions, and another concerning an infinite cracked orthotropic plate with a straight stringer. The method may be extended to solve a wide category of problems encountered in praxis.

1. Introduction

DURING THEIR SERVICE life, engineering structures are subjected not only to static and dynamic loads, but usually they are also affected by the presence of thermal fields. Thermal influences may sometimes alter the physico-mechanical properties of the materials and consequently, they may affect their strength properties and the resistance of the structure to loads. In the general case, the resulting expansions (contractions) are not occuring freely in the continuous medium. Instead, they produce thermal stresses which, in combination with the mechanical ones (due to external loading), can contribute to the initiation and propagation of cracks. In spite of the relatively large information about the various rupture phenomena occurring in these cases, their mechanisms which are complicated in nature have not been completely investigated as yet and demand the interdisciplinary cooperation of researchers from various scientific branches.

Even if the failure mechanism cannot, in many cases, be completely described only by the propagation of cracks in materials, the investigation of the conditions which trigger the initiation of a crack or a crack system from the pre-existing defects in the material (cracks, inclusions, cavities, welded joints etc.) is of great theoretical and practical importance. For this reason, the present investigation is concerned with the study of the stress-deformation state of a body under the influence of mechanical and thermal fields of forces, in the regions where singularities or stress concentrators exist, by using the complex functions method

(*) Paper presented at 30th Polish Solid Mechanics Conference, Zakopane, September 5–9, 1994.

and the theory of singular integral equations [1, 2, 3]. The methodology applied is based on the theory of linear elasticity and thermoelasticity of the anisotropic medium and is an extension of a previous work [4], since it includes the effects of curvilinear (in the form of circular arcs) thin strip inclusions and holes.

The present development of this general method permits one to use it effectively for studying the interaction between various types of defects in an isotropic or anisotropic material and reinforcements, in the presence of mechanical and thermal fields of forces, and furthermore to extend it for solving many important problems of engineering practice.

2. Fundamental equations of plane problems in thermoconductivity and thermoelasticity

For the formulation of the mathematical theory of the strength of isotropic or anisotropic bodies characterized by defects in the form of cracks, holes, inclusions etc., under the influence of mechanical and thermal fields of forces, the model of the linear thermoelastic body is used [4]. A general theory of this model assumes that:

a) the strain components are infinitesimal;

b) the relationships between various components of stresses and strains are given by the generalized linear Hooke's law, and

c) the elastic and thermal properties of the body are, in general, different in different directions, but they are independent of the temperature and stress.

Furthermore, it is assumed that at any point of an anisotropic body, a plane of elastic and thermal symmetry exists. Also, it is assumed that the temperature $T(x, y, z, t)$ in an anisotropic body is a continuous function of spatial coordinates x, y, z and time t; and that this holds also for the first differential coefficient with respect to t and for the first and second differential coefficients with respect to x, y and z. The body is referred to a Cartesian or curvilinear coordinate system with unit vectors **i**, **j** and **k**. Accordingly, an elementary surface characterized by a normal vector **n** which contains a random point of the body is considered. At the point under consideration, the thermoconductivity vector $\mathbf{K_n}$, which refers to the elementary surface with normal vector **n** is defined by

$$\mathbf{K_n} = a_1 k_{11}\mathbf{i} + a_2 k_{22}\mathbf{j} + a_3 k_{33}\mathbf{k}, \tag{2.1}$$

where k_{ii} $(i = \overline{1,3})$ are the coefficients of thermal conductivity, and a_i are the direction cosines between the vector **n** and the unit vectors **i**, **j** and **k**. The surfaces where the thermal conductivity vector $\mathbf{K}_n$ coincides with the normal vector **n** are called principal surfaces of thermal conductivity, whereas the directions normal to them are called principal directions of thermal conductivity. Accordingly, the

density of the thermal flux q_n across the elementary surface with normal direction **n** is defined as

$$q_n = -(\mathbf{K_n} \cdot \operatorname{grad} T). \tag{2.2}$$

The surface which is crossed by the thermal flux of maximum density is called principal surface of thermal flux, and the direction perpendicular to it is called principal direction of thermal flux at the point under consideration.

In the case where the axes of the reference system coincide with the principal directions of the thermal conductivity, the thermal field is described by the following differential equation

$$k_{11}\frac{\partial^2 T}{\partial x^2} + k_{22}\frac{\partial^2 T}{\partial y^2} + k_{33}\frac{\partial^2 T}{\partial z^2} = c\rho\frac{\partial T}{\partial t} - Q, \tag{2.3}$$

where c is the specific heat of the body, ρ expresses its density, and Q is the quantity of heat which is radiated from the unit volume per unit of time.

In order to find the solution of the partial differential equation (2.3) in space and time domains, the initial and boundary conditions should be known *a priori*. The boundary or surface conditions of thermal conductivity encountered in practice are [5]:

i. Boundary conditions of the first kind, when the values of temperature are given at all points of the surface of the body,

$$T = f_1(x, y, z, t). \tag{2.4}$$

ii. Boundary conditions of the second kind, when the values of density of the thermal flux are given at all points of the surface of the body,

$$\mathbf{K_n} \cdot \operatorname{grad} T = f_2(x, y, z, t). \tag{2.5}$$

iii. Boundary conditions of the third kind, called also "radiation boundary conditions", when the conditions of thermal exchange with the surrounding medium (of temperature T_0) are given at all points of the surface of the body,

$$\mathbf{K_n} \cdot \operatorname{grad} T = \lambda(T - T_0), \tag{2.6}$$

where λ is the coefficient of surface heat transfer.

In the sequel, the fundamental equations of thermoelasticity will be given. For this purpose let us consider a cylindrical body with the generatrix of its lateral surface perpendicular to the plane of the Cartesian coordinate system, and its end faces being thermally insulated. Further it is assumed that the temperature at any point of the body depends on the spatial coordinates x, y, and that the body is characterized by linear thermal anisotropy, such that at any point one of the principal directions of thermal conductivity is perpendicular to the plane

$x0y$. If the body is homogeneous and it does not contain any thermal source, then Eq. (2.3) takes the form

$$\lambda_{11}\frac{\partial^2 T}{\partial x^2} + 2\lambda_{12}\frac{\partial^2 T}{\partial x \partial y} + \lambda_{22}\frac{\partial^2 T}{\partial y^2} = 0, \tag{2.7}$$

where

$$\begin{aligned} \lambda_{11} &= k_{11}\cos^2 a + k_{22}\sin^2 a, \\ \lambda_{22} &= k_{11}\sin^2 a + k_{22}\cos^2 a, \\ \lambda_{12} &= (k_{11} - k_{22})\sin a \cos a, \end{aligned} \tag{2.8}$$

with a being the angle between the Ox-axis and one of the principal directions of thermal conductivity, and the quantities k_{ij}, λ_{ij} $(i, j = 1, 2)$ are constant.

The general solution of Eq. (2.7) is given in the form [6]:

$$T = F(z_3) + \overline{F(z_3)} = 2\mathrm{Re}\, F(z_3), \tag{2.9}$$

where the overbar denotes complex conjugate, Re denotes the real part of what follows and $F(z_3)$ is an analytic function of the complex variable z_3. Parameter μ_3 is one of the roots of the characteristic equation

$$\lambda_{22}\mu^2 + 2\lambda_{12}\mu + \lambda_{11} = 0, \tag{2.10}$$

where

$$\mu_3 = -\lambda_{12} + i\frac{(k_{11}k_{22})^{1/2}}{\lambda_{22}},$$

with i denoting the usual imaginary unit.

The thermal flux as a function of $F(z_3)$ is expressed by a function of β_1, β_2 which are the direction cosines between the normal vector $\mathbf{n}$ and the element ds

$$\mathbf{K_n} \cdot \mathrm{grad}\, T = \left(\lambda_{11}\frac{\partial T}{\partial x} + \lambda_{12}\frac{\partial T}{\partial y}\right)\beta_1 + \left(\lambda_{12}\frac{\partial T}{\partial x} + \lambda_{22}\frac{\partial T}{\partial y}\right)\beta_2. \tag{2.11}$$

By virtue of Eq. (2.9), relationship (2.11) assumes the following form:

$$\mathbf{K_n} \cdot \mathrm{grad}\, T = A_1^* F'(z_3) + \overline{A_1^* F'(z_3)}, \tag{2.12}$$

where $\left(' \equiv \frac{d}{dz_3}\right)$, and

$$A_1^* = (\lambda_{12} + \mu_3\lambda_{22})(-\beta_2 + \mu_3\beta_1).$$

Basing on relationships (2.9) and (2.12), we can find the temperature and the thermal flux at any point of the body, if the mathematical form of the thermal potential $F(z_3)$ is *a priori* known.

At any point of a homogeneous and anisotropic body under a plane strain state, there exists a plane of elastic symmetry which is perpendicular to Oz-axis and coincides with one of the principal directions of thermal conductivity. The generalized Hooke's law in this case takes the form

$$
\begin{aligned}
\varepsilon_x &= a_{11}\sigma_x + a_{12}\sigma_y + a_{13}\sigma_z + a_{16}\tau_{xy} + \beta_{11}T,\\
\varepsilon_y &= a_{12}\sigma_x + a_{22}\sigma_y + a_{23}\sigma_z + a_{26}\tau_{xy} + \beta_{22}T,\\
\gamma_{xy} &= a_{16}\sigma_x + a_{26}\sigma_y + a_{36}\sigma_z + a_{66}\tau_{xy} - 2\beta_{66}T,\\
\varepsilon_z &= a_{13}\sigma_x + a_{23}\sigma_y + a_{33}\sigma_z + a_{36}\tau_{xy} + \beta_{33}T = 0,\\
\gamma_{yz} &= a_{44}\tau_{yz} + a_{45}\tau_{xz} = 0,\\
\gamma_{xz} &= a_{45}\tau_{yz} + a_{55}\tau_{xz} = 0,
\end{aligned}
\tag{2.13}
$$

or alternatively

$$
\begin{aligned}
\varepsilon_x &= c_{11}\sigma_x + c_{12}\sigma_y + c_{16}\tau_{xy} + a_1 T,\\
\varepsilon_y &= c_{12}\sigma_x + c_{22}\sigma_y + c_{26}\tau_{xy} + a_2 T,\\
\gamma_{xy} &= c_{16}\sigma_x + c_{26}\sigma_y + c_{66}\tau_{xy} - 2a_6 T,
\end{aligned}
\tag{2.14}
$$

where a_{ij}, c_{ij} express the elasticity coefficients and are related by

$$
c_{ij} = a_{ij} - \frac{a_{i3}a_{j3}}{a_{33}}, \qquad i,j = 1,\ 2,\ 6. \tag{2.15}
$$

In the sequel β_{ij} are the coefficients which give the strain tensor components of a body element free form external tractions, due to a temperature change of one degree. For these coefficients the following relationships hold true:

$$
\begin{aligned}
a_i &= \beta_{ii} - \beta_{33}\frac{a_{i3}}{a_{33}}, \quad i = 1,\ 2,\\
a_6 &= \beta_{66} + \beta_{33}\frac{a_{36}}{2a_{33}}.
\end{aligned}
\tag{2.15'}
$$

Under the condition that coefficients $c_{ij}, a_i, \lambda_{ij}$ remain constant and independent of the variations of the stress components and the temperature of the body, the relationships giving the stresses and displacements as a function of the complex potentials $\Phi(z_1)$, $\Psi(z_2)$ and $F(z_3)$ are the following [6]:

$$
\begin{aligned}
\sigma_x &= 2\mathrm{Re}\left[\mu_1^2\Phi(z_1) + \mu_2^2\Psi(z_2) + n_0\mu_3 F(z_3)\right],\\
\sigma_y &= 2\mathrm{Re}\left[\Phi(z_1) + \Psi(z_2) + n_0 F(z_3)\right],\\
\tau_{xy} &= -2\mathrm{Re}\left[\mu_1\Phi(z_1) + \mu_2\Psi(z_2) + n_0\mu_3 F(z_3)\right],\\
u &= 2\mathrm{Re}\left[p_1\varphi(z_1) + p_2\psi(z_2) + p_*\psi(z_3)\right],\\
v &= 2\mathrm{Re}\left[q_1\varphi(z_1) + q_2\psi(z_2) + q_*\psi(z_3)\right],
\end{aligned}
\tag{2.16}
$$

where

$$p_j = c_{11}\mu_j^2 + c_{12} - c_{16}\mu_j\,,$$
$$\mu_j q_j = c_{12}\mu_j^2 + c_{22} - c_{26}\mu_j\,, \qquad j = 1,\ 2$$

and

$$\begin{aligned} p_* &= a_1 + n_0(c_{11}\mu_3^2 - c_{16}\mu_3 + c_{12}),\\ \mu_3 p_* &= a_2 + n_0(c_{11}\mu_3^2 - c_{26}\mu_3 + c_{22}),\\ n_0 &= -(a_1\mu_3^2 + 2a_6\mu_3 + a_2)/\Delta(\mu_3),\\ \Delta(\mu_3) &= c_{11}(\mu_3 - \mu_1)(\mu_3 - \mu_2)(\mu_3 - \overline{\mu_1})(\mu_3 - \overline{\mu_2}),\\ \Phi(z_1) &= \varphi'(z_1), \qquad \Psi(z_2) = \psi'(z_2), \qquad F(z_3) = \psi'(z_3). \end{aligned} \tag{2.17}$$

For the transversely isotropic body, Hooke's law in plane strain conditions takes the following simplified form

$$\begin{aligned} \varepsilon_x &= \frac{1}{E}\sigma_x - \frac{\nu}{E}\sigma_y - \frac{\nu_z}{E_z}\sigma_z + \beta_{11}T,\\ \varepsilon_y &= -\frac{\nu}{E}\sigma_x + \frac{1}{E}\sigma_y - \frac{\nu_z}{E_z}\sigma_z + \beta_{11}T,\\ \varepsilon_z &= -\frac{\nu_z}{E_z}(\sigma_x + \sigma_y) + \frac{1}{E}\sigma_z + \beta_{33}T = 0,\\ \gamma_{xy} &= \frac{1}{G_{xy}}\tau_{xy}, \end{aligned} \tag{2.18}$$

and for the generally isotropic body,

$$\begin{aligned} \varepsilon_x &= \frac{1}{E}(\sigma_x - \nu\sigma_y) + aT,\\ \varepsilon_y &= \frac{1}{E}(\sigma_y - \nu\sigma_x) + aT,\\ \gamma_{xy} &= \frac{1}{G}\tau_{xy}. \end{aligned} \tag{2.19}$$

In the above relations the coefficients β_{11} and β_{33} are, respectively, the thermal coefficients of linear expansion on the plane of isotropy (parallel to the plane $x0y$), and along the direction perpendicular to the plane of isotropy.

The relationships for the derivation of the stress tensor and displacement vector components are simplified as follows:

$$\begin{aligned} \sigma_x + \sigma_y &= 2[\Phi(z) + \overline{\Phi(z)}] = 2\mathrm{Re}\,\Phi(z),\\ (\sigma_y - \sigma_x) + 2i\tau_{xy} &= 2\left[\overline{z}\Phi'(z) + \Psi(z)\right],\\ 2\mu(u + iv) &= \kappa\varphi(z) - z\overline{\Phi(z)} - \overline{\psi(z)} + \beta\int f(z)\,dz,\\ T(x, y) &= \mathrm{Re}\, f(z), \end{aligned} \tag{2.20}$$

where for the case of transversely isotropic body

(a)
$$\kappa = 1 + \frac{2E}{1+\nu}\left(\frac{1-\nu}{E} - \frac{2\nu_z}{E_z}\right), \qquad \beta = \frac{2E}{1+\nu}(\beta_{11} + \nu_z\beta_{33}),$$
(plane strain case),

(b)
$$\kappa = \frac{3-\nu}{1+\nu}, \qquad \beta = \frac{2E\beta_{11}}{1+\nu},$$
(generalized plane stress case),

and for the isotropic body

(c)
$$\kappa = 3 - 4\nu, \qquad \beta = aE,$$
(plane strain case),

(d)
$$\kappa = \frac{3-4\nu}{1+\nu}, \qquad \beta = \frac{aE}{1+\nu},$$
(generalized plane stress case).

In the case where at the point (x_0, y_0) inside the orthotropic medium a thermal source of power q_0 exists, the complex potentials in the region enclosing this point take the form

$$\begin{aligned} \varphi(z_1) &= a_0'(z_1 - t_1)\ln(z_1 - t_1), \\ \psi(z_2) &= \beta_0'(z_2 - t_2)\ln(z_2 - t_2), \\ \psi(z_3) &= m_0(z_3 - t_3)\ln(z_3 - t_3), \end{aligned} \tag{2.21}$$

where

$$m_0 = -\frac{q_0}{4\pi\sqrt{k_{11}k_{22}}},$$
$$t_j = x_0 + \mu_j y_0, \qquad j = \overline{1,3},$$

and the coefficients α_0', β_0' are given from the following relations:

$$a_0' = \frac{m - n\mu_2}{\mu_1 - \mu_2}, \qquad \beta_0' = -\frac{m - n\mu_1}{\mu_1 - \mu_2},$$

$$\operatorname{Im}[m(\mu_1 + \mu_2) - n\mu_1\mu_2 - m\lambda_0/c_{11}] = 0,$$

$$\operatorname{Im}[m\mu_1\mu_2 + n\mu_1\mu_2(\mu_1 + \mu_2) - m_0(a_1\mu_3 - \lambda_0(\mu_3 - \mu_1 - \mu_2))/c_{11}] = 0,$$

with

$$\lambda_0 = \frac{(a_1\mu_3^2 + 2a_6\mu_3 + a_2)}{(\mu_3 - \overline{\mu_1})(\mu_3 - \overline{\mu_2})}.$$

For the case of the transversely isotropic or generally isotropic medium, the corresponding complex potentials take the following form:

$$\begin{aligned} \Phi(z) &= A_0 \ln(z - z_0), \\ \Psi(z) &= -\frac{A_0 \overline{z_0}}{z - z_0}, \\ F(z) &= m_0 \ln(z - z_0), \end{aligned} \tag{2.22}$$

where

$$A_0 = -\frac{\beta m_0}{1 + \kappa}, \qquad m_0 = -\frac{q_0}{4\pi\lambda}.$$

Recapitulating, the solution of the plane problem of steady state thermoelasticity is derived in two consecutive stages. In the first stage the steady thermal field $T(x, y)$ is derived statisfying one of the boundary conditions (2.4) – (2.6) and the differential thermoelasticity equation (2.7) for the anisotropic medium, or the Laplace equation

$$\frac{\partial^2 T(x, y)}{\partial x^2} + \frac{\partial^2 T(x, y)}{\partial y^2} = 0 \tag{2.23}$$

for the isotropic medium. The second stage refers to the derivation of the stress tensor and displacement vector components by using relations (2.16) or (2.20).

3. Thermal contact conditions between two bodies

At the first stage of the solution of the thermoelastic problem for bodies with thin inclusions and cracks it is of great importance to describe correctly the phenomenon of thermal conductivity along the lips of the crack and the contact interfaces of the thin inclusion with the body. This is achieved by properly choosing the representative computational model of thermal contact between the bodies characterized by different elastic and thermal constants. Following PODSTRIGACH'S [7] approach to the formulation of the model which describes the condition of thermal contact, it is assumed that the contact surfaces are separated by a thin interlayer (inclusion) with the same thermo-physical parameters (Fig. 1). If these parameters are assumed to be constant and the thickness of the interlayer tends to zero, it takes the form of a physical separating surface of the two bodies, and the corresponding boundary conditions on this surface correspond to the real contact condition of the two bodies.

The thermoconductivity equation of the embedded layer (isotropic inclusion) referred to the curvilinear coordinate system (n, s) is the following:

$$\frac{\partial^2 T_c}{\partial n^2} + \frac{\partial^2 T_c}{\partial s^2} = 0. \tag{3.1}$$

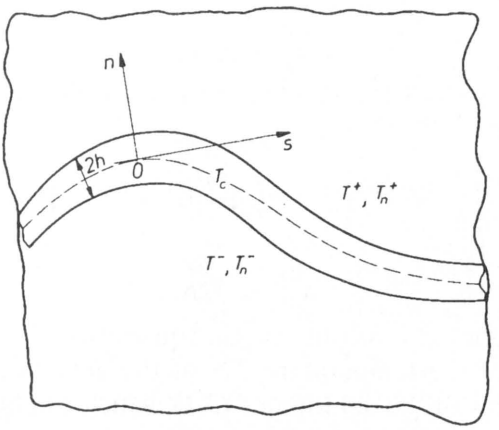

FIG. 1. Contact of two infinite elastic bodies, with the contact region to be represented by a thin inclusion characterized by the same thermophysical properties as those of the two bodies.

On the separating surfaces $n = \pm h$ of the isotropic inclusion and the anisotropic medium, the following conditions of thermal contact are satisfied

$$T_c(s, \pm h) = T^{\pm}, \tag{3.2}$$

$$-\lambda \frac{\partial T_c}{\partial n}\Big|_{n=\pm h} = T_n^{\pm}, \tag{3.3}$$

where λ is the coefficient of thermal conductivity of the inclusion,

$$T_n^{\pm} = -(\mathbf{K_n} \cdot \overline{\operatorname{grad} T})^{\pm}$$

and $T^{\pm}$, $T_n^{\pm}$ express the limiting values of the temperature and the thermal flux along the boundary $n = \pm h$ of the anisotropic medium.

Then the following integral representations are introduced:

$$T_c^* = \frac{1}{2h} \int_{-h}^{h} T_c \, dn, \tag{3.4}$$

$$T_c^{**} = \frac{3}{2h^2} \int_{-h}^{h} T_c n \, dn. \tag{3.5}$$

Multiplying relationship (3.1) by $1/2h$ and integrating with respect to n in the range $(-h, h)$ and by virtue of the relations (3.2) and (3.3), the following equation is derived:

$$\lambda_s \frac{\partial^2 T_c^*}{\partial s^2} + (T_n^+ - T_n^-) = 0, \tag{3.6}$$

where

$$\lambda_s = 2\lambda h.$$

Furthermore, multiplying (3.1) by $3n/2h^2$ and integrating with respect to n in the range $(-h, h)$ we get

$$\lambda_s \frac{\partial^2 T_c^{**}}{\partial s^2} + 3\lambda(T_n^+ + T_n^-) - 6\lambda_n(T^+ - T^-) = 0, \tag{3.7}$$

where

$$\lambda_n = \lambda/2h.$$

In order to derive the expressions for the quantities T_c^*, T_c^{**} with respect to the limiting values of the temperature $T^{\pm}$ of the anisotropic body, we use the operational expression of the solution of (3.1), which can be written as follows:

$$\frac{\partial^2 T_c}{\partial n^2} + p^2 T_c = 0 \qquad \left(p^2 = \frac{\partial^2}{\partial s^2}\right). \tag{3.8}$$

By considering condition (3.2), the expression (3.8) gives the following solution;

$$T_c = \frac{(T^+ + T^-)}{2\cos ph}\cos pn + \frac{(T^+ + T^-)}{2\sin ph}\sin pn. \tag{3.9}$$

By virtue of (3.9), relationships (3.4) and (3.5) become

$$\begin{aligned} T_c^* &= \frac{T^+ + T^-}{2ph}\operatorname{tg} ph, \\ T_c^{**} &= \frac{3}{2p^2h^2}(T^+ + T^-)(1 - ph\operatorname{ctg} ph). \end{aligned} \tag{3.10}$$

Substituting the values of T_c^* and T_c^{**} found from (3.10) into relations (3.6) and (3.7), respectively, and for $h \to 0$, we get the following relations:

$$\begin{aligned} &\lambda_s \frac{\partial^2}{\partial s^2}(T^+ + T^-) + 2\left[(\mathbf{K_n}\cdot\operatorname{grad} T)^+ - (\mathbf{K_n}\cdot\operatorname{grad} T)^-\right] = 0, \\ &\lambda_s \frac{\partial^2}{\partial s^2}(T^+ - T^-) + 6\left[(\mathbf{K_n}\cdot\operatorname{grad} T)^+ + (\mathbf{K_n}\cdot\operatorname{grad} T)^-\right] \\ &\qquad -12\lambda_n(T^+ - T^-) = 0. \end{aligned} \tag{3.11}$$

The above relations represent the conditions of "non-ideal thermal contact" at the surface of the anisotropic medium. In the case of the isotropic medium, relations (3.11) are simplified as follows,

$$\begin{aligned} &\lambda_s \frac{\partial^2}{\partial s^2}(T^+ + T^-) + 2\lambda^*\left[\left(\frac{\partial T}{\partial n}\right)^+ - \left(\frac{\partial T}{\partial n}\right)^-\right] = 0, \\ &\lambda_s \frac{\partial^2}{\partial s^2}(T^+ - T^-) + 6\lambda^*\left[\left(\frac{\partial T}{\partial n}\right)^+ + \left(\frac{\partial T}{\partial n}\right)^-\right] - 12\lambda_n(T^+ - T^-) = 0, \end{aligned} \tag{3.12}$$

where λ^* is the coefficient of thermal conductivity of the isotropic medium.

In the case when instead of a thin inclusion we have a crack, the values of λ_s and λ_n characterize its thermal conductivity in the longitudinal and transverse directions, respectively. Depending on thermal conductivity we distinguish three categories of cracks:

a) a thermally conducting crack for $\lambda_s \neq 0$, $\lambda_n \neq 0$;

b) a longitudinally thermally insulating crack for $\lambda_s = 0$, $\lambda_n \neq 0$;

c) a thermally insulating crack for $\lambda_s = \lambda_n = 0$.

In plane thermoconductivity problems of cracked bodies with inclusions, the temperature field $T(x, y)$ is expressed as follows:

$$T(x, y) = T_0(x, y) + T_*(x, y), \tag{3.13}$$

where $T_0(x, y)$ is the known thermal field induced to the continuous medium, and $T_*(x, y)$ – the perturbed thermal field due to the presence of defects in the body.

Depending on the thermal contact conditions at the boundaries of the crack and the thin inclusion, we have the following three relationships:

$$T_*^{\pm} = f^{\pm}(t) - T_0, \tag{3.14}$$

$$(\mathbf{K_n} \cdot \operatorname{grad} T_*)^{\pm} = Q^{\pm}(t) - (\mathbf{K_n} \cdot \operatorname{grad} T_0), \tag{3.15}$$

$$\begin{aligned} &\lambda_s \frac{\partial^2}{\partial s^2}(T_*^+ + T_*^-) + 2\left[(\mathbf{K_n} \cdot \operatorname{grad} T_*)^+ - (\mathbf{K_n} \cdot \operatorname{grad} T_*)^-\right] = -2\lambda s \frac{\partial^2 T_0}{\partial s^2}, \\ &\lambda_s \frac{\partial^2}{\partial s^2}(T_*^+ - T_*^-) + 6\left[(\mathbf{K_n} \cdot \operatorname{grad} T_*)^+ + (\mathbf{K_n} \cdot \operatorname{grad} T_*)^-\right] \\ &\qquad -12\lambda_n(T_*^+ - T_*^-) = -12(\mathbf{K_n} \cdot \operatorname{grad} T_0), \end{aligned} \tag{3.16}$$

where the quantities $f^{\pm}(t)$ and $Q^{\pm}(t)$ express the known temperatures and thermal fluxes along the boundaries of the crack or the thin inclusion.

Finally, in the case of plane thin inclusions inside an anisotropic body we have the following ideal thermal contact conditions which must be satisfied along their interfaces

$$\begin{aligned} T^+ &= T^-, \\ (\mathbf{K_n} \cdot \operatorname{grad} T)^+ &= (\mathbf{K_n} \cdot \operatorname{grad} T)^- \end{aligned} \tag{3.17}$$

or, alternatively, for the isotropic body

$$\begin{aligned} T^+ &= T^-, \\ \lambda_1 \left(\frac{\partial T}{\partial n}\right)^+ &= \lambda^* \left(\frac{\partial T}{\partial n}\right)^-, \end{aligned} \tag{3.17'}$$

where λ_1, λ^* are the thermoconductivity coefficients of the inclusion and the body, respectively.

4. Integro-differential equations of the plane thermoconductivity and thermoelasticity problem for the infinite cracked isotropic plate with holes and reinforcements

The method which is applied to the solution of the problem, consists in the formulation of a system of singular integro-differential equations similar to the method used in [1, 8–11]. An infinite isotropic plate S containing M internal curvilinear cracks l_j ($j = \overline{1, M}$), N thin strip inclusions (stringers) L_j ($j = \overline{1, N} = 1, \overline{n_1' + n_2'}$) with n_1' being the number of straight stringers, whereas n_2' is the number of curvilinear (circular arcs) stringers, and L holes γ_j ($j = \overline{1, L}$), is considered (Fig. 2). The plate is subjected to a biaxial state of stresses (N_1, N_2) at infinity and is under the influence of a homogeneous thermal flow q_∞. Besides these loading conditions, concentrated forces $P_j + iQ_j$ are acting at the points z_j^* ($j = \overline{1, k_1}$), moments M_j at the points z_j^{**} ($j = \overline{1, k_2}$), and k_3 thermal sources of powers q_j at the points a_j ($j = \overline{1, k_3}$) on the plane of the plate.

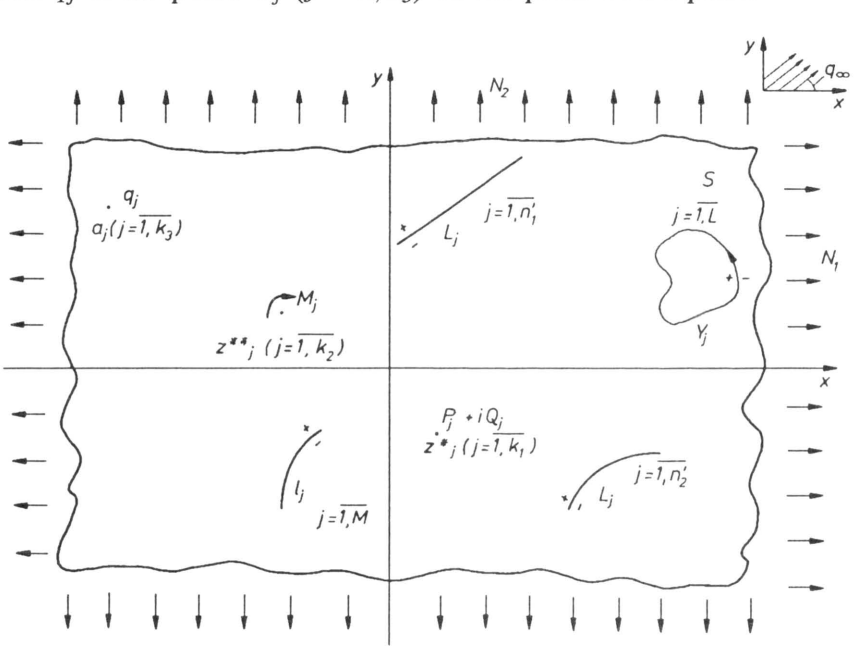

FIG. 2. Infinite isotropic thin plate containing M curvilinear cracks, $N(= n_1 + n_2)$ thin strip inclusions and L holes, which is subjected at infinity to a biaxial state of stress $(N_1 + N_2)$ and to a homogeneous thermal flow q_∞.

In order to simplify somewhat the problem it is assumed that the only deformation, which can be sustained by the straight stringers, is directed along their longitudinal axis and furthermore, both the straight and the curvilinear stringers have zero bending stiffness.

Depending on the nature of thermal contact at the boundaries l_j, L_j and γ_j, we formulate the thermal boundary conditions known from the previous section,

$$T_*^{\pm} = f_j^{\pm} - T_0, \qquad j = \overline{1, n_1}, \qquad t \in L_{1j}^*, \tag{4.1}$$

$$\lambda^* \left(\frac{\partial T_*}{\partial n}\right)^{\pm} = \pm Q_j^{\pm} - \lambda^* \frac{\partial T_0}{\partial n}, \qquad j = \overline{(n_1 + 1, n_1 + n_2)}, \qquad t \in L_{2j}^*, \tag{4.2}$$

$$\begin{aligned} &\lambda_s \frac{\partial^2}{\partial s^2}(T_*^+ - T_*^-) + 6\lambda^* \left[\left(\frac{\partial T_*}{\partial n}\right)^+ + \left(\frac{\partial T_*}{\partial n}\right)^-\right] \\ &\qquad - 12\lambda_n (T_*^+ - T_*^-) = -12\lambda^* \frac{\partial T_0}{\partial n}, \\ &\lambda_s \frac{\partial^2}{\partial s^2}(T_*^+ + T_*^-) + 2\lambda^* \left[\left(\frac{\partial T_*}{\partial n}\right)^+ - \left(\frac{\partial T_*}{\partial n}\right)^-\right] = -2\lambda_s \frac{\partial^2 T_0}{\partial s^2}, \\ &\qquad j = \overline{(n_1 + n_2 + 1,\ N + M + L)}, \qquad t \in L_{3j}^*, \end{aligned} \tag{4.3}$$

where t is the complex coordinate of a point on the contour.

The above relationships form the basis for the solution of the thermoconductivity problem and for the determination of the thermal field in the plate. Along the hole boundaries one of the first two thermal conditions can be applied.

The thermal potential $F(z)$ [$T(x, y) = 2\mathrm{Re}\, F(z)$] of the steady thermal field $T(x, y)$ is expressed as follows:

$$F(z) = \frac{q_\infty}{2} z e^{-i\beta_0} - \sum_{j=1}^{k_3} \frac{q_j}{2\pi\lambda^*} \ln(z - a_j) + F_*(z), \tag{4.4}$$

where $F_*(z)$ is given as

$$\begin{aligned} F_*(z) = &\sum_{j=1}^{n_1} \frac{1}{2\pi i} \int_{L_{1j}^*} \frac{f_j^*(\tau) + i\varphi_j^{(2)}(\tau)}{\tau - z} d\tau \\ &+ \sum_{j=n_1+1}^{n_1+n_2} \left[\frac{1}{2\pi i} \int_{L_{2j}^*} f_j^{**}(\tau) e^{-ia_j} \ln(\tau - z) d\tau + \frac{1}{2\pi i} \int_{L_{2j}^*} \frac{\varphi_j^{(1)}(\tau)}{\tau - z} d\tau\right] \\ &+ \sum_{j=n_1+n_2+1}^{N+M+L} \frac{1}{2\pi i} \int_{L_{3j}^*} \frac{\varphi_j^{(1)} + i\varphi_j^{(2)}}{\tau - z} d\tau, \end{aligned} \tag{4.5}$$

and represents the thermal potential which expresses the perturbed thermal field with $(\varphi_j^{(1)} + i\varphi_j^{(2)})$ being the densities along the crack, stringer, and hole boundaries.

The quantities $f_j^*(t)$ and $f_j^{**}(t)$ are expressed as

$$f_j^*(t) = \frac{1}{2}\left[f_j^+(t) - f_j^-(t)\right],$$

$$f_j^{**}(t) = -\frac{1}{2\lambda^*}\left[Q^+(t) + Q^-(t)\right].$$

Substituting in (4.1)–(4.3) the limiting values (4.4) of the thermal potential, the following system of integro-differential equations is obtained:

$$\begin{aligned}
(4.6)\qquad 2\mathrm{Re}\Bigg[\Bigg[\frac{1}{\pi}\int\limits_{L_{1k}^*}\frac{\varphi_k^{(2)}(\tau)}{\tau-t}d\tau\Bigg] &+ \sum_{\substack{j=1\\ j\neq k}}^{n_1}\frac{1}{\pi}\int\limits_{L_{1j}^*}\frac{\varphi_j^{(2)}(\tau)}{\tau-t}d\tau \\
&+ \sum_{j=n_1+1}^{n_1+n_2}\frac{1}{\pi i}\int\limits_{L_{2j}^*}\frac{\varphi_j^{(1)}(\tau)}{\tau-t}d\tau + \sum_{j=n_1+n_2+1}^{N+M+L}\frac{\varphi_j^{(1)}+i\varphi_j^{(2)}}{\tau-t}d\tau\Bigg] \\
&= f_k^+(t) + f_k^-(t) - 2\mathrm{Re}\Bigg[\sum_{j=1}^{n_1}\frac{1}{\pi i}\int\limits_{L_{1j}^*}\frac{f_j^*(\tau)}{\tau-t}d\tau \\
&+ \sum_{j=n_1+1}^{n_1+n_2}\frac{1}{\pi i}\int\limits_{L_{2j}^*} f_j^{**}(\tau)e^{-ia_j}\ln(\tau-t)\,d\tau + \frac{q_\infty}{2}te^{-i\beta_0} \\
&+ \sum_{j=1}^{k_3}\frac{q_j}{2\pi\lambda^*}\ln(t-a_j)\Bigg], \qquad t\in L_{1k}^*, \qquad k=\overline{1,n_1};
\end{aligned}$$

$$\begin{aligned}
(4.7)\qquad 2\mathrm{Re}\Bigg\{e^{ia_k(t)}\Bigg[\frac{1}{\pi i}\int\limits_{L_{2k}^*}\frac{\varphi^{(1)\prime}(\tau)}{\tau-t}\,d\tau &+ \sum_{\substack{j=n_1+1\\ j\neq k}}^{n_1+n_2}\frac{1}{\pi i}\int\limits_{L_{2j}^*}\frac{\varphi_j^{(2)\prime}(\tau)}{\tau-t}\,d\tau \\
&+ \sum_{j=1}^{n_1}\frac{1}{\pi}\int\limits_{L_{1j}^*}\frac{\varphi^{(2)\prime}(\tau)}{\tau-t}\,d\tau + \sum_{j=n_1+n_2+1}^{N+M+L}\frac{1}{\pi i}\int\limits_{L_{3j}^*}\frac{\left[\varphi_j^{(1)}(\tau)+i\varphi_j^{(2)}(\tau)\right]}{\tau-t}\,d\tau\Bigg]\Bigg\} \\
&= \frac{Q_k^+(t)-Q_k^-(t)}{\lambda^*} - 2\mathrm{Re}\Bigg[e^{ia_k(t)}ia_k(t)\Bigg[\Bigg(\frac{q_\infty}{2}e^{-i\beta_0} - \sum_{j=1}^{k_3}\frac{q_j}{2\pi\lambda^*}\frac{1}{t-a_j}\Bigg) \\
&+ \sum_{j=1}^{n_1}\frac{1}{\pi i}\int\limits_{L_{1j}^*}\frac{f_j^*(\tau)}{(\tau-t)^2}d\tau + \sum_{j=n_1+1}^{n_1+n_2}\frac{1}{\pi i}\int\limits_{L_{2j}^*}\frac{f_j^{**}(\tau)e^{-ia_j(\tau)}}{\tau-t}\,d\tau\Bigg]\Bigg], \\
&\qquad t\in L_{2k}^*, \qquad k=\overline{n_1+1,\ n_1+n_2};
\end{aligned}$$

$$(4.8)_1 \quad \operatorname{Re}\left[\omega_k(s)e^{ia_k(t)}\left[\frac{1}{\pi i}\int\limits_{L_{3k}^*}\frac{\varphi_k^{'(1)}(\tau)+i\varphi_k^{'(2)}(\tau)}{\tau-t}\,d\tau-\frac{e^{2ia_k(t)}}{\pi i}\right.\right.$$

$$\times\int\limits_{L_{3k}^*}\frac{\varphi_k^{''(1)}(\tau)+i\varphi_k^{''(2)}(\tau)}{\tau-t}\,d\tau\Bigg]+\sum_{\substack{j=n_1+n_2+1\\ j\neq k}}^{N+M+L}\left[\frac{1}{\pi i}\int\limits_{L_{3j}}\frac{\varphi_j^{'(1)}(\tau)+i\varphi_j^{'(2)}(\tau)}{\tau-t}\,d\tau\right.$$

$$-\frac{e^{2ia_k(t)}}{\pi i}\int\limits_{L_{3j}^*}\frac{\varphi_j^{''(1)}(\tau)+i\varphi_j^{''(2)}(\tau)}{(\tau-t)}\,d\tau\Bigg]+\sum_{j=1}^{n_1}\left[\frac{1}{\pi i}\int\limits_{L_{1j}^*}\frac{i\varphi_j^{'(2)}}{\tau-t}\,d\tau\right.$$

$$-\frac{e^{2ia_k(t)}}{\pi i}\int\limits_{L_{1j}^*}\frac{i\varphi_j^{''(2)}(\tau)}{\tau-t}\,d\tau\Bigg]+\sum_{j=n_1+1}^{n_1+n_2}\left[\frac{1}{\pi i}\int\limits_{L_{2j}^*}\frac{\varphi_j^{'(1)}(\tau)}{\tau-t}-\frac{e^{2ia_k(t)}}{\pi i}\right.$$

$$\left.\left.\times\int\limits_{L_{2j}^*}\frac{\varphi_j^{''(1)}(\tau)}{\tau-t}\,d\tau\Bigg]+\frac{\lambda^*}{\lambda_s}\left[e^{ia_k(t)}(\varphi_k^{'(1)}(t)+i\varphi_k^{'(2)}(t))\right]\right]$$

$$=-2\operatorname{Re}\left[\omega_k(s)e^{ia_k(t)}\left[\frac{q_\infty}{2}e^{-i\beta_0}-\sum_{j=1}^{k_3}\frac{q_j}{2\pi\lambda^*}\left[\frac{1}{t-a_j}-\frac{e^{2ia_k(t)}}{(t-a_j)^2}\right]\right]\right.$$

$$-\frac{1}{2}\left[\sum_{j=1}^{k_1}\frac{1}{\pi i}\int\limits_{L_{1j}^*}\frac{f_j'^*(\tau)}{\tau-t}\,d\tau-\frac{e^{2ia_k(t)}}{\pi i}\right.$$

$$\times\int\limits_{L_{1j}^*}\frac{f_j''(\tau)}{\tau-t}\,d\tau+\sum_{j=n_1+1}^{n_1+n_2}\left[\frac{1}{\pi i}\int\limits_{L_{2j}}f_j^{**}(\tau)\frac{e^{-ia_j(\tau)}}{\tau-t}\,d\tau-\frac{e^{2ia_k(t)}}{\pi i}\right.$$

$$\left.\left.\left.\left.\times\int\limits_{L_{2j}^*}\left(\omega_j(s)e^{-ia_j(s)}f_j^{**}(\tau)+f_j'^{**}(\tau)\right)e^{-ia_j(\tau)}\,\frac{d\tau}{\tau-t}\right]\right]\right];$$

$$(4.8)_2 \quad \operatorname{Re}\left\{\omega_k(s)e^{ia_k(t)}\left[\varphi_k^{'(1)}(t)+i\varphi_k^{'(2)}(t)-e^{2ia_k(t)}\left(\varphi_k^{''(1)}(t)+i\varphi_k^{''(2)}(t)\right)\right]\right.$$

$$\left.+6\frac{\lambda^*}{\lambda_s}e^{ia_k(t)}\left[\frac{1}{\pi i}\int\limits_{L_{3k}^*}\frac{\varphi_k^{'(1)}(\tau)+i\varphi_k^{'(2)}(\tau)}{\tau-t}\,d\tau\right]\right.$$

(4.8)$_2$ [cont.]

$$+\sum_{\substack{j=n_1+n_2+1\\ j\neq k}}^{M+N+L}\left[\frac{1}{\pi i}\int_{L_{3j}^*}\frac{\varphi_j^{\prime(1)}+i\varphi_j^{\prime(2)}(\tau)}{\tau-t}\,d\tau+\sum_{j=1}^{n_1}\frac{1}{\pi i}\right.$$

$$\left.\times\int_{L_{1j}^*}\frac{i\varphi_j^{\prime(2)}(\tau)}{\tau-t}\,d\tau+\sum_{j=n_1+1}^{n_1+n_2}\frac{1}{\pi i}\int_{L_{2j}^*}\frac{\varphi_j^{\prime(1)}(\tau)}{\tau-t}\,d\tau\right]$$

$$-12\frac{\lambda_n}{\lambda_s}\left(\varphi_k^{(1)}(t)+i\varphi_k^{(2)}(t)\right)\Bigg\}=-12\frac{\lambda^*}{\lambda_s}\mathrm{Re}\left[e^{ia_k(t)}\left(\frac{q_\infty}{2}e^{-i\beta_0}\right.\right.$$

$$-\sum_{j=1}^{k_3}\frac{q_j}{2\pi\lambda^*}\frac{1}{t-a_j}\Bigg)-\frac{1}{12}\left(\sum_{j=1}^{n_1}\frac{1}{\pi i}\int_{L_{1j}^*}\frac{f_j^{\prime *}(\tau)}{\tau-t}\,d\tau\right.$$

$$\left.\left.+\sum_{j=n_1+1}^{n_1+n_2}\frac{1}{\pi i}\int f_j^{**}\frac{e^{-ia_j(\tau)}}{\tau-t}\,d\tau\right)\right],$$

$$t\in L_{3k}^*,\qquad k=\overline{n_1+n_2+1,\ N+M+L}.$$

Here

$$\omega_k(s)=a_k'(s)=-ia_k(t)a_k'(t).$$

Besides the thermal boundary condition (4.1)–(4.3) on the crack, stringer and hole boundaries, the following mechanical boundary conditions are also given [8, 9]:

1. The normal and shear stresses applied along the boundaries l_k of the crack, as well as on the boundaries of the hole γ_j are known,

$$(\sigma_n^{\pm}-i\sigma_t^{\pm})\big|_{l_k},\qquad k=\overline{1,M}, \tag{4.9}$$

$$(\sigma_n-i\sigma_t)|_{\gamma_j},\qquad j=\overline{1,L}. \tag{4.10}$$

2a. Along the boundary of the straight stringer L_k the following relations hold true:

$$\sigma_n^+=\sigma_n^-,\qquad \varepsilon_0=\frac{du_t^+}{dx_k}=\frac{du_t^-}{dx_k},$$
$$u_n^++iu_t^+=u_n^-+iu_t^-\quad\text{on}\quad L_k,\quad k=\overline{1,n_1'}, \tag{4.11}$$

where x_k denotes the abcissa referred to the local coordinate system $x_k0_ky_k$ positioned at the mid-point of the stringer L_k.

By virtue of the condition of equilibrium and Hooke's law for the case of generalized plane stress, relationships (4.11) take the form

$$ih\left[(\sigma_n^+ - i\sigma_t^+) - (\sigma_n^- - i\sigma_t^-)\right] + \frac{E^{(k)}S^{(k)}}{E} ie^{i\theta_k} \frac{d}{dt}\left[(\sigma_n^+ + \sigma_s^+) - (1+\nu)\sigma_n^+\right] = 0, \qquad t \in L_k, \qquad k = \overline{1, n_1'}, \tag{4.12}$$

where t is the complex coordinate of a point on L_k, h is the thickness of the plate, $E^{(k)}$, $S^{(k)}$ express the modulus of elasticity and cross-sectional area, respectively, of the stringer L_k, and θ_k denotes the angle formed by the positive directions of stringer's axis $0x_k$ and $0x$ axis; E, ν express the modulus of elasticity and Poisson's ratio, respectively, of the plate.

3. Furthermore, along the curvilinear (circular arc) boundary of the stringer L_k^* ($k = \overline{n_1' + 1, N}$), the following relationships are satisfied:

$$\begin{aligned} &-\frac{T(\theta)}{R_k} + h(\sigma_n^+ - \sigma_n^-) = 0, \\ &\frac{1}{R_k}\frac{dT(\theta)}{d\theta} + h(\sigma_t^+ - \sigma_t^-) = 0, \\ &u_n^+ + iu_t^+ = u_n^- + iu_t^-, \qquad \varepsilon_0 = \frac{du_t^+}{dt} = \frac{du_t^-}{dt}, \end{aligned} \tag{4.13}$$

which lead to the following relationship, if Hooke's law in generalized plane stress conditions is considered:

$$ER_k h\left[(\sigma_n^+ - \sigma_n^-) - i(\sigma_t^+ - \sigma_t^-)\right] - E^{(k)}S^{(k)}\left[1 - \left(t - m_k e^{ib_k}\right)\frac{d}{dt_k}\right] \times \left[(\sigma_n^+ + \sigma_s^+) - (1+\nu)\sigma_n^+\right] = 0, \tag{4.14}$$

where $T(\theta)$ is the circumferential component of the force which acts along the line in the middle plane of the stringer, and in generalized plane stress conditions are given by the formula

$$T(\theta) = E^{(k)}S^{(k)}\varepsilon_0^{\mathrm{str}}, \tag{4.15}$$

with $\varepsilon_\theta^{\mathrm{str}}$ being the circumferential component of strain along the line in the middle plane of the stringer

$$\varepsilon_0^{\mathrm{str}} = \frac{1}{E}(\sigma_s - \nu\sigma_n). \tag{4.16}$$

Also, $(\sigma_n^\pm, \sigma_t^\pm, \sigma_s^\pm)$ express the normal, shear and circumferential components of the stress tensor, respectively, and the relation $t = m_k e^{ib_k} + t_k$ transforms the points $t_k = R_k e^{i\theta_k}$ referred to the local coordinate system of the curvilinear

stringer, with centre of curvature at 0_k and radius of curvature R_k, to the global coordinate system, with b_k denoting the angle between the lines 00_k and $0x$ and m_k; 00_k is the intercentre distance.

For the description of the boundary conditions (4.9)–(4.14), the complex potentials $\Phi_0(z)$ and $\Psi_0(z)$ are defined as follows:

$$\Phi_0(z) = \Gamma - \sum_{j=1}^{k_1} \frac{P_j + iQ_j}{2\pi(1+\kappa)} \frac{1}{z - z_j^*} + \frac{\beta}{1+\kappa} \sum_{j=1}^{k_3} \frac{q_j}{2\pi\lambda^*} \ln(z - a_j) + \Phi(z), \tag{4.17}$$

$$\begin{aligned} \Psi_0(z) = \Gamma' + \sum_{j=1}^{k_1} \left[\frac{\kappa(P_j - iQ_j)}{2\pi(1+\kappa)} \frac{1}{z - z_j^*} - \frac{\overline{z_j^*}(P_j + iQ_j)}{2\pi(1+\kappa)} \frac{1}{(z - z_j^*)^2} \right] \\ - \sum_{j=1}^{k_2} \frac{M_j}{2\pi} \frac{1}{(z - z_j^{**})^2} - \frac{\beta}{1+\kappa} \sum_{j=1}^{k_3} \frac{q_j}{2\pi\lambda^*} \frac{\overline{aj}}{z - a_j} + \Psi(z), \end{aligned} \tag{4.18}$$

where

$$\Gamma = \frac{1}{4}(N_1 + N_2), \qquad \Gamma' = -\frac{1}{2}(N_1 - N_2),$$

$$\Phi(z) = \sum_{j=1}^{M} \frac{1}{2\pi i} \int_{l_j} \frac{G_{1j}(\tau)}{\tau - z} d\tau + \sum_{j=1}^{N} \frac{1}{2\pi i} \int_{L_j} \frac{G_{2j}(\tau)}{\tau - z} d\tau + \frac{1}{2\pi i} \oint_{\gamma_j} \frac{G_{3j}(\tau)}{\tau - z} d\tau, \tag{4.19}$$

with $G_{1j}(t)$, $G_{2j}(t)$, $G_{3j}(t)$ denoting the densities on l_j, L_j and γ_j, respectively.

By virtue of the boundary conditions (4.9)–(4.11) and (4.13), as well as formulae (2.20), we find the following integral representation for $\Psi(z)$:

$$\begin{aligned} \Psi(z) = \sum_{j=1}^{M} \left[\frac{1}{2\pi i} \int_{l_j} \frac{q_{1j}(\tau)}{\tau - z} d\overline{\tau} - \frac{1}{2\pi i} \int_{l_j} \frac{\overline{G_{1j}(\tau)}}{\tau - z} d\overline{\tau} - \frac{1}{2\pi i} \int_{l_j} \frac{\overline{\tau} G_{1j}(\tau)}{(\tau - z)^2} d\tau \right] \\ + \sum_{j=1}^{N} \left[\frac{\kappa}{2\pi i} \int_{L_j} \frac{\overline{G_{2j}(\tau)}}{\tau - z} \overline{d\tau} - \frac{1}{2\pi i} \int_{L_j} \frac{\overline{\tau} G_{2j}}{(\tau - z)^2} d\tau \right] \\ + \sum_{j=1}^{L} \left[\frac{1}{2\pi i} \oint_{\gamma_j} \frac{q_{1j}^*(\tau)}{\tau - z} d\overline{\tau} - \frac{1}{2\pi i} \oint_{\gamma_j} \frac{\overline{G_{3j}(\tau)}}{\tau - z} d\overline{\tau} - \frac{1}{2\pi i} \oint_{\gamma_j} \frac{\overline{\tau} G_{3j}(\tau)}{(\tau - z)^2} d\tau \right], \end{aligned} \tag{4.20}$$

where

$$\begin{aligned} q_{1j}(t) &= (\sigma_n^+ - \sigma_n^-) - i(\sigma_t^+ - \sigma_t^-), \qquad t \in l_j, \qquad j = \overline{1, M}, \\ q_{1j}^*(t) &= (\sigma_n - i\sigma_t), \qquad t \in \gamma_j, \qquad j = \overline{1, L}. \end{aligned}$$

The combination of boundary conditions (4.9) and (4.12), with relationships (2.20) and Plemelj formulae [1] for the integral representations of $\Phi(z)$, $\Psi(z)$ and $F_*(z)$, gives the following system of singular equations:

$$
\begin{aligned}
(4.21)\qquad & \frac{1}{\pi i}\int_{l_k}\frac{G_{1k}(\tau)}{\tau-t}\,d\tau-\frac{1}{\pi i}\int_{l_k}\frac{\overline{G_{1k}(\tau)}}{\overline{\tau}-\overline{t}}\,\overline{d\tau}\\
&-\frac{dt}{\overline{dt}}\left[\frac{1}{\pi i}\int_{l_k}\frac{\overline{G_{1k}(\tau)}}{\tau-t}\,\overline{d\tau}+\frac{1}{2\pi i}\int_{l_k}\frac{\overline{\tau}-\overline{t}}{(\tau-t)^2}\,G_{1k}(\tau)\,d\tau\right]\\
&+\sum_{\substack{j=1\\ j\neq k}}^{M}\left[\frac{1}{\pi i}\int_{l_j}\frac{G_{1j}(\tau)}{\tau-t}\,d\tau-\frac{1}{\pi i}\int_{l_j}\frac{\overline{G_{1j}(\tau)}}{\tau-t}\,\overline{d\tau}\right.\\
&\left.-\frac{dt}{\overline{dt}}\left[\frac{1}{\pi i}\int_{l_j}\frac{\overline{G_{1j}(\tau)}}{(\tau-t)}\,\overline{d\tau}+\frac{1}{\pi i}\int_{l_j}\frac{\overline{\tau}-\overline{t}}{(\tau-t)^2}\,G_{1j}(\tau)\,d\tau\right]\right]\\
&+\sum_{j=1}^{N}\left[\frac{1}{\pi i}\int_{L_j}\frac{G_{2j}(\tau)}{\tau-t}\,d\tau-\frac{1}{\pi i}\int_{L_j}\frac{\overline{G_{2j}(\tau)}}{\overline{\tau}-\overline{t}}\,\overline{d\tau}\right.\\
&\left.-\frac{dt}{\overline{dt}}\left[-\frac{\kappa}{\pi i}\int_{L_j}\frac{\overline{G_{2j}(\tau)}}{\tau-t}\,\overline{d\tau}+\frac{1}{\pi i}\int_{L_j}\frac{\overline{\tau}-\overline{t}}{(\tau-t)^2}G_{2j}(\tau)\,d\tau\right]\right]\\
&+\sum_{j=1}^{L}\left[\frac{1}{\pi i}\oint_{\gamma_j}\frac{G_{3j}(\tau)}{\tau-t}\,d\tau-\frac{1}{\pi i}\oint_{\gamma_j}\frac{\overline{G_{3j}(\tau)}}{\overline{\tau}-\overline{t}}\,\overline{d\tau}\right.\\
&\left.-\frac{dt}{\overline{dt}}\left[\frac{1}{\pi i}\oint_{\gamma_j}\frac{\overline{G_{3j}(\tau)}}{\tau-t}\,\overline{dt}+\frac{1}{\pi i}\oint_{\gamma_j}\frac{\overline{\tau}-\overline{t}}{(\tau-t)^2}\,G_{3j}(\tau)\,d\tau\right]\right]\\
&=A_{1k}(t,\overline{t})-\frac{dt}{\overline{dt}}\left[\frac{1}{\pi i}\int_{l_k}\frac{q_{1k}(\tau)}{\tau-t}\,d\tau+\sum_{\substack{j=1\\ j\neq k}}^{M}\frac{1}{\pi i}\int_{l_j}\frac{q_{1j}(\tau)}{\tau-t}\,d\tau+\sum_{j=1}^{L}\frac{1}{\pi i}\oint_{\gamma_j}\frac{q^*_{1j}(\tau)}{\tau-t}\,d\tau\right],\\
&\qquad\qquad t\in l_k,\qquad k=\overline{1,M},
\end{aligned}
$$

$$
\begin{aligned}
(4.22)\qquad & ih\left[(\kappa+1)G_{2k}(t)+\beta\varphi_{2k}(t)\right]+\frac{E^{(\kappa)}S^{(\kappa)}}{E}ie^{i\theta_k}\\
&\times\frac{d}{dt}\left(\mathrm{Re}\left[\frac{3-\nu-\kappa(1+\nu)}{2}G_{2k}(t)-\frac{\beta(1+\nu)}{2}\varphi_{2k}(t)\right.\right.
\end{aligned}
$$

(4.22) [cont.]

$$+\frac{1-\nu}{2}\int\limits_{L_k}\frac{G_{2k}(\tau)}{\tau-t}\,d\tau-(1+\nu)\frac{dt}{d\overline{t}}\left[\frac{\kappa}{2\pi i}\int\limits_{L_k}\frac{\overline{G_{2k}(\tau)}}{\tau-t}\,\overline{d\tau}\right.$$

$$\left.-\frac{1}{2\pi i}\int\limits_{L_k}\frac{\overline{\tau}-\overline{t}}{(\tau-t)^2}\,G_{2k}(\tau)\,d\tau+\frac{\beta}{2\pi i}\int\limits_{L_k}\frac{\overline{\varphi_{2k}(\tau)}}{\tau-t}\,\overline{d\tau}\right]+\sum_{\substack{j=1\\ j\neq k}}^{N}\left[\frac{1-\nu}{\pi i}\int\limits_{L_j}\frac{G_{2j}(\tau)}{\tau-t}\,d\tau\right.$$

$$-(1+\nu)\frac{dt}{d\overline{t}}\left(\frac{\kappa}{2\pi i}\int\limits_{L_j}\frac{\overline{G_{2j}(\tau)}}{\tau-t}\,\overline{d\tau}-\frac{1}{2\pi i}\int\limits_{L_k}\frac{\overline{\tau}-\overline{t}}{(\tau-t)^2}\,G_{2k}(\tau)\,d\tau\right.$$

$$\left.+\frac{\beta}{2\pi i}\int\limits_{L_k}\frac{\overline{\varphi_{2k}(\tau)}}{\tau-t}\,\overline{d\tau}\right)+\sum_{\substack{j=1\\ j\neq k}}^{N}\left[\frac{1-\nu}{\pi i}\int\limits_{L_j}\frac{G_{2j}(\tau)}{\tau-t}\,d\tau\right.$$

$$-(1+\nu)\frac{dt}{d\overline{t}}\left(\frac{\kappa}{2\pi i}\int\limits_{L_j}\frac{\overline{G_{2j}(\tau)}}{\tau-t}\,\overline{d\tau}-\frac{1}{2\pi i}\int\limits_{L_j}\frac{\overline{\tau}-\overline{t}}{(\tau-t)^2}\,G_{2j}(\tau)\,d\tau\right.$$

$$\left.\left.+\frac{\beta}{2\pi i}\int\limits_{L_j}\frac{\overline{\varphi_{2j}(\tau)}}{\tau-t}\,\overline{d\tau}\right)\right]+\sum_{\substack{j=1\\ j\neq k}}^{M}\left[\frac{1-\nu}{\pi i}\int\limits_{l_j}\frac{G_{1j}(\tau)}{\tau-t}\,d\tau\right.$$

$$\left.+(1+\nu)\frac{dt}{d\overline{\tau}}\left(\frac{1}{2\pi i}\int\limits_{l_j}\frac{\overline{G_{1j}(\tau)}}{\tau-t}\,\overline{d\tau}+\frac{1}{2\pi i}\int\limits_{l_j}\frac{\overline{\tau}-\overline{t}}{(\tau-t)^2}\,G_{1j}(\tau)\,d\tau\right)\right]$$

$$+\sum_{j=1}^{L}\left[\frac{1-\nu}{\pi i}\oint\limits_{\gamma_j}\frac{G_{3j}(\tau)}{\tau-t}\,d\tau+(1+\nu)\frac{dt}{d\overline{t}}\left(\frac{1}{2\pi i}\oint\limits_{\gamma_j}\frac{\overline{G_{3j}(\tau)}}{\tau-t}\,\overline{d\tau}\right.\right.$$

$$\left.\left.\left.+\frac{1}{2\pi i}\oint\limits_{\gamma_j}\frac{\overline{\tau}-\overline{t}}{(\tau-t)^2}G_{3j}(\tau)\,d\tau\right)\right]\right]=A_{2k}(t,\overline{t}),\qquad t\in L_k,\qquad k=\overline{1,n_1'}.$$

Here

$$A_{1k}(t,\overline{t})=(\sigma_n^+ + \sigma_n^-)-i(\sigma_t^+ + \sigma_t^-)-2\left(\Gamma+\overline{\Gamma}+\frac{dt}{d\overline{t}}\Gamma'\right)$$

$$+\sum_{j=1}^{k_1}\left[2\mathrm{Re}\,\frac{P_j+iQ_j}{\pi(1+\kappa)}\,\frac{1}{t-z_j^*}-\frac{dt}{d\overline{t}}\left[\frac{\kappa(P_j+iQ_j)}{\pi(1+\kappa)}\,\frac{1}{t-z_j^*}+\frac{P_j+iQ_j}{\pi(1+\kappa)}\,\frac{\overline{t}-\overline{z_j^*}}{(t-z_j^*)^2}\right]\right]$$

$$-i\sum_{j=1}^{k_2}\frac{dt}{d\overline{t}}\,\frac{M_j}{\pi}\,\frac{1}{(t-z_j^{**})^2}-\frac{\beta}{1+\kappa}\sum_{j=1}^{k_3}\frac{q_j}{2\pi\lambda^*}\left[\mathrm{Re}\ln(t-a_j)+\frac{dt}{d\overline{t}}\,\frac{\overline{t}-\overline{a_j}}{t-a_j}\right],$$

$$A_{2k}(t,\bar{t}) = \frac{E^{(k)}S^{(k)}}{E} ie^{i\theta_k} \frac{d}{d\bar{t}} \mathrm{Re}\left[\frac{dt}{d\bar{t}}\left(\sum_{j=1}^{M}\frac{1}{\pi i}\int_{l_j}\frac{q_{1j}(\tau)}{\tau - t}\,\overline{d\tau}\right.\right.$$
$$\left.\left. + \sum_{j=1}^{L}\frac{1}{\pi i}\oint_{\gamma_j}\frac{q^*_{1j}(\tau)}{\tau - t}\,\overline{d\tau}\right)\right] + \sum_{j=1}^{k_1}(1-\nu)\frac{P_j + iQ_j}{\pi(1+\kappa)}\frac{1}{t - z_j^*}$$
$$-\frac{dt}{d\bar{t}}\left(\frac{\kappa(P_j - iQ_j)}{2\pi(1+\kappa)}\frac{1}{t - z_j^*} + \frac{P_j + iQ_j}{2\pi(1+\kappa)}\frac{\bar{t} - \overline{z_j^*}}{(t - z_j^*)^2}\right)$$
$$-i\sum_{j=1}^{k_2}\frac{dt}{d\bar{t}}\frac{M_j}{2\pi}\frac{1}{(t - z_j^{**})^2} - \frac{\beta}{(1+\kappa)}\sum_{j=1}^{k_3}\frac{q_j}{2\pi\lambda^*}$$
$$\times\left[2(1-\nu)\ln(t - a_j) + \frac{dt}{d\bar{t}}\frac{\bar{t} - \overline{a_j}}{t - a_j}\right].$$

Analysis of the boundary conditions (4.10), (4.14) on the one hand, and (4.9), (4.13) on the other hand, leads to the conclusion that they are analogous. This fact gives the opportunity for the other two categories of integro-differential equations on the curvilinear thin inclusions L_j^* ($j = \overline{n_1' + 1, N}$) and on the holes γ_j ($j = \overline{1, L}$) to be obtained in a similar manner. This has not been done in this paper by reason of economy of space.

Finally, the system of integro-differential equations (4.21), (4.22) is supplemented with the conditions for singlevaluedness of the displacement along l_k ($k = \overline{(1, M)}$),

$$\int_{l_k} G_{1k}(t)\,dt = \frac{1}{1+\kappa}\int_{l_k}\overline{q_{1k}(t)}\,dt$$
$$-\frac{\beta}{1+\kappa}\int_{l_k}\varphi_{1k}(t)\,dt, \qquad t \in l_k, \qquad k = \overline{(1, M)}. \tag{4.23}$$

Representations of the densities $G_{1k}(t)$, $G_{2k}(t)$, $G_{3k}(t)$ on the cracks, stringers and holes, respectively, assume the following forms:

$$G_{1k}(t) = \frac{q_{1k}(t)}{1+\kappa} + g_{1k}(t) - \frac{\beta}{1+\kappa}\varphi_{1k}(t), \quad t \in l_k, \quad k = \overline{1, M},$$
$$G_{2k}(t) = \frac{i(\sigma_t^+ - \sigma_t^-)}{1+\kappa} - \frac{\beta}{1+\kappa}\varphi_{2k}(t), \quad t = \in L_k, \quad k = \overline{1, N}, \tag{4.24}$$
$$G_{3k}(t) = \frac{q^*_{1k}(t)}{1+\kappa} + g_{3k}(t) - \frac{\beta}{1+\kappa}\varphi_{3k}(t), \quad t \in \gamma_k, \quad k = \overline{1, L},$$

where

$$g_{1k}(t) = \frac{2\mu}{1+\kappa}\frac{d}{dt}\left[(u^+(t) - u^-(t)) + i(v^+(t) - v^-(t))\right],$$

$$g_{3k}(t) = \frac{2\mu}{1+\kappa}\frac{d}{dt}(u(t) + iv(t)).$$

The system of equations (4.21)–(4.22), in combination with the integro-differential equations (4.6)–(4.8) and the appropriate conditions for equilibrium of the temperature factor, permits one to describe completely in quantitative terms the stress and thermal fields in the cracked, partially non-homogeneous, and multiply connected infinite isotropic plate.

5. Integro-differential equations of the plane thermoelasticity problem for the infinite cracked orthotropic plate with reinforcements

Let us consider an infinite orthotropic plate which is under the action of a mechanical and thermal field. The body contains an internal curvilinear crack ℓ and a straight stringer L, and is subjected to the stresses σ_x^∞, σ_y^∞, τ_{xy}^∞, as well as to the homogeneous thermal flow q_∞ at an angle β_0 with respect to $0x$-axis, at infinity. Also, a concentrated force $(X + iY)$ and a moment M_0 are acting at the points z^*, z^{**}, respectively, while a thermal source of power q_0 is located at the point a^*. Furthermore, it is assumed that the direction of reinforcement coincides with one of the principal elasticity axes $0x$ (Fig. 3).

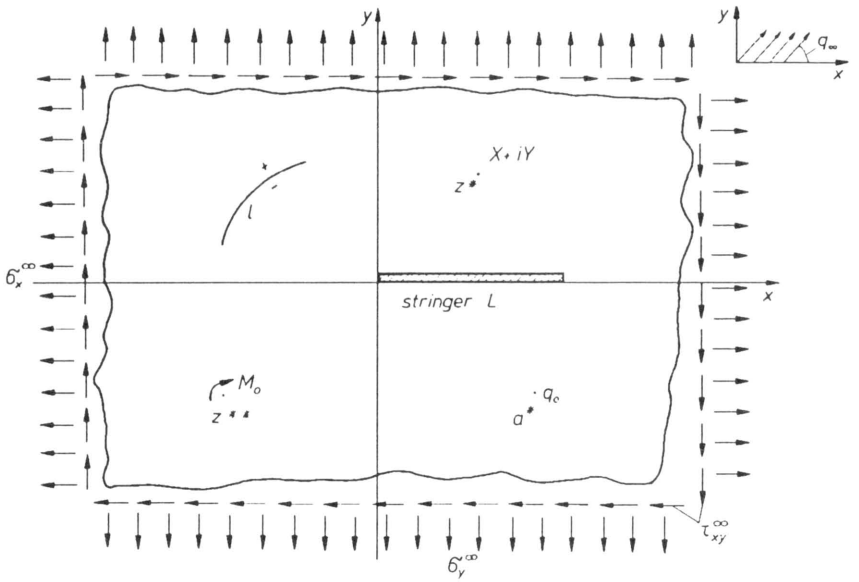

FIG. 3. Infinite orthotropic thin plate under the influence of stress and thermal fields, containing a curvilinear crack and a straight stringer.

Depending on the type of thermal contact along the boundaries of the crack ℓ and along the stringer L, one of the three thermal surface conditions expressed by the relationships (3.14)–(3.16), is possible. Additionally, the mechanical boundary

conditions along the lips of the crack ℓ and the stringer L are analogous to those of the isotropic medium (4.9) and (4.11), whereas relation (4.12), in the case of the orthotropic body, takes the form [11]

$$ih\left[(\sigma_n^+ - i\sigma_t^+) - (\sigma_n^- - i\sigma_t^-)\right] + E_0 S_0 \frac{d}{dt}\left[\frac{1}{E_x}\sigma_s^+ - \frac{\nu_y}{E_y}\sigma_n^+\right] = 0. \tag{5.1}$$

The complex potentials $\Phi_0(z_1)$, $\Psi_0(z_2)$, $F(z_3)$ which describe the mechanical boundary conditions on ℓ and L, by considering also relationships (2.21), are given in the following form [11]:

$$\Phi_0(z_1) = \Gamma + \frac{C_{11}X + C_{12}Y}{z_1 - \xi_1^*} - i\frac{M_0}{8\pi}\frac{1}{(z_1 - \xi_1^{**})^2} + a_0'[1 + \ln(z_1 - a_1^*)] + \Phi(z_1), \tag{5.2}$$

$$\Psi_0(z_2) = \Gamma' + \frac{C_{21}X - C_{22}Y}{z_2 - \xi_2^*} - i\frac{M_0}{8\pi}\frac{1}{(z_2 - \xi_2^{**})^2} + b_0'[1 + \ln(z_2 - a_2^*)] + \Psi(z_2), \tag{5.3}$$

$$F(z_3) = m_0[1 + \ln(z_3 - a_3^*)] + \frac{(\cos\beta_0 + \overline{\mu}_3 \sin\beta_0)z_3}{2\sqrt{k_{11}k_{22}}\,\mathrm{Im}\,\mu_3} q^\infty + F_*(z_3), \tag{5.4}$$

where the constants C_{11}, C_{12}, C_{21}, C_{22}, Γ, Γ' are determined from the relationships

$$C_{11} = \frac{1}{2\pi i}\frac{\mu_2 + \overline{\mu}_2 + \overline{\mu}_1 + \mu_2\overline{\mu}_1\overline{\mu}_2\dfrac{\nu_x E_y}{E_x}}{(\mu_1 - \mu_2)(\mu_1 - \overline{\mu}_1)\left(1 - \dfrac{\overline{\mu}_2}{\mu_1}\right)},$$

$$C_{12} = \frac{1}{2\pi i}\frac{\mu_2\overline{\mu}_2 + \overline{\mu}_1\mu_2 + \overline{\mu}_1\overline{\mu}_2\nu_x}{(\mu_1 - \mu_2)(\mu_1 - \overline{\mu}_1)\left(1 - \dfrac{\overline{\mu}_2}{\mu_1}\right)},$$

$$C_{21} = \frac{1}{2\pi i}\frac{\mu_1 + \overline{\mu}_1 + \overline{\mu}_2 + \mu_1\overline{\mu}_1\mu_2\dfrac{\nu_x E_y}{E_x}}{(\mu_2 - \mu_1)(\mu_2 - \overline{\mu}_2)\left(1 - \dfrac{\overline{\mu}_1}{\mu_2}\right)},$$

$$C_{22} = \frac{1}{2\pi i}\frac{\mu_1\overline{\mu}_1 + \overline{\mu}_2\mu_1 + \overline{\mu}_2\overline{\mu}_1\nu_x}{(\mu_2 - \mu_1)(\mu_2 - \overline{\mu}_2)\left(1 - \dfrac{\overline{\mu}_1}{\mu_2}\right)},$$

$$\begin{aligned}
\Gamma - \overline{\Gamma} &= 0,\\
\mu_1^2\Gamma + \overline{\mu}_1^2\overline{\Gamma} + \mu_2^2\Gamma' + \overline{\mu}_2^2\overline{\Gamma}' &= \sigma_x^\infty,\\
\Gamma + \overline{\Gamma} + \Gamma' + \overline{\Gamma}' &= \sigma_y^\infty,\\
\mu_1\Gamma + \overline{\mu}_1\overline{\Gamma} + \mu_2\Gamma' + \overline{\mu}_2\overline{\Gamma}' &= -\tau_{xy}^\infty,
\end{aligned}$$

whereas

$$\Phi(z_1) = \frac{1}{2\pi i}\int_{L_1} \frac{\varphi(\tau_1)}{\tau_1 - z_1}\,d\tau_1 + \frac{1}{2\pi i}\int_{\ell_1} \frac{g(\tau_1)}{\tau_1 - z_1}\,d\tau_1\,, \tag{5.5}$$

$$\Psi(z_2) = \frac{1}{2\pi i}\int_{L_2} \frac{\psi(\tau_2)}{\tau_2 - z_2}\,d\tau_2 + \frac{1}{2\pi i}\int_{\ell_2} \frac{g(\tau_2)}{\tau_2 - z_2}\,d\tau_2, \tag{5.6}$$

$$\begin{aligned} F_*(z_3) = {} & \frac{1}{2\pi i}\int_{L_3} \frac{\mu_{11}(\tau_3)}{\tau_3 - z_3}\,d\tau_3 + \frac{1}{2\pi i}\int_{L_3} \mu_{12}(\tau_3)e^{-ia_1(\tau_3)}\ln(\tau_3 - z_3)\,d\tau_3 \\ & + \frac{1}{2\pi i}\int_{\ell_3} \frac{\mu_{21}(\tau_3)}{\tau_3 - z_3}\,d\tau_3 + \frac{1}{2\pi i}\int_{\ell_3} \mu_{22}(\tau_3)e^{-ia_2(\tau_3)}\ln(\tau_3 - z_3)\,d\tau_3. \end{aligned} \tag{5.7}$$

Depending on the type of thermal contact on ℓ and L, we select the corresponding condition from relationships (3.14)–(3.16), where we substitute the limiting values of $F(z)$. From this operation, a system of integro-differential equations with respect to $\mu_{11}(t)$, $\mu_{12}(t)$, $\mu_{21}(t)$, $\mu_{22}(t)$ is derived. Basing on this system, the determination of the thermal field $T(x, y)$ of the cracked anisotropic plate reinforced by stringers is possible. This system is analogous to the system (4.6)–(4.8) of the isotropic medium.

By taking into consideration the mechanical boundary conditions (4.9) and (5.1) on ℓ and L, respectively, as well as the limiting values of $\Phi_0(z_1)$, $\Psi_0(z_2)$, $F_0(z_3)$, and after some algebraic manipulations analogous to those presented in [11], we formulate the following system of singular integro-differential equations:

$$\begin{aligned} & \frac{\mu_1 - \overline{\mu}_2}{\pi i}\frac{dt_1}{dt}\left[\int_{\ell_1} \frac{g(\tau_1)}{\tau_1 - t_1}\,d\tau_1 + \int_{L_1} \frac{\varphi(\tau_1)}{\tau_1 - t_1}\,d\tau_1\right] \\ & \qquad - \frac{\overline{\mu}_1 - \overline{\mu}_2}{\pi i}\frac{\overline{dt_1}}{dt}\left[\int_{\ell_1} \frac{\overline{g(\tau_1)}}{\overline{\tau}_1 - \overline{t}_1}\,\overline{d\tau_1} + \int_{L_1} \frac{\overline{\varphi(\tau_1)}}{\overline{\tau}_1 - \overline{t}_1}\,\overline{d\tau_1}\right] \\ & + n_0(\mu_3 - \overline{\mu}_2)\frac{dt_3}{dt}\left[\frac{1}{\pi i}\int_{\ell_3} \frac{\mu_{21}(\tau_3)}{\tau_3 - t_3}\,d\tau_3 + \frac{1}{\pi i}\int_{\ell_3} \mu_{22}(\tau_3)e^{-ia_2(\tau_3)}\ln(\tau_3 - t_3)\,d\tau_3\right. \\ & \qquad \left. + \frac{1}{\pi i}\int_{L_3} \frac{\mu_{11}(\tau_3)}{\tau_3 - t_3}\,d\tau_3 + \frac{1}{\pi i}\int_{L_3} \mu_{12}(\tau_3)e^{-ia_1(\tau_3)}\ln(\tau_3 - t_3)\,d\tau_3\right] \\ & - n_0(\overline{\mu}_3 - \overline{\mu}_2)\frac{\overline{dt_3}}{dt}\left[\frac{1}{\pi i}\int_{\ell_3} \frac{\mu_{21}(\tau_3)}{\overline{\tau}_3 - \overline{t}_3}\,\overline{d\tau_3} + \frac{1}{\pi i}\int_{\ell_3} \mu_{22}(\tau_3)\overline{e^{-ia_1(\tau_3)}\ln(\tau_3 - t_3)}\,\overline{d\tau_3}\right. \end{aligned} \tag{5.8}$$

(5.8) [cont.]

$$+\frac{1}{\pi i}\int\limits_{L_3}\frac{\mu_{11}(\tau_3)}{\overline{\tau}_3-\overline{t}_3}\,\overline{d\tau_3}+\frac{1}{\pi i}\int\limits_{L_3}\mu_{12}(\tau_3)\overline{e^{-ia_1(\tau_3)}\ln(\tau_3-t_3)\,d\tau_3}\Bigg]$$

$$-\frac{\mu_2-\overline{\mu}_2}{\pi i}\frac{dt_2}{dt}\Bigg[\frac{\mu_1-\overline{\mu}_2}{\mu_2-\overline{\mu}_2}\int\limits_{\ell_1}\frac{g(\tau_1)}{\tau_2-t_2}\,d\tau_1+\frac{\overline{\mu}_1-\overline{\mu}_2}{\mu_2-\overline{\mu}_2}\int\limits_{\ell_1}\frac{\overline{g(\tau_1)}}{\tau_2-t_2}\,\overline{d\tau_1}$$

$$+n_0\frac{\mu_3-\overline{\mu}_2}{\mu_2-\overline{\mu}_2}\int\limits_{\ell_3}\frac{\mu_{21}(\tau_3)}{\tau_3-t_3}\,d\tau_3+n_0\frac{\overline{\mu}_3-\overline{\mu}_2}{\mu_2-\overline{\mu}_2}\int\limits_{L_3}\frac{\mu_{21}(\tau_3)}{\tau_3-t_3}\,\overline{d\tau_3}$$

$$-\frac{p_1\overline{q}_2-\overline{p}_2q_1}{\overline{p}_2q_1-p_1\overline{q}_2}\int\limits_{L_1}\frac{\varphi(\tau_1)}{\tau_2-t_2}\,d\tau_1-\frac{\overline{p_1q_2}-\overline{p_2q_1}}{\overline{p}_2q_2-p_2\overline{q}_2}\int\limits_{\ell_1}\frac{\overline{\varphi(\tau_1)}}{\tau_2-t_2}\,\overline{d\tau_1}$$

$$-\frac{p_*\overline{q}_2-p_2\overline{q}_*}{\overline{p}_2q_2-p_2\overline{q}_2}\int\limits_{L_3}\frac{\mu_{11}(\tau_3)}{\tau_2-t_2}\,d\tau_3+\frac{\overline{p_*q_2}-\overline{p_2q_*}}{\overline{p}_2q_2-p_2\overline{q}_2}\int\limits_{L_3}\frac{\mu_{11}(\tau_3)}{\tau_2-t_2}\,\overline{d\tau_3}\Bigg]$$

$$=q^+(t)+q^-(t)-\frac{dt_2}{dt}\frac{1}{\pi i}\int\limits_{\ell}\frac{q^+(\tau)-q^-(\tau)}{\tau_2-t_2}\,d\tau,\quad t,t_1,t_2,t_3\in\ell,\ell_1,\ell_2,\ell_3;$$

(5.9)

$$ih\left[(1-i\mu_1)+(1-i\mu_2)\frac{p_1\overline{q}_2-\overline{p}_2q_1}{\overline{p}_2q_2-p_2\overline{q}_2}+(1-i\overline{\mu}_2)\frac{p_1q_2-p_2q_1}{p_2\overline{q}_2-\overline{p}_2q_2}\right]\frac{dt_1}{dt}\varphi(t_1)$$

$$+\left[(1-i\overline{\mu}_1)+(1-i\mu_2)\frac{\overline{p_1q_2}-\overline{p_2q_1}}{\overline{p}_2q_2-p_2\overline{q}_2}+(1-i\overline{\mu}_2)\frac{\overline{p}_1q_2-p_2\overline{q}_1}{p_2\overline{q}_2-\overline{p}_2q_2}\right]\frac{\overline{dt_1}}{\overline{dt}}\,\overline{\varphi(t_1)}$$

$$+n_0\left[(1-i\mu_3)+(1-i\mu_2)\frac{p_*\overline{q}_2-\overline{p}_2q_*}{\overline{p}_2q_2-p_2\overline{q}_2}+(1-i\overline{\mu}_2)\frac{p_*q_2-p_2q_*}{p_2\overline{q}_2-\overline{p}_2q_2}\right]\frac{dt_3}{dt}\mu_{11}(t_3)$$

$$+n_0\left[(1-i\overline{\mu}_3)+(1-i\mu_2)\frac{\overline{p_*q_2}-\overline{p_2q_*}}{\overline{p}_2q_2-p_2\overline{q}_2}+(1-i\overline{\mu_2})\frac{\overline{p}_*q_2-p_2\overline{q}_*}{p_2\overline{q}_2-\overline{p}_2q_2}\right]\frac{\overline{dt_3}}{dt}\,\overline{\mu_{11}(t_3)}$$

$$+\frac{E_0S_0}{4}\frac{d}{dt}\Bigg\{\left(B_1+B_3\frac{p_1\overline{q}_2-\overline{p}_2q_1}{\overline{p}_2q_2-p_2\overline{q}_2}\frac{dt_1}{dt_2}+B_4\frac{p_1q_2-p_2q_1}{p_2\overline{q}_2-\overline{p}_2q_2}\frac{\overline{dt_1}}{\overline{dt_2}}\right)\varphi(t_1)$$

$$+\left(B_2+B_3\frac{\overline{p_1q_2}-\overline{p_2q_1}}{\overline{p}_2q_2-p_2\overline{q}_2}\frac{\overline{dt_1}}{dt_2}+B_4\frac{\overline{p}_1q_2-p_2\overline{q}_1}{p_2\overline{q}_2-\overline{p}_2q_2}\frac{\overline{dt_1}}{\overline{dt_2}}\right)\overline{\varphi(t_1)}$$

$$+\Bigg[B_5+B_6+B_3\left(\frac{p_*\overline{q}_2-\overline{p}_2q_*}{\overline{p}_2q_2-p_2\overline{q}_2}\frac{dt_3}{dt_2}+\frac{\overline{p_*q_2}-\overline{p_2q_*}}{\overline{p}_2q_2-p_2\overline{q}_2}\frac{\overline{dt_3}}{dt_2}\right)$$

$$+B_4\left(\frac{p_*q_2-p_2q_*}{p_2\overline{q}_2-\overline{p}_2q_2}\frac{dt_3}{dt_2}+\frac{\overline{p}_*q_2-p_2\overline{q}_*}{p_2\overline{q}_2-\overline{p}_2q_2}\frac{\overline{dt_3}}{dt_2}\right)\Bigg]\mu_{11}(t_3)$$

$$+\frac{B_1}{\pi i}\int\limits_{L_1}\frac{\varphi(\tau_1)}{\tau-t_1}\,d\tau_1-\frac{B_2}{\pi i}\int\limits_{L_1}\frac{\overline{\varphi(\tau_1)}}{\overline{\tau}_1-\overline{t}_1}\,\overline{d\tau_1}+\frac{B_3}{\pi i}\left(\frac{p_1\overline{q}_2-\overline{p}_2q_1}{\overline{p}_2q_2-p_2\overline{q}_2}\int\limits_{L_1}\frac{\varphi(\tau_1)}{\tau_2-t_2}\,d\tau_1\right.$$

(5.9) [cont.]

$$+\frac{\overline{p_1q_2-\overline{p_2q_1}}}{\overline{p}_2q_2-p_2\overline{q}_2}\int\limits_{L_1}\frac{\overline{\varphi(\tau_1)}}{\tau_2-t_2}\,\overline{d\tau_1}+\frac{p_*\overline{q}_2-\overline{p}_2q_*}{\overline{p}_2q_2-p_2\overline{q}_2}\int\limits_{L_1}\frac{\mu_{11}(\tau_3)}{\tau_2-t_2}\,d\tau_3$$

$$+\frac{\overline{p_*q_2}-\overline{p_2q_*}}{\overline{p}_2q_2-p_2\overline{q}_2}\int\limits_{L_3}\overline{\frac{\mu_{11}(\tau_3)}{\tau_2-t_2}\,d\tau_3}\Bigg)-\frac{B_4}{\pi i}\Bigg(\frac{p_1q_2-p_2q_1}{p_2\overline{q}_2-\overline{p}_2q_2}\int\limits_{L_1}\frac{\varphi(\tau_1)}{\overline{\tau}_2-\overline{t}_2}\,d\tau_1$$

$$+\frac{\overline{p}_1q_2-p_2\overline{q}_1}{p_2\overline{q}_2-\overline{p}_2q_2}\int\limits_{L_1}\overline{\frac{\varphi(\tau_1)}{\overline{\tau}_2-\overline{t}_2}}\,\overline{d\tau_1}$$

$$+\frac{p_*q_2-p_2q_*}{p_2\overline{q}_2-\overline{p}_2q_2}\int\limits_{L_3}\frac{\mu_{11}(\tau_3)}{\overline{\tau}_2-\overline{t}_2}\,d\tau_3+\frac{\overline{p}_*q_2-p_2\overline{q}_*}{p_2\overline{q}_2-\overline{p}_2q_2}\int\limits_{L_3}\frac{\mu_{11}(\tau_3)}{\overline{\tau}_2-\overline{t}_2}\,d\tau_3\Bigg)$$

$$+B_5\Bigg[\frac{1}{\pi i}\int\limits_{L_3}\frac{\mu_{11}(\tau_3)}{\tau_3-t_3}\,d\tau_3+\frac{1}{\pi i}\int\limits_{L_3}\mu_{12}(\tau_3)e^{-ia_1(\tau_3)}\ln(\tau_3-t_3)\,d\tau_3$$

$$+\frac{1}{\pi i}\int\limits_{L_3}\frac{\mu_{21}(\tau_3)}{\tau_3-t_3}\,d\tau_3+\frac{1}{\pi i}\int\limits_{L_3}\mu_{22}(\tau_3)e^{-ia_2(\tau_3)}\ln(\tau_3-t_3)\,d\tau_3\Bigg]$$

$$-B_6\Bigg[\frac{1}{\pi i}\int\limits_{L_3}\frac{\mu_{11}(\tau_3)}{\overline{\tau}_2-\overline{t}_3}\,d\overline{\tau}_3+\frac{1}{\pi i}\int\limits_{L_3}\mu_{12}(\tau_3)\overline{e^{-ia_1(\tau_3)}\ln(\tau_3-t_3)\,d\tau_3}$$

$$+\frac{1}{\pi i}\int\limits_{L_3}\frac{\mu_{21}(\tau_3)}{\overline{\tau}_3-\overline{t}_3}\,d\overline{\tau}_3+\frac{1}{\pi i}\int\limits_{L_3}\mu_{22}(\tau_3)\overline{e^{-ia_2(\tau_3)}\ln(\tau_3-t_3)\,d\tau_3}\Bigg]$$

$$+\frac{B_1}{\pi i}\int\limits_{\ell_1}\frac{g(\tau_1)}{\tau_1-t_1}\,d\tau_1-\frac{B_2}{\pi i}\int\limits_{\ell_1}\overline{\frac{g(\tau_1)}{\overline{\tau}_1-\overline{t}_1}}\,\overline{d\tau_1}-\frac{B_3}{\pi i}\Bigg[\frac{\mu_1-\overline{\mu}_2}{\mu_2-\overline{\mu}_2}\int\limits_{\ell_1}\frac{g(\tau_1)}{\tau_2-t_2}\,d\tau_1$$

$$+\frac{\overline{\mu}_1-\overline{\mu}_2}{\mu_2-\overline{\mu}_2}\int\limits_{\ell_1}\overline{\frac{g(\tau_1)}{\tau_2-t_2}}\,\overline{d\tau_1}+n_0\frac{\mu_3-\overline{\mu}_2}{\mu_2-\overline{\mu}_2}\int\limits_{\ell_3}\frac{\mu_{21}(\tau_3)}{\tau_3-t_3}\,d\tau_3$$

$$+n_0\frac{\overline{\mu}_3-\overline{\mu}_2}{\mu_2-\overline{\mu}_2}\int\limits_{\ell_3}\frac{\mu_{21}(\tau_3)}{\tau_3-t_3}\,\overline{d\tau_3}\Bigg]+\frac{B_4}{\pi i}\Bigg[\frac{\overline{\mu}_1-\mu_2}{\overline{\mu}_2-\mu_2}\int\limits_{\ell_1}\overline{\frac{g(\tau_1)}{\overline{\tau}_2-\overline{t}_2}}\,\overline{d\tau_1}$$

$$+\frac{\mu_1-\mu_2}{\overline{\mu}_2-\mu_2}\int\limits_{\ell_3}\frac{g(\tau_1)}{\overline{\tau}_2-\overline{t}_2}\,d\tau_1+n_0\frac{\overline{\mu}_3-\mu_2}{\overline{\mu}_2-\mu_2}\int\limits_{\ell_3}\frac{\mu_{21}(\tau_3)}{\overline{\tau}_3-\overline{t}_3}\,\overline{d\tau_3}+n_0\frac{\mu_3-\mu_2}{\overline{\mu}_2-\mu_2}$$

(5.9) [cont.)

$$\times \int_{\ell_3} \frac{\mu_{21}(\tau_3)}{\overline{\tau}_3 - \overline{t}_3}\, \overline{d\tau_3} \Bigg] \Bigg\} = A(t,\overline{t}) - \frac{E_0 S_0}{4} \frac{d}{dt} \Bigg[\frac{B_3}{\pi i(\mu_2 - \overline{\mu}_2)} \int_{\ell} \frac{q^+(\tau) - q^-(\tau)}{\tau_2 - t_2}\, d\tau$$

$$- \frac{B_4}{\pi i(\overline{\mu}_2 - \mu_2)} \int_{\ell} \frac{\overline{q^+(\tau) - q^-(\tau)}}{\overline{\tau}_2 - \overline{t}_2}\, \overline{d\tau} \Bigg], \qquad t, t_1, t_2, t_3 \in L, L_1, L_2, L_3,$$

where

$$q^{\pm}(t) = -i(1 - i\overline{\mu}_2) f^{\pm}(t) + i\frac{d\overline{t}}{dt}(1 + i\overline{\mu}_2) f^{\pm}(t),$$

$$f^{\pm}(t) = \sigma_n^{\pm} + i\sigma_t^{\pm} - \frac{1}{2}\Big\{2\mathrm{Re}\left[(1 + \mu_1^2)A_{11} + (1 + \mu_2^2)A_{12} + n_0(1 + \mu_3^2)A_{13}\right]$$

$$+ \frac{\overline{dt}}{dt}\left[(1 + i\mu_1)^2 A_{11} + (1 + i\mu_2)^2 A_{12} + n_0(1 + i\mu_3)^2 A_{13}\right.$$

$$\left. + (1 + i\overline{\mu}_1)^2 \overline{A_{11}} + (1 + i\overline{\mu}_2)^2 \overline{A_{12}} + n_0(1 + i\overline{\mu}_3)^2 \overline{A_{13}}\right]\Big\},$$

$$A_{11} = \Gamma + \frac{C_{11}X + C_{12}Y}{t_1 - \xi_1^*} - i\frac{M_0}{8\pi} \frac{1}{(t_1 - \xi_1^{**})^2} + a_0'[1 + \ln(t_1 - a_1^*)],$$

$$A_{12} = \Gamma' + \frac{C_{21}X - C_{22}Y}{t_2 - \xi_2^*} - i\frac{M_0}{8\pi} \frac{1}{(t_2 - \xi_2^{**})^2} + b_0'[1 + \ln(t_2 - a_2^*)],$$

$$A_{13} = m_0[1 + \ln(t_3 - a_3^*)],$$

$$A(t,\overline{t}) = -\frac{E_0 S_0}{2} \frac{d}{dt}\left\{B_1 A_{21} + B_2 \overline{A_{21}} + B_3 A_{22} + B_4 \overline{A_{22}} + B_5 A_{23} + B_6 \overline{A_{23}}\right\},$$

$$A_{21} = A_{11} - \Gamma, \qquad A_{22} = A_{12} - \Gamma', \qquad A_{13} = A_{23},$$

$$B_1 = \frac{1}{E_x}\left[2 + 2\mu_1^2 - (1 + i\mu_1)\frac{dt_1}{dt} - (1 - i\mu_1)\frac{dt_1}{dt}\right]$$

$$- \frac{\nu_y}{E_y}\left[(1 + i\mu_1)\frac{dt_1}{dt} + (1 - i\mu_1)\frac{dt_1}{dt}\right],$$

$$B_3 = \frac{1}{E_x}\left[2 + 2\mu_2^2 - (1 + i\mu_2)\frac{dt_2}{dt} - (1 - i\mu_2)\frac{dt_2}{dt}\right]$$

$$- \frac{\nu_y}{E_y}\left[(1 + i\mu_2)\frac{dt_2}{dt} + (1 - i\mu_2)\frac{dt_2}{dt}\right],$$

$$B_5 = \frac{n_0}{E_x}\left[2 + 2\mu_3^2 - (1 + i\mu_3)\frac{dt_3}{dt} - (1 - i\mu_3)\frac{dt_3}{dt}\right]$$

$$- \frac{n_0\nu_y}{E_y}\left[(1 + i\mu_3)\frac{dt_3}{dt} + (1 - i\mu_3)\frac{dt_3}{dt}\right],$$

$$B_2 = \overline{B}_1, \qquad B_4 = \overline{B}_3, \qquad B_6 = \overline{B}_5.$$

The systems (5.8) and (5.9) must be completed by the condition of singlevaluedness of displacements along the lips of the crack ℓ, which is expressed as follows:

$$
\begin{aligned}
(5.10)\qquad & \left[(p_1+iq_1)-(p_2+iq_2)\frac{\mu_1-\overline{\mu}_2}{\mu_2-\overline{\mu}_2}-(\overline{p}_2+i\overline{q}_2)\frac{\mu_1-\mu_2}{\overline{\mu}_2-\mu_2}\right]\int_{\ell_1} g(t_1)\,dt_1 \\
& +\left[(\overline{p}_1+i\overline{q}_1)-(\overline{p}_2+i\overline{q}_2)\frac{\overline{\mu}_1-\overline{\mu}_2}{\mu_2-\overline{\mu}_2}-(\overline{p}_2+i\overline{q}_2)\frac{\overline{\mu}_1-\mu_2}{\overline{\mu}_2-\mu_2}\right]\int_{\ell_1}\overline{g(t_1)}\,\overline{dt_1} \\
& +n_0\left[(p_*+iq_*)-(p_2+iq_2)\frac{\mu_3-\overline{\mu}_2}{\mu_2-\overline{\mu}_2}-(\overline{p}_2+i\overline{q}_2)\frac{\mu_3-\mu_2}{\overline{\mu}_2-\mu_2}\right]\int_{\ell_3}\mu_{21}(t_3)\,dt_3 \\
& +n_0\left[(\overline{p}_*+i\overline{q}_*)-(\overline{p}_2+i\overline{q}_2)\frac{\overline{\mu}_3-\overline{\mu}_2}{\mu_2-\overline{\mu}_2}-(\overline{p}_2+i\overline{q}_2)\frac{\overline{\mu}_3-\mu_2}{\overline{\mu}_2-\mu_2}\right]\int_{\ell_3}\overline{\mu_{21}(t_3)}\,\overline{dt_3} \\
& =-\frac{p_2+iq_2}{\mu_2-\overline{\mu}_2}\int_{\ell}\left[q^+(t)-q^-(t)\right]dt-\frac{\overline{p}_2+i\overline{q}_2}{\overline{\mu}_2-\mu_2}\int_{\ell}\left[\overline{q^+(t)}-\overline{q^-(t)}\right]dt.
\end{aligned}
$$

The system of equations (5.8) – (5.10) combined with the integro-differential equations of thermoconductivity, which are obtained from the conditions (3.14) – (3.16), can fully describe the stress and thermal fields of the problem under consideration.

In the case when the direction of the stringer does not coincide with any of the principal axes and it is located on the plane of the elastic symmetry of the plate, the relationship (5.1) takes the following form

$$
(5.11)\qquad ih\left[(\sigma_n^+-i\sigma_t^+)-(\sigma_n^--i\sigma_t^-)\right]+E_0S_0\frac{d}{dt}\left[\frac{1}{E_x'}\sigma_s^+-\frac{\nu_y'}{E_y'}\sigma_n^++a_1\sigma_t^+\right]=0.
$$

From the above condition a singular integral equation is derived along the stringer L which is analogous to (5.9). The new elastic constants appearing in (5.11) are derived from the relations which give the elastic constants with respect to two mutually orthogonal systems, when the principal coordinate system has been rotated around its origin through some angle [11]. From the above remark, it is evident that the problem can be extended to the case of a finite number of cracks and straight, as well as curvilinear stringers of random orientation, concentrated forces, moments, and thermal sources, with the only restriction that the stringers and cracks do not mutually intersect each other.

Furthermore, the important geomechanical problem of a circular hole (drill hole, wellbore, tunnel etc.) reinforced fully or partially along its perimeter by a stringer, inside a cracked either isotropic or anisotropic geomaterial, under the influence of stress and thermal (geothermal, due to the presence of nuclear waste etc.) fields can be examined by the above method.

6. Concluding remarks

Basing on the method of complex functions and the theory of singular integral equations, a general method was proposed for solving plane thermoelasticity and thermoconductivity problems for cracked, isotropic or anisotropic, multiply connected bodies with linear and curvilinear stringers.

Many important engineering problems can be solved by the above general method, such as the body with a partially of fully supported hole and periodic linear and circularly symmetric arrays of cracks, stringers, inclusions etc., as well as other plane elastic problems of a generic geometry which may be encountered in actual engineering applications. It is obvious that the important aspect of prediction of the behaviour of a body under the influence of existing singularities inside the mechanical and thermal fields of forces can be considered by using the proposed method.

Furthermore, the principles and procedures of the method can be effectively applied to extend it to a large category of problems, such as bodies with inclusions and bodies in contact containing or not a system of cracks.

Acknowledgements

This work is supported by INTAS of European Union under the contract INTAS-93-2600. This support is kindly acknowledged.

References

1. N.I. MUSKHELISHVILI, *Some basic problems of the mathemathical theory of elasticity*, P. Noordhoff, Groningen 1965.
2. N.I. MUSKHELISHVILI, *Singular integral equations*, Wolters-Noordhoff Publishing, Groningen 1958.
3. F.D. GAKHOV, *Boundary value problems*, Pergamon, Oxford 1966.
4. P.S. THEOCARIS, D. BARDZOKAS and V.Z. PARTON, *Plane problems of the theory of elasticity, thermoelasticity and thermoconductivity for cracked isotropic or anisotropic bodies with reinforcements* [in Greek], Minutes of the Academy of Athens, **65**, 206–236, 1990.
5. H.S. CARSLAW and J.C. JAEGER, *Conduction of heat in solids*, 2nd Edition, Clarendon Press, Oxford 1959.
6. I.A. PRUSOV, *Some problems of thermoelasticity* [in Russian], Izd. Beloruskogo In-ta, Minsk 1971.
7. I.S. PODSTRIGACH, *Influence of inhomogeneous inclusions on the distribution of thermal fields and stresses in elastic bodies* [in Russian], Stress Concentration, **1**, 207–218, 1965.
8. P.S. THEOCARIS and D. BARDZOKAS, *The influence of a finite stringer on the stress intensities around cracks in plates*, Engng. Fract. Mech., **14**, 493–507, 1981.
9. P.S. THEOCARIS and D. BARDZOKAS, *Reinforcement of cracked plate by a loaded strip inclusion*, Ing. Archiv, **55**, 45–56, 1985.
10. D. BARDZOKAS, V.Z. PARTON and P.S. THEOCARIS, *Integral equations of the theory of elasticity for the multiply connected bodies with inclusions* [in Russian], P.M.M., **53**, 3, 485–495, 1989.

11. D. BARDZOKAS, V.Z. PARTON and P.S. THEOCARIS, *Plane problem of the theory of elasticity for orthotropic bodies with defects* [in Russian], D.A.N. U.S.S.R., **309**, 5, 1072–1077, 1989.

NATIONAL TECHNICAL UNIVERSITY OF ATHENS,
DEPARTMENT OF ENGINEERING SCIENCE, SECTION OF MECHANICS, ATHENS, GREECE
and
TECHNICAL UNIVERSITY OF CRETE,
DEPARTMENT OF MINERAL RESOURCES ENGINEERING, LABORATORY OF ROCK MECHANICS, CHANIA, GREECE.

Received December 16, 1994.

Arch. Mech., 47, 2, pp. 203–222, Warszawa 1995

Determination of finite plastic deformations in single crystals (*)

A. BERTRAM and M. KRASKA (BERLIN)

THE CONCEPT of finite inelastic or plastic deformations, based on the assumption of isomorphic elastic ranges, leads to a nonsymmetric second order tensor-variable, called *inelastic transformation*, that plays the role which is usually attributed to some "plastic deformation". Its evolution law can be either isotropic or anisotropic, rate-independent or rate-dependent, etc., and thus it leaves the material class rather general. The theory is specified (1) within the context of classical isotropic plasticity and (2) within crystal plasticity. For the latter case, the Schmid law induces a flow potential, which determines the directions of the inelastic transformation. The (uniaxial) constitutive law or relation on the level of slip-systems can be viscous, plastic, viscoplastic, or other. Computations of finite crystal deformations show interesting effects due to anisotropy.

1. Introduction

SINCE THE PIONEERING WORKS of Green/Naghdi, Mandel, Lee, and others three decades ago, a tremendous number of papers in the field of finite plasticity has been published. But, as NAGHDI [14] remarks in his critical review on the state of this subject, the constitutive theory is still in its primitive stages and has not been fully understood, even in its basic concepts. There has been a long and intensive dispute on the different approaches, and it has not yet come to an end. For example, the decomposition of the strains into elastic and plastic ones is an important constituent of most of these theories. But in what we will present, such a decomposition, as well as the existence of an unloaded placement, turn out to be unnecessary.

The present approach differs from the quoted ones in many aspects. First of all, we chose stress and strain variables for the constitutive modelling which are material ones, that is invariant under Euclidean transformations, but without using a reference placement, which often led to confusion rather than to conceptual clarity. This *intrinsic* description is based on a suggestion by NOLL [15] and has been used only by a few authors [3, 7, 10, 16], despite its clear advantages. After introducing these variables, we will try to work out the basic features of what is commonly understood by *elastoplastic* behaviour. The very basic assumption of the present theory is that there are *elastic ranges*, which have equal elastic properties. Of course, this statement requires a precise formulation. Having established them, it turns out that most of the current theories in finite plasticity are essentially using or complying with the same assumptions, some of them in a rather implicit or hidden way.

(*) Paper presented at 30th Polish Solid Mechanics Conference, Zakopane, September 5–9, 1994.

The notion of *equal elastic properties* leads to the concept of *plastic isomorphism* or *transformation* which plays the key role in the present theory. This variable is generally non-symmetric. For its evolution equation two examples are given. For the first one we chose the most familiar concepts such as the Huber-Mises yield criterion, Drucker's postulate, and kinematic and isotropic hardening. The second one is the slip system theory of crystal plasticity, a physically well-substantiated theory which gives us clear interpretations of our concepts. In particular, it can be shown that the plastic transformation can be derived from a potential in this case, too. There is no need for artificially introducing something like a "plastic spin", a rather controversial concept in the literature.

When compared with the theories of multiplicative and additive decomposition [8, 9, 11, 13], we can precisely work out their validity ranges and the limitations by embedding them in the present framework.

A number of computational results show the ability of the present model to describe the single crystal behaviour under large inelastic deformations. Some interesting effects due to the anisotropy of the model can be computed and studied in our examples.

2. Notations

Γ symmetry group of the elastic law,
κ (global) placement of the body,
κ_R (global) reference placement of the body,
ρ mass density,
ρ_R mass density in the reference placement,
B body manifold,
$\mathbf{C} = \mathbf{F}^*\mathbf{G}^E\mathbf{F}$ right Cauchy-Green strain tensor,
$\mathbb{C}$ elasticity tensor,
$\mathbf{d}_i$ slip direction,
$\mathcal{E}$ elastic range,
E Euclidean point space,
$\mathbf{e}_i$ lattice vector,
$\mathbf{F}$ deformation gradient,
$\mathbf{G} = \mathbf{K}^*\mathbf{G}^E\mathbf{K}$ intrinsic configuration,
$\mathbf{G}^E$ Euclidean metric,
$\mathbf{G}_u$ undistorted configuration,
$\mathbf{K} = d\kappa$ (local) placement,
$\mathbf{K}_R = d\kappa_R$ (local) reference placement,
$\mathbf{K}_Z$ (local) intermediate placement,
$\mathbf{L}$ velocity gradient,
$\mathbf{n}^i$ normal to the slip plane,
$\mathbf{P}_t$ plastic transformation from $\mathcal{E}_0$ to $\mathcal{E}_t$,
p stress power,

$\mathbf{S}$ intrinsic stress tensor,
$\mathbf{T}^{\mathrm{E}}$ Cauchy-Euler stress tensor,
$\mathbf{T}^{\mathrm{P}}$ 2nd Piola-Kirchhoff stress tensor,
$T_X B$ tangent space in X to the body,
V vector space of Euclidean shifters.

Throughout this text, a superposed asterisk will denote duality, either of spaces or of mappings. A suffix t indicates time-dependence.

Let B be the body manifold, and for a material point $X \in B$, $T_X B$ be the tangent space and $T_X^* B$ its dual, the cotangent space. Let E be the Euclidean point space and V its associated vector space of the Euclidean shifters endowed with the Euclidean metric, i.e. a symmetric and positive definite linear mapping

$$\mathbf{G}^E : \quad V \to V^* . \tag{2.1}$$

The placement of the body is a global diffeomorphic embedding in the Euclidean space

$$\kappa : \quad B \to E, \tag{2.2}$$

which may be time-dependent. The local *placement* at some material point X is the tangent map or the differential of the global placement

$$\mathbf{K}_X := d\kappa(X) : \quad T_X B \to V. \tag{2.3}$$

By means of this mapping we can push forward or pull back all local concepts between the material and the spacial description, such as the pull-back of the Euclidean metric

$$\mathbf{G}_X := \mathbf{K}_X^* \mathbf{G}^E \mathbf{K}_X : \quad T_X B \to T_X^* B, \tag{2.4}$$

a metric in the tangent space, which is called the (local intrinsic) *configuration*, and the pull-back of the Cauchy-Euler stress tensor $\mathbf{T}^{\mathrm{E}}$

$$\mathbf{S}_X := \mathbf{K}_X^{-1} \mathbf{T}^{\mathrm{E}} \mathbf{K}_X^{-*} : \quad T_X^* B \to T_X B, \tag{2.5}$$

the *intrinsic stresses*. When it is clear from the context to which material point these local concepts are related, we will suppress the suffix X. Note, that no reference placement has been (and will be) used to formulate our material theory. The intrinsic configuration (in contrast to placements) and stresses are invariant under Euclidean transformations which may be interpreted as both the change of observer or the superimposed rigid body motion. This property makes them most appropriate for any constitutive modelling, as the principle of material objectivity is identically fulfilled by any relation between them [3, 10, 15]. Moreover, they are power conjugate variables, as the stress power can be expressed as

$$p := \operatorname{tr}(\mathbf{T}^{\mathrm{E}} \mathbf{L}) = \frac{1}{2} \operatorname{tr}(\mathbf{S} \mathbf{G}^{\cdot}), \tag{2.6}$$

with $\mathbf{L}$ denoting the spatial velocity gradient.

3. Elastic ranges

Since elasticity is fundamental notion for understanding plasticity, we will first review some basic concepts from the (finite) elasticity theory [3, 15]. An elastic material element is characterized by an elastic law

$$h_X : \mathbf{G}_X \longmapsto \mathbf{S}_X , \tag{3.1}$$

which can be both linear or nonlinear. We will use such laws to describe the behaviour of elastoplastic materials within their elastic ranges. If one wants to compare the elastic elements at two different material points X and Y with elastic laws h_X and h_Y, one needs, first of all, an identification of the tangent spaces at these two points, i.e. a linear bijection

$$\mathbf{P} : T_Y B \to T_X B. \tag{3.2}$$

We call the elastic behaviour of X and Y *isomorphic*, if such a *material isomorphism* $\mathbf{P}$ *exists* that the following isomorphy condition for the elastic laws holds for all configurations

$$h_X(\mathbf{G}_X) = \mathbf{P} h_Y(\mathbf{P}^* \mathbf{G}_X \mathbf{P}) \mathbf{P}^* . \tag{3.3}$$

Material isomorphy constitutes an equivalence relation on material elements. If two elastic material elements are isomorphic, all their properties can be considered as being equal. That means, for example, that they necessarily belong to the same crystal class. Moreover, material isomorphisms relate configurations which describe the same state of the elements. If, for example, $\mathbf{G}_X$ is stress-free or unloaded for h_X, then the *isomorphic configuration* $\mathbf{P}^* \mathbf{G}_X \mathbf{P}$ is stress-free for h_Y, too. Or, if one configuration is undistorted, then so is any isomorphic one.

Clearly, if $X \equiv Y$, the identity in the tangent space can always be used as a material automorphism. But in all cases, this is not the only one. The set of all such *symmetry transformations* forms a group under composition, the *symmetry group* of the (elastic) material

$$\Gamma_x := \{\mathbf{H} : T_X B \to T_X B, \quad \text{linear, invertible} \quad | h_X(\cdot) = \mathbf{H} h_X(\mathbf{H}^* \cdot \mathbf{H}) \mathbf{H}^* \}$$

which is used to characterize fluids, solids etc. As we are here exclusively interested in solid materials, we assume that for every elastic law there exists an undistorted configuration $\mathbf{G}_u$ with respect to which the symmetry group is a subgroup of the orthogonal group. The structure of the symmetry group is used for the classification of the 13 crystal classes, ranging from the triclinic solid to the isotropic one, as extremes [18].

Naturally, the concepts of material isomorphy and symmetry are closely related to one another, as will be shown by the following theorems.

THEOREM 1. *Let* $h_{1,2}$ *be elastic elements with symmetry groups* $\Gamma_{1,2}$, *and* $\mathbf{P}$ *a material isomorphism between them. Then* $\Gamma_2 = \mathbf{P}\Gamma_1\mathbf{P}^{-1}$ *holds.*

THEOREM 2. *Let* $h_{1,2}$ *be elastic elements with symmetry groups* $\Gamma_{1,2}$, *and* $\mathbf{P}$ *a material isomorphism between them. Then also* $\mathbf{H}_2\mathbf{P}\mathbf{H}_1$ *is a material isomorphism between them for all* $\mathbf{H}_1 \in \Gamma_1$ *and all* $\mathbf{H}_2 \in \Gamma_2$.

THEOREM 3. *Let* $h_{1,2}$ *be the elastic elements with symmetry groups* $\Gamma_{1,2}$, *and* $\mathbf{P}$ *and* $\underline{\mathbf{P}}$ *– the material isomorphisms between them. Then* $\mathbf{P}^{-1}\underline{\mathbf{P}}$ *is in* Γ_1 *and* $\underline{\mathbf{P}}\mathbf{P}^{-1}$ *in* Γ_2.

The proofs are straightforward and can be found in [5].

All these concepts which are based on the material isomorphy can be defined for any simple material, whether elastic or not [2, 3]. We have limited our considerations to elastic materials for two reasons. First, we will use them only for this special case, and, second, the definitions turn out to be much simpler in the elastic case.

In the general inelastic case the stresses do not depend solely on the actual configuration, but also on the past configurations process. This can be mathematically formalized by introducing the process class, i.e. a set of configuration processes defined on finite time intervals, and by a stress functional that assigns to each of these processes the stresses with which the material responds at the end of such a process. A formal structure of such a material system can be found in detail in [2, 3, 10].

In the present context, however, we do not need such a general framework, as we will limit our consideration to *materials with elastic ranges*. Such materials are characterized by the following property: at any instant t when the material element happens to be in some configuration $\mathbf{G}_0$, there exists

(i) a connected neighbourhood $\mathcal{E}_t$ of $\mathbf{G}_0$ in the configuration space, and

(ii) an elastic law h_t

such that, for any continuation of the configuration process that remains in $\mathcal{E}_t$, the stresses are determined by h_t. In other words, the material behaves elastically, as long as the deformation remains within the elastic range. $\mathcal{E}_t$ can be determined by a yield criterion in the configuration space, or, if the elastic law is bijective, in the stress space as $h_t(\mathcal{E}_t)$, equivalently. If, however, the configuration process leaves the current elastic range by hitting some yield limit, the deformation is no longer elastic and the material changes its current elastic range. This is the underlying assumption within most theories of plasticity.

The other common feature of these theories is the assumption, that the elastic behaviour or the elastic stiffness is not changed by the plastic flow. In our context this means that the elastic laws of all elastic ranges are materially isomorphic. Or, more precisely, for any elastic ranges $\mathcal{E}_{1,2}$ with elastic laws $h_{1,2}$ there exists a

material isomorphism $\mathbf{P}_2^1$ such that the isomorphy condition holds in the form

$$h_2(\cdot) = \mathbf{P}_2^1 h_1(\mathbf{P}_2^{1*} \cdot \mathbf{P}_2^1)\mathbf{P}_2^{1*}. \tag{3.4}$$

Note that the elastic behaviour within the elastic ranges is equal, which does not imply that the size or shape of the elastic ranges, which may be affected by hardening or softening, is equal.

The advantage of this assumption for the modelling and identification task lies in the following fact. The elastic behaviour in all elastic ranges is determined by two notions, first, the elastic law of one arbitrarily chosen elastic reference range h_0 and, second, the material isomorphisms $\mathbf{P}_t$ between the reference law and the laws h_t of each of the other elastic ranges $\mathcal{E}_t$. In fact we can compute the stresses at any instant by the *isomorphy condition* in the form

$$h_t(\mathbf{G}_t) = \mathbf{P}_t h_0(\mathbf{P}_t^* \mathbf{G}_t \mathbf{P}_t)\mathbf{P}_t^*. \tag{3.5}$$

Note that all quantities with suffix t depend on the time and have current values. In the case of h_t this means that not only the value of this function, but the function itself depends on time. This should be taken into account if one prefers an incremental form of the stress law:

$$\begin{aligned} \mathbf{S}_t^\cdot &= [h_t(\mathbf{G}_t)]^\cdot \\ &= \mathbf{P}_t^\cdot h_0(\mathbf{P}_t^* \mathbf{G}_t \mathbf{P}_t)\mathbf{P}_t^* + \mathbf{P}_t h_0(\mathbf{P}_t^* \mathbf{G}_t \mathbf{P}_t)\mathbf{P}_t^{\cdot *} \\ &\qquad + \mathbf{P}_t dh_0[\mathbf{P}_t^{\cdot *} \mathbf{G}_t \mathbf{P}_t + \mathbf{P}_t^* \mathbf{G}_t \mathbf{P}_t^\cdot + \mathbf{P}_t^* \mathbf{G}_t^\cdot \mathbf{P}_t]\mathbf{P}_t^*, \end{aligned} \tag{3.6}$$

where the dh_0 stands for the gradient of h_0, i.e. the elastic tangent tensor.

As $\mathbf{P}_t$, which plays the key-role in our theory, expresses the influence of the (plastic) predeformation on the current elastic behaviour, we call it *plastic transformation*. It does not have the form or dimension of a deformation or configuration and, thus, does not imply any decomposition of the deformation into elastic and plastic parts. In general $\mathbf{P}_t$ is fully non-symmetric, i.e. nine-dimensional. Only one dimension can be reduced by assuming that isomorphisms are generally preserving the mass element, see [12].

The main problem left to solve is the determination of the plastic transformation. If the material is given in its initial state, we can choose the initial elastic law as a reference, without loss of generality. That means that we can take the identity of the tangent space as the initial value for the plastic transformation. And as long as the material remains within the same elastic range, the plastic transformation is constant. As soon as the material state hits the limit of the elastic range in the form of a yield criterion, yielding or plastic flow may occur and the plastic transformation will vary. Therefore, an evolution equation for $\mathbf{P}_t$ is needed and it is assumed to exist in the following incremental form

$$\mathbf{P}_t^\cdot = g(\mathbf{P}_t, \mathbf{G}_t, \mathbf{G}_t^\cdot, \alpha_t), \tag{3.7}$$

where α_t is the current vector of internal variables such as hardening parameters. g may be rate-independent, as in the plastic case, or rate-dependent, as in the viscoplastic case. The value of g is expected to be zero as long as the current configuration $\mathbf{G}_t$ remains in the interior of the current elastic range. In this case the incremental equation (3.6) for the stresses reduces to

$$\mathbf{S}_t^{\circ} = \mathbf{P}_t dh_0[\mathbf{P}_t^* \mathbf{G}_t^{\circ} \mathbf{P}_t]\mathbf{P}_t^* , \tag{3.8}$$

the usual elastic increment.

The complete constitutive model of the present theory consists of two constitutive equations, namely, the elastic reference law h_0 and the evolution equation of the plastic transformation (3.7).

According to Theorem 2, the plastic transformation is unique only up to the both-sided symmetry transformations of the elastic laws. For practical purposes it is sufficient if the evolution equation gives just one plastic transformation out of the set of all possible ones.

4. Theories based on intermediate placements

In order to establish the relation between the current theory and those based on the concept of intermediate or isoclinic placements, we first choose an arbitrary reference placement κ_R with tangent mapping

$$\mathbf{K}_R := d\kappa_R(X) \; : \; T_X B \to V. \tag{4.1}$$

Next, we introduce the (local) intermediate placement

$$\mathbf{K}_{Zt} := \mathbf{K}_R \mathbf{P}_t^{-1} . \tag{4.2}$$

Generally, this is not the differential of a global placement, since compatibility cannot be assured. The plastic transformation is time-dependent and, thus, so is the intermediate placement. The displacement from the reference placement to the intermediate one is called "plastic deformation"

$$\mathbf{F}_p := \mathbf{K}_{Zt}\mathbf{K}_R^{-1} = \mathbf{K}_R \mathbf{P}_t^{-1} \mathbf{K}_R^{-1} , \tag{4.3}$$

and that from the intermediate to the current one – the "elastic deformation"

$$\mathbf{F}_e := \mathbf{K}\mathbf{K}_{Zt}^{-1} = \mathbf{F}\mathbf{F}_p^{-1} = \mathbf{K}\mathbf{P}_t\mathbf{K}_R^{-1} , \tag{4.4}$$

such that the multiplicative decomposition holds

$$\mathbf{F} = \mathbf{F}_e \mathbf{F}_p . \tag{4.5}$$

Note that neither $\mathbf{F}_e$ nor $\mathbf{F}_p$ is a gradient, in general. We will next transform the intrinsic elastic law to these variables. The Cauchy-Euler stress tensor is

$$
\begin{aligned}
\mathbf{T}^E &= \mathbf{K}\,\mathbf{S}\,\mathbf{K}^* \\
&= \mathbf{K} h_t(\mathbf{G}_t)\mathbf{K}^* \\
&= \mathbf{K}\,\mathbf{P}_t h_0(\mathbf{P}_t^* \mathbf{G}_t \mathbf{P}_t)\mathbf{P}_t^* \mathbf{K}^* \\
&= \mathbf{K}\mathbf{P}_t h_0(\mathbf{P}_t^* \mathbf{K}^* \mathbf{G}^E \mathbf{K}\,\mathbf{P}_t)\mathbf{P}_t^* \mathbf{K}^* \\
&= \mathbf{F}_e \mathbf{K}_R h_0(\mathbf{K}_R^* \mathbf{F}_e^* \mathbf{G}^E \mathbf{F}_e \mathbf{K}_R)\mathbf{K}_R^* \mathbf{F}_e^* \\
&= \rho/\rho_R \mathbf{F}_e p_0(\mathbf{C}_e) F_e^* \,,
\end{aligned} \tag{4.6}
$$

with

$$
\mathbf{C}_e := \mathbf{F}_e^* \mathbf{G}^E \mathbf{F}_e \,, \tag{4.7}
$$

and

$$
p_0(\mathbf{C}_e) := \rho_R/\rho \mathbf{K}_R h_0(\mathbf{K}_R^* \mathbf{C}_e \mathbf{K}_R)\mathbf{K}_R^* \,. \tag{4.8}
$$

This result corresponds to LEE's [11]. The approach with multiplicative decomposition, if properly identified, has just been proven to be in accordance with the principle of material objectivity; it is also applicable to anisotropic materials, and renders isomorphy of the elastic ranges.

With the same decomposition we can also define another "plastic deformation tensor", such as the symmetric

$$
\mathbf{C}_p := \mathbf{F}_p^* \mathbf{G}^E \mathbf{F}_p \tag{4.9}
$$

and the elastic one due to the additive decomposition of the total right Cauchy-Green tensor

$$
\mathbf{C} = \mathbf{C}_p + \mathbf{C}^e \tag{4.10}
$$

according to GREEN/NAGHDI [8, 9]. Note that $\mathbf{C}_e$ and $\mathbf{C}^e$ are not identical. If we use the 2nd Piola-Kirchhoff stress tensor

$$
\mathbf{T}^{\mathrm{P}} = \rho/\rho_R \mathbf{F}^{-1} \mathbf{T}^{\mathrm{E}} \mathbf{F}^* \,, \tag{4.11}
$$

we obtain

$$
\begin{aligned}
\mathbf{T}^{\mathrm{P}} &= \rho/\rho_R \mathbf{F}_p^{-1} \mathbf{K}_R h_0(\mathbf{K}_R^* [\mathbf{G}^E + \mathbf{F}_p^{-*} \mathbf{C}^e \mathbf{F}_p^*] \mathbf{K}_R)\mathbf{K}_R^* \mathbf{F}_p^{-*} \\
&=: q(\mathbf{C}^e, \mathbf{F}_p).
\end{aligned} \tag{4.12}
$$

The main difference with Eq. (5.4) in GREEN/NAGHDI [8] is, first of all, that they used a symmetric variable instead of $\mathbf{F}_p$ which is insufficient in the general

anisotropic case. And second, that the function q of its two arguments cannot be arbitrary but must have the specific form of (4.12) if one assumes isomorphic elastic ranges.

When we introduced the intermediate placement by Eq. (4.2), this is by no means unique. The reference placement $\mathbf{K}_R$ is arbitrary and the plastic transformation $\mathbf{P}_t$ is only determined up to both-sided symmetry transformations (Theorem 2). Moreover, we did not use the assumption that the intermediate placement was stress-free or unloaded. What is important, however, is that for all elastic ranges the intermediate placement leads to isomorphic configurations. To show this we first define the configurations that correspond to the reference placement

$$\mathbf{G}_R := \mathbf{K}_R^* \mathbf{G}^E \mathbf{K}_R , \tag{4.13}$$

and those that correspond to the intermediate placements

$$\mathbf{G}_{Zt} := \mathbf{K}_{Zt}^* \mathbf{G}^E \mathbf{K}_{Zt} . \tag{4.14}$$

If we now evaluate the isomorphy condition (3.5) for the value $\mathbf{G}_t \equiv \mathbf{G}_{Zt}$, we obtain

$$h_t(\mathbf{G}_{Zt}) = \mathbf{P}_t h_0(\mathbf{P}_t^* \mathbf{G}_{Zt} \mathbf{P}_t) \mathbf{P}_t^* = \mathbf{P}_t h_0(\mathbf{G}_R) \mathbf{P}_t^* . \tag{4.15}$$

All intermediate placements correspond to the same configuration in the reference law and they are therefore isomorphic. Of course, the same holds if the intermediate placements were subjected to arbitrary rotations, which do not affect their corresponding configuration.

5. Example I. Isotropic plasticity

Let us follow the schemes of classical plasticity with a linear elastic law, a yield criterion, normality rule, kinematic and isotropic hardening which is associated with names such as Hooke, Prandtl, Reuss, Huber, Mises, Drucker, Ziegler, Prager, and others. If the elastic deformations are small, a linear elastic reference law will be sufficient. We linearize the intrinsic stresses with respect to deformations near to the undistorted state $\mathbf{G}_{\mathrm{ut}}$

$$\mathbf{S} = h_t(\mathbf{G}_t) = \mathbb{C}_t[\mathbf{G}_t - \mathbf{G}_{\mathrm{ut}}]. \tag{5.1}$$

$\mathbb{C}_t$ is the fourth rank elasticity tensor. Note, that this law is still applicable for finite deformations, since it is objective.

As a yield criterion we choose the Huber-Mises one, which can be reduced to the intrinsic form

$$\psi(\mathbf{S}\mathbf{G}_t) = 3\mathrm{tr}\,(\mathbf{S}\mathbf{G}_t)^2 - \mathrm{tr}^2(\mathbf{S}\mathbf{G}_t) - \sigma_v^2 , \tag{5.2}$$

with the critical equivalent stress σ_v which may vary due to isotropic hardening. If one wants to include kinematic hardening, a symmetric intrinsic back-stress $\mathbf{R}$ has to be introduced into the flow rule by substituting the stress $\mathbf{S}$ with the difference $\mathbf{S}-\mathbf{R}$. For the back-stress we denote an evolution equation of the Prager–Ziegler type

$$\mathbf{R}^{\cdot} = \lambda c(\mathbf{S}-\mathbf{R}), \tag{5.3}$$

with the material constant c and a real variable λ which appears in the flow rule below. By using the elastic law we can express the stresses in the yield criterion by the actual configuration, or, *vice versa*, the configuration by the stresses, if one prefers the stress space notations.

The flow rule can be taken as the normal with respect to the yield criterion

$$\mathbf{P}_t^{\cdot}\,\mathbf{P}_t^{-1} = \lambda d\psi/d(\mathbf{S}\mathbf{G}_t) \qquad \text{if} \qquad \psi([\mathbf{S}-\mathbf{R}]\mathbf{G}_t) = 0 \tag{5.4}$$

and

$$\mathbf{P}_t^{\cdot} = \mathbf{0}$$

otherwise. This completes the model of classical plasticity.

6. Example II. Crystal Plasticity

As another example, we consider crystal plasticity based on the slip systems. Since the early works by Taylor, Elam, Schmid and others of the twenties, we know that plastic deformations in metal grains can be modeled by shear in slip systems. Such a system consists of a slip plane indicated by its normal $\mathbf{n}^i \in T_X^* B$ and a slip direction indicated by a tangent vector $\mathbf{d}_i \in T_X B$. The resolved shear stress in such a slip system (with index i) can be computed by

$$\tau_i := |\langle \mathbf{n}^i, \mathbf{S}\mathbf{G}_t(\mathbf{d}_i)\rangle|. \tag{6.1}$$

If the resolved shear stress reaches the critical Schmid stress τ_{ic} in one or several slip systems, the Schmid yield criterion of the form

$$\psi(\mathbf{S}\mathbf{G}_t) = |\langle \mathbf{n}^i, \mathbf{S}\mathbf{G}_t(\mathbf{d}_i)\rangle| - \tau_{ic} \tag{6.2}$$

is fulfilled for that particular slip system and yielding can occur in the form of a simple shear in the active slip system

$$\mathbf{P}_t^{\cdot}\,\mathbf{P}_t^{-1} = -\mu_i^{\cdot}\,\mathbf{d}_i \otimes \mathbf{n}^i = \lambda d\psi/d(\mathbf{S}\mathbf{G}_t), \tag{6.3}$$

where μ_i is the shear number. Again, the increment of the plastic transformation is normal to the yield surface, i.e. normality holds with respect to the Schmid yield criterion as a plastic potential. If more than one slip system is active, the

different shears can be superimposed by taking the sum over i on the right-hand side. The shear number μ_i of each slip system must be determined by an additional constitutive equation on the slip system level, i.e. a uniaxial constitutive relation between the shear number and the resolved shear stress. Such a law can be plastic, viscous, or viscoplastic with or without hardening.

The elastic law h_t of single crystals will generally be anisotropic with respect to the lattice directions [4]. If we describe these directions by *lattice vectors*, i.e. tangent vectors $\mathbf{e}_j \in T_X B$ that momentarily coincide with the lattice directions, and the lattice planes by covectors $\mathbf{e}^j \in T_X^* B$, then one can show by means of the isomorphy condition (3.5) that the plastic transformation transforms these vectors from the elastic reference law into the current one. The same holds for the slip system (co-)vectors, since they can be expressed as a linear combination of the lattice (co-)vectors. By this transformation rule the concept of plastic transformation, which was introduced in a rather general and abstract way, gains a clear physical interpretation.

7. Computational results

The material model discussed above has been implemented into a finite element code for the simulation of large inelastic deformations on face-centred cubic single crystals. For simplicity, constant strain tetrahedron elements are used. The FE mesh consists of cubes, each of them containig five tetrahedrons. There are two different ways to assemble a cube from tetrahedrons. In order to minimize the mesh-induced anisotropy, the two cube segmentations alternate in each direction.

The elastic and inelastic constitutive relations account for the cubic anisotropy. The inelastic behaviour is modelled by the theory of slip systems with the 12 octahedral $\{111\}\langle 110\rangle$ slip systems of the fcc single crystal. On the slip system level we use a viscoplastic constitutive relation between the crystallographic glide and the resolved shear stress. Combined with the lattice elasticity, this leads to a Bingham-type behaviour. The relation is characterized by the critical resolved shear stress τ_0 and the viscosity η. For η approaching 0 we intend to model plastic behaviour. For $\tau_0 = 0$ the material is linear viscous (Fig. 1).

We distinguish self- and latent hardening as well as isotropic and kinematic hardening [1, 19]. However, for simplicity, hardening has been neglected in the present paper. A detailed study of the hardening dependence is projected for forthcoming papers. Some aspects can be found in [6].

The integration of the inelastic transformation is done by an explicit Euler scheme. Thus one has to adjust properly the time-step length, preventing instabilities. Inelastic incompressibility is guaranteed by enforcing the condition of the plastic transformation to be unimodular ($\det \mathbf{P} = 1$) after each increment.

Special attention has been paid to the effects of lattice rotation. The behaviour of single crystals shows strong dependence on the initial lattice orientation relative

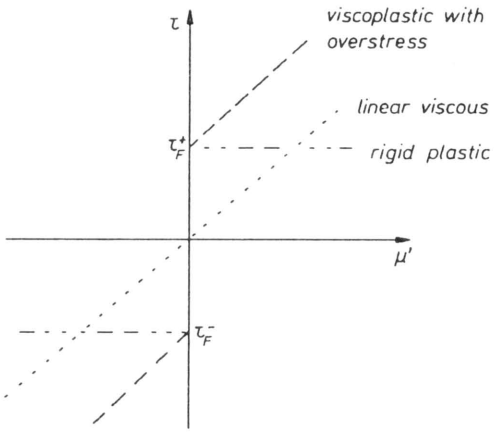

FIG. 1. Inelastic constitutive law on slip system level.

to the imposed deformation. If a process is accompanied by lattice rotations, this strongly affects the response of the specimen.

Most common FE postprocessors do not provide convenient tools for lattice visualization. So the following method has been used: Brick elements, representing the local cubic lattice, are added to the displacement plots. The edges of the bricks are parallel to the lattice vectors and proportional in length to the (deformed) lattice constants. Thus, the brick elements, plotted for selected points, show the orientation of the lattice and the elastic deformation which determine the stresses (Fig. 2, 6–9).

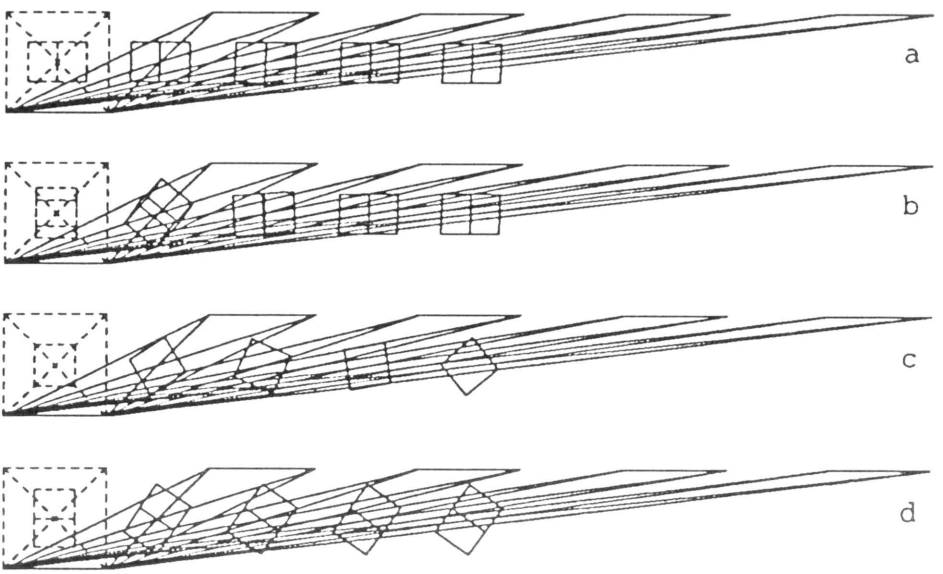

FIG. 2. Simple shear with different initial orientations. Deformation and lattice orientation for shear numbers 0, 2, 4, 6, and 8.

The lattice rotation dependence of the material behaviour can be demonstrated by elastic-viscoplastic simple shear simulations. Figure 2 gives some examples for the lattice rotation in simple shear, up to an amount of 8. The corresponding normalized shear stresses are given in Fig. 3. Starting from different initial orientations, three main modes can be observed:

- The lattice remains in the initial position. The shear stress is constant (a).
- The lattice rotates steadily. The shear stress oscillates (c).
- The lattice converges to a stable position after an initial rotation (b, d). The shear also converges.

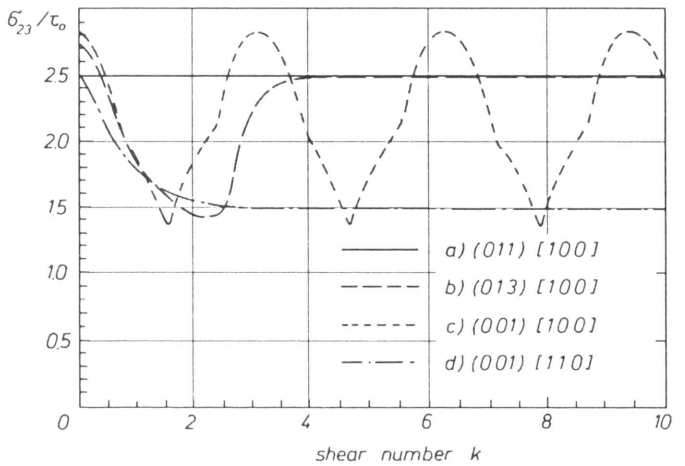

FIG. 3. Normalized shear stress versus shear number, corresponding to Fig. 2. Initial orientations are indicated by (global shear plane) [global shear direction] relative to the crystallographic axes.

Figure 4 gives a detailed picture of the initial phase of case (c). One can observe opposite directions of lattice spin and material spin. The stress oscillation

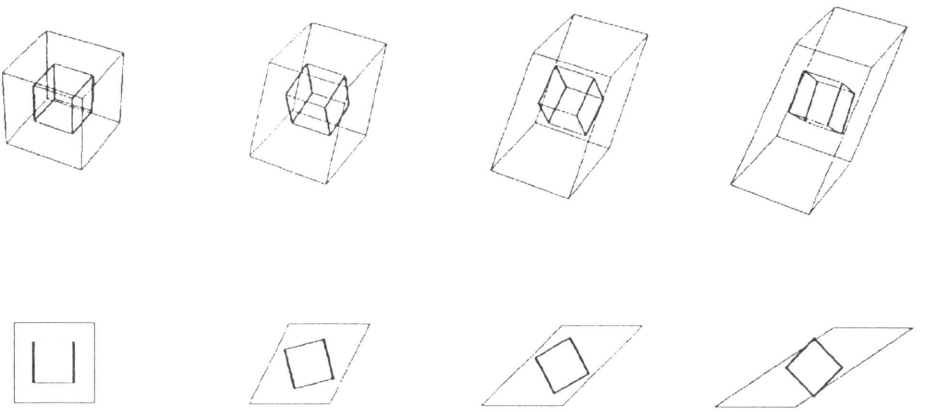

FIG. 4. Global deformation and lattice orientation (bold) for shear numbers 0, 0.5, 1.0, and 1.5 (case (c) of Fig. 2). Notice: opposite direction of material and lattice spin.

corresponds to the change of the slip system position relative to the global coordinate system via their Schmid factors. The normalized resolved shear stress of the 12 octahedral slip systems versus the amount of shear is plotted in Fig. 5. One can observe three groups (each of four slip systems), switching between three levels of shear stress: large positive, around zero and large negative.

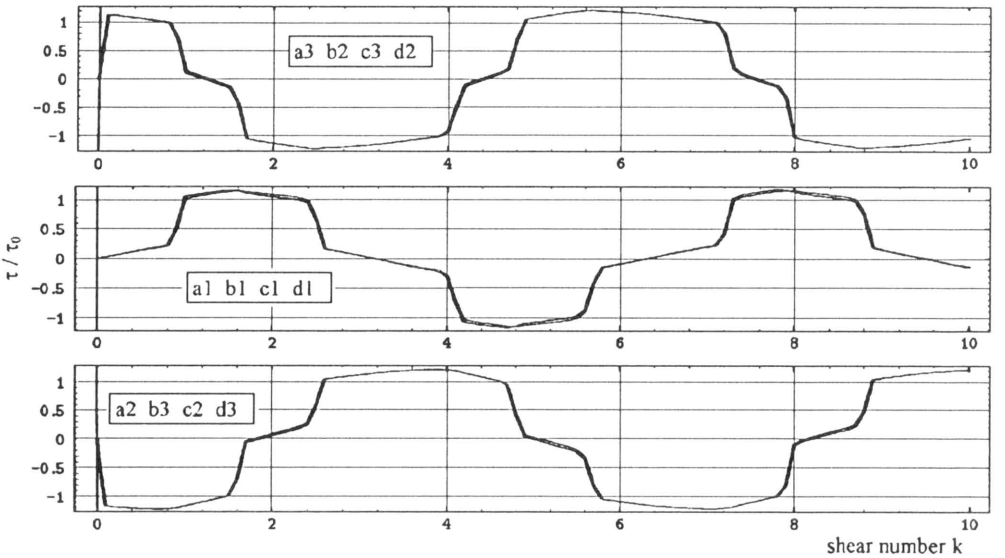

plane	(111)			$(\bar{1}\bar{1}\bar{1})$			$(\bar{1}11)$			$(1\bar{1}1)$		
direction	$[0\bar{1}1]$	$[10\bar{1}]$	$[\bar{1}10]$	$[011]$	$[\bar{1}0\bar{1}]$	$[1\bar{1}0]$	$[0\bar{1}1]$	$[\bar{1}0\bar{1}]$	$[110]$	$[011]$	$[10\bar{1}]$	$[\bar{1}\bar{1}0]$
system	a1	a2	a3	b1	b2	b3	c1	c2	c3	d1	d2	d3

FIG. 5. Normalized resolved shear stress versus global shear number (case (c) of Fig. 2). Slip system labels corresponding to [17].

The influence of different constitutive laws on the relation between material deformation and lattice rotation is demonstrated in the tensile test. Figures 6–9 show simulations of tensile tests up to 50% extension with identical initial orientation, boundary conditions, and elastic response. The values of the inelastic parameters are given in the following table:

displacement plot	Fig. 6	Fig. 7	Fig. 8	Fig. 9
Critical shear stress τ_0 [GPa]	∞	0	1	1
Viscosity η [GPas]	–	500	500	50
simulates	elasticity	viscoelasticity	viscoplasticity	plasticity

Figure 6 was calculated elastically. The following features can be observed:
- S-shape bending of the specimen axis,
- shear straining of the central region,
- lattice deformation being identical to material deformation.

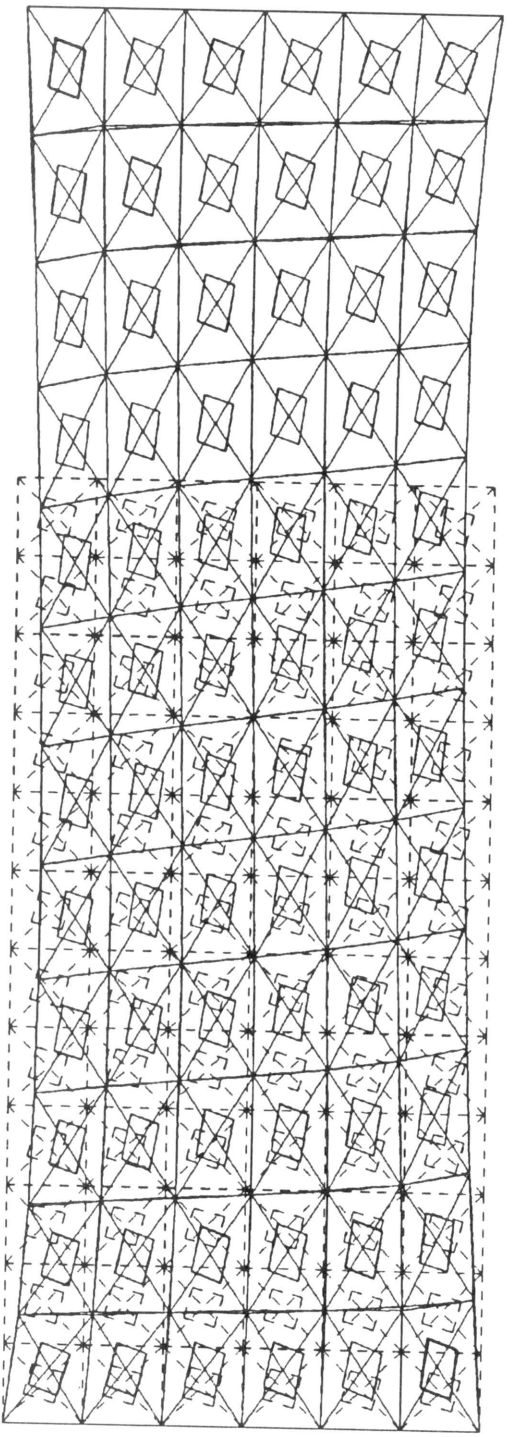

FIG. 6. Tensile test. Elastic simulation.

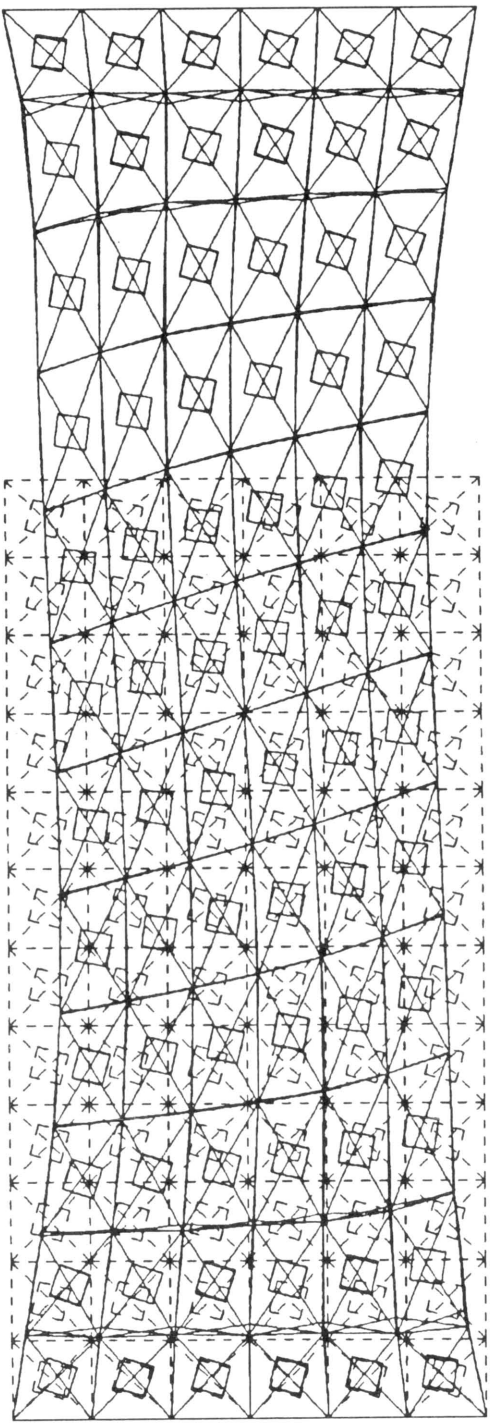

FIG. 7. Tensile test. Visco-elastic simulation.

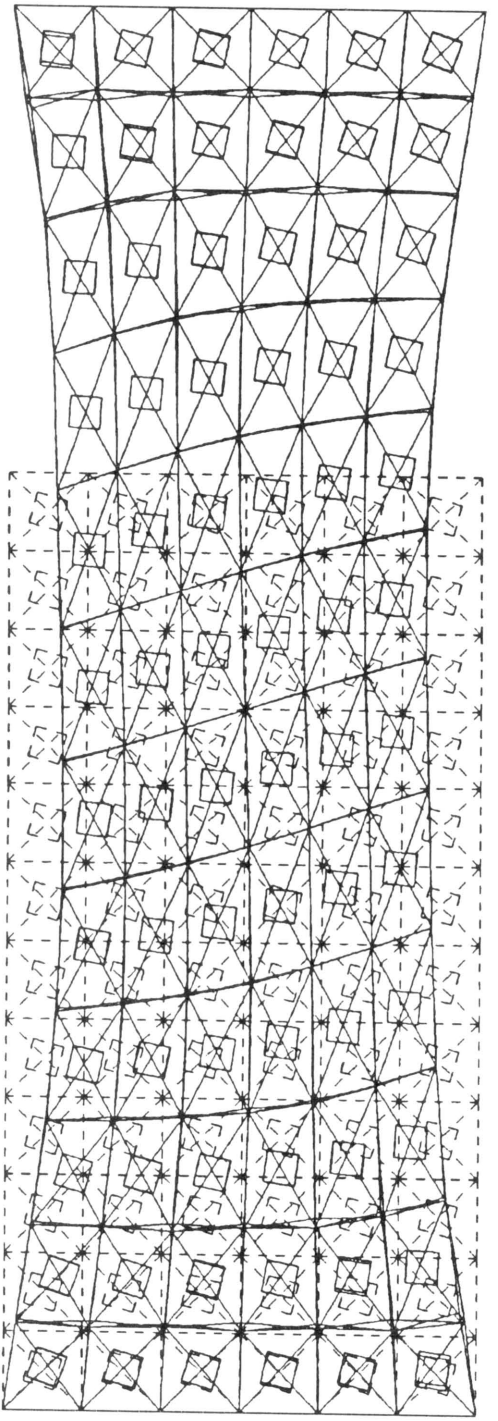

FIG. 8. Tensile test. Elasto-viscoplastic simulation.

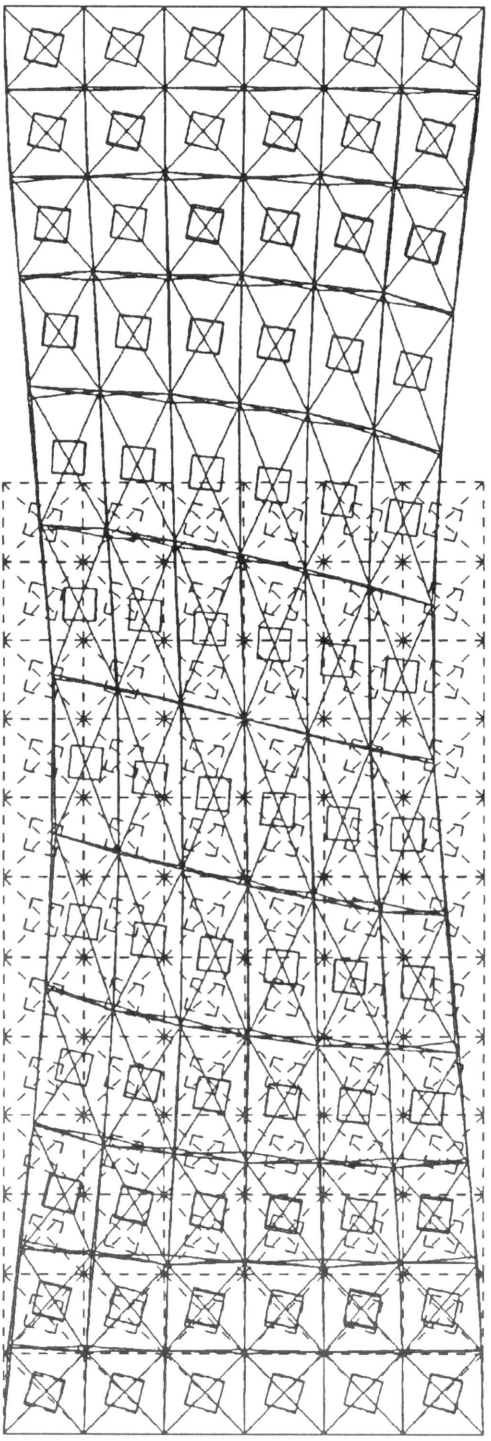

FIG. 9. Tensile test. Elasto-plastic simulation.

The first two features are typical for tensile tests on asymmetrically oriented anisotropic specimens, the latter holds generally for elastic deformations.

Figure 7 is the result of a viscoelastic simulation. The inhomogeneity of the deformation is stronger than in the elastic case. The lattice deformation is not visible, only rotations towards the tensile axis can be observed. The cross-sections rotate in the same sense as the lattice.

If we set τ_0 to 1 GPa (Fig. 8), the behaviour slightly changes. The final lattice orientation is closer to the tensile axis than in the previous case. Also, the stiffening effect of the boundary conditions can be observed.

Approaching the ideal plastic behaviour (Fig. 9), the deformation concentrates in the central part of the specimen. No imperfection has been used, the necking-like behaviour is due to the inelastic incompressibility (reduction of the net cross-section) and the boundary conditions. A significant difference to Figs. 6–8 is that the directions of lattice and material spin are opposite to Fig. 9. This is the same effect as in Fig. 4 (simple shear).

8. Conclusions

Based on the assumption of isomorphic elastic ranges, the concept of a plastic transformation is derived in a natural way. This quantity describes the effect of yielding to the elastic laws within the elastic ranges, and enables us to transform the current elastic law to a time-independent reference law by the isomorphy condition. The complete model is constituted by only two laws, (i) the elastic reference law h_0 and (ii) by the evolution equation for the plastic transformation g which is usually given by a flow rule.

This flow rule, however, can be rather complicated. It can be time-independent (plastic) or time-dependent (viscoplastic), isotropic or anisotropic, with any type of hardening or softening, etc.

The elastic reference law is not limited to small elastic deformations. It can be linear or nonlinear and will fulfill the principle of material objectivity identically, as it is formulated in the intrinsic variables. The same holds for the whole model.

A decomposition into elastic and plastic deformations has not been made and is unnecessary. If the material deforms within one elastic range, one could call the deformations (purely) elastic. If yielding occurs, the total deformation is considered as inelastic.

The key role in our theory is played by the plastic transformation, a fully non-symmetric quantity, which cannot be interpreted as a deformation. There is neither the need nor advantage to decompose this quantity or its rate into symmetric and skew-symmetric parts. It can be shown, however, that the skew-symmetric part of $\mathbf{P}_t^{\cdot}\,\mathbf{P}_t^{-1}$ does not contribute to the stress power and thus may be related to the "plastic spin" in other theories.

We would like to emphasize that the implementation of this model into an FEM-code was done using the intrinsic variables.

References

1. R.J. ASARO, *Micromechanics of crystals and polycrystals*, 1–115 [in:] Advances in Applied Mechanics, J.W. HUTCHINSON, T.Y. WU [Eds.], Academic Press, New York 1983.
2. A. BERTRAM, *Material systems – a framework for the description of material behavior*, Arch. Rat. Mech. Anal., **80**, 99–133, 1982.
3. A. BERTRAM, *Axiomatische Einführung in die Kontinuumsmechanik*, BI Wissenschaftsverlag, Mannheim, Wien, Zürich 1989.
4. A. BERTRAM and J. OLSCHEWSKI, *Formulation of anisotropic linear viscoelastic constitutive laws by a projection method*, 129–137 [in:] MD-Vol 26/AMD-Vol. 121, High Temperature Constitutive Modelling – Theory and Application, A. FREED, K.P. WALKER [Eds.], ASME, 1991.
5. A. BERTRAM, *Description of finite inelastic deformations*, 821–835 [in:] MECAMAT'92 Multiaxial Plasticity, Sept. 1–4, 1992, Cachan, France, A. BENALLAL, R. BILLARDON and D. MARQUIS [Eds.], 1993.
6. A. BERTRAM and M. KRASKA, *Description of finite plastic deformations in single crystals by material isomorphisms*, [in press] Proc. of IUTAM & ISIMM Symposium on Anisotropy, Inhomogeneity and Nonlinearity in Solid Mechanics, Kluwer Academic Publ., Nottingham, Aug. 8 – Sept. 9, 1994.
7. G. DEL PIERO, *On the elastic-plastic material element*, Arch. Rat. Mech. Anal., **59**, 111–129, 1975.
8. A.E. GREEN and P.M. NAGHDI, *A general theory of an elastic-plastic continuum*, Arch. Rat. Mech. Anal., **18**, 4, 251–281, 1965.
9. A.E. GREEN and P.M. NAGHDI, *Some remarks on elastic-plastic deformation at finite strain*, Int. J. Engng. Sci., **9**, 1219–1229, 1971.
10. A. KRAWIETZ, *Materialtheorie*, Springer-Verlag, Berlin, Heidelberg, New York, Tokyo 1986.
11. E. LEE, *Elastic-plastic deformations at finite strains*, J. Appl. Mech., **36**, 1–6, 1969.
12. I.-S. LIU, *On the requirement that material symmetry shall preserve density*, Arch. Rat. Mech. Anal., **68**, 19–26, 1982.
13. J. MANDEL, *Equations constitutive et directeur dans les milieux plastiques et viscoplastique*, Int. J. Sol. Struct., 9, 725–740, 1973.
14. P.M. NAGHDI, *A critical review of the state of finite plasticity*, J. Appl. Math. Phys., **41**, 387–394, 1990.
15. W. NOLL, *A new mathematical theory of simple materials*, Arch. Rat. Mech. Anal., **48**, 1–50, 1972.
16. M. ŠILHAVÝ and J. KRATOCHVÍL, *A theory of inelastic behavior of materials, Part I. Ideal Inelastic materials*, Arch. Rat. Mech. Anal., **65**, 97–129, 1977; *Part II. Inelastic materials*, Arch. Rat. Mech. Anal., **65**, 131–152, 1977.
17. G.I. TAYLOR and C.F. ELAM, *The distortion of an aluminum crystal during a tensile test*, Proc. R. Soc. London, A, **102**, 643–667, 1923.
18. C. TRUESDELL and W. NOLL, *The non-linear field theories of mechanics*, [in:] Handbuch der Physik III/3, S. FLÜGGE [Ed.], Springer-Verlag, Berlin, Heidelberg, New York 1965.
19. K.S. HAVNER, *Finite plastic deformation of crystalline solids*, Cambridge University Press, Cambridge 1992.

BUNDESANSTALT FÜR MATERIALFORSCHUNG UND PRÜFUNG (BAM), BERLIN, GERMANY
and
TECHNICAL UNIVERSITY BERLIN, GERMANY.

Received October 10, 1994.

Arch. Mech., 47, 2, pp. 223–246, Warszawa 1995

The elastic constants of a material containing spherical coated holes (*)

É. HERVÉ and O. PELLEGRINI (PALAISEAU)

FIRST WE DERIVE the elastic strain and stress fields in an infinite medium consisting of an n-layered isotropic spherical inclusion, embedded in a matrix subjected to uniform stress or strain conditions at infinity, and where the innermost phase of the composite inclusion is a pore. The solution of this problem is then used for the expression of a Generalized Self-Consistent Scheme and the calculation of Hashin-Shtrikman type bounds of isotropic Generalized Composite Spheres Assemblages. Finally, comparison between experimental results and predictions of the models are given by means of a forced resonance vibration technique.

1. Introduction

WITH THE INCREASE of light-weight structures in any industrial branch, estimates of the overall effective elastic properties of elastic solids which contain voids become of considerable interest. Different micro-mechanics models can be used to predict the overall elastic moduli of such composites: Self-consistent ones (HILL [1], BUDIANSKY [2], or variational ones (HASHIN-SHTRIKMAN [3]). In order to study the elastic behaviour of two-phase matrix-inclusion composites, MACKENSIE [4] and CHRISTENSEN and LO [5] have proposed generalized Self-Consistent Schemes. In those approaches the inclusion (void in [4]) is surrounded by a matrix shell which in turn is surrounded by the effective (bounded in [4] and infinite in [5]) medium. HASHIN [6] has defined composite spheres assemblages (C.S.A) and has derived bounds for those assemblages. HERVÉ, STOLZ and ZAOUI [7] have improved the bounding of isotropic C.S.A.'s.

The present work is intended to provide models to predict the behaviour of multiply coated hole-filled materials with a matrix-inclusion-type geometry, and extends the work of HERVÉ and ZAOUI [8] on n-layered inclusion-based modelling in the case when the innermost phase is a void.

2. n-layered spherical inclusion

This section is concerned with the derivation of the elastic strain and stress fields in an infinite medium consisting of an n-layered spherical inclusion, surrounded by a matrix subjected to uniform stress or strain conditions at infinity.

Each phase is homogeneous, linearly elastic and isotropic. In addition, perfect bonding is assumed at the interfaces.

(*) Paper presented at 30th Polish Solid Mechanics Conference, Zakopane, September 5–9, 1994.

The layers are numbered, beginning with the innermost phase (Fig. 1) which is numbered 1 and represents a void. Let phase (i) lie within the shell limited by the spheres with the radii R_{i-1}, and R_i and let (μ_i, ν_i, K_i) be respectively the shear modulus, Poisson's ratio and bulk modulus of phase (i) (here $i \in [1, n+1]$, $R_0 = 0$, $R_{n+1} \to \infty$). The configuration under study is referred to a Cartesian coordinate system $x_1x_2x_3$ (with the unit vectors $\mathbf{e}_1$, $\mathbf{e}_2$, $\mathbf{e}_3$). We use a spherical (r, θ, ϕ) coordinate system with the origin at the center of the composite sphere.

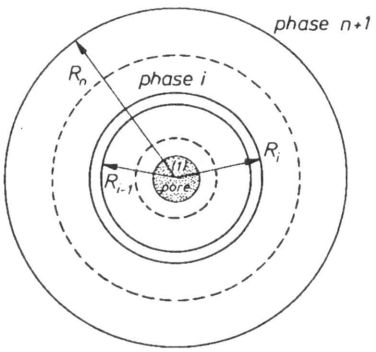

FIG. 1. The n-layered inclusion embedded in an infinite matrix.

The approach used in this paper is similar to the one developed by HERVÉ and ZAOUI in [8], except that here the innermost phase is void. Making use of isotropy and spherical symmetry of the structure, the general solution may be obtained from the solution of two elementary problems: hydrostatic pressure and simple shear applied at infinity.

2.1. Hydrostatic pressure

The following system of tractions is applied to the boundary of the body in the stress approach:

$$\mathbf{T}^0 = \frac{\sigma_0}{3}\mathbf{n}, \tag{2.1}$$

where σ_0 is a constant and $\mathbf{n}$ is the unit outward normal.

In the displacement approach the boundary displacements are taken in the form:

$$\mathbf{u}^0 = r\frac{\theta_0}{3}\mathbf{e}_r\,, \tag{2.2}$$

where θ_0 is a constant and $\mathbf{e}_r$ is the first unit vector of the spherical coordinate system.

In both approaches, the problem has spherical symmetry and thus is one-dimensional. It is easy to show that the following displacement component field u_r satisfies the single equibrium equation:

$$u_r^{(i)} = F_i r + \frac{G_i}{r^2}, \tag{2.3}$$

where F_i and G_i are constants and $i \in [2, n+1]$. The corresponding stresses are found to be:

$$\begin{aligned} \sigma_{rr}^{(i)} &= 3k_i F_i - \frac{4\mu_i}{r^3} G_i, \\ \sigma_{\theta\theta}^{(i)} &= \sigma_{\phi\phi}^{(i)} = 3k_i F_i + \frac{2\mu_i}{r^3} G_i, \\ \sigma_{r\theta}^{(i)} &= \sigma_{r\phi}^{(i)} = \sigma_{\theta\phi}^{(i)} = 0. \end{aligned} \tag{2.4}$$

The perfect bonding at the interface $r = R_k$ requires the continuity of the stress vectors and of the displacement field. These conditions may be written in the form:

$$\mathbf{J}_k(R_k)\mathbf{V}_k = \mathbf{J}_{k+1}(R_k)\mathbf{V}_{k+1}, \tag{2.5}$$

where $\mathbf{V}_k = (A_k, B_k)$, $k \in [2, n]$ and $\mathbf{J}_i(r)$ is the following matrix:

$$\mathbf{J}_i(r) = \begin{pmatrix} r & \frac{1}{r^2} \\ -\frac{4\mu_i}{r^3} & 3K_i \end{pmatrix}. \tag{2.6}$$

The system of Eqs. (2.5) is solved for $\mathbf{V}_{k+1}$ by means of the "transfer matrices" $\mathbf{N}^{(k)}$

$$\mathbf{V}_{k+1} = \mathbf{N}^{(k)}\mathbf{V}_k, \tag{2.7}$$

where

$$\mathbf{N}^{(k)} = \mathbf{J}_{k+1}^{-1}(R_k)\mathbf{J}_k(R_k), \tag{2.8}$$

$$\mathbf{N}^{(k)} = \frac{1}{3K_{k+1} + 4\mu_{k+1}} \begin{pmatrix} 3K_k + 4\mu_{k+1} & \frac{4}{R_k^3}(\mu_{k+1} - \mu_k) \\ 3(K_{k+1} - K_k)R_k^3 & 3K_{k+1} + 4\mu_k \end{pmatrix}. \tag{2.9}$$

Therefore one gets

$$\mathbf{V}_{k+1} = \prod_{j=k}^{2} \mathbf{N}^{(j)}\mathbf{V}_2 = \mathbf{Q}^{(k)}\mathbf{V}_2. \tag{2.10}$$

At the interface $r = R_1$ the stress vector vanishes, so that

$$G_2 = \frac{3K_2F_2R_1^3}{4\mu_2}. \tag{2.11}$$

From (2.10) and (2.11) we find

$$F_{n+1} = \left(Q_{11}^{(n)} + \frac{3K_2R_1^3}{4\mu_2}Q_{12}^{(n)}\right)F_2. \tag{2.12}$$

Thus all the coefficients A_k, B_k may be derived as

$$\begin{aligned} F_k &= \frac{4\mu_2Q_{11}^{(k-1)} + 3K_2R_1^3Q_{12}^{(k-1)}}{4\mu_2Q_{11}^{(n)} + 3K_2R_1^3Q_{12}^{(n)}}F_{n+1}, \\ G_k &= \frac{4\mu_2Q_{21}^{(k-1)} + 3K_2R_1^3Q_{22}^{(k-1)}}{4\mu_2Q_{11}^{(n)} + 3K_2R_1^3Q_{12}^{(n)}}F_{n+1}, \qquad k \in [2, n+1], \end{aligned} \tag{2.13}$$

where

$$\begin{aligned} F_{n+1} &= \frac{\sigma_0}{9K_{n+1}} \qquad \text{in the stress approach,} \\ F_{n+1} &= \frac{\theta_0}{3} \qquad \text{in the displacement approach.} \end{aligned} \tag{2.14}$$

2.2. Simple shear

In the displacement approach the boundary displacements are chosen in the form

$$u_1^0 = \gamma x_1, \qquad u_2^0 = -\gamma x_2, \qquad u_3^0 = 0. \tag{2.15}$$

The traction system:

$$T_1^0 = \tau n_1, \qquad T_2^0 = -\tau n_2, \qquad T_3^0 = 0 \tag{2.16}$$

is applied to the boundary in the stress approach. In phase (i), the displacement field **u** has the form (from LOVE [9] and CHRISTENSEN and LO [5]):

$$\begin{aligned} u_r^{(i)} &= \left(A_ir - \frac{6\nu_i}{1-2\nu_i}B_ir^3 + 3\frac{C_i}{r^4} + \frac{5-4\nu_i}{1-2\nu_i}\frac{D_i}{r^2}\right)\sin^2(\theta)\cos(2\phi), \\ u_\theta^{(i)} &= \left(A_ir - \frac{7-4\nu_i}{1-2\nu_i}B_ir^3 - 2\frac{C_i}{r^4} + 2\frac{D_i}{r^2}\right)\sin(\theta)\cos(\theta)\cos(2\phi), \\ u_\phi^{(i)} &= -\left(A_ir - \frac{7-4\nu_i}{1-2\nu_i}B_ir^3 - 2\frac{C_i}{r^4} + 2\frac{D_i}{r^2}\right)\sin(\theta)\sin(2\phi), \end{aligned} \tag{2.17}$$

where A_i, B_i, C_i, D_i are constants ($i \in [2, n+1]$), B_{n+1} vanishes ($r \to \infty$) and A_{n+1} is determined by the boundary conditions at infinity. The perfect bonding at $r = R_k$ requires the continuity of σ_{rr}, $\sigma_{r\theta}$, $\sigma_{r\phi}$, u_r, u_θ, u_ϕ but only four of these conditions are independent. They may be expressed in the form:

$$\mathbf{L}_k(R_k)\mathbf{W}_k = \mathbf{L}_{k+1}(R_k)\mathbf{W}_{k+1}\,, \qquad k \in [2, n], \tag{2.18}$$

where the matrix $\mathbf{L}_i(r)$ is defined by

$$\mathbf{J}_i(r) = \begin{pmatrix} r & -\dfrac{6\nu_i}{1-2\nu_i}r^3 & \dfrac{3}{r^4} & \dfrac{5-4\nu_i}{1-2\nu_i}\dfrac{1}{r^2} \\ r & -\dfrac{7-4\nu_i}{1-2\nu_i}r^3 & -\dfrac{2}{r^4} & \dfrac{2}{r^2} \\ \mu_i & \dfrac{3\nu_i}{1-2\nu_i}\mu_i r^2 & -\dfrac{12}{r^5}\mu_i & 2\dfrac{\nu_i-5}{1-2\nu_i}\dfrac{\mu_i}{r^3} \\ \mu_i & -\dfrac{7+2\nu_i}{1-2\nu_i}\mu_i r^2 & \dfrac{8}{r^5}\mu_i & 2\dfrac{1+\nu_i}{1-2\nu_i}\dfrac{\mu_i}{r^3} \end{pmatrix}. \tag{2.19}$$

The system of Eqs. (2.18) is solved for $\mathbf{W}_{k+1}$ by means of the "transfer matrices" $\mathbf{M}^{(k)}$:

$$\mathbf{W}_{k+1} = \mathbf{M}^{(k)}\mathbf{W}_k\,, \tag{2.20}$$

where

$$\mathbf{M}^{(k)} = \mathbf{L}_{k+1}^{-1}(R_k)\mathbf{L}_k(R_k)\,,$$

$$\mathbf{M}^{(k)} = \frac{1}{5(1-\nu_{k+1})} \begin{pmatrix} \dfrac{c_k}{3} & \dfrac{R_k^2(3b_k-7c_k)}{5(1-2\nu_k)} & -\dfrac{12\alpha_k}{R_k^5} & \dfrac{4(f_k-27\alpha_k)}{15(1-2\nu_k)R_k^3} \\ 0 & \dfrac{(1-2\nu_{k+1})b_k}{7(1-2\nu_k)} & -\dfrac{20(1-2\nu_{k+1})\alpha_k}{7R_k^7} & -\dfrac{12\alpha_k(1-2\nu_{k+1})}{7(1-2\nu_k)R_k^5} \\ \dfrac{R_k^5\alpha_k}{2} & -\dfrac{R_k^7(2a_k+147\alpha_k)}{70(1-2\nu_k)} & \dfrac{d_k}{7} & \dfrac{R_k^2[105(1-\nu_{k+1})+12\alpha_k(7-10\nu_{k+1})-7e_k]}{35(1-2\nu_k)} \\ -\dfrac{5}{6}(1-2\nu_{k+1})\alpha_k R_k^3 & \dfrac{7(1-2\nu_{k+1})\alpha_k R_k^5}{2(1-2\nu_k)} & 0 & \dfrac{e_K(1-2\nu_{k+1})}{3(1-2\nu_k)} \end{pmatrix}, \tag{2.22}$$

with

$$
\begin{aligned}
a_k &= (7+5\nu_k)(7-10\nu_{k+1})\frac{\mu_k}{\mu_{k+1}} - (7-10\nu_k)(7+5\nu_{k+1}),\\
b_k &= 4(7-10\nu_k) + (7+5\nu_k)\frac{\mu_k}{\mu_{k+1}},\\
c_k &= (7-5\nu_{k+1}) + 2(4-5\nu_{k+1})\frac{\mu_k}{\mu_{k+1}},\\
d_k &= (7+5\nu_{k+1}) + 4(7-10\nu_{k+1})\frac{\mu_k}{\mu_{k+1}},\\
e_k &= 2(4-5\nu_k) + (7-5\nu_k)\frac{\mu_k}{\mu_{k+1}},\\
f_k &= (4-5\nu_k)(7-5\nu_{k+1}) - (4-5\nu_{k+1})(7-5\nu_k)\frac{\mu_k}{\mu_{k+1}},\\
\alpha_k &= \frac{\mu_k}{\mu_{k+1}} - 1.
\end{aligned}
$$

Consequently, we have

$$
\mathbf{W}_{k+1} = \prod_{j=k}^{2} \mathbf{M}^{(j)}\mathbf{W}_2 = \mathbf{P}^{(k)}\mathbf{W}_2\,. \tag{2.23}
$$

At the interface $r = R_1$ the traction vanishes, so that

$$
\begin{aligned}
A_2 &= \frac{21}{5(1-2\nu_2)}R_1^2 B_2 + \frac{2(7-5\nu_2)}{5(1-2\nu_2 R_1^3)}D_2\,,\\
C_2 &= \frac{1}{20}\frac{(7+5\nu_2)}{(1-2\nu_2)}R_1^7 B_2 - \frac{3}{5}\frac{R_1^2}{(1-2\nu_2)}D_2\,.
\end{aligned} \tag{2.24}
$$

Since $B_{n+1} = 0$, we get from (2.23) (with $k = n$):

$$
\begin{aligned}
A_2 &= \beta\,\frac{A_{n+1}}{P_{11}^{(n)}\beta + P_{12}^{(n)}\gamma + P_{13}^{(n)}\delta + P_{14}^{(n)}}\,,\\
B_2 &= \gamma\,\frac{A_{n+1}}{P_{11}^{(n)}\beta + P_{12}^{(n)}\gamma + P_{13}^{(n)}\delta + P_{14}^{(n)}}\,,\\
C_2 &= \delta\,\frac{A_{n+1}}{P_{11}^{(n)}\beta + P_{12}^{(n)}\gamma + P_{13}^{(n)}\delta + P_{14}^{(n)}}\,,\\
D_2 &= \frac{A_{n+1}}{P_{11}^{(n)}\beta + P_{12}^{(n)}\gamma + P_{13}^{(n)}\delta + P_{14}^{(n)}}\,,
\end{aligned} \tag{2.25}
$$

with:

$$\Delta = 84R_1^5P_{21}^{(n)} + 20(1-2\nu_2)R_1^3P_{22}^{(n)} + (7+5\nu_2)R_1^{10}P_{23}^{(n)},$$

$$\beta = \frac{252R_1^{10}P_{23}^{(n)} - 420R_1^8P_{24}^{(n)} + 40(1-2\nu_2)(7-5\nu_2)R_1^3P_{22}^{(n)}}{5(1-2\nu_2)R_1^3\Delta}$$

$$+ \frac{2(7-5\nu_2)(7+5\nu_2)R_1^{10}P_{23}^{(n)}}{5(1-2\nu_2)R_1^3\Delta}, \tag{2.26}$$

$$\gamma = -\frac{8(7-5\nu_2)P_{21}^{(n)} - 12R_1^5P_{23}^{(n)} + 20(1-2\nu_2)R_1^3P_{24}^{(n)}}{\Delta},$$

$$\delta = \frac{-8[(7-5\nu_2)(7+5\nu_2)+126]R_1^7P_{21}^{(n)} - 20(7+5\nu_2)(1-2\nu_2)R_1^{10}P_{24}^{(n)}}{20(1-2\nu_2)\Delta}$$

$$- \frac{240(1-2\nu_2)R_1^5P_{22}^{(n)}}{20(1-2\nu_2)\Delta}.$$

Consequently, all the coefficients A_i, B_i, C_i, D_i are given in terms of D_{n+1} by

$$\mathbf{W}_i = \frac{A_{n+1}}{P_{11}^{(n)}\beta + P_{12}^{(n)}\gamma + P_{13}^{(n)}\delta + P_{14}^{(n)}}\mathbf{P}^{(i-1)}\begin{bmatrix}\beta\\ \gamma\\ \delta\\ 1\end{bmatrix}, \quad i \in [2, n+1], \tag{2.27}$$

where

$$\begin{aligned} A_{n+1} &= \frac{\tau}{2\mu_{n+1}} && \text{in the stress approach,}\\ A_{n+1} &= \gamma && \text{in the displacement approach.} \end{aligned} \tag{2.28}$$

From (2.3), (2.13) and (2.14) and from (2.17), (2.27) and (2.28), the displacement field $\mathbf{u}^{(i)}$ may be calculated for uniform strain or stress conditions at infinity.

2.3. Average strains and stresses

From these solutions, the average strain and stress fields in each phase are easily calculated. The same method as the one developed by HERVÉ and ZAOUI [8] is used. When uniform strain conditions are prescribed at infinity

$$\boldsymbol{\varepsilon}_0 = \frac{\theta_0}{3}\mathbf{I} + \mathbf{e}_0, \tag{2.29}$$

the average strain tensor in phase (k) is given by

$$\overline{\boldsymbol{\varepsilon}^{(k)}} = \frac{F_k}{F_{n+1}}\frac{\theta_0}{3}\mathbf{I} + \frac{1}{A_{n+1}}\left(A_k - \frac{21}{5}\frac{R_k^5 - R_{k-1}^5}{(1-2\nu_k)(R_k^3 - R_{k-1}^3)}B_k\right)\mathbf{e}_0. \tag{2.30}$$

This average strain may also be calculated in the whole n-layered inclusion

$$\bar{\boldsymbol{\varepsilon}} = \frac{\bar{\theta}}{3}\mathbf{I} + \bar{\mathbf{e}} = \left(1 + \frac{G_{n+1}}{F_{n+1}R_n^2}\right)\frac{\theta_0}{3}\mathbf{I} + \left(1 + \frac{4}{5}\frac{4-5\nu_{n+1}}{1-2\nu_{n+1}}\frac{D_{n+1}}{A_{n+1}R_n^3}\right)\mathbf{e}_0 . \tag{2.31}$$

Correspondingly, when uniform stress conditions are prescribed at infinity:

$$\boldsymbol{\sigma}_0 = \frac{\sigma_0}{3}\mathbf{I} + \mathbf{s}_0 , \tag{2.32}$$

the average stress tensor in phase (k) is given by

$$\overline{\boldsymbol{\sigma}^{(k)}} = \frac{K_k F_k}{K_{n+1}F_{n+1}}\frac{\sigma_0}{3}\mathbf{I} + \frac{1}{2\mu_{n+1}A_{n+1}}\left(A_k - \frac{21}{5}\frac{R_k^5 - R_{k-1}^5}{(1-2\nu_k)(R_k^3 - R_{k-1}^3)}B_k\right)\mathbf{s}_0 , \tag{2.33}$$

and the average stress in the whole n-layered inclusion is

$$\bar{\boldsymbol{\sigma}} = \frac{\overline{\mathrm{Tr}(\boldsymbol{\sigma})}}{3}\mathbf{I} + \bar{\mathbf{s}} = \left(1 - \frac{4\mu_{n+1}G_{n+1}}{3K_{n+1}F_{n+1}R_n^3}\right)\frac{\sigma_0}{3}\mathbf{I} + \left(1 - \frac{2}{5}\frac{7-5\nu_{n+1}}{1-2\nu_{n+1}}\frac{D_{n+1}}{A_{n+1}R_n^3}\right)\mathbf{s}_0 . \tag{2.34}$$

These solutions may be used to derive bounds for generalized Hashin's assemblages (cf. Sec. 3). They can also be used when K_{n+1} and μ_{n+1} denote the effective moduli of a composite material according to the $(n+1)$ phase model defined in Sec. 4.

3. Variational approach

In order to represent the situation of an isotropic two-phase material, consisting of a matrix in which perfectly spherical inclusions are embedded, HASHIN [6] has proposed a particular assemblage made of two-phase similar spheres. In the following, we consider generalized Hashin's assemblages where the basic composite spheres of the assemblage are of the n-layered-type described in Sec. 2. So the whole body is composed of such composite spheres of any size, including infinitesimal ones, so as to fill up the whole space. It is a particular case of the media studied by STOLZ and ZAOUI [10] which are decomposed into representative morphological patterns. An application of the general method presented in [10] has already been examined by HERVÉ, STOLZ and ZAOUI [7] in order to give "bounds" of the elastic overall characteristics of Hashin's isotropic composite spheres assemblage.

Consider here an isotropic distribution of phases (λ) composed of N_λ "morphological" identical composite spherical patterns $S_{\lambda k}$ with the center $X_{\lambda k}$. Let this set of families be referred to as the representative volume element considered as an infinite medium under homogeneous strain boundary conditions. In this particular case, making use of the general method presented in [10], the Hashin-Shtrikman functional HS

$$HS(\mathbf{E}, \boldsymbol{\varepsilon}_\lambda^M) = \frac{1}{2}\mathbf{E} : \mathbf{C}_0 : \mathbf{E} + \frac{1}{2V}\sum_\lambda N_\lambda \mathbf{E} : \int_{S_\lambda} \delta\mathbf{c}_0(x) : \boldsymbol{\varepsilon}_\lambda^M(x)\, d\omega \tag{3.1}$$

provides bounds for the quadratic form $1/2 < \boldsymbol{\varepsilon} : \mathbf{c} : \boldsymbol{\varepsilon} >$, when $\delta\mathbf{c}_0(x) = \mathbf{c}(x) - \mathbf{C}_0$ is positive or negative definite at each point ($\mathbf{C}_0$ denotes the elastic stiffness tensor of the reference medium), and $\boldsymbol{\varepsilon}_\lambda^M$ is the solution of the following integral equation:

$$\boldsymbol{\varepsilon}_\lambda^M(x) + \int_{S_\lambda} \boldsymbol{\Gamma}^0(x, x') : \delta\mathbf{c}_0(x') : \boldsymbol{\varepsilon}_\lambda^M(x')\, d\omega' = \boldsymbol{\varepsilon}_0. \tag{3.2}$$

The Green operator $\boldsymbol{\Gamma}^0(x, x')$ is obtained by differentiation of the Green tensor ($\mathbf{G}^0$) of the reference medium subjected to homogeneous strain ($\mathbf{E}$) conditions at infinity:

$$\Gamma^0_{ijkl}(x, x') = \frac{\partial^2}{\partial x_j \partial x'_l} \mathbf{G}^0_{ik}(x, x')_{(ij)(kl)}\,. \tag{3.3}$$

$\boldsymbol{\varepsilon}_\lambda^M$ is defined as the average strain over the homologous points $(x + X_{\lambda k})$ of the patterns $S_{\lambda k}$. All the translated patterns of the $S_{\lambda k}$ at the origin constitute the sphere S_λ. We can get ε_0 by the following average conditions:

$$\mathbf{E} = \sum_\lambda \frac{c_\lambda}{S_\lambda} \int_{S_\lambda} \boldsymbol{\varepsilon}_\lambda^M(x)\, d\omega\,, \tag{3.4}$$

where c_λ denotes the volume fraction of phase λ. The solution of Eq. (3.2) represents the solution of the problem of a composite spherical inhomogeneity embedded in an infinite homogeneous matrix subjected to the strain ε_0 at infinity. In this particular case of assemblage, and by taking into account the fact that the average strain does not depend on the size of the similar composite n-layered spheres S_λ, the Hashin-Shtrikman functional may be written as

$$HS = \frac{1}{2}\mathbf{E} : \sum_{i=1}^{n} f_i \mathbf{C}_i : \bar{\boldsymbol{\varepsilon}}_i^M = \frac{1}{2}\mathbf{E} :< \mathbf{C}_i : \bar{\boldsymbol{\varepsilon}}_i^M >\,, \tag{3.5}$$

where f_i is the volume fraction of the phase of shell (i) in the n-layered composite sphere and $\mathbf{C}_i$ are its elastic moduli. $\boldsymbol{\varepsilon}_i^M$ may be expressed in the form:

$$\begin{aligned} \bar{\boldsymbol{\varepsilon}}_i^M &= \bar{\boldsymbol{\varepsilon}}^i = \mathbf{A}^i : \boldsymbol{\varepsilon}_0 , \\ \bar{\boldsymbol{\varepsilon}}^i &= (a_i^* \mathbf{J} + b_i^* \mathbf{K}) : \boldsymbol{\varepsilon}_0 = a_i^* \mathbf{e}_0 + b_i^* \frac{\theta_0}{3} \mathbf{I}, \end{aligned} \tag{3.6}$$

with

$$\mathbf{I} = \mathbf{J} + \mathbf{K}, \qquad K_{ijkl} = \frac{1}{3}\delta_{ij}\delta_{kl} , \qquad I_{ijkl} = \frac{1}{2}(\delta_{ik}\delta_{jl} + \delta_{il}\delta_{jk}), \tag{3.7}$$

and where a_i^* and b_i^* are derived by means of Eq. (2.30). We get from (3.4)

$$\mathbf{E} = < \bar{\boldsymbol{\varepsilon}}_i^M > = < \mathbf{A}^i > : \boldsymbol{\varepsilon}_0 \tag{3.8}$$

and finally,

$$HS = \frac{1}{2}\mathbf{E} :< \mathbf{C}_i : \mathbf{A}_i >:< \mathbf{A}_i >^{-1} : \mathbf{E} . \tag{3.9}$$

Hashin-Shtrikman-type bounds ($\mu^{\pm II}$ and $K^{\pm II}$) are then given, according to (3.9), (3.6) and (2.30) by

$$\mu^{\pm II} = < \mu_i a_i^* >< a_i^* >^{-1} , \qquad K^{\pm II} = < K_i b_i^* >< b_i^* >^{-1} \tag{3.10}$$

or making use of (2.31), (2.34) and (2.27), by

$$\mu^{\pm II} = \mu_0 \frac{1 - \dfrac{9K_0 + 8\mu_0}{5\mu_0 R_n^3} \dfrac{P_{41}^{(n)}\beta + P_{42}^{(n)}\gamma + P_{43}^{(n)}\delta + P_{44}^{(n)}}{P_{11}^{(n)}\beta + P_{12}^{(n)}\gamma + P_{13}^{(n)}\delta + P_{14}^{(n)}}}{1 + \dfrac{6K_0 + 12\mu_0}{5\mu_0 R_n^3} \dfrac{P_{41}^{(n)}\beta + P_{42}^{(n)}\gamma + P_{43}^{(n)}\delta + P_{44}^{(n)}}{P_{11}^{(n)}\beta + P_{12}^{(n)}\gamma + P_{13}^{(n)}\delta + P_{14}^{(n)}}} , \tag{3.11}$$

$$K^{+II} = K^{-II} = K , \tag{3.12}$$

where $\mu_0 = \mu_{n+1} = \mathrm{Sup}_{i=1,n}(\mu_i)$; $K_0 = K_{n+1} = \sup_{i=1,n}(K_i)$ for the upper bound (replace Sup by 0 for the lower bound). Note the coincidence of K^{+II} and K^{-II} with the $(n+1)$-phase model estimate (4.5).

In order to bound the effective elastic moduli of such assemblages, Hashin's approach [6] can be applied. The basic concept of this method is to use the solutions for such a n-layered spherical sphere, submitted to a hydrostatic pressure or to a simple shear loading, as admissible fields for the principles of minimum potential and minimum complementary energy. These Voigt-Reuss-type bounds ($\mu^{\pm I}$ and $K^{\pm I}$) can also be derived by using (3.11), with μ_0 and K_0 tending to

infinity for the upper bounds, and to zero for the lower bounds. Therefore μ^{-I} and μ^{-II} coincide.

An application of this treatement has been made for simple porous spheres assemblage. In that case all the bounds of the bulk modulus coincide with (4.6) and the recurrence relation (3.11) may be expressed in the form

$$\frac{\mu}{\mu_2} = 1 + c\, h(\gamma_0), \tag{3.13}$$

with $\gamma_0 = \mu_0/\mu_2$ and

$$h = \frac{15(\nu_2 - 1)}{7 - 5\nu_2 + 2c(4 - 5\nu_2) - 126c(1 - c^{\frac{2}{3}})^2 A'},$$
$$A' = \frac{1 - \gamma_0}{7 + 5\nu_2\left[1 - c^{\frac{7}{3}}(1 - \gamma_0) + 4\gamma_0(7 - 10\nu_2)\right]}, \tag{3.14}$$

where index 2 stands for the matrix and c denotes the porosity. It is worth noting that, in this particular case, μ^{+II} coincide with the classical Hashin-Shtrikman's upper bound.

4. A $(n+1)$-phase model

Let us consider now that the composite n-layered inclusion under study is embedded in an unknown isotropic infinite matrix of the equivalent homogeneous medium. HERVÉ and ZAOUI [11] have shown that CHRISTENSEN and LO's energy condition [5] defined for the three-phase model, applied to the more general case where the composite inclusion is an inhomogeneous elastic ellipsoidal inclusion, is equivalent to the requirement that the average strain in the composite inclusion be the same as the macroscopic strain imposed to the composite medium at infinity ($\overline{\boldsymbol{\varepsilon}} = \boldsymbol{\varepsilon}_0$). The present n-phase composite sphere is a particular case of such an inclusion. So this strain condition is used to determine the effective moduli K and μ of an isotropic composite material defined by this "$(n+1)$-phase model".

4.1. Bulk modulus

Consider just the problem of pure dilatation at infinity. The above-mentioned condition ($\overline{\varepsilon} = \varepsilon_0$) becomes in that case

$$\overline{\theta} = \theta_0\,, \tag{4.1}$$

and from (2.31) it reduces to

$$G_{n+1} = 0. \tag{4.2}$$

K and μ contributes only to the matrix $N^{(n)}$ so that relation (2.10) may be written in the form

$$\mathbf{V}_{n+1} = N^{(n)} \prod_{j=n-1}^{2} \mathbf{N}^{(j)} \mathbf{V}_2 = N^{(n)} \mathbf{Q}^{(n-1)} \mathbf{V}_2 . \tag{4.3}$$

In (4.3) we may substitute the expression (2.9) for N^n with $\mu_{n+1} = \mu$ and $K_{n+1} = K$ so that G_{n+1} is given by

$$G_{n+1} = \frac{F_2}{3K + 4\mu} \left[\left\{ 3(K - K_n) R_n^3 Q_{11}^{(n-1)} + (3K + 4\mu_n) Q_{21}^{(n-1)} \right\} + \frac{3K_2 R_1^3}{4\mu_2} \left\{ 3(K - K_n) R_n^3 Q_{12}^{(n-1)} + (3K + 4\mu_n) Q_{22}^{(n-1)} \right\} \right] , \tag{4.4}$$

where (2.11) has been used. The effective bulk modulus K is then

$$K = \frac{H_1}{H_2} , \tag{4.5}$$

where

$$H_1 = 3K_n R_n^3 \left[4\mu_2 Q_{11}^{(n-1)} + 3K_2 R_1^3 Q_{12}^{(n-1)} \right] - 4\mu_n \left[4\mu_2 Q_{21}^{(n-1)} + 3K_2 R_1^3 Q_{22}^{(n-1)} \right] ,$$
$$H_2 = 3 \left\{ R_n^3 \left[4\mu_2 Q_{11}^{(n-1)} + 3K_2 R_1^3 Q_{12}^{(n-1)} \right] + 4\mu_2 Q_{21}^{(n-1)} + 3K_2 R_1^3 Q_{22}^{(n-1)} \right\} .$$

If $n = 2$ this equation yields

$$K = \frac{4\mu_2 K_2 (1 - c)}{4\mu_2 + 3K_2 c} , \tag{4.6}$$

where $c = (R_1/R_2)^3$ is the volume fraction of the pore. If $n = 3$ (4.5) reduces to

$$K = K_3 + \frac{H_3}{H_4} , \tag{4.7}$$

where

$$H_3 = 4\mu_2 (3K_2 + 4\mu_3)(K_2 - K_3) R_2^3 - -K_2 R_1^3 (3K_3 + 4\mu_3)(3K_3 + 4\mu_2),$$
$$H_4 = 4\mu_2 R_3^3 (3K_2 + 4\mu_3) + 12\mu_2 (K_3 - K_2) R_2^3 + 12K_2 \frac{R_1^3 R_3^3}{R_2^3} (\mu_3 - \mu_2) + 3K_2 R_1^3 (3K_3 + 4\mu_2) .$$

4.2. Shear modulus

Consider the case of a prescribed state of simple shear deformation at infinity: the requirement that the average strain of the n-layered composite sphere should be the same as the macroscopic strain imposed at infinity leads, making use of (2.31), to

$$D_{n+1} = 0. \tag{4.8}$$

Equation (4.8) gives the condition for determining the effective shear modulus $\mu = \mu_{n+1}$. The same procedure can be followed to determine the shear modulus. K and μ contributes only to the matrix $\mathbf{M}^{(n)}$, so that we can write $\mathbf{W}_{n+1}$ in the form:

$$\mathbf{W}_{n+1} = \mathbf{P}^{(n)}\mathbf{W}_2 = \mathbf{M}^{(n)} \prod_{j=n-1}^{2} \mathbf{M}^{(j)}\mathbf{W}_2 = \mathbf{M}^{(n)}\mathbf{P}^{(n-1)}\mathbf{W}_2 . \tag{4.9}$$

By substituting the expression (2.22) for $\mathbf{M}^{(n)}$, the condition $B_{n+1} = 0$ is equivalent to

$$\begin{aligned} &\frac{b_n}{7(1-2\nu_n)}\left[P_{21}^{(n-1)}A_2 + P_{22}^{(n-1)}B_2 + P_{23}^{(n-1)}C_2 + P_{24}^{(n-1)}D_2\right] \\ &\quad -\frac{20\alpha_n}{7R_n^7)}\left[P_{31}^{(n-1)}A_2 + P_{32}^{(n-1)}B_2 + P_{33}^{(n-1)}C_2 + P_{34}^{(n-1)}D_2\right] \\ &-\frac{12\alpha_n}{7(1-2\nu_n)R_n^5)}\left[P_{41}^{(n-1)}A_2 + P_{42}^{(n-1)}B_2 + P_{43}^{(n-1)}C_2 + P_{44}^{(n-1)}D_2\right] = 0, \end{aligned} \tag{4.10}$$

and the condition $D_{n+1} = 0$, to

$$\begin{aligned} &-5\alpha_n R_n^3(1-2\nu_n)\left[P_{11}^{(n-1)}A_2 + P_{12}^{(n-1)}B_2 + P_{13}^{(n-1)}C_2 + P_{14}^{(n-1)}D_2\right] \\ &\quad +21\alpha_n R_n^5\left[P_{21}^{(n-1)}A_2 + P_{22}^{(n-1)}B_2 + P_{23}^{(n-1)}C_2 + P_{24}^{(n-1)}D_2\right] \\ &\quad +2e_n\left[P_{41}^{(n-1)}A_2 + P_{42}^{(n-1)}B_2 + P_{43}^{(n-1)}C_2 + P_{44}^{(n-1)}D_2\right] = 0. \end{aligned} \tag{4.11}$$

Finally, making use of (2.24), the solution of the system made of (4.10) and (4.11) leads to a second order equation for μ:

$$A\left(\frac{\mu}{\mu_n}\right)^2 + B\left(\frac{\mu}{\mu_n}\right) + C = 0 \tag{4.12}$$

with:

$$\begin{aligned} A &= 5(1-2\nu_n)R_n^3 f_1(D_\mu, N_\mu) - 21R_n^5 f_2(D_\mu, N_\mu) + 4(4-5\nu_n)f_4(D_\mu, N_\mu), \\ B &= 5(1-2\nu_n)R_n^3 f_1(D_c - D_\mu, N_c - N_\mu) + 21R_n^5 f_2(D_\mu - D_c, N_\mu - N_c) \\ &\quad + 2f_4\left[2(4-5\nu_n)D_c + (7-5\nu_n)D_\mu, 2(4-5\nu_n)N_c + (7-5\nu_n)N_\mu\right], \\ C &= -5(1-2\nu_n)R_n^3 f_1(D_c, N_c) + 21R_n^5 f_2(D_c, N_c) + 2(7-5\nu_n)f_4(D_c, N_c); \end{aligned} \tag{4.13}$$

$$
\begin{aligned}
N_\mu &= 4(7-10\nu_n)R_n^7 f_2(1,0) + 20(1-2\nu_n)f_3(1,0) + 12R_n^2 f_4(1,0),\\
N_c &= (7+5\nu_n)R_n^7 f_2(1,0) - 20(1-2\nu_n)f_3(1,0) - 12R_n^2 f_4(1,0),\\
D_\mu &= 4(7-10\nu_n)R_n^7 f_2(0,-1) + 20(1-2\nu_n)f_3(0,-1) + 12R_n^2 f_4(0,-1),\\
D_c &= (7+5\nu_n)R_n^7 f_2(0,-1) - 20(1-2\nu_n)f_3(0,-1) - 12R_n^2 f_4(0,-1).
\end{aligned}
\tag{4.14}
$$

f_i denotes the following function:

$$
\begin{aligned}
f_i(x,y) = P_{i1}^{(n-1)}\left[84R_1^2 x + 8(7-5\nu_2)y\right] + 20(1-2\nu_2)xP_{i2}^{(n-1)}\\
+P_{i3}^{(n-1)}\left[(7+5\nu_2)R_1^7 x - 12R_1^5 y\right] + 20(1-2\nu_2)R_1^3 y P_{i4}^{(n-1)}.
\end{aligned}
\tag{4.15}
$$

If $n = 2$ A, B and C are given by:

$$
\begin{aligned}
A &= 2(4-5\nu_2)(7+5\nu_2)c^{\frac{10}{3}} - 25(\nu_2^2-7)c^{\frac{7}{3}} - 252c^{\frac{5}{3}}\\
&\quad +50(7-12\nu_2+8\nu_2^2)c + 4(7-10\nu_2)(7-5\nu_2),\\
B &= -(7+5\nu_2)(1-5\nu_2)c^{\frac{10}{3}} + 50(\nu_2^2-7)c^{\frac{7}{3}} + 504c^{\frac{5}{3}}\\
&\quad +150\nu_2(\nu_2-3)c + 3(15\nu_2-7)(7-5\nu_2),\\
C &= (5\nu_2-7)(7+5\nu_2)c^{\frac{10}{3}} - 25(\nu_2^2-7)c^{\frac{7}{3}} - 252c^{\frac{5}{3}}\\
&\quad -25(\nu_2^2-7)c - (7+5\nu_2)(7-5\nu_2).
\end{aligned}
\tag{4.16}
$$

It is worth noting that the foregoing results for K (4.5) and for μ (4.12) have also been derived by considering that, in the $(n+1)$-phase model proposed by HERVÉ and ZAOUI [8], the bulk and shear moduli of the innermost phase tend to zero.

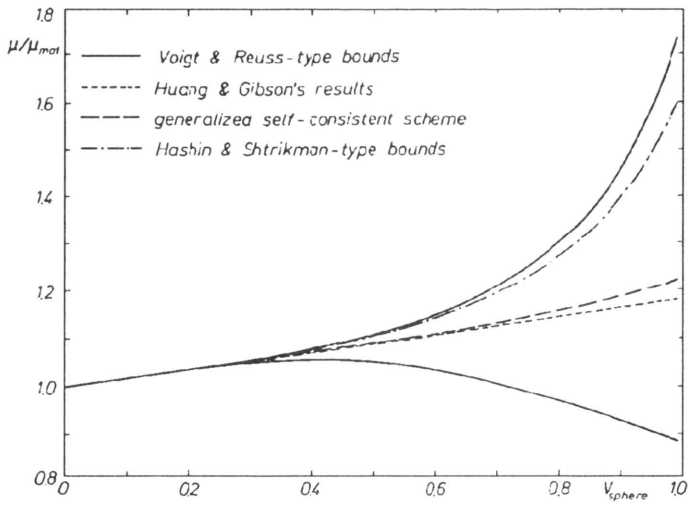

FIG. 2. Normalized shear modulus (μ/μ_{mat}) of a composite made of hollow spheres in a matrix versus the volume fraction of hollow spheres (phase 1 pore, $\nu_2 = \nu_3 = 0.3$, $\mu_2/\mu_3 = 10$, $R_1/R_2 = 0.9$).

Figure 2 shows comparison between all these different bounds and estimates in the case of a composite made of hollow spheres in a matrix. The approximation proposed by HUANG and GIBSON [12] consists in replacing the reference medium by the matrix and is valid for low void volume fraction only.

5. Experimental method

The dynamic properties of the spherical inclusion-type material are measured on rod-specimens using a forced resonant vibration technique. The forced resonant vibration measurement technique consists in applying a sinusoidal longitudinal or torsional inertial force at one end of the rod-specimen with a piezoelectric ceramic transducer. The vibration can be picked up by an equivalent sensing element attached at the other end of the rod. The transducer induces a longitudinal or a torsional force into the rod (cf. Fig. 3 for the different types of transducers).

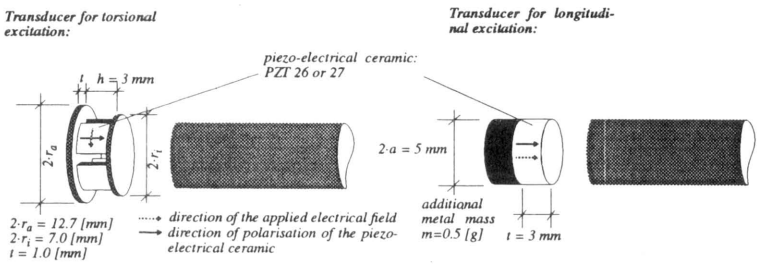

FIG. 3. The piezoelectric transducers.

The phase angle between the sending and sensing transducer signal is measured with a lock-in amplifier built in a closed loop control circuit. In order to get a constant phase angle of $\pi/2$, corresponding to the definition of resonance, the lock-in amplifier's phase sensitivity detector signal is integrated in a controller and fed back appropriately into the function generator (Fig. 4). This feedback loop provides an accurate measurement of the resonant frequency of ± 1 Hz within a frequency range of 5 to 150 kHz for the given specimens and the given setup.

Measurements of the longitudinal and torsional modes of the rods lead to a complete determination of the dynamic elastic or viscoelastic constants of the present isotropic material. In order to decrease a possible frequency-dependence of the properties of the specimens, comparative measurements are used. The results of the filled specimens are normalized by the ones of the unfilled specimens. The normalization renders the values comparable to theoretical results and nearly independent of the frequency. The Young's and shear moduli are directly extracted from the measured resonance frequency associated with the corresponding mode number, the geometry and density of the rod. The transducers are taken

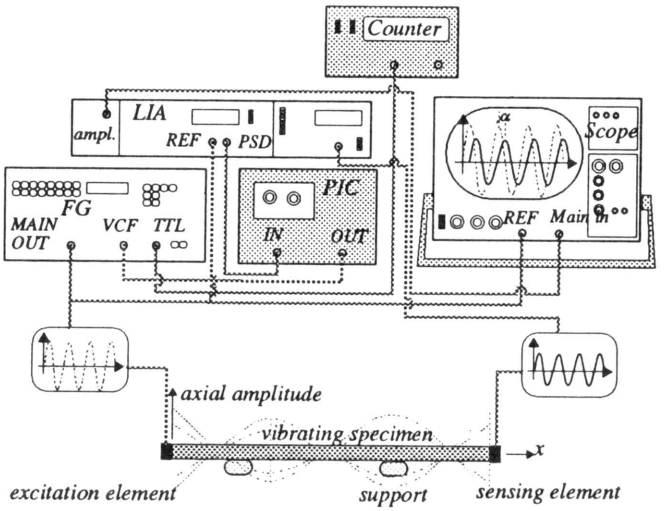

LIA: Lock-in amplifier
FG: Function Generator
PIC: Proportional-Integral Controller

FIG. 4. Experimental setup.

into account as rigid masses. Geometric dispersion that occurs at higher modes of the longitudinal vibration is considered using the Pochhammer-Chree's theory. For the normalized results, the dispersion correction is not necessary as far as the "compared rods" have the same geometry and approximately the same density.

Earlier static tension tests on polyester specimens revealed a non-negligible viscoelastic behaviour that affects a possible extraction of a Young's modulus from the test data. One has to define at which stress or strain levels the slope of the stress-strain-curve has to be taken to get a tangent or a secant modulus. In the case of glass microballoon-filled polyester, especially at higher concentrations, it is difficult to know at which stress levels damage occurs and the value of this damage (observations of fractured sections of the bar show that the greatest part of the microballoons lying in the fracture plane remain intact). The displacement ranges, at which the static tension tests operate, are supposed to cause debonding between glass particles and the matrix materials whereas the resonant vibration technique operates at displacement ranges from 10 to 100 nm (measured with a laser interferometer: Vibrometer Polytec OFV 300/OFV 2100), where smaller scattering of the results occurs. Using the described experimental setup, the modulus can be measured (for the present rod-specimens) at a precision of $1-2\%$ (cf. SAYIR [13]).

5.1. The rod-specimens and their dynamic behaviour

The microballoon-filled specimens were manufactured by mixing microballons into a polyester resin. The mixture is evacuated before adding the hardener. Then, the slurry has to be aspirated into a flexible polyethylene pipe fixed inside a glass tube. After hardening, the specimen is extracted from the PE-pipe and cured for

14 hours in an oven at a temperature of 80° C. Contents up to 46% of fly ash microballons could be incorporated (cf. Table 1).

Table 1. Description of the microballoon-filled specimens.

Volume concentration of voids in %	Matrix material	Geometry(1) of the specimen in mm^3	Density in kg/m^3
0	Polyester	674 $(\pi 5.72^2/4)$	1206
9	Polyester	681 $(\pi 5.72^2/4)$	1164
20	Polyester	675 $(\pi 5.73^2/4)$	1088
28	Polyester	676 $(\pi 5.75^2/4)$	1050
34	Polyester	676 $(\pi 5.78^2/4)$	1010
38	Polyester	673 $(\pi 5.77^2/4)$	992
40	Polyester	674 $(\pi 5.76^2/4)$	977
46	Polyester	665 $(\pi 5.78^2/4)$	932

(1) For a rectangular rod: $l \cdot a_0 \cdot b_0$; for a circular bar: $l \cdot \pi \cdot \frac{d_0^2}{4}$.

Observations under a light microscope and comparative estimations of the material densities reveal that a possible void content, that might have been introduced during the manufacturing process, should be insignificant. In a similar way, simply by stirring, voids are introduced into epoxy resin (Araldit F by Ciba-Geigy). The hardening and cure conditions for the mixture are mostly the same as those for polyester. Contents of spherical voids of 17% could be achieved. For higher concentrations, measurements have been done on rectangular bars of a commercialized PVC-based material (Kömatex 05 and 07 by Tettovil AG Kunststoffwerk CH-3432 Lüthelflüh). As it can be seen in Fig. 6, the pores are still closed and more or less spherical.

The dynamic reponse of all the matrix materials, the polyester, the epoxy and the PVC, is frequency-dependent. The major part of this viscoelastic behaviour can be described by the complex formulation of the moduli as a function of the frequency or the time (less important influences due to coupling effecs between the transducers and the rod are visible and affect the accuracy). Both are interrelated through the correspondence principle. From the dynamic measurements one gets the complex moduli in the frequency space. The complex Young's modulus

$$E^* = E_0(1 + i\phi) \tag{5.1}$$

is determined by using longitudinal vibrations, and the complex shear modulus by using torsional vibrations (measured only on the epoxy specimens). Figure 5 shows the typical evolution of the real part of the complex Young's modulus of

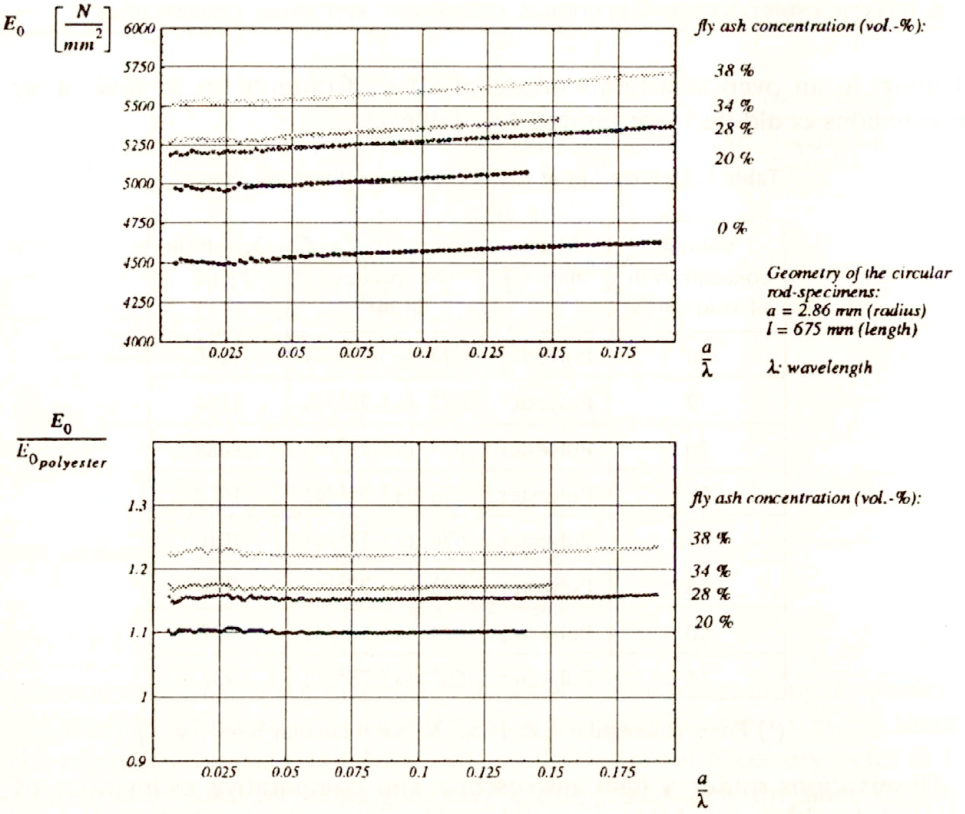

FIG. 5. The dynamic Young's modulus of a selection of Fly Ash-filled Polyester specimens versus a/λ.

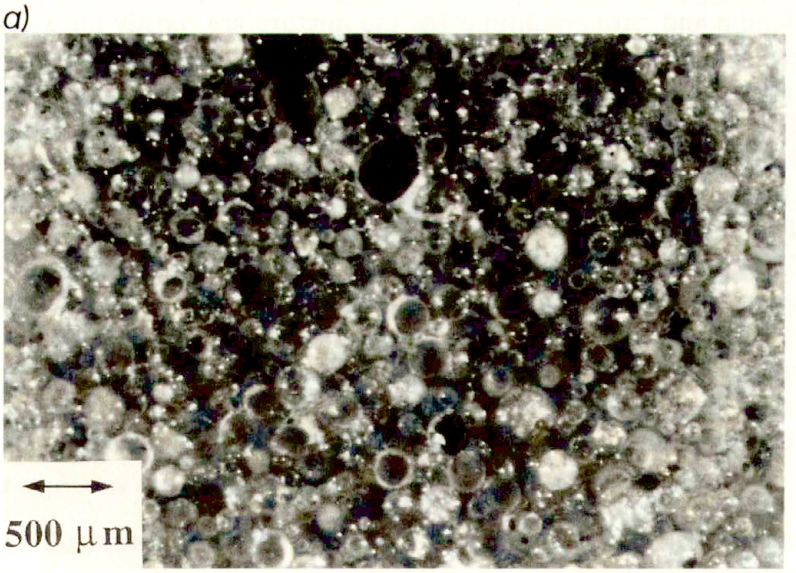

[FIG. 6]

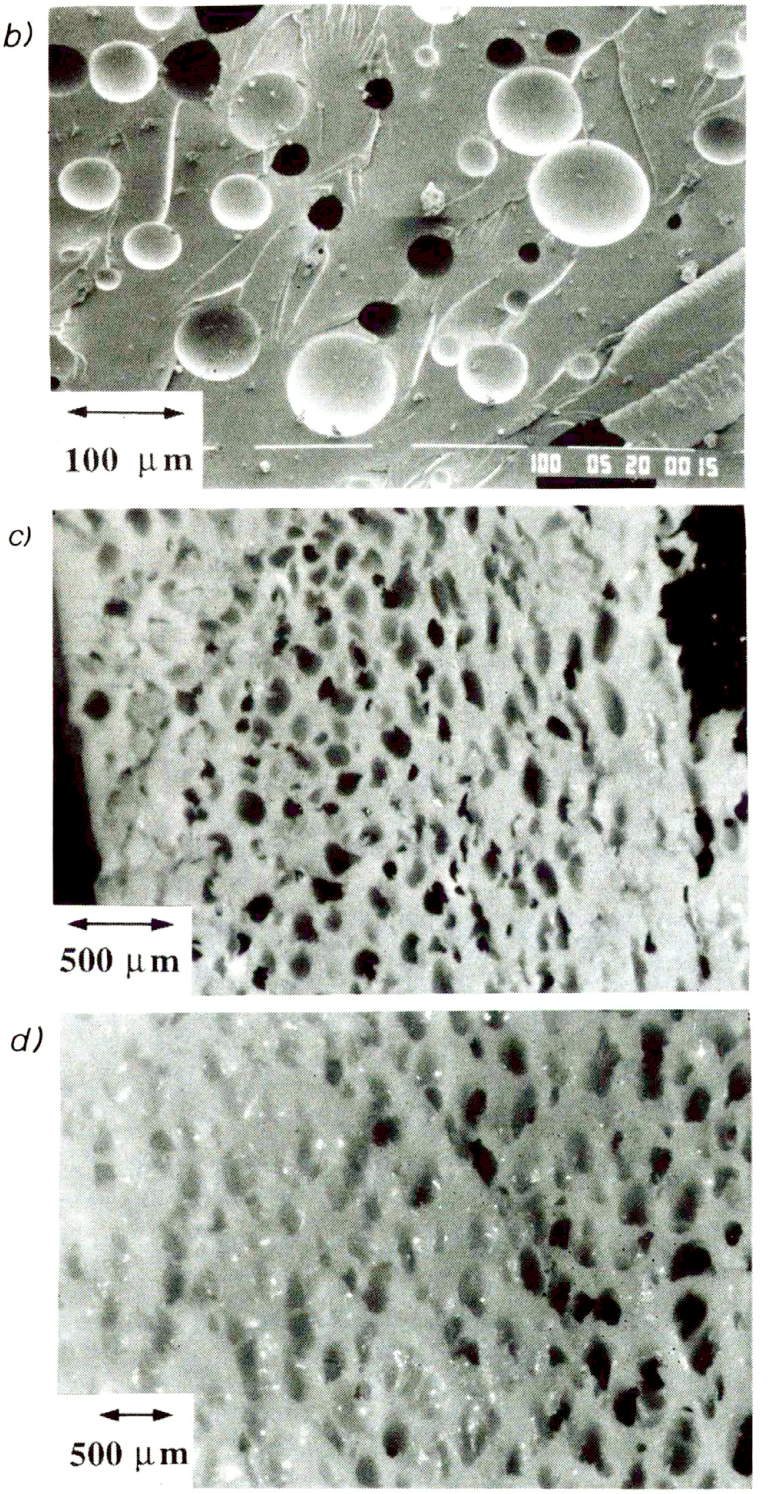

FIG. 6. Photographs of fractured cross-section of microballoon-filled Polyester (a), void-filled Epoxy (b) and cut surfaces of Kömatex with a porosity of 49% (c) and 61% (d).

the polyester filled with fly ash microballoons at different concentrations. The damping coefficient ϕ varies between 0.01 and 0.02. A similar frequency dependence is observed for the void-filled epoxy and a polyvinylchloride. The properties of the used materials are given in Table 2.

Table 2. Description of the spherical void-filled specimens.

Volume concentration of voids in %	Matrix material	Geometry of the specimen in mm^3	Density in kg/m^3
0	Epoxy	610 ($\pi 5.89^2/4$)	1171
6	Epoxy	608 ($\pi 5.91^2/4$)	1107
11	Epoxy	599 ($\pi 5.91^2/4$)	1044
16	Epoxy	399 ($\pi 5.91^2/4$)	979
0	PVC	294 (6.01 · 3.12)	1425
49	PVC (*Kömatex 07*)	303 (9.86 · 6.20)	714
61	PVC (*Kömatex 05*)	301 (10.30 · 9.86)	554

The final value of the relative Young's modulus for the given concentrations of inclusions is extracted from the data of the second diagram in Fig. 5 by taking the mean value of the relative modulus over the whole range of a/λ (this relative value is nearly independent of a/λ, the same kind of approach is used to determine the shear modulus). Those results are compared to theoretical predictions in the next section.

6. Comparison between experiments and predictions

6.1. Spherical void-filled materials

In order to consider this kind of materials over an important range of porosity, all the materials described in Table 2 have been studied. The normalized Young's modulus of these composite materials has been, on the one hand, calculated by means of (4.6) and (4.16) and on the other hand – measured by using the experimental method described hereabove (cf. Fig. 7). The Poisson's ratio of the matrix, used in the calculation, is 0.41 (mean value of the one of PVC and the one of Epoxy). Figure 7 shows that the values of the normalized Young's modulus predicted by the three-phase model and the experimental results are very close to each other, whereas the predictions from the classical self-consistent model are drastically different for higher porosities. These results show that the connectedness of the matrix is a major, primary morphological property which is taken into account quite well by the three-phase model.

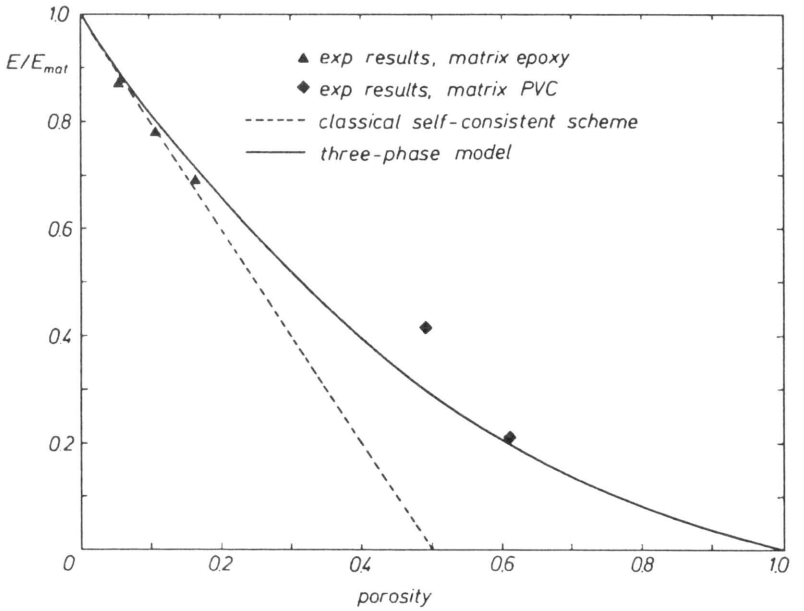

FIG. 7. Normalized Young's modulus E/E_{mat} of void-filled materials versus the porosity. ($\nu_{mat} = 0.41$).

6.2. Microballoon-filled materials

Consider now the hollow spheres composites processed by HUANG and GIBSON [12] made of hollow glass spheres ($\mu_2 = 28.5$ GPa, $\nu_1 = 0.23$) in a polyester resin ($E_3 = 4.89$ GPa, $\nu_3 = 0.4$). Their measured Young's moduli are plotted against the volume fraction of hollow spheres and compared with their approximation and the predictions of the Generalized Self-Consistent Scheme (G.S.C.S) (here our four-phase model) in Fig. 8. The poor agreement for volume fractions of hollow spheres higher than 0.08 cannot be explained only by the fact that the interactions between spheres have not been taken into account (the G.S.C.S takes them into account); more likely it is due to the fact that the experimental method, based on a tensile test, induces damage and then gives weaker values for the measured Young's moduli.

The normalized Young's moduli of the specimen described in Table 3 have been measured by the forced resonance method described above and plotted in Fig. 9. The G.S.C.S, used here as an inverse model, yields the value of the elastic Young's modulus of the Glass of the Fly ash microballoons (33.7 – 37.5 GPa, cf. Table 3). These results are in good agreement with the fact that the composition of this glass in mass % is (SiO_2 55 – 60%, porosity 10 – 20%, Al_2O_3 25 – 30%, Fe_2O_3 4 – 10%, CaO 0.2 – 0.6%, MgO 1 – 2%, Na_2O and Na_2O 0.5 – 4%), so that the Young's modulus of the used glass is weaker than the one of a "pure" glass (about 70 GPa).

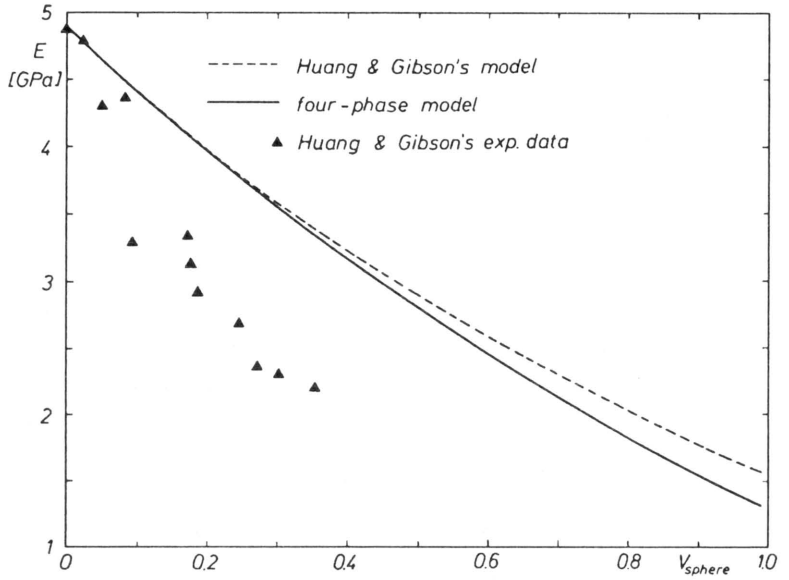

FIG. 8. Young's modulus of the composite versus the volume fraction of hollow spheres. ($\mu_2 = 28.5$ GPa, $\nu_2 = 0.23$, $E_3 = 4.89$ GPa, $\nu_3 = 0.4$).

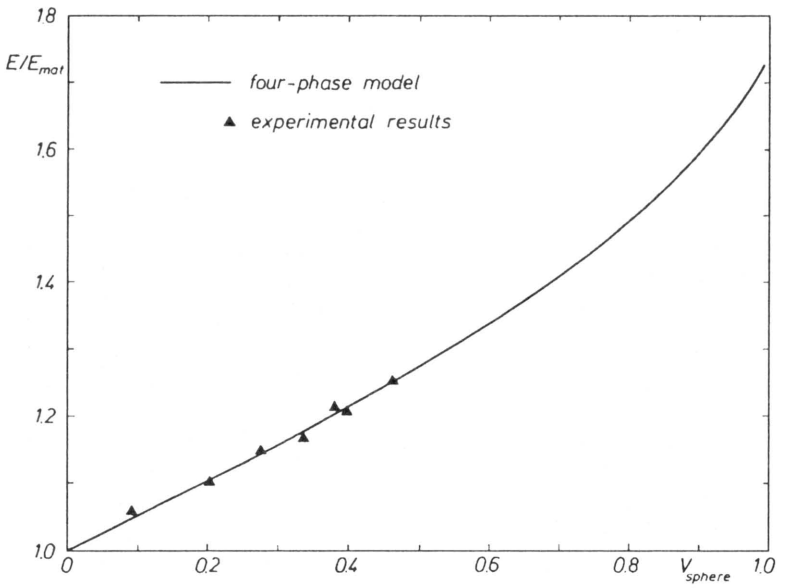

FIG. 9. Normalized Young's modulus E/E_{mat} of a composite made of hollow glass spheres in polyester versus the volume fraction of hollow spheres. ($E_2/E_3 = 7.5$, $\nu_2 = 0.23$, $\nu_3 = 0.37$).

Table 3. Properties of the matrix materials Polyester, Epoxy and PVC and properties of the spherical inclusions.

Property	Polyester([1])	Epoxy	PVC mineral filled	Fly ash microballoons([2])
Density	1220 ± 4 kg/m^3	1170 ± 4 kg/m^3	1400 ± 4 kg/m^3	$400 - 700$ ([3]) kg/m^3
Dynamic Young's modulus E(5-100kHz)	$4.5 - 5$ ([4]) GPa	$3.9 - 4.36$ ([5]) GPa	$3.7 - 4$ ([5]) GPa	$33.7 - 37.5$ ([6]) GPa
Poisson's ratio ν	0.37 ([7])	0.42 ([7])	0.40 ([8])	0.23 ([9])

([1]) Polyester 8039 MV Reichhold Chemie, admixtures to the resin: 1.33 MEKP50 and 0.3 accelerator C1 (quantities in mass-%).

([2]) PQ 1900 Potters Ballotini, wall thickness: 1/10 of diameter, mean diameter: 40% 150 - 250 μm, 60% 10 - 150μm. (taken from data sheet of PQ 1900).

([3]) taken from data sheet of PQ 1900.

([4]) Measured with the forced resonance method.

([5]) Measured with forced resonance method.

([6]) No data available (see comments in the text later).

([7]) Deduced from the measured Young's and shear modulus with forced resonance method (mean value).

([8]) Similar to polymethylmethacrylate.

([9]) Estimated (similar to glass).

7. Conclusion

The aim of this paper was to extend the field of possible application of the $(n+1)$-phase model to porous materials and to provide a method of bounding the effective moduli of Generalized Composite sphere assemblages where the inner phase is a pore. This extension has been performed by using the solution of the problem of a composite spherical inhomogeneity in an infinite matrix. This elementary solution could be used in more general models, for instance self-consistent mixtures of n-phase patterns for the case of different kinds of porous particles dispersed in the same continuous matrix. It is necessary to perform such models especially for the prediction of the shear modulus since there is no recursive algorithm for this modulus. The illustrative examples of Sec. 6 show that the Generalized Self-Consistent Scheme (G.S.C.S) predictions and the experimental results are close in the case of void-filled materials (cf. Fig. 7) and that, in the case of composites filled by hollow spheres, it is possible to predict by means of the G.S.C.S the behaviour of an unknown phase (cf. Fig. 8). Other extensions could be considered, for instance in order to yield refined estimates (in the line of [11]) of nonlinear behaviour, or to deal with composites with gradient of properties.

References

1. R. HILL, *A self-consistent mechanics of composite materials*, J. Mech. Phys. Solids, **13**, 213, 1965.
2. B. BUDIANSKY, *On the elastic moduli of some heterogeneous materials*, J. Mech. Phys. Solids, **13**, 223, 1965.
3. Z. HASHIN and SHTRIKMAN, *A variational approach to the theory of the elastic behavior of multiphase materials*, J. Mech. Phys. Solids, **11**, 127–140, 1963.
4. J.K. MACKENSIE, *The elastic constants of a solid containing spherical holes*, Proc. Roy. Soc., **63**, 2–11, 1950.
5. R.M. CHRISTENSEN and K.H. LO, *Solutions for effective shear properties in three-phase sphere and cylinder models*, J. Mech. Phys. Solids, **27**, 315–330, 1979. Erratum, **34**, 639, 1986.
6. Z. HASHIN, *The elastic moduli of heterogeneous materials*, J. Appl. Mech., **29**, 143–150, 1962.
7. É. HERVÉ, C. STOLZ and A. ZAOUI, *A propos de l'assemblage de sphères composites de Hashin*, Comptes-Rendus à l'Académie des Sciences, **313** (II), 857–862, 1991.
8. É. HERVÉ and A. ZAOUI, *n-layered inclusion-based micromechanical modelling*, Int. J. Engng. Sci., **31**, 1–10, 1993.
9. A.E.H. LOVE, *A treatise on the mathematical theory of elasticity*, Dover, New York 1944.
10. C. STOLZ and A. ZAOUI, *Analyse morphologique et approches variationnelles du comportement d'un milieu élastique hét'erogènes*, Comptes-Rendus à l'Académie des Sciences, **312** (II), 143–150, 1991.
11. É. HERVÉ and A. ZAOUI, *Modelling the effective behavior of nonlinear matrix-inclusion composites*, Eur. J. Mech., A/Solids, **9**, 6, 505–515, 1990.
12. J.S. HUANG and L.J. GIBSON, *Elastic moduli of a composite of hollow spheres in a matrix*, J. Mech. Phys. Solids, **41**, 1, 55–75, 1993.
13. M.B. SAYIR, F. PFÄFFLI and M. PARTL, *An experimental study on the elastodynamic behaviour of fibre-reinforced cement*, Composites, **22**, 1, p. 9, 1991.

LABORATOIRE DE MÉCANIQUE DES SOLIDES
ECOLE POLYTECHNIQUE, PALAISEAU CEDEX, FRANCE
and
INSTITUT FÜR MECHANIK, ZÜRICH, SUISSE.

Received November 22, 1994.

Arch. Mech., 47, 2, pp. 247–260, Warszawa 1995

Modelling the role of microstructure on the superplastic behaviour of a titanium alloy (*)

I. KATRAMADOS and F.P.E. DUNNE (MANCHESTER)

MULTIAXIAL CONSTITUTIVE EQUATIONS have been given for the superplastic deformation of a titanium alloy. The equations include a description of grain size kinetics, and their coupling with the deformation, hence enabling us to model the influence of microstructure on superplastic deformation. The equations have been implemented in a general purpose nonlinear finite element solver, and the model employed to investigate the suitability of a typical uniaxial test specimen for the generation of superplastic materials data. While the specimen design enables the establishment of uniform gauge length stress and strain fields, the strain rates obtained are not necessarily those that are desired, and may lead to the determination of stresses that are up to 20% in error. A modified displacement loading history has been developed to reduce the error. The effect of initially non-uniform distributions of grain sizes has been investigated. It is found that the non-uniformity of grain size leads to inhomogeneity of deformation, and that the material ductility decreases with increasing grain size range.

1. Introduction

SUPERPLASTIC FORMING is an important manufacturing process that is employed, for example, for the production of fan blades for aero-engines. An important feature of the process is its ability to enable very large strains to be achieved in the absence of necking, cavitation, and failure. It is therefore used in a range of applications requiring the forming of metal sheet at large strains, under tensile loading.

In order to facilitate superplastic behaviour in a material, it is necessary to prescribe and control the regimes of strain, strain rate and temperature applied [1]. The regimes of strain rate and temperature required for ideal superplastic behaviour may be rather narrowly defined. An additional feature that is recognised to be important in influencing superplastic material behaviour is the grain size [2]. Usually, a small ($< 10\,\mu$m), equi-axed grain size is required to facilitate grain boundary sliding, which is thought to be the predominant deformation mechanism of superplasticity occurring simultaneously with grain accommodation through diffusion-controlled processes [3]. However, in practice, it is usually not possible to obtain the desired completely uniform grain size, and quite considerable variations can be seen in the commercial grade titanium alloy Ti-6Al-4V [2], for example.

During the superplastic forming of engineering components, because of the geometrical and loading conditions, it is not possible to maintain uniform plastic

(*) Paper presented at 30th Polish Solid Mechanics Conference, Zakopane, September 5–9, 1994.

strain rates in the deforming material. The resulting stress fields are therefore also non-uniform. Regions of the material suffering the highest levels of strain may also be subject to local thinning (in the out-of-plane direction) and necking, leading possibly to rupture. Occurrences such as these are not permitted in components to be employed, for example, in critical, high performance applications. In order to enable the design of superplastic forming processes that could avoid the problems discussed above, it is necessary to establish constitutive equations for superplastic behaviour which, when implemented in appropriate finite element software, enable the simulation of superplastic forming.

In particular, however, it is necessary to have a predictive capability for the evolving microstructure of the superplastically deforming material and its influence on the thinning and necking processes, which limit the material's ductility. These issues have not been addressed before, and are therefore the subject of the present paper. Before considering the establishment of suitable constitutive equations, however, experimental procedures for the generation of material data, and the results of experimental test programmes relevant to the above are reviewed.

1.1. Material data for superplasticity in Ti-6Al-4V

Because of its importance as a structural alloy in aero-engine components, and because of the availability of material data in the literature, the titanium alloy Ti-6Al-4V is chosen for consideration in the present paper. GHOSH and HAMILTON [4] have carried out uniaxial tensile tests on specimens cut from Ti-6Al-4V sheet. The specimen employed is shown in Fig. 1. The ends of the specimen are gripped between two plates under load, imposed by means of pins, which pass through

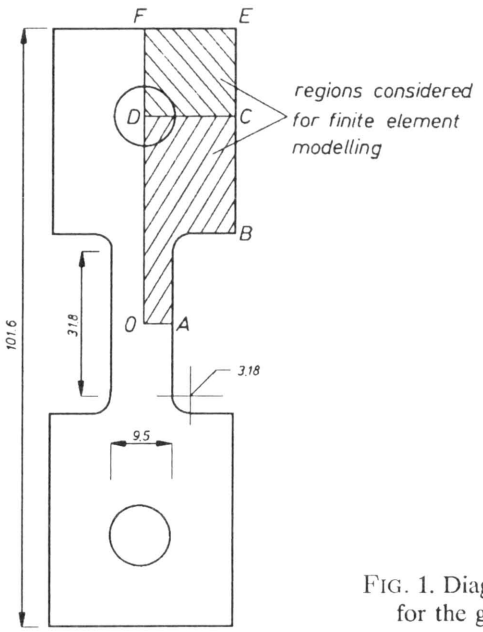

FIG. 1. Diagram showing a typical uniaxial specimen used for the generation of superplasticity materials data.

the specimen ends. The hole through which a pin passes is shown, for example, centred at D in Fig. 1. The axial load acting on the specimen is imposed partly through the pin, and partly through the gripping plates discussed above. Poor gripping may lead to the majority of the load being transmitted by the pin, the consequences of which are discussed later. In an attempt to ensure that the gauge length of the specimen undergoes constant strain rate loading, variable displacement control was employed by Ghosh and Hamilton which was calculated on the basis that only the specimen gauge length deforms; that is, the specimen ends are assumed to be rigid. The effectiveness of this approach, and validity of the assumption, are also addressed in a later section.

A sample of the experimental data obtained by GHOSH and HAMILTON [4] is shown by the symbols in Figs. 2a and b. The experimental true stress versus true strain data in Fig. 2a for the three strain rates $5.0 \times 10^{-5}s^{-1}$, $2.0 \times 10^{-4}s^{-1}$, and

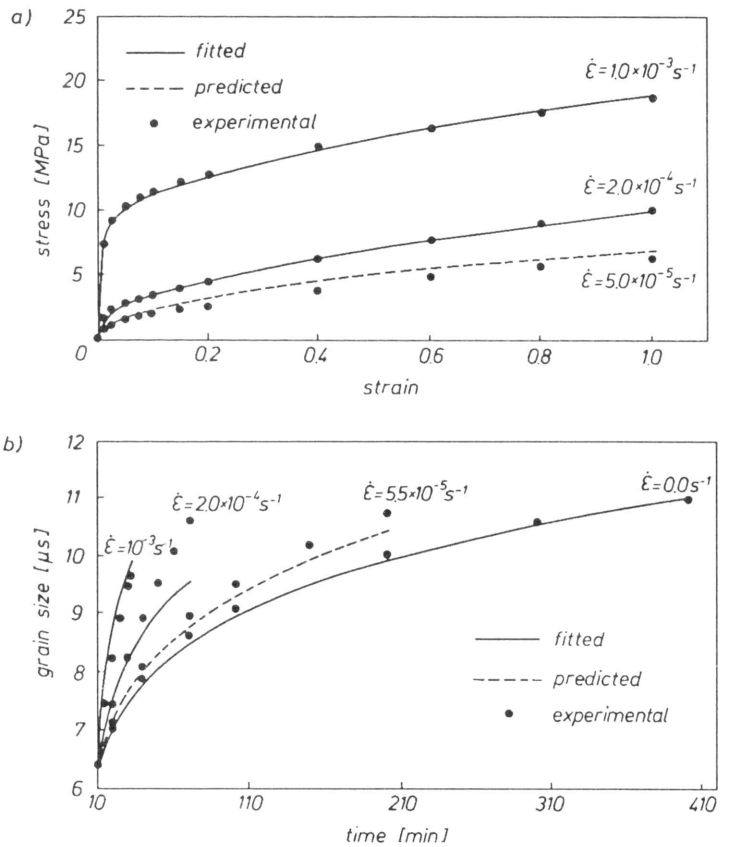

FIG. 2. a) Graph showing the computed and experimental true stress-strain curves for Ti-6Al-4V at 927°C with an initial grain size of 6.4 μm. b) Graph showing the computed and experimental variation of grain size with time for Ti-6Al-4V at 927°C, with an initial grain size of 6.4 μm. The symbols represent experimental data [4], and the lines – the predictions obtained from both the uniaxial constitutive equations, and the equations implemented in ABAQUS.

$1.0 \times 10^{-3}s^{-1}$ show that a pronounced strain rate effect exists for this material at 927°C. By carrying out microstructural examination, Ghosh and Hamilton were also able to identify the occurrence of significant grain growth, as shown in Fig. 2b by the symbols.

A considerably more detailed analysis of the evolution of microstructure during superplasticity has been carried out by PATON and HAMILTON [1]. In this work various batches of initially undeformed commercial grade titanium alloy Ti-6Al-4V were examined, and the microstructures were quantified in terms of the grain size distributions measured for each batch. While the mean grain size was reasonably uniform ($\sim$ 4.0 μm) across all batches, the variation of grain size within individual batches was significant, with grains ranging from less than 1 μm to above 20 μm in particular batches. Because the distributions of grain size are employed in the present paper in a later section, the results obtained by PATON and HAMILTON [1] are shown in Fig. 3. In subsequent tensile tests carried

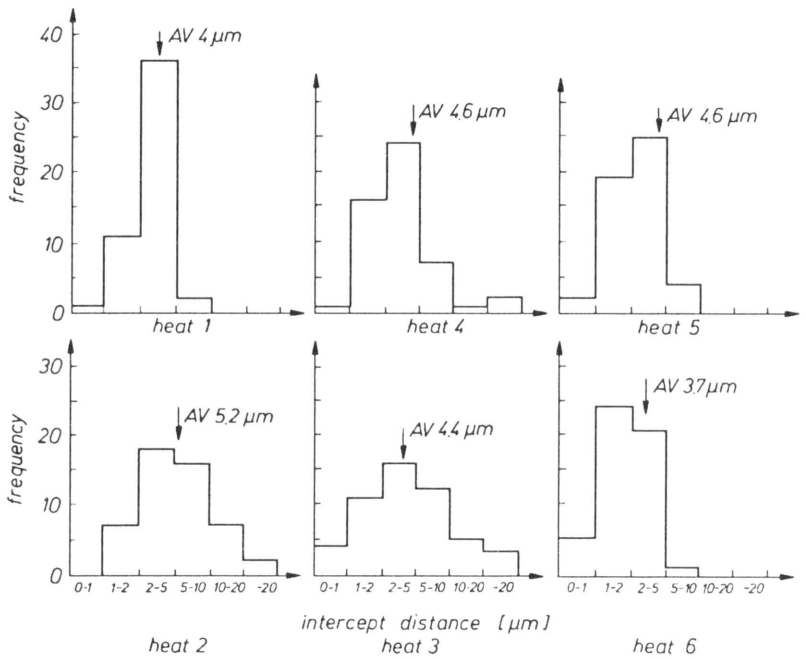

FIG. 3. Diagrams showing the experimentally obtained distributions of grain size for Ti-6Al-4V [2].

out on the material, the non-uniformity of the grain size was seen to be preserved by the material during superplastic deformation. In particular, however, the non-uniformity of the grain size was thought to lead to the significantly inhomogeneous deformation observed, which was characterised by the formation of multiple necks in the specimens, and widely varying local thickness [1]. In addition, the results indicated that an increase in the range of grain size, or an

increase in the maximum grain size, played a role in decreasing overall ductility of the material. The observations of PATON and HAMILTON [1] discussed above are considered later in the present paper, but from a computational and predictive standpoint, based on the constitutive equations reviewed in the following section.

1.2. Constitutive equations for the superplastic behaviour of Ti-6Al-4V

Uniaxial constitutive equations, and computational techniques for their determination, have been established by ZHOU and DUNNE [5] for the superplastic behaviour of Ti-6Al-4V. For the temperature and strain-rate range considered, the equations reflect the likelihood of the predominant deformation mechanisms occurring, being those of grain boundary sliding together with grain accommodation by dislocation creep. The processes assumed to lead to the material hardening seen are the grain growth and the hardening processes associated with dislocation creep. The mechanisms identified by the techniques discussed in [5] are in accord with those discussed by GHOSH and HAMILTON [6] and PAN and COCKS [3].

The constitutive equations have been shown to provide a good representation of the uniaxial behaviour of Ti-6Al-4V observed experimentally. In particular the equations successfully predict the evolution of grain size during superplastic deformation. The strain hardening observed to occur through grain growth [4] is also predicted correctly by a direct coupling of the grain size with the strain rate equation, and the true stress-true strain behaviour is therefore correctly represented over the broad range of strain rate considered. It is for the reasons given above that the constitutive equations of ZHOU and DUNNE [5] are employed in the present work, and are discussed further in a subsequent section.

1.3. Scope of the present paper

Because of the importance of inhomogeneous deformation leading to thinning and necking in industrial superplastic forming processes, this issue is addressed in the present paper. Inhomogeneous deformation is assumed to occur through the influence of spatial microstructural variations, in the absence of cavitation processes, for the titanium alloy Ti-6Al-4V in particular. Because of the need to provide a simulation capability for superplastic forming processes, the issues outlined above are addressed from a modelling and predictive standpoint.

In the following section, constitutive equations are discussed for the titanium alloy, which are implemented in an appropriate finite element solver, enabling the solution of initial value – boundary value problems. A typical uniaxial superplasticity test specimen is then examined using the constitutive equations for Ti-6Al-4V implemented in the finite element solver. The suitability of the specimen design for the generation of material data for superplasticity is evaluated. In the next section, the influence of microstructure on superplastic deformation is examined. In particular, the influence of initial grain size distribution and maximum grain size on the ductility of Ti-6Al-4V undergoing superplastic deformation

is modelled. Whenever possible, the results obtained are compared with the experimental data available in the literature.

2. Constitutive equations

An elastic-viscoplastic material model is employed for the titanium alloy considered. The importance of rate effects, and time-dependent processes that occur for the material over the range of temperature and strain rate necessitate the use of such a model. The mechanistic background to the development of the constitutive equations is discussed by ZHOU and DUNNE [5], but the equations are given here in multiaxial form as

$$
\begin{aligned}
\mathbf{D}_p &= \frac{3\alpha}{2d^{\mu}} \operatorname{Sinh} \beta [J(\boldsymbol{\sigma} - \mathbf{x}) - k] \frac{\boldsymbol{\sigma}' - \mathbf{x}'}{J(\boldsymbol{\sigma} - \mathbf{x})}, \\
\dot{\mathbf{x}} &= \frac{2}{3} C \mathbf{D}_p - \gamma \mathbf{x}\, \dot{p}\ , \\
\dot{d} &= (\alpha' + \beta'\, \dot{p}\ )\, / d^{\gamma'}, \\
\overset{\nabla}{\boldsymbol{\sigma}} &= E(\mathbf{D} - \mathbf{D}_p),
\end{aligned}
\tag{2.1}
$$

and where

$$
\begin{aligned}
\dot{p} &= \left(\frac{2}{3} \mathbf{D}_p : \mathbf{D}_p\right)^{1/2}, \\
J(\boldsymbol{\sigma} - \mathbf{x}) &= \left[\frac{2}{3} (\boldsymbol{\sigma}' - \mathbf{x}') : (\boldsymbol{\sigma}' - \mathbf{x}')\right]^{1/2}.
\end{aligned}
\tag{2.2}
$$

$\mathbf{D}_p$ is the rate of plastic deformation, d the grain size, $\boldsymbol{\sigma}$ the Cauchy stress (which may be considered since the elastic strains are infinitesimally small, making the Kirchhoff stress almost identical to the Cauchy stress), x an internal variable to describe hardening associated with dislocation creep and grain accommodation, and $\mathbf{D}$ the rate of total deformation. $\mathbf{E}$ is the elasticity tensor, and $\alpha, \beta, \kappa, \mu, C, \gamma, \alpha', \beta'$ and γ' are material-dependent parameters. The Jaumman rate of stress $\overset{\nabla}{\boldsymbol{\sigma}}$ is calculated from

$$
\dot{\boldsymbol{\sigma}} = \overset{\nabla}{\boldsymbol{\sigma}} + \mathbf{W}\boldsymbol{\sigma} + \boldsymbol{\sigma}\mathbf{W}^T \tag{2.3}
$$

in which $\mathbf{W}$ is the spin tensor. The constitutive equations have been implemented in the general purpose nonlinear finite element solver ABAQUS [6] by means of a user-defined subroutine, employing an explicit time integration scheme.

2.1. Model validation

In order to validate the model, the uniaxial, plane stress behaviour of Ti-6Al-4V was simulated under conditions of constant strain rate loading at a temperature of 927°C. The strain rates considered are those employed in the experiments of GHOSH and HAMILTON [4], and by ZHOU and DUNNE [5] in the independent numerical integration of the constitutive equations (2.1) and (2.2).

A simple four-element mesh was considered, employing eight-noded, plane stress, quadrilateral elements, and the results of the calculations are shown in Figs. 2a and 2b. The symbols shown in the figures represent the experimentally obtained data of GHOSH and HAMILTON [4], and the solid and broken lines are the predictions obtained by two methods: firstly, the uniaxial form of the constitutive equations given in (2.1) and (2.2) were integrated numerically and secondly, predictions were obtained using ABAQUS as discussed above. The broken line is used only to indicate that the experimental data corresponding to this strain rate was not employed in the fitting process to obtain the material parameters [5]. The finite element solutions obtained using the constitutive equations can be seen to be identical to those obtained from the independent numerical integration scheme which, in turn, can be seen to compare well with the experimentally obtained data. Having validated the implementation of the constitutive equations into ABAQUS, the model is employed to evaluate the suitability of a test specimen design for the generation of superplasticity material data. This is discussed in the following section.

3. Evaluation of test specimen design

The test specimen considered in the present work is that used by GHOSH and HAMILTON [4] for the generation of the superplasticity material data shown in Figs. 2a and 2b. The specimen is shown in Fig. 1.

It was mentioned in the Introduction that the axial loading can be transmitted to the specimen in two ways. The specimen ends are each gripped by means of two plates which are loaded in the direction normal to the specimen plane. The axial load is therefore transmitted to the specimen by shear at the interface between the loading plates and the specimen faces. However, because the uniaxial strains are large, the specimen consequently thins, and the frictional constraint, by which the shear force is transmitted may drop, therefore enabling some sliding of the loading plates relative to the specimen ends. As a result of this, some of the axial load carried by the specimen may be transmitted through the pins, which pass through holes in the specimen ends, shown in Fig. 1. Testing under these conditions leads to elongation of the pin holes, which is observed in experiments.

The exact conditions of loading vary from test to test, and are therefore difficult to model. Consequently, two extreme conditions are considered so that the bounds of the resulting specimen behaviour may be established. One extreme

assumes that the gripping is perfect so that no load is transmitted through the pin. This can be modelled by the imposition of displacement control on an appropriate horizontal boundary of the specimen which is chosen here as line CD in Fig. 1. The other extreme is that all the axial load is transferred through the pin, and that no load is transferred through the grips. This can be modelled by imposing displacement control on a rigid pin located in the hole in the end of the specimen. Through symmetry conditions, only a quadrant of the specimen can be considered, and for the two cases outlined above, the two regions modelled are shown in Fig. 1. The boundary conditions imposed in each case are shown in Figs. 4a and 4b. For the case of ideal gripping, the hole is not considered in the model, as shown in Fig. 4a. The prescribed displacement is imposed along the top boundary CD. In the case of the load being imposed entirely through the pin, the boundary conditions are shown in Fig. 4b. In this case, the hole in the specimen end is included, and the prescribed displacement is imposed by means of a rigid pin. The interacting surfaces between the specimen and the pin are assumed to be frictionless.

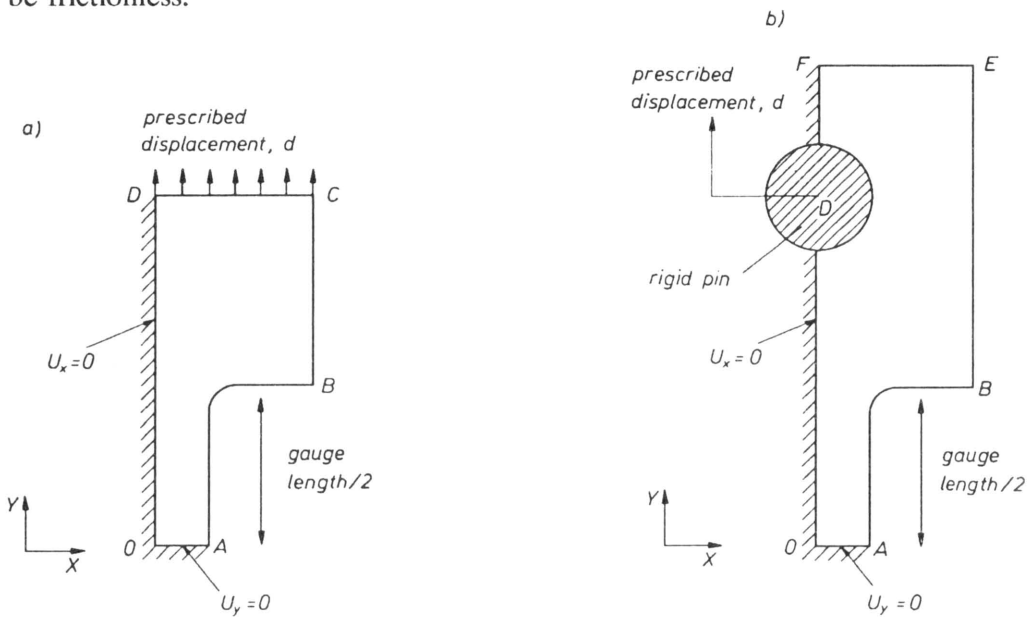

FIG. 4. Diagrams showing the models and boundary conditions employed for the finite element analysis of the uniaxial specimen shown in Fig. 1, a) without a loading pin, and b) with a loading pin.

3.1. Prescribed displacement

The prescribed displacement imposed is that specified by GHOSH and HAMILTON [4] in which the displacement rate was chosen in such a way that constant true strain rate could be maintained in the specimen gauge length. The assump-

tion made by Ghosh and Hamilton is that the specimen ends, because of their significantly increased width, are almost rigid in comparison to the gauge length material. The prescribed displacement, d, therefore varies with time in the following way:

$$d = l_0 \left(e^{\dot{\varepsilon} t} - 1 \right) \tag{3.1}$$

in which l_0 is half of the initial specimen gauge length, $\dot{\varepsilon}$ the required strain rate, and t the time. The results of the test simulations for each set of loading conditions are discussed in the following section.

3.2. Results of test simulations

For the case of each of the loading conditions shown in Fig. 4, a strain rate of $2.0 \times 10^{-4} s^{-1}$ was selected, and the specimens deformed up to a gauge length strain of approximately 1.1. Results, at this strain level, for the conditions shown in Fig. 4a are shown in Fig. 5.

The axial stresses (yy-stresses) generated at a gauge length strain of 1.1 are shown in Fig. 5a. The original, undeformed configurations of the specimens are shown by the broken black lines in the figures. The results show for this loading case that the stresses generated in the gauge length region are uniform, as desired. In addition, comparison of the stress achieved with that shown in Fig. 2a shows reasonable agreement, but that the stresses are approximately 20% higher, indicating that the stress-strain data obtained from tests carried out using this specimen are good approximations of the true material uniaxial, stress-strain behaviour. While some non-uniformity of stress can be seen in the region of the change of section of the specimen, the stresses in the important region of the gauge length at the specimen mid-point are uniform. The differences in stress observed are discussed later.

Figure 5b shows, for the same specimen in the same configuration, the predicted grain size. Again, while a non-uniform field of grain sizes exists in the specimen, the grain size in the important region of the gauge length at the specimen mid-point, can be seen to be uniform. For the purposes of this analysis, the initial grain size was assumed to be uniform throughout the specimen, and to have a value of 6.4 μm, which was measured by GHOSH and HAMILTON [4]. The final grain size in the gauge length region can be seen to be approximately 10.0 μm, which compares reasonably well with that shown in Fig. 2b, and calculated on the basis of true uniaxial loading conditions.

The results obtained based on analysis of the specimen loading conditions shown in Fig. 4b are shown in Fig. 6. Figure 6a shows the predicted axial (yy) strain field obtained for a gauge length strain of approximately 1.0. The strain in the region of the gauge length of the specimen can be seen to be uniform. The deformed configuration of the specimen shows that considerable elongation

of the originally circular hole has taken place, resulting in strains less than that desired in the gauge length region at any given time. This, in effect, results in strain rates in the gauge length region that are less than those desired and specified by the prescribed displacement control. Specimen gauge length strain rates are addressed in the next section. Elongation of the pin holes in the direction of loading has been observed in experiments on a considerable number of occasions. Figure 6b shows, for the same specimen configuration, the resulting grain sizes at the end of the deformation, again predicted on the basis of an initially uniform grain size of 6.4 μm. The final grain size in the gauge length region can be seen to be close to that obtained on the basis of the previous loading conditions.

3.3. Specimen gauge length strain rates

It is important to establish that the strain rates imposed on the gauge length material are in fact those that are required, and specified by controlling the variation of the specimen grip displacement with time. This is the case because of the very strong rate-dependence of the titanium alloy considered, which shows significant changes in stress level generated for a given level of strain, for comparatively small changes in strain rate. For example, Fig. 2a shows that for a given strain level, increasing the strain rate from $2.0 \times 10^{-4}s^{-1}$ to $1.0 \times 10^{-3}s^{-1}$, that is a factor of increase of 5, leads to an increase in the stress of 100%.

Strain rates were calculated for the specimen gauge length mid-point, on the basis of the loading conditions shown in Figs. 4a and 4b, and are plotted against the axial strain at the same point over the entire loading history of the specimen. The results are shown in Fig. 7, in which the calculated strain rates have been normalised by the desired constant strain rate, labelled the nominal strain rate, in the figure. Hence, a normalised strain rate of 1 indicates that the strain rate in the gauge length is equal to that desired. The results therefore show that a considerable variation in strain rate occurs. The strain rate varies from a minimum of approximately 0.5, to a maximum of 1.3 of the nominal strain rate.

It is anticipated that early in the loading history, the gauge length strain rates are likely to be less than the nominal strain rates, since it is assumed by Ghosh and Hamilton in choosing the loading conditions that there is no strain in the specimen ends. The effective gauge length of the specimen is therefore somewhat larger than assumed, leading to reduced normalised strain rates. As the deformation continues, however, the normalised strain rate can be seen to increase for both sets of loading conditions, and at a strain of approximately 0.75, it exceeds unity; that is, the gauge length strain rate has exceeded that originally specified as the constant strain rate. Because the loading is displacement-controlled, this is only possible with a reduction in the effective gauge length. Examination of Figs. 6a and 6b reveals how this takes place.

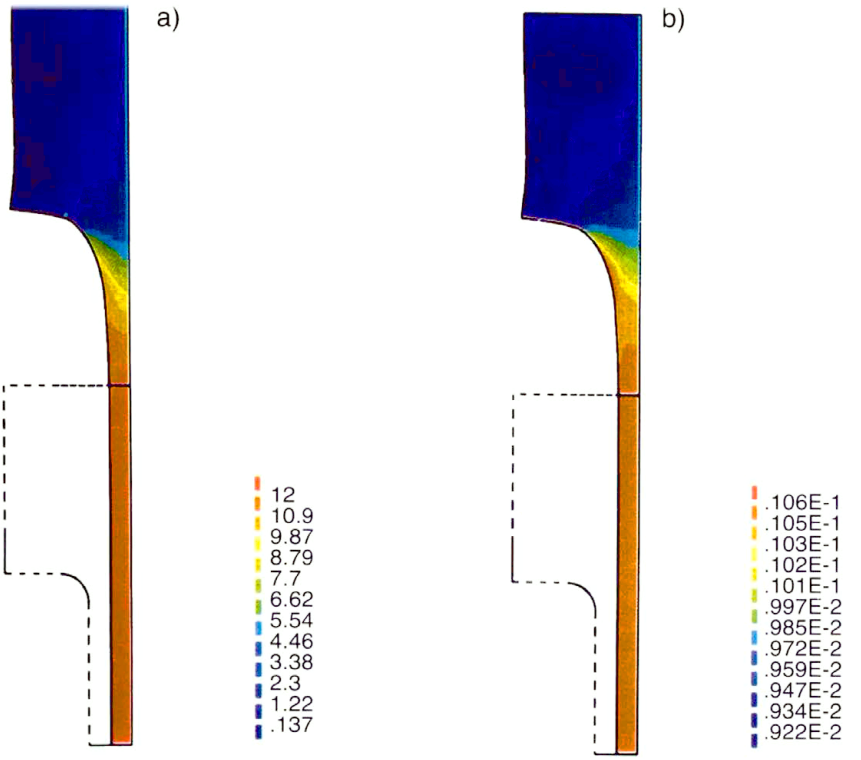

FIG. 5. Predicted field variations of (a) loading direction stress, and (b) grain size for the loading conditions shown in Fig. 4a, for a bulk gauge length strain of approximately 1.1.

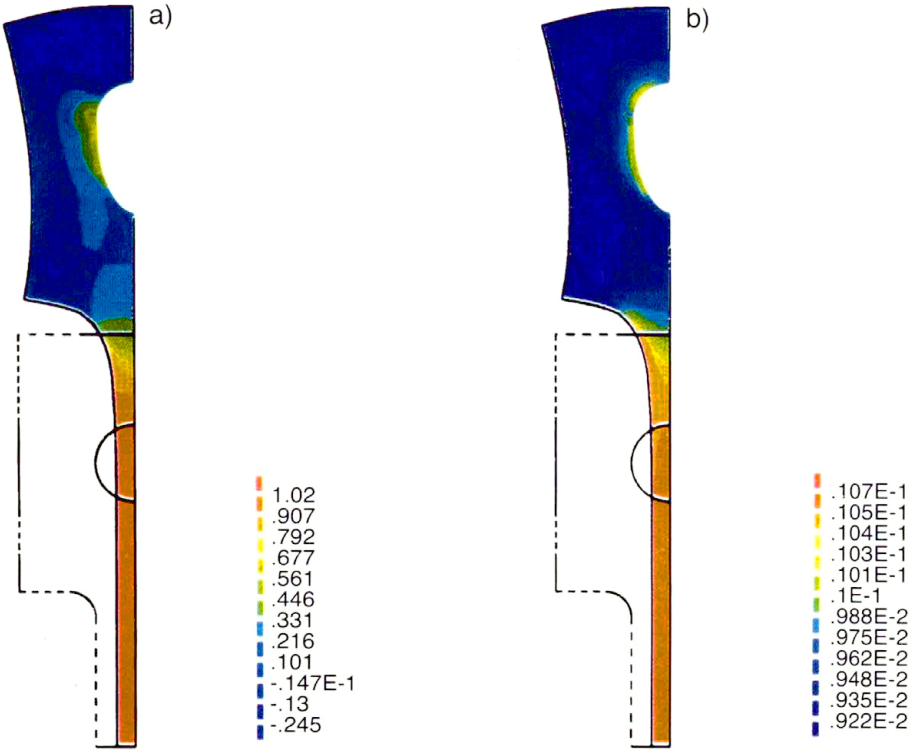

FIG. 6. Predicted field variations of (a) loading direction strain, and (b) grain size for the loading conditions shown in Fig. 4b for a bulk gauge length strain of approximately 1.0.

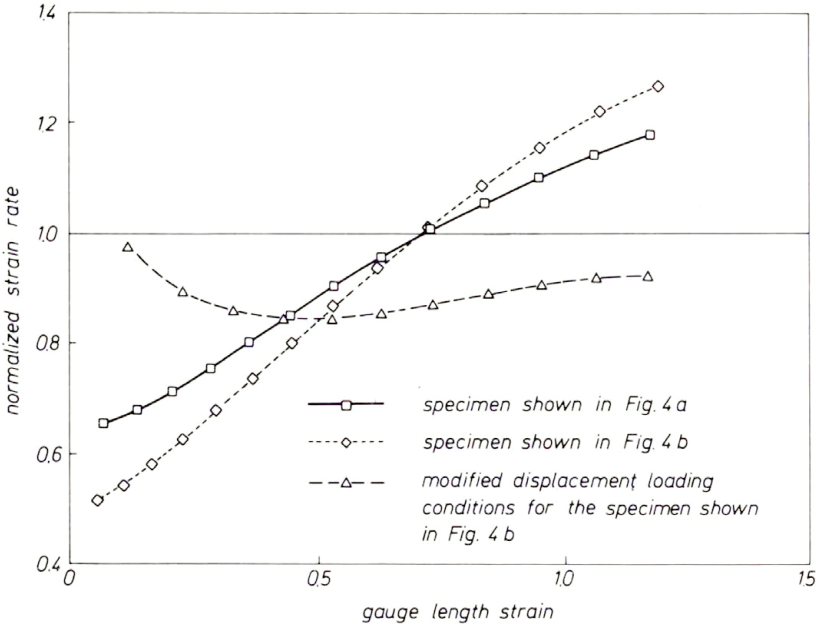

FIG. 7. Graph showing the variation of specimen gauge length normalised strain rate with gauge length strain for the loading conditions shown in Figs. 4a and 4b for nominal strain rate $2.0 \times 10^{-4}s^{-1}$.

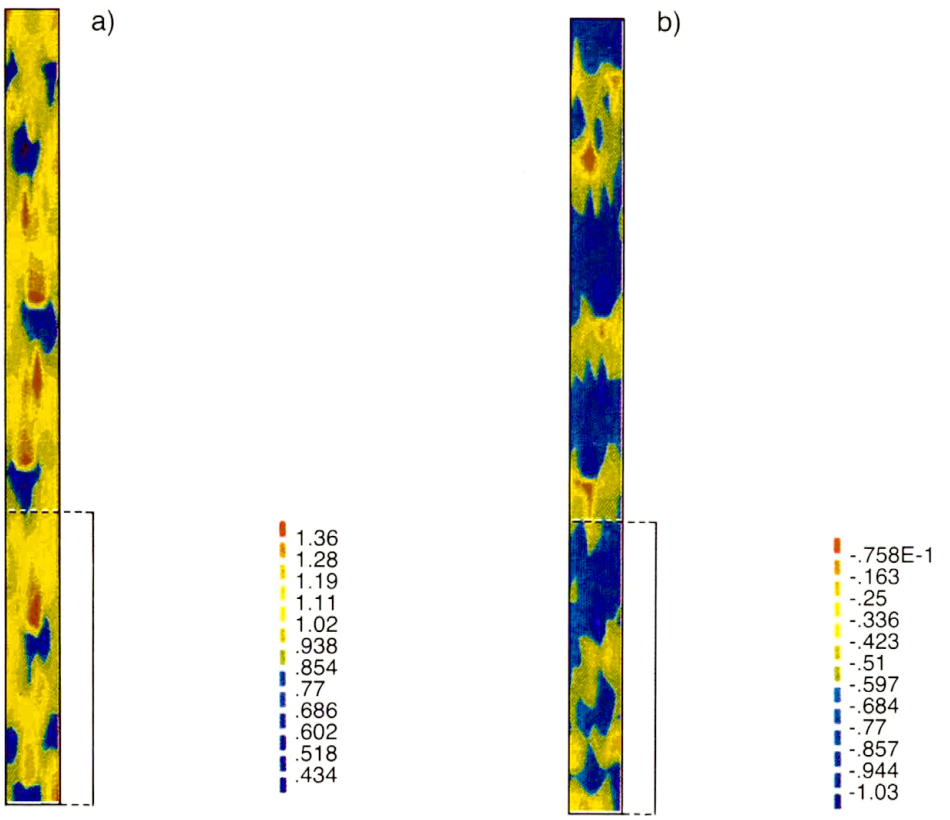

FIG. 8. Predicted field variations of the loading direction strain (a), and the out of plane strain (b) for a cell model with initially non-uniform microstructure.

As the deformation proceeds in the gauge length, the average grain size increases, leading to material hardening. However, a region of the specimen can be seen in Fig. 6b in which a smaller grain size exists, permitting further deformation to take place preferentially, and at a higher rate than in the gauge length. This ultimately enables deformation to take place preferentially within an effective gauge length which is smaller than the true gauge length, therefore leading to nominal strain rates greater than 1.0.

Figure 7 also demonstrates that for the loading conditions shown in Fig. 4b, that is, for the case in which load is transferred through the pin, considerably larger variations in strain rate arise than for the conditions shown in Fig. 4a, as would be expected.

3.4. Discussion of results

The results of the analyses demonstrate that uniform states of strain, stress, and grain size are generated within the gauge length region near the mid-point of the specimen. The strain, stress and grain size measurements obtained experimentally from such a specimen design can therefore be considered to be representative for uniaxial loading. The uniformity of the fields was not influenced by the two loading types considered, therefore indicating that in this context, the method of loading is not a critical feature. This is not necessarily the case, however, when considering gauge length strain rates, and hence stress levels, which can be influenced significantly by the loading conditions.

The results of the analyses have shown that the specimen gauge length strain rate is not constant during a test, but varies within approximately $\pm 35\%$ of the desired strain rate, even with compensated prescribed displacement control. For most applications, it is unlikely that such a variation in strain rate would be of major concern, since its influence on stress level may not be all that significant. However, the implication of the result is that for the material considered, the stress levels determined from a test may be in error by as much as $\pm 20\%$.

In order to reduce the variation of gauge length strain rate obtained in a test, an effective gauge length has been introduced, which is assumed to vary with deformation. The prescribed displacement loading given in Eq. (3.1) is therefore re-written as

$$d = l_e \left(e^{\dot{\varepsilon}} - 1 \right), \tag{3.2}$$

in which l_e, the effective gauge length, is written as a function of a specified specimen strain, ε_s, as

$$l_e = l_0/(a + b\varepsilon_s), \tag{3.3}$$

in which a and b are constants. For the pinned specimen, the specimen strain is chosen to be the loading direction strain at a point adjacent to the pin, and a

and b take the values 0.451 and 0.424 respectively. The resulting gauge length strain rates obtained are shown in Fig. 7, in which a considerable improvement over those discussed earlier can be seen. The appropriate selection of the effective gauge length, l_e, through computational studies, can therefore provide a corrected prescribed displacement to enable a more constant gauge length strain rate to be achieved.

4. Modelling the influence of microstructure on superplastic deformation

The results of the previous section have shown that in the testing of a superplastic material, with the specimen design shown in Fig. 1, the strain and stress fields developed in the gauge length region of the specimen are uniform. However, this is based on the assumption that a uniform microstructure exists initially, and this has been shown not to be the case in the experimental work of PATON and HAMILTON [2]. The distributions of grain sizes observed in several batches of Ti-6Al-4V are shown in Fig. 3. The existence of an initial non-uniform distribution of grain size may contribute to the development of inhomogeneous deformation fields, which are characterised by the development of multiple necks and specimen thinning. The objective, in the present section, is to model the influence of initial non-uniform microstructure and to investigate its influence on subsequent superplastic behaviour. In particular, by modelling experimentally the observed non-uniform grain size distributions, it is investigated whether such distributions can be predicted to lead to significant inhomogeneity of deformation.

4.1. Finite element model

In earlier sections, it has been shown that the stress and strain fields established in the specimen gauge length regions, are uniform. In the present section, therefore, in which non-uniform microstructures are examined, the loading conditions considered are uniform. In place of uniform grain size distributions considered earlier, the grain size distributions given in Fig. 3 are assumed for the initial state. The initial microstructure is defined in the finite element model by assigning a particular grain size to each element in turn, in such a way that three of the distributions of grain sizes shown in Fig. 3 were reproduced (heats 3, 4 and 5). In addition, further microstructures were created by increasing the maximum grain sizes shown in Fig. 3 up to a maximum of 40 μm.

In the model considered, the unit analysed represents a repeating cell within an infinite body, so that all the cell boundaries are axes of symmetry, and remain straight during deformation. The top boundary of the cell is subject to prescribed displacement which leads to a constant cell true strain rate of $2.0 \times 10^{-4} s^{-1}$, which is imposed until the overall cell strain is approximately 1.0. Typical results obtained from the analyses are shown in Fig. 8.

Figure 8a shows the strain field obtained in the loading direction, and Fig. 8b the out-of-plane strain. The figures show the level of inhomogeneity obtained for an initial grain size range of 1 to 20 μm, which arises simply through the enhanced strain hardening provided by the initially larger grains. The range of loading direction strain observed varies between 0.157 and 1.31, showing that non-uniform microstructures can lead to considerable inhomogeneity of deformation. While grain growth does take place during the deformation, it occurs predominantly for the initially smaller grains, and at the completion of the loading, considerable variation of grain size still exists. This is in keeping with the experimental observations of PATON and HAMILTON [2].

4.2. Ductility

In order to investigate the influence of initial non-uniform microstructure on overall material ductility, the ductility for the cell model discussed above has been defined in the following way. When the maximum local out-of-plane strain for the cell model has achieved a value of 0.7, the corresponding cell overall axial strain is calculated and is considered to be the material ductility. Ductilities have been calculated in this way for each of the initial microstructures considered, each of which has a given maximum grain size, and a corresponding grain size range. The results of these calculations are shown in Fig. 9, in which the calculated ductility is plotted against the maximum grain size. The figure shows that for smaller maximum grain sizes (and hence ranges of grain size), larger ductilities are achieved which decrease with increasing grain size range. Similar trends are observed in experimental tests. In addition, for increasing grain size range, the predicted, normalised ductility appears to be stabilising.

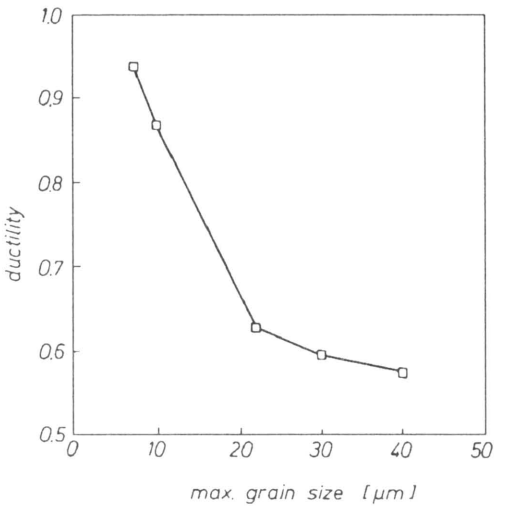

FIG. 9. Graph showing the variation of normalised ductility with maximum grain size for the cell model with various initial non-uniform microstructures.

5. Conclusions

Multiaxial constitutive equations for superplasticity have been implemented in a finite element solver, and the model has been employed to investigate the suitability of a uniaxial test piece for the generation of material data. While the specimen design enables the establishment of stress and strain fields that are uniform in the gauge length region, the strain rates obtained in this region are not necessarily those that are desired, and may lead to the measurement of stresses that are up to $\pm 20\%$ in error.

The effect of initially non-uniform distributions of grain size has been investigated. It is found that the material ductility decreases with increasing grain size range, and that the non-uniformity of grain size leads to inhomogeneity of deformation. Non-uniformity of grain size in superplastically deformed materials is likely therefore, to be a contributing factor in the development of thinning and necking observed in superplastic forming processes.

References

1. J. PILLING and N. RIDLEY, *Superplasticity in crystalline solids*, Institute of Metals, 1989.
2. N.E. PATON and C.H. HAMILTON, *Microstructural influences on superplasticity in* Ti-6Al-4V, Met. Trans. A., **10A**, 241–250, February 1979.
3. J. PAN and A.C.F. COCKS, *Computer simulation of superplastic deformation*, Comp. Mats. Sci., **1**, 95–109, 1993.
4. A.K. GHOSH and C.H. HAMILTON, *Mechanical behaviour and hardening characteristics of a superplastic* Ti-6Al-4V, Met. Trans. A., **10A**, 699–706, June, 1979.
5. M. ZHOU and F.P.E. DUNNE, *Mechanisms-based constitutive equations for high temperature titanium alloys*, Internal Report DMM.93.11, Dept. of Mech. Eng., UMIST, UK 1993.
6. HIBBITT, KARLSSON and SORENSON, *ABAQUS user manuals*, ver. 5.2, HKS Inc., Pawtucket, Rhode Island, Providence, USA 1993.

DEPARTMENT OF MECHANICAL ENGINEERING
UNIVERSITY OF MANCHESTER
INSTITUTE OF SCIENCE AND TECHNOLOGY (UMIST), MANCHESTER, UK.

Received December 16, 1994.

Arch. Mech., 47, 2, pp. 261–279, Warszawa 1995

Investigation of a high accuracy uni-axial creep testpiece with slit extensometer ridges (*)

Z. L. KOWALEWSKI (WARSZAWA),

J. LIN and D.R. HAYHURST (MANCHESTER)

THE ACCURATE DETECTION AND MEASUREMENT of strain at high temperature are regarded as the most difficult aspects in many types of material property measurements. In order to detect the creep extension within the measured gauge length by the use of an extensometer to a suitable degree of accuracy, the uni-axial creep testpiece must be machined to the appropriate standards. The paper evaluates both experimentally and theoretically a new design of the uni-axial creep testpiece with slit extensometer ridges to improve the accuracy of strain measurement during creep testing. The results of experiments are reported on slitted and unslitted ridged testpieces; and they are used together with theoretical studies to evaluate the effectiveness of the slitted ridged testpiece design for different specimen gauge lengths. A physically-based constitutive equation set which utilises two damage parameters was used to model tertiary creep behaviour. It has been shown that the distribution of stress in the gauge area for the slitted ridged testpiece is more uniform than for the unslitted one, and how the accuracy of the creep strain measurement is, as a consequence, greatly improved.

1. Introduction

THE UNIAXIAL CREEP testpiece is most often used to test the creep behaviour of many engineering materials. Its successful design involves several factors, one of the most difficult being the attachment of the extensometer to a fixed gauge length in such way that the measured material properties are not affected. One of the widely used high-temperature strain measurements techniques used to examine creep process in laboratory tests utilises ridged extensometer testpieces and mechanical extensometers. The ridges on the testpiece are machined to identify the gauge length over which strain is to be measured. Mechanical extensometers are fitted to these ridges which are used to transfer the gauge length displacements occuring during creep test to a location outside of the high-temperature furnace where linear voltage displacement transducers can precisely measure displacement at ambient temperature. The measured displacements are then used to compute the variation of strain with time. Since the extensometer ridges influence the deformation process due to the circumferential reinforcement of the testpiece, there is a need to limit such effect as much as possible. There are several ways to improve the accuracy of the strain measurement for the testpiece: (i) to increase the gauge length [1]; (ii) to decrease the radius connecting the

(*) Paper presented at 30th Polish Solid Mechanics Conference, Zakopane, September 5–9, 1994.

parallel gauge length section to the extensometer ridges [1]; (iii) to release the constraints in the hoop direction of the ridges by removing some of the material from the ridges [2, 3, 4]. Since in the first case buckling problems may occur, and in the second, premature failure of the material may occur at the transition regions, the third technique is recommended. Although the creep testpiece design which has slitted extensometer ridges is complex in geometry, its manufacture can easily be achieved by the use of modern numerically controlled manufacturing machines.

The effect of circumferential reinforcement of the testpiece due to the extensometer ridges has been studied experimentally by OHASHI *et al.* [5] in thin-walled tubular specimens subjected to internal pressure. Their experimental programme required extremly high accuracy of the strain measurement technique, since they investigated secondary effects occurring in the plastic deformation. They have shown that the unslitted ridged thin-walled tubular testpieces typically used in the plasticity tests are not suitable for experiments involving internal pressure, because the circumferential strain in the axial direction between the extensometer ridges cannot be uniform due to effects of the circumferential ridges and the thickness variations between the ridges and the shanks. The distributions of increases in diameter between the extensometer ridges occurring under internal pressure were examined with the use of mechanical extensometer for: the specimens without extensometer ridges; the unslitted ridged specimens; and the specimens in which the geometry of the extensometer ridge was varied, as shown in Fig. 1. The external diameters were measured on the 50 [mm] gauge length at different distances from the centre of the specimen. The investigations proved that the radial expansion between extensometer ridges for specimen *B*, Fig. 1, was more uniform in comparison with the unslitted ridged specimen; however, the effect of the ridges was still significant. This effect was markedly reduced for specimen *A*, Fig. 1, on which only those parts of the ridges necessary to hold a device for measuring displacements were left. The results for this specimen were close to those for the specimen without ridges.

LIN *et al.* [2, 3] have considered this problem theoretically and have shown how the errors in measured creep strains can be reduced. Results obtained by LIN *et al.* [2, 3] have been confirmed experimentally by KOWALEWSKI *et al.* [4], and these data will be summarized in this report.

The objective of this research is to investigate by both experiment and computation the creep-rupture behaviour, lifetime and accuracy of the strain measurement for the proposed testpiece with slit extensometer ridges. The results of experiments are reported which have been carried out on unslitted and slitted testpieces with different gauge lengths. The experimental results are compared with those determined theoretically from the knowledge of the uni-axial constitutive equations, and the multi-axial rupture criterion of the material.

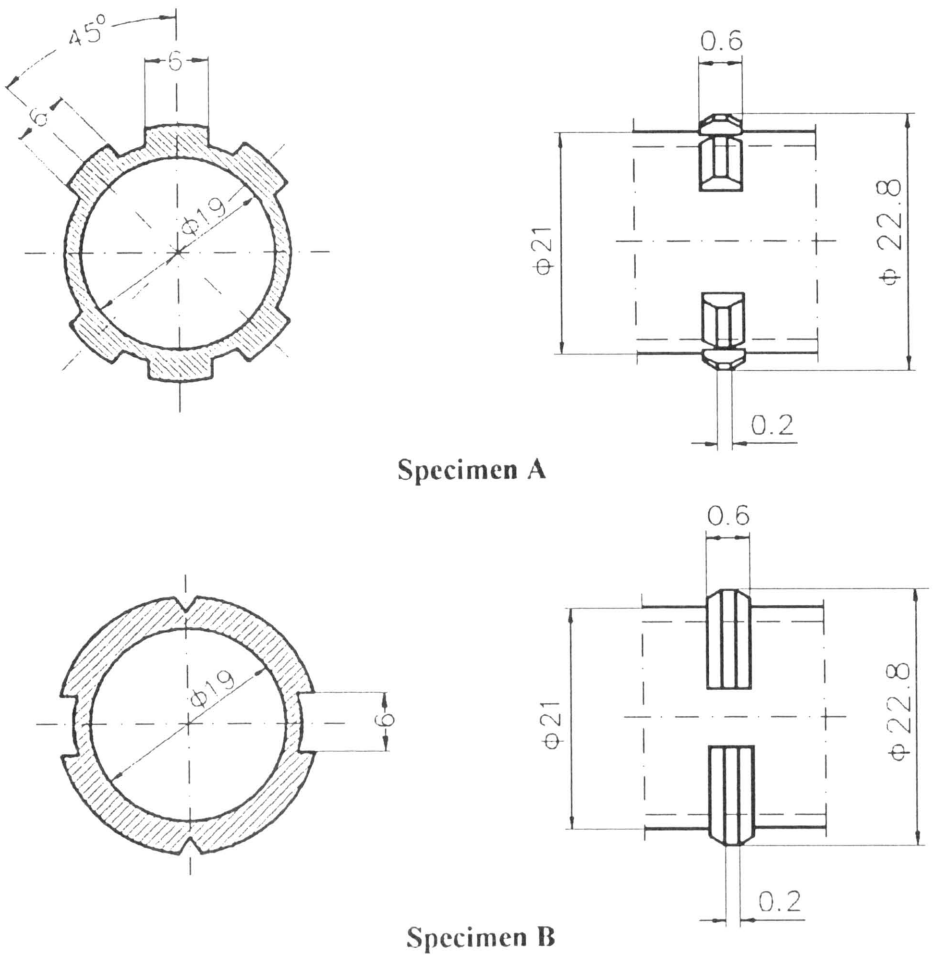

FIG. 1. Engineering drawing of the slitted extensometer ridges on the thin-walled tubular testpieces used by OHASHI *et al.*, [5].

2. Material, testpiece and tensile creep testing equipment

A precipitation hardened aluminium-magnesium-silicon alloy manufactured to British Standard Specification B.S. 1472 has been selected for the experimental investigation.

The creep tension testpieces were manufactured to the specifications given in the engineering drawing of Fig. 2a. An engineering drawing of the extensometer ridge without slits is shown in Fig. 2b, whereas the slitted one is given in Fig. 2c. The extensometer ridges cause non-uniformity of the stress state close to their location. In order to reduce this effect, twenty-four slits were machined into each extensometer ridge and, as a consequence, the slitted extensometer ridges were subjected approximately to plane stress conditions [3].

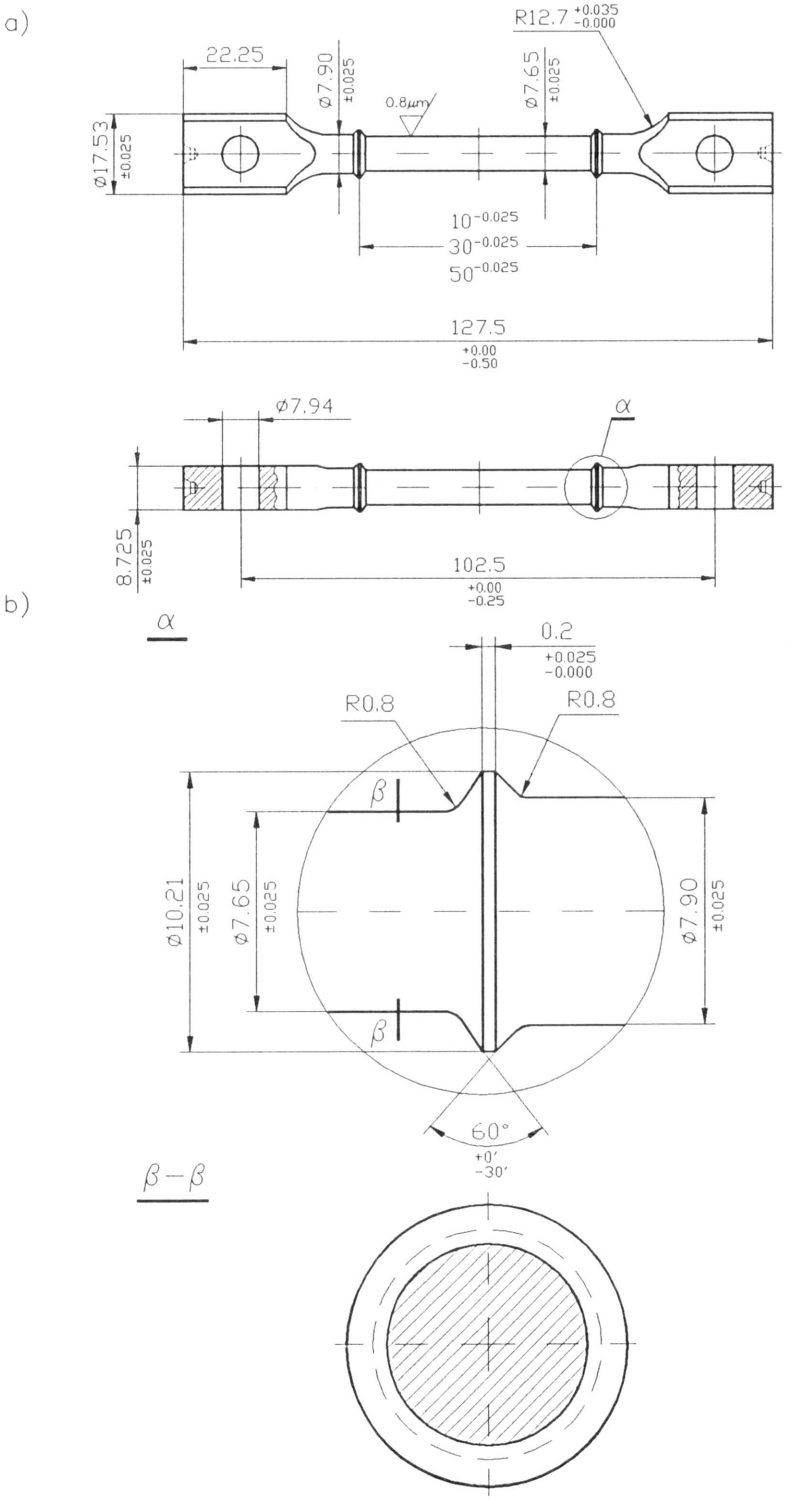

[FIG. 2]

[264]

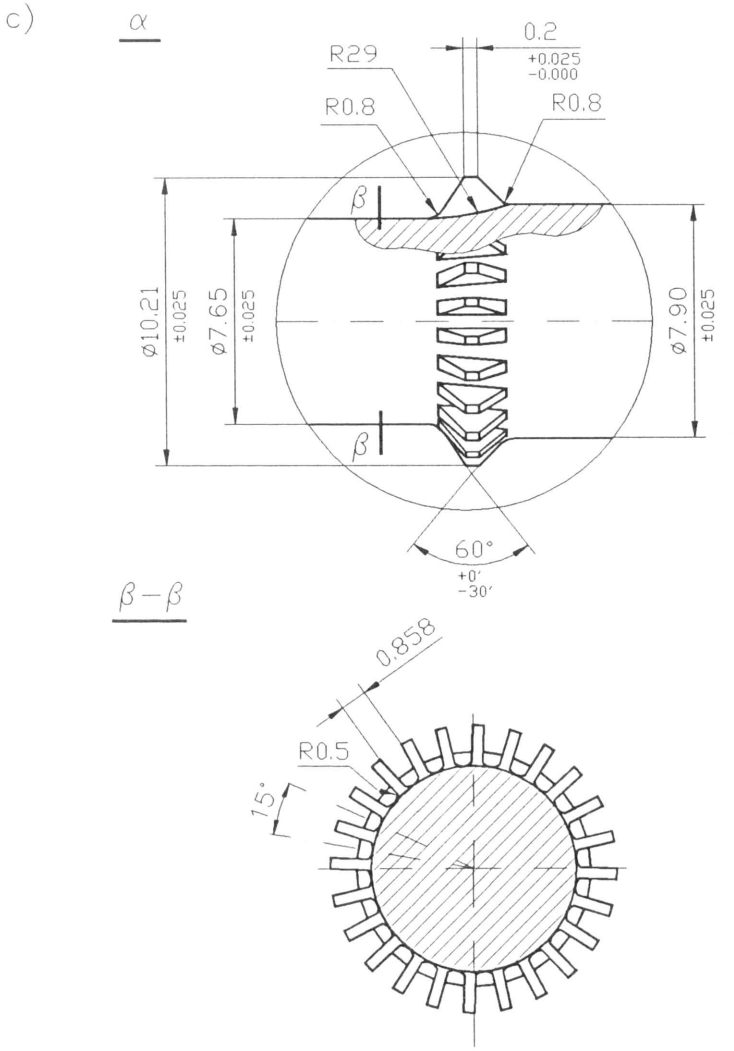

FIG. 2. a) Geometry of the testpiece. b) Magnified view of detail α given in Fig. 2a for the testpiece with unslitted extensometer ridges. c) Magnified view of detail α given in Fig. 2a for the testpiece with slitted extensometer ridges.

Three identical, constant load, uni-axial tension creep rigs were used for the creep tests. The creep testpiece was held at either end by clamping blocks which utilise bolts and ceramic collars. The load was transferred from the load hanger via a 1:10 lever-ratio load arm, supported on a knife edge fulcrum. The load was then transferred through a knife-edge, a universal joint and a pull rod, to the testpiece top clamping block and then to the creep testpiece. Such an arrangement of knife-edges and universal joints incorporated into the load-train restricts the induced bending stresses in the creep testpiece to very low levels (below 6%).

The test load was applied at a constant rate at the start of a test by a hydraulic jack, which was manually controlled by the operator. The constant temperature during tests was ensured by a Donaldson 3-zone electrical resistance heating furnace, which was linked to a proportional temperature controller to provide temperature feedback control. Three separate manual potentiometers were used to control the bias of each of the three furnace zones to ensure there was no temperature gradient greater than $\pm 0.5^\circ$ C along the testpiece.

A deformation of the testpiece was measured with the use of mechanical extensometer which was connected to the testpiece ridges and to a linear voltage displacement transducer (L.V.D.T.) to measure the extension of the gauge length during a test.

A strain bridge-type load cell was connected to the lower pull rod to measure the actual load transferred to the testpiece.

Analogue signals from all the measuring devices were converted to digital form by means of a digital voltmeter connected to a Solatron switch box, which was controlled remotely by the microcomputer using an IEEE 488 interface board. An expert system developed by DUNNE *et al.* [6] was used to record sensor readings at specified or automatically determined intervals of time. The digital readings were stored in files on a hard disc and could be periodically examined between logging times using the expert system graph facility.

All test equipment was surrounded by a controlled atmosphere monitored to be at 20° C $\pm 0.5^\circ$ C by a laboratory air conditioner, which improved the accuracy control of test temperature and ensured that machine and instrumentation deflection changes were minimised by counteracting ambient temperature changes.

3. Experimental results

3.1. Results for unslitted ridged testpiece

In order to determine the constants in the constitutive equations, developed by KOWALEWSKI *et al.* [7], four stress levels were selected at which the entire creep curves were measured; the stress levels selected were: 241.3, 250.0, 262.0 and 275.0 MPa. All these tests were carried out on testpieces having gauge lengths of 50 mm since, according to previous considerations [2, 3], it introduces relatively small errors in the measured creep strains. Creep curves from these tests are shown by the continuous lines in Fig. 3. Lifetimes and minimum creep rates are presented in Table 1.

To investigate the effect of gauge length on the measured creep curves, three tests were carried out with gauge lengths of 50, 30 and 10 mm, all at the same stress level of 250.0 MPa and the same testing temperature of 150° C $\pm 0.5^\circ$ C. Creep curves obtained from these tests are shown in Fig. 4. It may be seen that the testpiece with the shorter gauge length exhibits the significant strengthening effect expressed by both the increase of the lifetime and the decrease of minimum

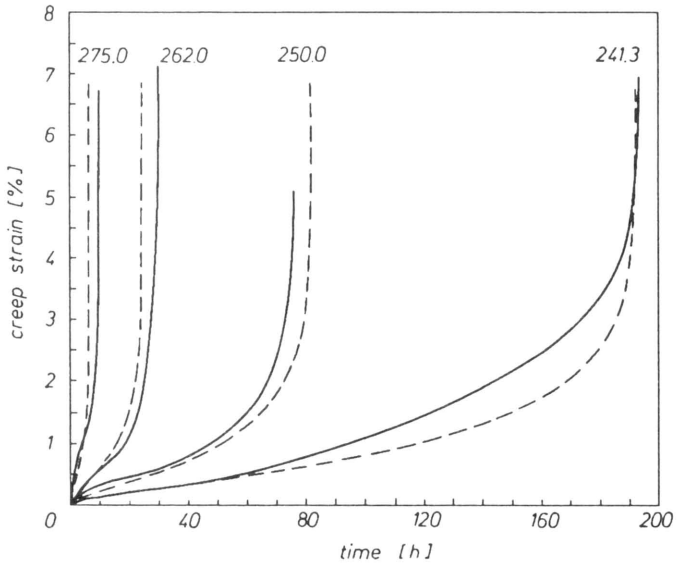

FIG. 3. Experimental and theoretical creep curves obtained for unslitted ridged testpieces with gauge length of 50 mm. The continuous lines denote experimental results and the broken lines denote theoretical predictions. The numbers given for each curve refer to stress levels in MPa.

Table 1. Minimum creep rates and lifetimes for the unslitted testpieces of 50 mm gauge length (theoretical predictions were obtained for the material constants determined from the first fit to the experimental data).

Stress level	241.3 [MPa]		250.0 [MPa]		262.0 [MPa]		275.0 [MPa]	
—	Exp.	Th.	Exp.	Th.	Exp.	Th.	Exp.	Th.
Minimum creep rate $[1/h] \times 10^{-5}$	5.4	5.0	14.5	14.0	40.0	43.0	140.0	155.0
Lifetime $[h]$	193	192	76	82	30	25	10	7

creep rate. Both these experimental values are presented in Table 2 for all gauge lengths examined.

The strengthening effect is due to the elevation of the first stress invariant and the resultant suppression of the effective stress in the region of the extensometer ridges. When the extensometer ridges are located close to each other, an interaction takes place between perturbed fields at each ridge. It may be seen that, in comparison to creep curve for the 10 mm gauge length, the creep curve for the 30 mm gauge length is of little difference to that for the 50 mm gauge length. This is due to the extensometer ridges being sufficiently well separated in both cases to avoid the interaction between the stress and strain fields generated by the ridges.

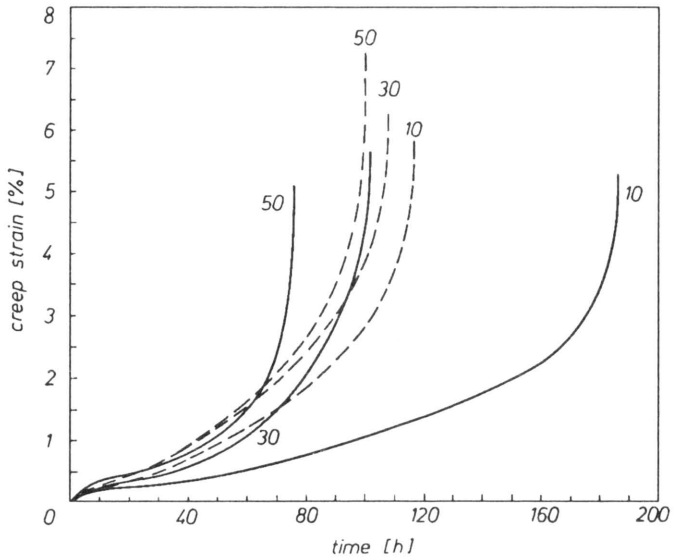

FIG. 4. Comparison of experimental creep curves for unslitted (continuous lines) and slitted (broken lines) ridged testpieces for tests carried out at the stress level of 250.0 MPa. The numbers given on the figure denote the gauge lengths of 50, 30 and 10 mm.

Table 2. Comparison of selected creep properties from tests carried out on the unslitted and slitted testpieces at stress level of 250 MPa for different specimen gauge lengths (theoretical predictions were obtained for the true material constants presented in Table 3).

Gauge length	10 mm				30 mm				50 mm			
Type of testpiece ridge	unslitted		slitted		unslitted		slitted		unslitted		slitted	
	Exp.	Th.	Exp.	Th.	Exp.	Th.	Exp.	Th.	Exp.	Th.	Exp.	Th.
Minimum creep rate $[1/h] \times 10^{-4}$	0.45	0.50	1.25	1.20	0.95	1.50	1.60	1.65	1.45	1.65	2.10	1.80
Lifetime $[h]$	187	178	117	118	102	89	108	88	76	86	100	86

3.2. Results for slitted ridged testpiece

In order to investigate the effect of gauge length on the creep characteristics of the slitted testpieces, tests have been carried out at the same stress level of 250 MPa and the same gauge lengths of 50, 30, 10 mm as those used to examine the unslitted testpieces. The resulting creep curves are shown in Fig. 4 by the broken lines. It is easy to note that the minimum creep rates in all three tests are much closer to each other than those for unslitted testpieces. Also the lifetimes are much closer than those for unslitted tespieces. Values of minimum creep rates and lifetimes obtained for slitted tespieces of different gauge lengths are

compared in Table 2. On the basis of these results it may be concluded that the slitted extensometer ridges reduce the degree of interaction between the stress and strain fields at the ridges and the reinforcement effect of the ridges, particularly in the case of the 10 mm gauge length. In case of the 50 and 30 mm gauge length testpieces, the creep curves are again close to each other for the same reasons discussed for the unslitted testpieces. Comparison of creep curves for slitted and unslitted ridged testpieces presented in Fig. 4 clearly demonstrates the improved accuracy of strain and lifetime measurements made by the slitted ridged tespieces.

4. Constitutive equations

In the following section the set of constitutive equations, recently proposed by KOWALEWSKI *et al.* [7], to carry out theoretical computations and to predict the behaviour of the slitted and unslitted testpieces is summarized. The stress level dependence of creep rate is described by a sinh function, and two damage state parameters are used to model tertiary creep softening caused by grain boundary nucleation and growth, and ageing of the particulate microstructure. Also primary creep period is described by the model.

4.1. The form of the constitutive equations for uni-axial conditions

The form of the constitutive equations proposed in [7] for uni-axial conditions is given by the following set of equations

$$
\begin{aligned}
\frac{d\varepsilon}{dt} &= \frac{A}{(1-\omega_2)^n}\sinh\left(\frac{B\sigma(1-H)}{1-\Phi}\right),\\
\frac{dH}{dt} &= \frac{h}{\sigma}\frac{d\varepsilon}{dt}\left(1-\frac{H}{H^*}\right),\\
\frac{d\Phi}{dt} &= \frac{K_c}{3}(1-\Phi)^4,\\
\frac{d\omega_2}{dt} &= \frac{DA}{(1-\omega_2)^n}\sinh\left(\frac{B\sigma(1-H)}{1-\Phi}\right),
\end{aligned}
\tag{4.1}
$$

where A, B, H^*, h, K_c, D are material constants, and n is given by

$$
n = \frac{B\sigma(1-H)}{1-\Phi}\coth\left(\frac{B\sigma(1-H)}{1-\Phi}\right).
$$

Material parameters which appear in this model may be divided into three groups, i.e.

(i) the constants h, H^* which describe primary creep;
(ii) the constants A and B which characterise secondary creep;
(iii) the constants K_c and D responsible for damage evolution and failure.

The second equation in set (4.1) describes primary creep using variable H, which varies from 0 at the beginning of the creep process to H^*, where H^* is the saturation value of H at the end of primary period and subsequently maintains this value until failure.

As shown in previous papers [6, 7, 8, 9], scalar parameters are suitable to describe with sufficient accuracy a damage evolution of a material during creep, and therefore, such type parameters have been also used in the new creep constitutive model proposed. The equation set contains two scalar damage state variables used to model tertiary softening mechanisms:

1) Φ, which is described by the third equation in set (4.1), is defined from the physics of ageing to lie within the range $0 - 1$ for mathematical convenience;

2) ω_2, which is defined by the fourth equation in set (4.1), describes grain boundary creep constrained cavitation, the magnitude of which is strongly sensitive to alloy composition and to processing route.

4.2. Generalisation of the equation set (4.1) into multi-axial conditions

The strain rate equation in set (4.1) without the damage parameters Φ, ω_2, and primary creep variable H reduces to a relation of the following form:

$$\frac{d\varepsilon}{dt} = A \sinh(B\sigma). \tag{4.2}$$

This equation can be generalised for multi-axial conditions by assuming an energy dissipation rate potential:

$$\Psi = \frac{A}{B} \cosh(B\sigma_e). \tag{4.3}$$

Assuming normality and the associated flow rule, the multi-axial relation is given by:

$$\frac{d\varepsilon_{ij}}{dt} = \frac{\partial \Psi}{\partial S_{ij}} = \frac{3}{2} A \left(\frac{\overline{S}_{ij}}{\sigma_e} \right) \sinh(B\sigma_e), \tag{4.4}$$

where $\sigma_e = (3\overline{S}_{ij}\overline{S}_{ij}/2)^{1/2}$, $\overline{S}_{ij}$ – deviatoric stress tensor.

On reintroduction of the damage variables Φ, ω_2, and the primary state variable H, the multi-axial equation set is obtained:

$$\begin{aligned}
\frac{d\varepsilon_{ij}}{dt} &= \frac{3}{2} \frac{A}{(1-\omega_2)^n} \left(\frac{\overline{S}_{ij}}{\sigma_e} \right) \sinh \left(\frac{B\sigma_e(1-H)}{1-\Phi} \right), \\
\frac{dH}{dt} &= \frac{h}{\sigma_e} \frac{A}{(1-\omega_2)^n} \sinh \left(\frac{B\sigma_e(1-H)}{1-\Phi} \right) \left(1 - \frac{H}{H^*} \right), \\
\frac{d\Phi}{dt} &= \frac{K_c}{3}(1-\Phi)^4, \\
\frac{d\omega_2}{dt} &= \frac{DA}{(1-\omega_2)^n} \left(\frac{\sigma_1}{\sigma_e} \right)^{\nu} N \sinh \left(\frac{B\sigma_e(1-H)}{1-\Phi} \right),
\end{aligned} \tag{4.5}$$

where N is a parameter used to indicate the state of loading; e.g. for σ_1 tensile $N = 1$; and for σ_1 compressive, $N = 0$. The creep strain rates, $\dot{\varepsilon}_{ij}$, are dependent upon both the effective stress σ_e and the deviatoric stresses $\overline{S}_{ij}$, while the damage rate, $\dot{\omega}_2$, is related to the maximum principal tension stress σ_1 and the effective stress σ_e.

4.3. Normalisation of the constitutive equations

The constitutive equations in set (4.5) can be normalised by introduction of the following terms:

$$\Sigma_{ij} = \frac{\sigma_{ij}}{\sigma_0}, \qquad \lambda_{ij} = \frac{\varepsilon_{ij}}{e_0}, \qquad S_{ij} = \frac{\overline{S}_{ij}}{\sigma_0}, \tag{4.6}$$

where $e_0 = \sigma_0/E$ and E is the elastic modulus. The normalised time may be defined as:

$$\tau = \int_0^t (EA/\sigma_0)\,dt = (EA/\sigma_0)t = \frac{A}{e_0}t. \tag{4.7}$$

Equations (4.5) may be rewritten using these parameters as:

$$\begin{aligned}
\frac{d\lambda_{ij}}{d\tau} &= \frac{3}{2}\frac{A}{(1-\omega_2)^n}\left(\frac{S_{ij}}{\Sigma_e}\right)\sinh\left(\frac{\alpha\Sigma_e(1-H)}{1-\Phi}\right),\\
\frac{dH}{d\tau} &= \frac{h}{E\Sigma_e}\frac{A}{(1-\omega_2)^n}\sinh\left(\frac{\alpha\Sigma_e(1-H)}{1-\Phi}\right)\left(1-\frac{H}{H^*}\right),\\
\frac{d\Phi}{d\tau} &= \frac{e_0}{A}\frac{K_c}{3}(1-\Phi)^4,\\
\frac{d\omega_2}{d\tau} &= \frac{De_0}{(1-\omega_2)^n}\left(\frac{\Sigma_1}{\Sigma_e}\right)^{\nu} N\sinh\left(\frac{\alpha\Sigma_e(1-H)}{1-\Phi}\right),
\end{aligned} \tag{4.8}$$

where $\alpha = B\sigma_0$ and

$$n = \frac{\alpha\Sigma_e(1-H)}{1-\Phi}\coth\left(\frac{\alpha\Sigma_e(1-H)}{1-\Phi}\right).$$

The normalised equations, together with the effective stress multi-axial rupture criterion, given by $\nu = 0$, as discussed by KOWALEWSKI *et al.* [7], have been used to determine the variation of the stress, strain and damage fields within the testpieces.

4.4. Determination of material constants

The task of determining values of the material constants in equation sets (4.1) and (4.5) is not trivial since they involve the use of nonlinear functions and contain six material constants. As a consequence, the use of automated numerical computer techniques was necessary. In order to solve the problem, a new methodology has been developed by KOWALEWSKI *et al.* [7] for the determination of the material constants in the constitutive equations (4.1). Since all equations in set (4.1) can be related to different parts of the creep process, it was decided to identify the three stages in the process which corresponded to: primary, secondary and tertiary; and, to use those equations which describe the corresponding behaviour to determine the constants in the relevant sequence. All details concerning the developed optimisation scheme are reported in [7].

The results of experimental tests on unslitted ridged testpieces with 50 mm gauge length carried out with stress levels of 241.3, 250.0, 262.0, and 275.0 MPa, (Fig. 3) have been used to determine the material constants in the constitutive equations (4.1), using the above mentioned methodology. The constitutive parameters determined in this way were subsequently employed in the Continuum Damage Mechanics solver DAMAGE XX to carry out finite element computations for the unslitted ridged testpieces for the four stress levels given. The true axial component of strain, ε_{yy}, in the testpiece gauge length at any time t, was determined as the volume average given by

$$\varepsilon_{yy} = \sum_{i=1}^{m} \varepsilon_{yy}^{e} V^{e} / \sum_{i=1}^{m} V^{e},$$

where i is finite element number, m – number of elements falling along the line joining the surface of the specimen with the centerline, in the plane of testpiece symmetry, V – volume of a finite element, and superscript e denotes the finite element values. This mean axial strain is considered as the uniformly distributed creep strain in the parallel-sided region of the testpiece.

The axial creep strain measured by the extensometer located on the testpiece ridges was determined from the following relation:

$$\overline{\varepsilon}_{ij} = \frac{\delta}{Y},$$

where δ is the axial displacement of the extensometer ridges, Y – the gauge length defined by the axial separation of the extensometer ridges.

The accuracy of the extensometer-measured average axial strain made during the creep tests for the testpiece with extensometer ridges was investigated using the R-ratio [2], which is defined by

$$R = \frac{\varepsilon_{yy}}{\overline{\varepsilon}_{yy}}.$$

The R-ratio, derived in this way, was applied to the new experimental data three times successively to derive "exact" creep curves with the effects of unslitted extensometer ridges totally removed. Three curves of the variation of the R-ratio with the normalised time fraction t/t_f for three iterations performed are given in Fig. 5 for the unslitted ridged extensometer testpiece of gauge length 50 mm at the

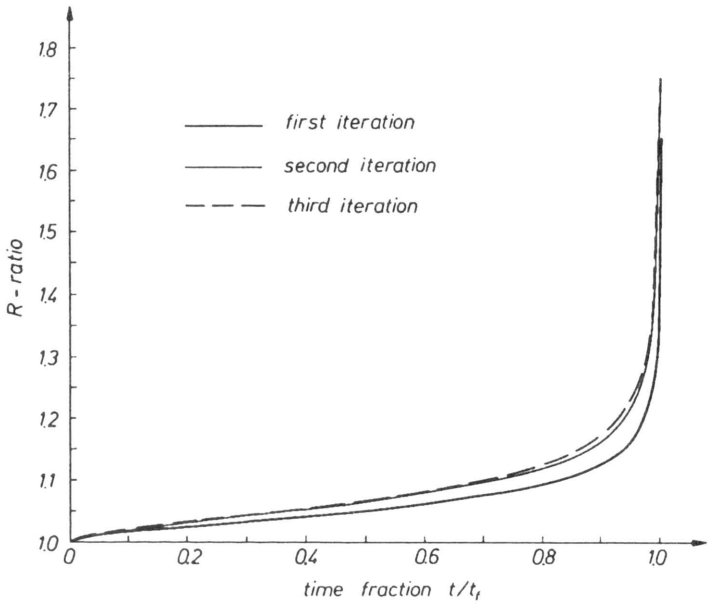

FIG. 5. Variation of the R-ratio with time fraction t/t_f for the testpiece with unslitted extensometer ridges determined using DAMAGE XX for σ = 250.0 MPa.

stress 250.0 MPa, and it has been used to correct the experimental creep curves presented in Fig. 3 for the aluminium alloy. The bold continuous line denotes the R-ratios used to correct the experimental creep curves presented in Fig. 3 in the first iteration. The thin continuous line denotes the R-ratios used in the second correction of the experimental creep curves presented in Fig. 3. The broken line denotes the R-ratios used in the final correction of the original experimental data. The use of the R-ratio determined at stress 250.0 MPa to correct creep curves obtained for different stress levels was possible since it has been found that this curve is independent of stress. The new set of creep curves which resulted from first iteration was then used as input to the optimisation scheme reported in [7] to redetermine the constitutive parameters. The procedure described was repeated until $R - t/t_f$ curves were almost identical, and the further corrections did not alter the creep curves obtained in previous iteration. The process may therefore be considered to have converged and the true constitutive parameters obtained, for which the constants are given in Table 3. More details about the determination of the true constitutive parameters of Eqs. (4.1) are given by KOWALEWSKI *et al.* in [4]. The final modifications to the experimental creep curves given in Fig. 3 are shown

in Fig. 6 by the continuous lines, and the broken lines denote the predictions made by the fitted data listed in Table 3. The constitutive equations with true material constants were then used to predict the behaviour of the unslitted and the slitted ridged testpieces.

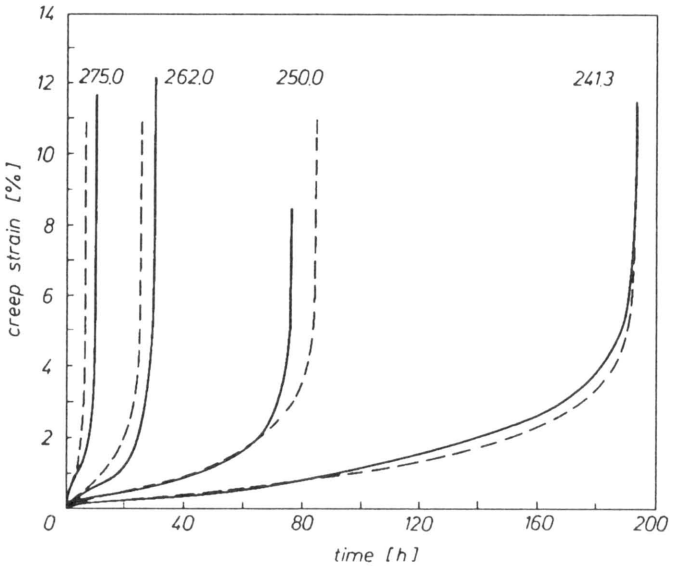

FIG. 6. Comparison of creep curves obtained from data originally presented in Fig. 3, corrected for errors due to the presence of extensometer ridges, with theoretical predictions made using Eqs. (4.1) with the true constitutive parameters. The continuous lines denote the final correction to the original experimental data, and the broken lines denote the theoretical predictions.

Table 3. True material constants for Eqs. (4.1).

A	B	h	H^*	K_c	D
(h^{-1})	(MPa^{-1})	(MPa)	(–)	(h^{-1})	(–)
4.04×10^{-15}	0.1126	2.95×10^{4}	0.1139	18.2×10^{-5}	2.75

5. Theoretical predictions and their comparison with experimental data

The constitutive equations with true material constants were used as input to the Finite Element Continuum Damage Mechanics solver DAMAGE XX to predict the behaviour of both slitted and unslitted tespieces for three different gauge lengths: 50, 30, 10 mm, subjected to the same stress level of 250.0 MPa. Because of the specimen symmetry, only a single quadrant containing the extensometer ridge was selected for analysis. The numerical procedure used to solve the boundary

value problems for creep-damage deformations was based on the finite element method and was that used by HAYHURST *et al.* [8]. The material was treated as a continuum. The finite element mesh generator package, FEMGEN, was used to generate the mesh in form of constant-strain triangular elements. The quadrant of the testpiece was divided into two regions: region one for the main part, including 506 elements, and region two for the extensometer ridge area including 60 elements. Entire quadrant contained 566 elements and 322 nodes. The elements were subjected to axisymmetric stressing in region one, and to plane stress in region two due to the release of hoop constraints by slitting [3]. The loaded boundary of the mesh was subjected to a constant normalised stress to ensure that the normalised stress level at the gauge area Σ_{yy} was equal to unity, and the boundaries of symmetry were subjected to zero normal displacement with $\Sigma_{xy} = 0$. The computations were carried out on an IBM 3090-600E computer at the Science and Engineering Research Council, Rutherford Appleton Laboratory. More details concerning the numerical techniques used and continuum damage mechanics finite element solver have been described in [8, 9].

5.1. Theoretical results for unslitted ridged testpiece

The theoretical creep curves, computed from the extensometer displacement, for the unslitted ridged testpieces are presented in Fig. 7 where they are denoted by the broken lines, and compared with the experimental results, denoted by the

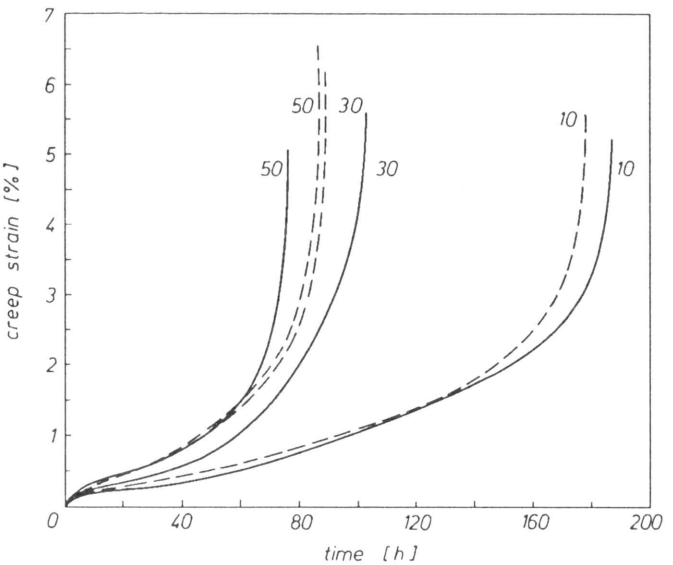

FIG. 7. Comparison of creep curves for unslitted ridged testpieces of 50, 30 and 10 mm gauge lengths under the stress level of 250 MPa, computed from the extensometer displacement using the solver DAMAGE XX (broken lines), with the experimental curves presented previously in Fig. 4.

continuous lines, previously presented in Fig. 4. The predicted creep curves for the 50 and 30 mm gauge lengths are almost identical, but the creep curve predicted for the 10 mm gauge length specimen has creep rates which are much lower, and lifetimes which are much longer than those for the 50 and 30 gauge lengths. The theoretical and experimental creep curves for the 10 mm gauge length are in close agreement, whereas the experimental creep curves for the 50 and 30 mm gauge lengths are in slight disagreement with the theoretical predictions. However, the differences are small, and they are within the typically observed experimental error.

5.2. Theoretical results for slitted ridged testpiece

The constitutive equations with true material constants have been again used in the solver DAMAGE XX to predict the creep curves at the stress level of 250 MPa for the slitted ridges testpieces. The resultant creep curves are shown in Fig. 8 using the broken lines for the three gauge lengths: 50, 30 and 10 mm,

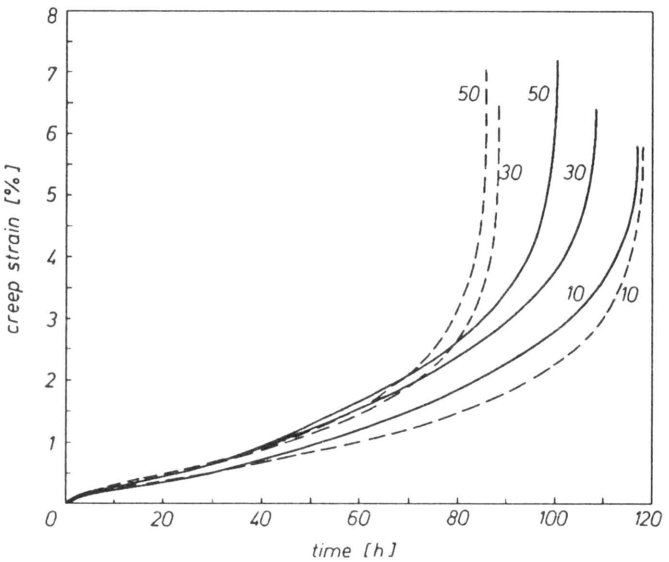

FIG. 8. Comparison of creep curves for slitted ridged testpieces of 50, 30 and 10 mm gauge lengths under the stress level of 250 MPa, computed from the extensometer displacement using the solver DAMAGE XX (broken lines), with the experimental curves presented previously in Fig. 4.

where they are compared with the experimental curves denoted by the continuous lines, previously shown by the broken lines in Fig. 4. The theoretical creep curves for the 50 and 30 mm gauge lengths are very close. The theoretical creep curve for the 10 mm gauge length, as in the case of the unslitted ridged specimen, shows minimum creep rates which are lower, and lifetimes which are longer than those for the 50 and 30 mm gauge lengths. However, the predicted degree

of strengthening, expressed as the ratio of lifetime of the 10 mm gauge length testpiece to that for the 50 mm gauge length testpiece, is significantly lower since it equals 1.37, in comparison to the value of the same ratio of 2.06 for the unslitted ridged testpiece. This theoretical result confirms the experimental observations. It also proves that the slits in the extensometer ridges relieves the constraint to deformation provided by the unslitted extensometer ridges.

5.3. Evaluation of errors in strain measurements of the presented results

Evaluation of errors in strain measurements has been carried out using $R-t/t_f$ curves computed with the true constitutive equations which are shown in Fig. 9 for the unslitted ridged testpieces (continuous lines) and the slitted ridged testpieces

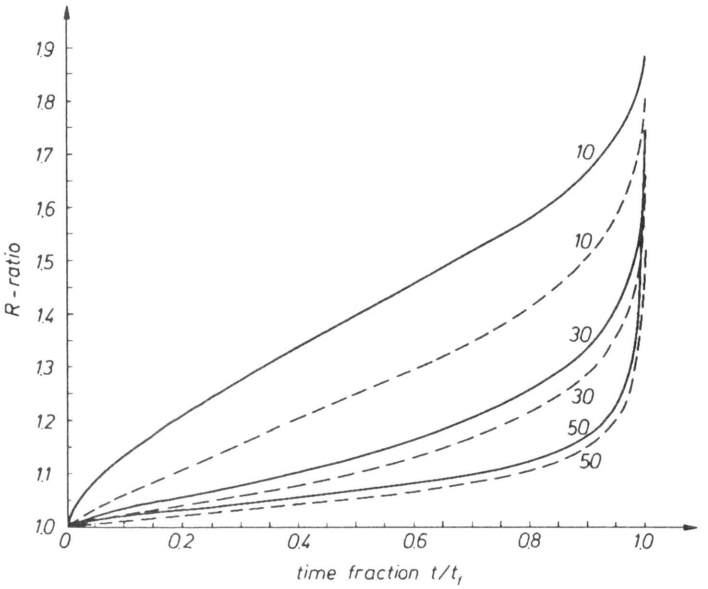

FIG. 9. Comparison of the variation of the R-ratio with the time fraction t/t_f for the slitted and unslitted ridged testpieces of 50, 30 and 10 mm gauge lengths obtained by using the solver DAMAGE XX for $\sigma = 250$ MPa. The continuous lines denote R-ratios for unslitted ridged specimens, the broken lines denote R-ratios for slitted ridged specimens. The numbers given in the figure denote the gauge lengths of 50, 30 and 10 mm.

(broken lines) with the three considered gauge lengths. The vertical downward shift of the unbroken curves to the broken curves indicates the improved accuracy achieved. More visible presentation of this effect is shown in Fig. 10 where the R-ratios are plotted versus the gauge length for three selected time fractions: 0.3, 0.6, 0.9. The broken lines $1', 2', 3'$ show the variation of the R-ratio with gauge length for the tespieces containing slit extensometer ridges, and the solid lines 1, 2, 3 correspond to the results for the unslitted testpiece. When the gauge length is about 10 mm, the maximum error of measured strain is about 70% for

the unslitted testpiece, and about 50% for the slitted one. It is clear that the new testpiece design results in a consistently lower error, however, this effect is most pronounced for the 10 mm gauge length. Despite this improvement in strain measurement, the remaining errors for the slitted ridged specimens are still significant and further improvements are required in the testpiece design.

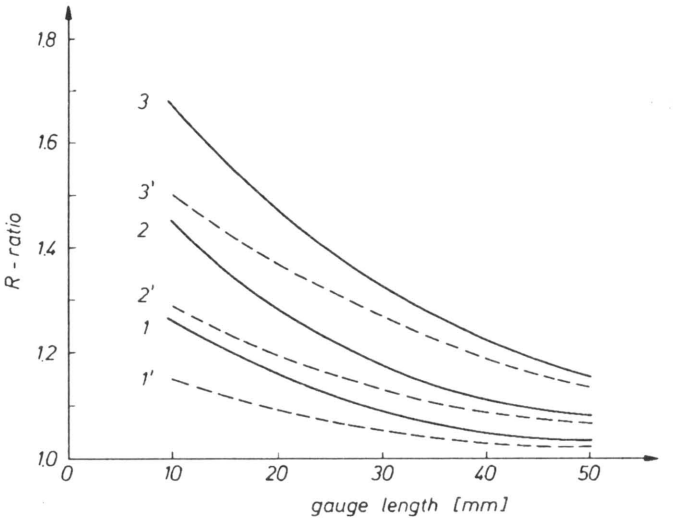

FIG. 10. Comparison of the variation of the R-ratio with gauge length for both slitted and unslitted ridged testpieces under the stress of 250 MPa. The continuous lines denote results for unslitted ridged testpiece, the broken lines denote results for slitted ridged testpiece. Various time fractions are shown: 1, 1′ – time fraction 0.3; 2, 2′ – time fraction 0.6; 3, 3′ – time fraction 0.9.

6. Conclusions

1. The advantage of the slit extensometer ridged testpieces considered in this work was evaluated theoretically by using the model which approximates the different stress states within the testpiece by an axisymmetric and plane-stress combinations, and experimentally for three different gauge lengths: 50, 30 and 10 mm.

2. The use of physically based material model with two damage variables within the Finite Element Continuum Damage Mechanics solver DAMAGE XX has demonstrated that the slitted testpieces reduce significantly the error in the measured creep strain and this result has been experimentally confirmed.

3. The effect of the slitted extensometer ridges on the accuracy of the measured creep strains, and on the lifetimes becomes more pronounced for the shorter testpiece gauge lengths. It is recommended that the testpiece with slitted extensometer ridges should be selected in combined cyclic plasticity and creep testing, where a shorter gauge length has to be used.

References

1. M.F. DAY and G.F. HARRISON, *Design and calibration of extensometer and transducers*, Measurement of High Temperature Mechanical Properties of Material, M.S. LOVEDAY, M.F DAY and B.F. DYSON [Eds.], HMSO, London, 225–240, 1982.
2. J. LIN, D.R. HAYHURST and B.F. DYSON, *The standard ridged uniaxial testpiece: computed accuracy of creep strain*, J. Strain Analysis, **28**, 101–115, 1993.
3. J. LIN, D.R. HAYHURST and B.F. DYSON, *A new design of uniaxial creep testpiece with slit extensometer ridges for improved accuracy of strain measurement*, Int. J. Mech. Sci, **35**, 63–78, 1993.
4. Z.L. KOWALEWSKI, J. LIN and D.R. HAYHURST, *Experimental and theoretical evaluation of a high-accuracy uni-axial creep testpiece with slit extensometer ridges*, Int. J. Mech. Sci., **36**, 751–769, 1994.
5. Y. OHASHI, M. TOKUDA and H. YAMASHITA, *Effect of third invariant of stress deviator on plastic deformation of mild steel*, J. Mech. Phys. Solids, **23**, 295–323, 1975.
6. F.P.E. DUNNE and D.R. HAYHURST, *An expert system for the determination of creep constitutive equations based on continuum damage mechanics*, J. Strain Analysis, **26**, 185–191, 1991.
7. Z.L. KOWALEWSKI, D.R. HAYHURST and B.F. DYSON, *Mechanisms-based creep constitutive equations for an aluminium alloy*, J. Strain Analysis, **29**, 309–316, 1994.
8. D.R. HAYHURST, P.R. BROWN and C.J. MORRISON, *The role of continuum damage in creep crack growth*, Phil. Trans. R. Soc. Lond., **A311**, 131, 1984.
9. D.R. HAYHURST, P.R. DIMMER and C.J. MORRISON, *Development of continuum damage in the creep rupture of notched bars*, Phil. Trans. R. Soc. Lond., **A311**, 103–129, 1984.

POLISH ACADEMY OF SCIENCES
INSTITUTE OF FUNDAMENTAL TECHNOLOGICAL RESEARCH
and
UMIST, DEPARTMENT OF MECHANICAL ENGINEERING, MANCHESTER, UK.

Received October 28, 1994.

Arch. Mech., 47, 2, pp. 281–293, Warszawa 1995

Recovery stress of TiNi shape memory alloy under constant strain (*)

P.H. LIN (NANJING), H. TOBUSHI (TOYOTA),
K. TANAKA (TOKYO), C. LEXCELLENT (BESANÇON)
and A. IKAI (TOYOTA)

THE RECOVERY STRESS associated with the martensitic transformation (MT) and the rhombohedral phase transformation (RPT) in TiNi shape memory alloy was investigated experimentally with respect to cyclic heating and cooling, under constant residual strain. The results are summarized as follows. 1) The recovery stress in the heating process increases along the reverse transformation lines of RPT and MT. The recovery stress increases in two stages when the maximum strain is in the region of MT. 2) The stress at high temperature takes an almost constant value when the maximum strain is in the region of MT. The recovery stress induced by heating and cooling takes a maximum value when the maximum strain is in the region of RPT completion. 3) The recovery stress varies slightly with cycling.

1. Introduction

IN TiNi SHAPE MEMORY ALLOY (SMA), two transformations occur: a martensitic transformation (MT) with a transformation strain of about 6%, and a rhombohedral phase transformation (RPT) with a transformation strain of about 0.6% [1–3]. At temperatures below the reverse transformation starting temperature, the transformation strain induced during the loading process appears after unloading as the irrecoverable strain due to both transformations. The residual strain disappears upon heating at temperatures above the reverse transformation completion point under no stress, a phenomenon which is called the shape memory effect [4]. If the material is heated while keeping the residual strain constant, a recovery stress appears [5, 6]. The recovery stress is used in many applications of SMA [7].

One of the practical applications of SMA which takes advantage of the recovery stress is a SMA pipe coupling. The principle of the coupling is as follows. The inner diameter of the shape-memorized SMA coupling is smaller than the outer diameter of a connecting pipe. The inner diameter of the SMA coupling is made larger than the outer diameter of the pipe at low temperatures. One inserts the pipe into the coupling and heats the coupling, which tightens the pipe. These processes complete the procedure. TiNi SMA has excellent corrosion resistance and the SMA coupling can be used in many special applications [7]. To remove the coupling, one cools the pipe and then it can be easily removed with very

(*) Paper presented at 30th Polish Solid Mechanics Conference, Zakopane, September 5–9, 1994.

little force. In the design and reliability evaluation of these SMA elements, it is important to understand the magnitude of the recovery stress and the conditions under which it appears [8–10].

For these purposes, the authors previously investigated the cyclic behaviour of the recovery stress with respect to the strain in the MT region [5, 6], and the property of the recovery stress with respect to the strain in the RPT region [11, 12]. From these investigations, it was ascertained that the recovery stress for each transformation increased along the reverse transformation line on the stress-temperature plane. Because both MT and RPT depend on the hysteresis of stress and temperature, it is necessary to make clear the dependence of the recovery stress on the hysteresis of strain.

In the present study, based on the previous investigations, we investigated the behaviour of the recovery stress due to both MT and RPT in combination, for TiNi SMA. By performing the heating-cooling tests under constant residual strain, we investigated the properties of the recovery stress due to both transformations. Based on the exprimental results, we shall discuss the influence of maximum strain, heating and cooling temperatures and of the number of cycles on the magnitude of the recovery stress and the conditions under which it appears.

2. Experimental method

2.1. Materials and specimen

The material was Ti-55.2wt%Ni SMA wire, which was produced by Furukawa Electric Co. The cross-section of the wire was uniform and the diameter was 0.75 mm. The total length, the length between grippers and the gauge length were 100 mm, 50 mm and 20 mm, respectively. The wire was heat-treated at 723 K for 20 min before being cooled in the oven, so that it memorized a straight line as its shape. The reverse transformation completion temperature A_f of the specimen was about 323 K.

2.2. Experimental apparatus

The exprimental apparatus was a shape-memory property testing machine which was composed of a tensile machine with a constant-temperature chamber and a temperature-control device [13]. The specimen was heated by a spray of hot compressed air in the atmosphere, or cooled by liquefied carbon dioxide. Axial force, temperature and displacement were measured with a load cell, a thermocouple and an extensometer, respectively. The gauge length of the extensometer was 20 mm.

2.3. Experimental procedure

First, the tensile tests were carried out with loading and unloading at constant temperature. The temperatures tested were between 293 K and 373 K at 10 K

intervals. Strain rate was 0.4%/min. Maximum strain was 1% for RPT and 6% for MT. The tensile tests were performed to determine the transformation lines due to RPT and MT which were necessary to analyze the behaviour of the recovery stress [14, 15].

Second, we carried out the heating-cooling tests under constant residual strain to examine the recovery stress. The schematic stress-strain relationship in the tests is shown in Fig. 1.

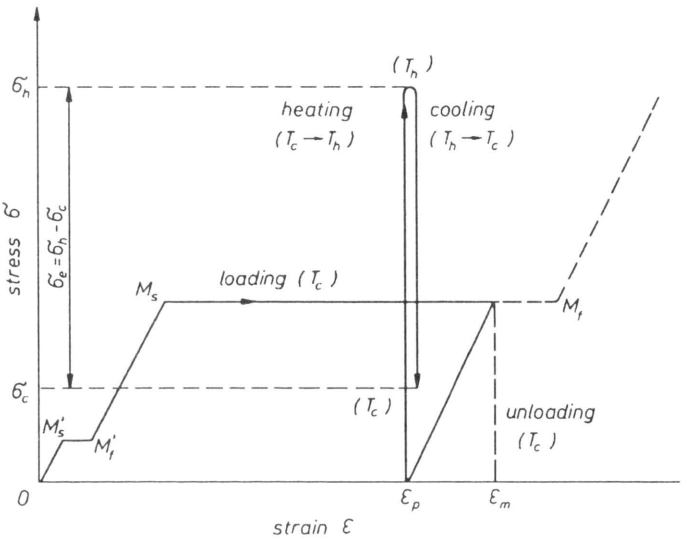

FIG. 1. The stress-strain relationships in the heating-cooling tests under constant residual strain.

As seen in Fig. 1, we first loaded the specimen to maximum strain ε_m and unloaded at temperature T_c below A_S. Holding residual strain ε_p constant, we heated it to temperature T_h above A_f and, subsequently, cooled to T_c. Heating and cooling between the temperatures T_h and T_c under constant ε_p were performed 10 times. Strain rate during the loading and unloading processes was 0.4%/min. T_c was 303 K and T_h 353 K. The rate of temperature variation during the heating and cooling processes was about 0.4 K/s. Values of ε_m were in the regions of RPT, R-phase, MT, and M-phase.

3. Experimental results and discussion

3.1. Stress-strain relationship and stress-temperature relationship

The stress-strain curves and stress-temperature curves obtained at the first cycle in the test of loading-unloading, followed by heating-cooling, are shown for different maximum strain ε_m in Fig. 2. As seen from the stress-strain curves in Fig. 2, RPT finishes at the strain of about 0.6%, MT starts at a strain of about 1.2% and finishes at a strain of about 5.5%. Strain larger than about 5.5% is in the

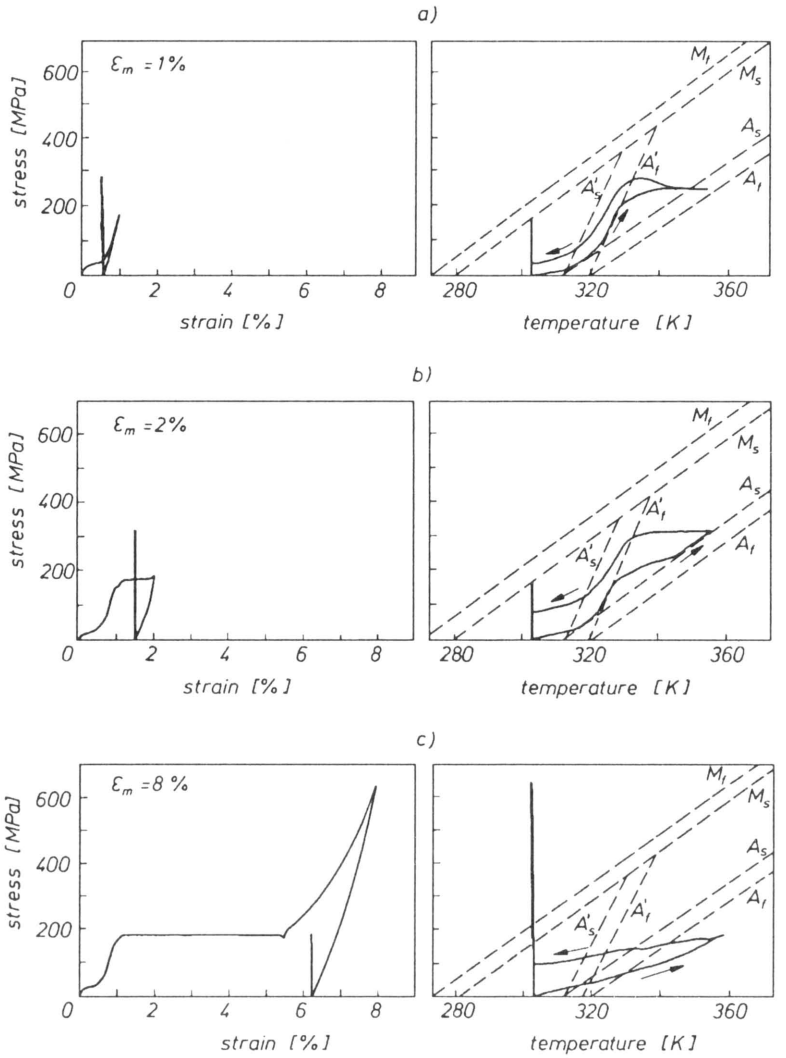

FIG. 2. Stress-strain curves and stress-temperature curves for the first cycle, a) $\varepsilon_m = 1\%$, b) $\varepsilon_m = 2\%$, c) $\varepsilon_m = 8\%$.

region of the M-phase. In the stress-temperature diagrams, the transformation start lines M_S, A_S and A'_S of MT, its reverse transformation and the reverse transformation RPT and the corresponding completion lines M_f, A_f and A'_f are shown by the dashed lines. These transformation lines were obtained by connecting the transformation stresses at each temperature with the straight lines. The transformation stresses were determined as the start and completion stresses of both transformations in the tensile test with loading and unloading at constant temperature [14, 15]. As seen in the stress-temperature diagrams, the MT region and its reverse transformation region are separated by about 200 MPa in the

vertical axis, and by about 40 K in the horizontal axis. In contrast, the RPT region and its reverse transformation region overlap. That is, the RPT start line M'_S almost coincides with the completion line of its reverse transformation A'_f, and the RPT completion line M'_f coincides with the start line of its reverse transformation A'_S [3, 13]. Therefore only the reverse transformation lines A'_S and A'_f are shown in Fig. 2.

In the case of ε_m in the RPT completion region ($\varepsilon_m = 1\%$), as seen from the stress-temperature curve for the heating process, stress increases remarkably along the RPT reverse transformation line from about 315 K, reaches a maximum value at about 330 K and is almost constant at about 250 MPa thereafter. During the cooling process, stress decreases remarkably along the RPT line from $\sim$ 330 K and is almost constant at about 30 MPa after completion of the RPT. The stress-temperature curve for the cooling process shows almost the same form as the curve for the heating process but is shifted to the low temperature side by about 5 K. As discussed in the previous paper [11, 12], the recovery stress is high when ε_m is large in the RPT region.

In the case of ε_m in the MT region ($\varepsilon_m = 2\%$), as seen from the stress-temperature curve for the heating process, stress increases in two stages. That is, during the heating process, stress increases remarkably along the RPT reverse transformation line between about 315 K and 325 K, is almost constant between 325 K and 345 K and increases along the MT reverse transformation line from $\sim$ 345 K. During the cooling process, stress decreases remarkably along the RPT line from $\sim$ 330 K and is almost constant at about 100 MPa below $\sim$ 320 K.

The behaviour of the recovery stress increasing in two stages is as follows. The stress increment along the RPT reverse transformation line is large when ε_m is small. In contrast, the stress increment along the MT reverse transformation line is large when ε_m is large (cf. $N = 1$ in Fig. 5). The dependence of the recovery stress on ε_m can be explained as follows. As discussed in the previous papers [14, 15], the stress-strain-temperature relation is expressed by the following equation;

$$\Delta\sigma = E \cdot \Delta\varepsilon + \Theta \cdot \Delta T + \Omega \cdot \Delta\xi \,, \tag{3.1}$$

where σ, ε, T and ξ denote stress, strain, temperature and the volume fraction of the induced phase, respectively. E, Θ and Ω represent modulus of elasticity, thermoelastic constant and coefficient prescribing the transformation range, respectively. If the influence of thermal expansion is small, the relation during the heating process under constant strain becomes as follows from Eq. (3.1)

$$\Delta\sigma = \Omega \cdot \Delta\xi \,. \tag{3.2}$$

As seen from Eq. (3.2), the recovery stress increases in proportion to the volume fraction of the induced phase. The interface between the induced phase and the parent phase in SMA expands with the progress of the deformation in the same manner as the progress of Luder's bands in the yield stage of mild

steel. As seen from the stress-strain curve during the loading process in Fig. 2, RPT occurs initially and MT appears afterwards. Therefore in the MT region, the volume fraction of the R-phase decreases and that of the M-phase increases. Thus, when ε_m is large in the MT region, the recovery stress along the RPT reverse transformation line decreases and the recovery stress along the MT reverse transformation line increases.

In the case of ε_m in the MT completion region ($\varepsilon_m = 8\%$), as seen from the stress-temperature curve during the heating process, stress increases in proportion to temperature and the rate of increase in stress is large above about 350 K. In this case, stress does not increase along the MT reverse transformation line A_S. This may be explained as follows. If ε_m in the MT completion region, the reverse transformation stresses σ_{As} and σ_{Af} decrease remarkably [16], and internal stress acts due to dislocation which appears during the loading process [17, 18]. The influence of the internal stress will be discussed in Sec. 3.4. During the cooling process, stress decreases in proportion to temperature from 150 MPa to 100 MPa.

3.2. Relationship between recovery stress and maximum strain

The stress-strain curves obtained during the loading-unloading process and the heating-cooling process in the first cycle for different maximum strains ε_m are shown in Fig. 3. The dependence of the stress at high temperature σ_h, the stress at low temperature σ_c and the recovery stress determined as the difference between both stresses $\sigma_e = \sigma_h - \sigma_c$ on ε_m is shown in Fig. 4.

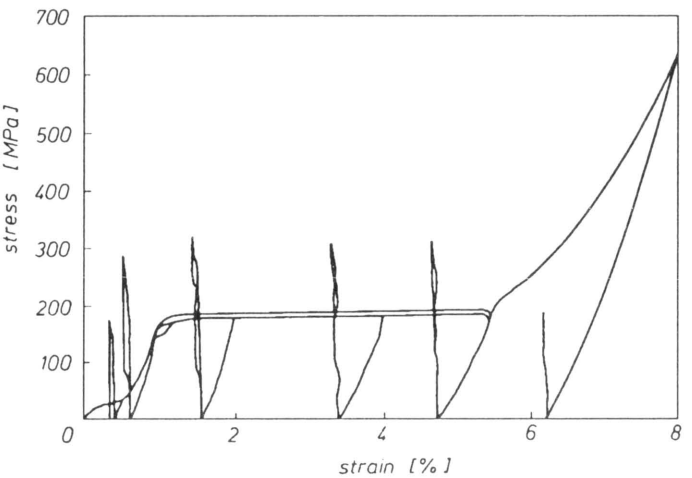

FIG. 3. Stress-strain curves for different maximum strains in the first cycle.

In practical applications of SMA, for example in the case of the SMA pipe coupling, σ_h is necessary to estimate the tightening force at high temperature, σ_c – to evaluate the force to remove the coupling at low temperature, and σ_e – to obtain the variation in tightening force if the temperature of fluid in a pipe varies.

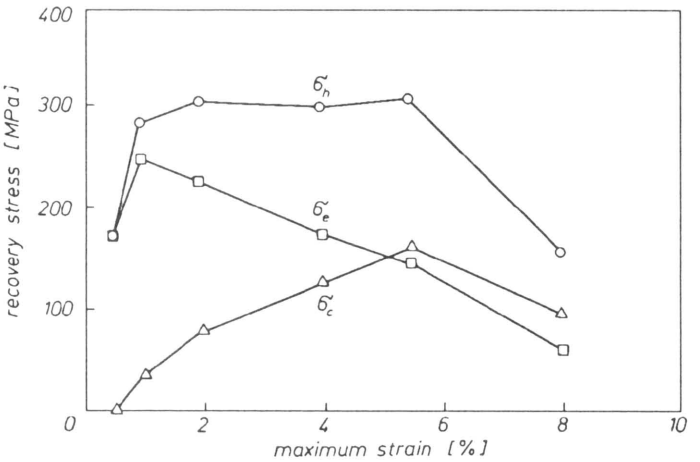

FIG. 4. Dependence of the stress at high temperature σ_h, the stress at low temperature σ_c and the recovery stress effective for heating-cooling σ_e on the maximum strain ε_m in the first cycle.

Furthermore, σ_e denotes the recovery stress necessary to prescribe the working force of SMA elements, such as actuators, robots and solid state engines which vary repeatedly between high temperature and low temperature.

As seen in Figs. 3 and 4, in the RPT region below $\varepsilon_m = 1\%$, all three types of stress increase with increasing ε_m. In this case, σ_h and σ_e increase remarkably but σ_c increases gradually. In the MT region of $\varepsilon_m = 2\% \sim 5.5\%$, σ_h is almost constant, σ_c increases in proportion to ε_m and σ_e decreases. In the case of the MT completion region, $\varepsilon_m = 8\%$, all types of stress are smaller than the values at $\varepsilon_m = 5.5\%$.

In conclusion, the following points are important for practical applications of SMA elements. 1) If σ_e is used under thermal cycling, $\varepsilon_m = 1\% \sim 2\%$ is optimum. 2) If σ_h is used under thermal cycling, $\varepsilon_m = 1\% \sim 2\%$ is enough. In this case, if a certain value of σ_c is necessary at low temperature, $\varepsilon_m = 4\% \sim 5.5\%$ is optimum. 3) If high σ_h and low σ_c are necessary, $\varepsilon_m = 1\%$ is optimum.

3.3. Cyclic properties of recovery stress

The stress-temperature curves obtained in the cyclic heating-cooling tests are shown for each maximum strain ε_m in Fig. 5. The relationships in the number of cycles $N = 1$ and $N = 10$ are shown. In Fig. 5, as in Fig. 2, the transformation lines of RPT and MT are shown by the dashed lines. As seen in Fig. 5, in the case when the recovery stress increases in two stages during the heating process in $N = 1$, the recovery stress increases in one stage in $N = 10$. This phenomenon occurs because MT does not occur during the cooling process in $N = 1$, and therefore only RPT and its reverse transformation occur repeatedly after the 2nd cycle. Based on this phenomenon, the stress-temperature curves show a hysteresis loop due to the RPT after the 2nd cycle.

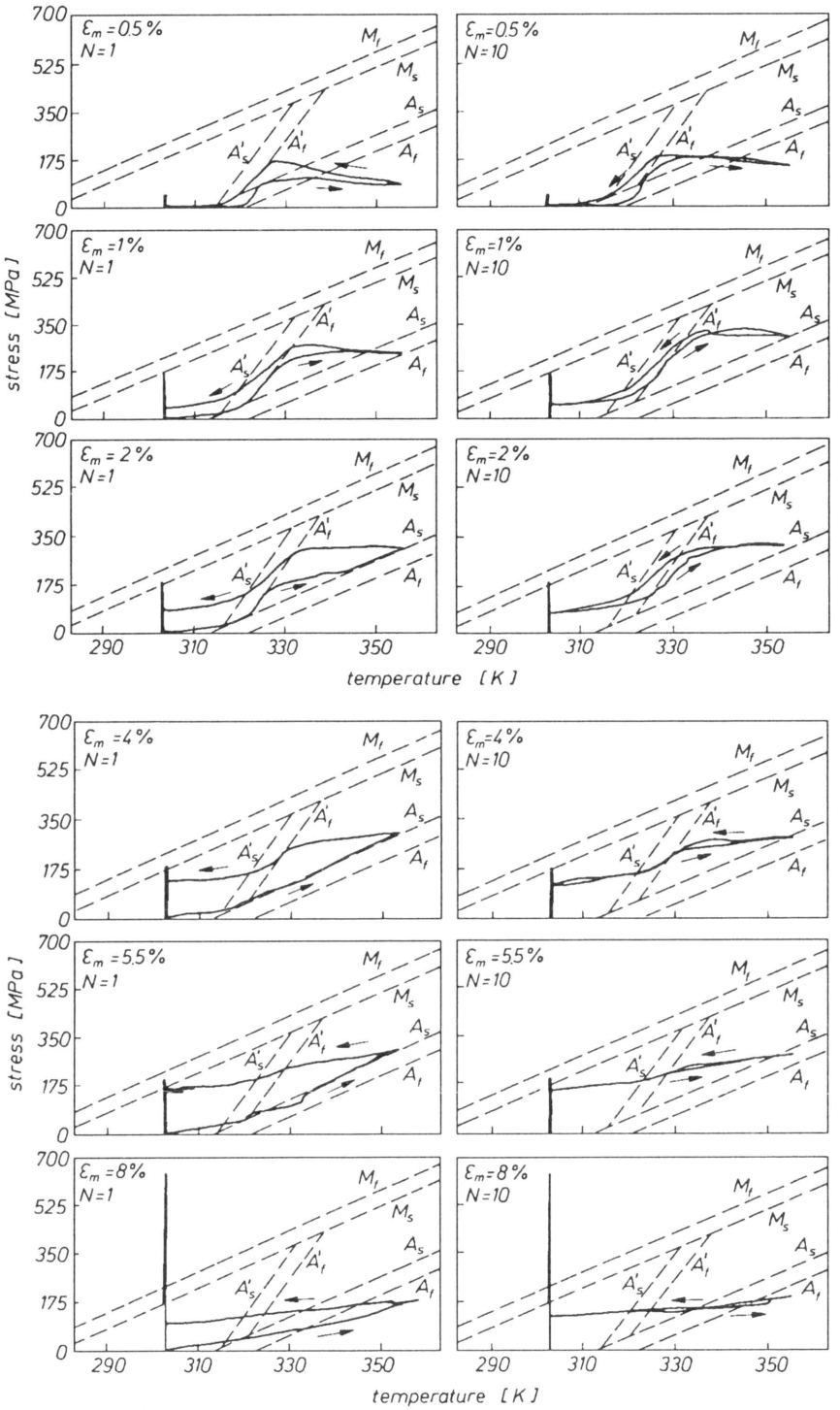

FIG. 5. Stress-temperature curves in cycles $N = 1$ and 10.

The dependence of the recovery stresses on maximum strain ε_m in the number of heating-cooling cycles $N = 1$ and 10 is shown in Fig. 6. In Fig. 6, stress at high temperature σ_h, stress at low temperature σ_c and effective recovery stress for heating-cooling σ_e are shown by several symbols and are connected. In Fig. 6, the loading-unloading curve in the case of $\varepsilon_m = 8\%$ is shown by the dashed curve.

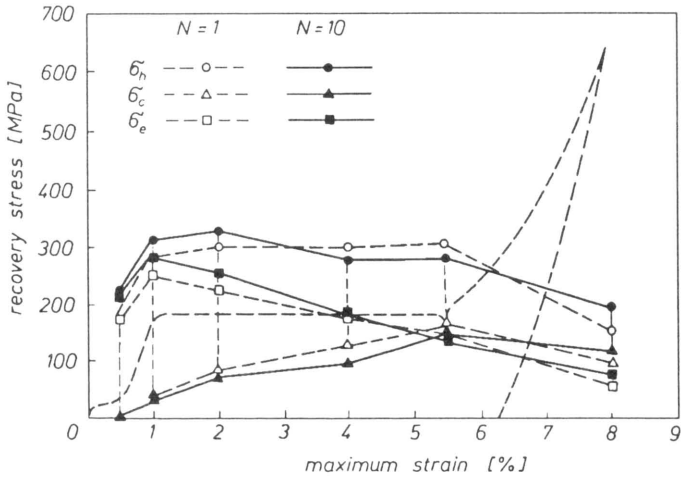

FIG. 6. Dependence of the stress at high temperature σ_h, the stress at low temperature σ_c and the recovery stress effective for heating-cooling σ_e on the maximum strain ε_m in cycles $N = 1$ and 10.

As seen in Fig. 6, the variation in each stress from $N = 1$ to 10 is smaller than 30 MPa. The variation in these stresses is small remembering that the MT stress subjected to cyclic strain with constant amplitude decreases by about 100 MPa $\sim$ 200 MPa in 10 cycles [19, 20]. The recovery stress is thus stable for cyclic heating and cooling. In the case of $\varepsilon_m = 4\%$ and 5.5%, because σ_h decreases with cycling, we should be careful with this phenomenon in the practical application. Therefore, if we use σ_h or σ_e repeatedly, $\varepsilon_m = 1\% \sim 2\%$ is optimum.

3.4. Shape memory effect and influnce of thermal expansion

In this section, we will discuss the recovery strain due to the shape memory effect and the variation in the stress due to thermal expansion.

In the case of maximum strain $\varepsilon_m = 8\%$, without holding constant the residual strain ε_p obtained by loading-unloading at temperature T_c, we heated the material to T_h under no load and cooled to T_c under no load. The strain-temperature curve obained by this test is shown in Fig. 7. As seen in Fig. 7, residual strain of about 6.3% appears after loading-unloading at $T_c = 303$ K. At this point, as seen from the stress-strain curve in Fig. 2, because $\varepsilon_m = 8\%$ is larger than the MT completion strain, the internal structure of the material is the M-phase. During the heating process, the reverse transformation starts at about 335 K and

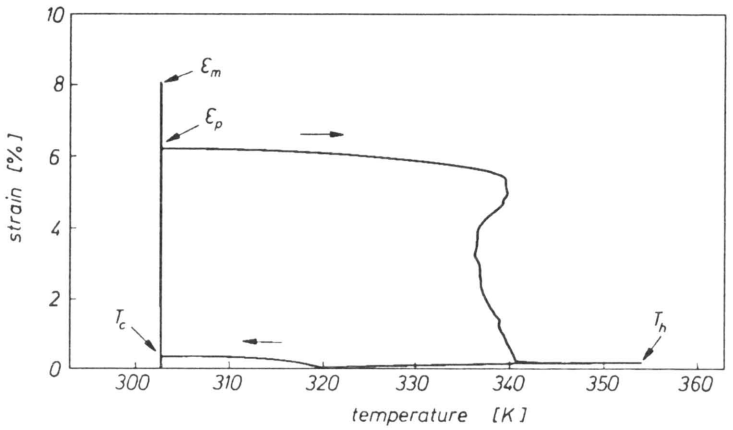

FIG. 7. Strain-temperature curve in the case of heating-cooling under no load after unloading.

completes at about 340 K. Strain decreases remarkably due to the reverse transformation. The phenomenon of strain recovery is called the shape memory effect. After completion of the reverse transformation, the crystal structure is the parent (austenite) phase. In the test following the reverse transformation, we heated the material to T_h = 353 K and cooled to T_c.

As seen in Fig. 7, at the start point of the reverse transformation, temperature rises transiently to about 340 K. The overshoot of temperature is the same phenomenon as the overshoot of stress at the start points of MT and the reverse transformation observed in the tensile test at constant temperature [21]. At the start point of the reverse transformation from the M-phase to the parent phase, the extra energy is necessary for creation of a nucleus to form the parent phase, and therefore the overshoot of temperature appears.

On the other hand, as seen in Fig. 7, during the heating process after unloading, strain of about 0.5% recovers from T_c to the reverse transformation start temeprature 335 K. If deformation occured due to a purely thermal expansion, then the strain would increase during the heating process. Because the strain decreases, some force to reduce the strain must be acting. The force may be caused by internal stress which occurs in the interface between the parent phase and the M-phase during the loading process [17, 18]. Because the internal stress acts as the force to recover the original shape, the effect of the internal stress is activated by heating, and therefore the strain recovers. It can be considered that, with respect to the stress-temperature curves in the case of ε_m = 8% in Figs. 2 and 5, the stress increasing gradually in proportion to temperature during the heating process is the recovery stress due to such internal stress.

As seen in Fig. 7, during the heating process from 340 K to 350 K, after completion of the reverse transformation, strain increases by about 3.3×10^{-2} %. Evaluating the increase in strain due to thermal expansion, the change in strain, $\Delta\varepsilon$, is as follows. Denoting the coefficient of thermal expansion by α, $\Delta\varepsilon$ due to

the variation in temperature ΔT is

$$\Delta\varepsilon = \alpha \cdot \Delta T. \tag{3.3}$$

The value of α is not necessarily constant and varies in a complex way, depending on temperature and its hysteresis [22]. If we take $\alpha = 10 \times 10^{-6}\,\mathrm{K}^{-1}$, $\Delta\varepsilon$ is $1 \times 10^{-2}\,\%$ for $\Delta T = 10\,\mathrm{K}$. This value is close to the strain increment $\Delta\varepsilon$ obtained by the experiment.

In the same manner, the recovery stress due to thermal expansion is explained as follows. The amount of decrease in stress due to purely thermal expansion under constant strain is

$$\Delta\sigma = E\alpha \cdot \Delta T. \tag{3.4}$$

The value of E varies considerably depending on the crystal structure and temperature [2]. If we take $E = 70\,\mathrm{GPa}$ and $\alpha = 10 \times 10^{-6}\,\mathrm{K}^{-1}$, $\Delta\sigma$ is 14 MPa for $\Delta T = 20\,\mathrm{K}$. As seen from the stress-temperature curves in Figs. 2 and 5, in the case of $\varepsilon_m = 0.5\%$ and 1%, the curves are straight lines decreasing to the right above the reverse transformation completion temperature. The amount of variation in stress $\Delta\sigma$ during the heating-cooling process is close to the value calculated above.

On the other hand, as seen in Fig. 7, strain increases from 320 K to 315 K during the cooling process. The phenomenon of increasing strain by cooling shows the two-way shape memory effect. The details of the dependence of the two-way shape memory effect on ε_m have not been determined.

4. Conclusions

We carried out the cyclic heating-cooling tests under constant residual strain for TiNi SMA and discussed the amount of recovery stress due to RPT and MT and the conditions under which it occurred. The main conclusions are as follows.

1. The recovery stress which occurs during the heating process increases along the reverse transformation lines of RPT and MT. For the maximum strain in the MT region, the recovery stress increases in two stages. With respect to the recovery stress increasing in two stages, the recovery stress due to MT is large when the maximum strain is large.

2. For the maximum strain in the MT region, the stress at high temperature is almost constant. With an increase in the maximum strain, the stress at low temperature increases and the recovery stress effective for cyclic heating-cooling decreases. Therefore if we use the recovery stress under thermal cycling, the maximum strain in the vicinity of the MT starting point is optimum.

3. Compared to the decrase in the MT stress subjected to strain variation, the amount of variation in the recovery stress under cyclic heating-cooling is very small.

Acknowledgements

The authors wish to express their gratitude to the students at Aichi Institute of Technology for their assistance in performing the exprimental work. The authors also wish to express their gratitude to Prof. K. KIMURA and Prof. H. IWANAGA for their support, and to the Scientific Foundation of the Japanese Ministry of Education, Science and Culture for financial support.

References

1. S. MIYAZAKI and K. OTSUKA, *Deformation and transition behavior associated with the R-phase in Ti-Ni alloys*, Metall. Trans. A, 17A, 53–63, 1986.
2. K. OTSUKA, *Introduction to the R-phase transition*, Engineering Aspects of Shape Memory Alloys, T.W. DUERIG, K.N. MELTON, D. STOCKEL and C.M. WAYMAN [Eds.], 36–45, Butterworth-Heinemann, 1990.
3. T. SAWADA, H. TOBUSHI, K. KIMURA, T. HATTORI, K. TANAKA and P.H. LIN, *Stress-strain-temperature relationship associated with the R-phase transformation in TiNi shape memory alloy*, JSME Inter. J, A, **36**, 4, 395–401, 1993.
4. H. FUNAKUBO [Ed.], *Shape memory alloys*, Gordon and Breach Science, New York 1987.
5. H. TOBUSHI, Y. OHASHI, T. HORI and S. KOJIMA, *Cyclic recovery stress of TiNi shape memory alloy under constant maximum strain*, Mechanical Behaviour of Materials – VI, M. JONO and T. INOUE [Eds.], 3, 255–260, Pergamon, 1991.
6. H. TOBUSHI, Y. OHASHI, H. SAIDA, T. HORI and S. SHIRAI, *Recovery stress and recovery strain of TiNi shape memory alloy*, JSME Inter. J., I, **35**, 1, 84–90, 1992.
7. H. HORIKAWA, Y. SUZUKI, A. HORIE, S. YAMAMOTO and Y. YASUDA, *Application of Ni-Ti-Nb shape memory alloy pipe couplings*, Proc. of Inter. Conf. on Martensitic Transformations, C.M. WAYMAN and J. PERKINS [Eds.], 1271–1276, Monterey Inst. for Advanced Studies, 1993.
8. T.W. DUERIG and K.N. MELTON, *Designing with the shape memory effect*, MRS Int'l. Mtg. on Adv. Mats., M. DOYAMA, S. SOMIYA and R.P.H. CHANG [Eds.], 9, 581–597, Mats. Res. Soc., 1989.
9. K. SUGIMOTO, K. KAMEI and M. NAKANIWA, *Cu-Al-Ni-Mn: A new shape memory alloy for high temperature applications*, 89–95, in Ref. 2.
10. J.L. PROFT and T.W. DUERIG, *The mechanical aspects of constrained recovery*, 115–129, in Ref. 2.
11. H. TOBUSHI, K. KIMURA, T. SAWADA, T. HATTORI and P.H. LIN, *Recovery stress associated with R-phase transformation in TiNi shape memory alloy*, JSME Inter. J., A, **37**, 2, 138–142, 1994.
12. S. LECLERCQ, C. LEXCELLENT, H. TOBUSHI and P.H. LIN, *Thermodynamical modelling of recovery stress associated with R-phase transformation in TiNi shape memory alloys*, Mats. Trans., JIM, **35**, 5, 325–331, 1994.
13. H. TOBUSHI, K. TANAKA, K. KIMURA, T. HORI and T. SAWADA, *Stress-strain-temperature relationship associated with the R-phase transformation in TiNi shape memory alloy*, JSME Inter. J., I, **35**, 3, 278–284, 1992.
14. K. TANAKA, S. KOBAYASHI and Y. SATO, *Thermomechanics of transformation pseudoelasticity and shape memory effect in alloys*, Inter. J. Plasticity, 2, 59–72, 1986.
15. K. TANAKA, T. HAYASHI, Y. ITOH and H. TOBUSHI, *Analysis of thermomechanical behaviour of shape memory alloys*, Mech. of Materials, **13**, 207–215, 1992.
16. H. TOBUSHI, K. TANAKA, T. HORI, T. SAWADA and T. HATTORI, *Pseudoelasticity of TiNi shape memory alloy*, JSME Inter. J., A, **36**, 3, 314–318, 1993.

17. S. MIYAZAKI, T. IMAI, Y. IGO and K. OTSUKA, *Effect of cyclic deformation on the pseudoelasticity characteristics of TiNi alloys*, Metall. Trans. A, **17A**, 115–120, 1986.

18. S. MIYAZAKI, *Thermal and stress cycling effects and fatigue properties of Ni-Ti alloys*, 394–413, in Ref. 2.

19. H. TOBUSHI, H. IWANAGA, K. TANAKA, T. HORI and T. SAWADA, *Deformation behaviour of TiNi shape memory alloy subjected to variable stress and temprature*, Continuum Mech. Thermodyn., 3, 79–93, 1991.

20. H. TOBUSHI, H. IWANAGA, K. TANAKA, T. HORI and T. SAWADA, *Stress-strain-temperature relationships of TiNi shape memory alloy suitable for thermomechanical cycling*, JSME Inter. J., I, **35**, 3, 271–277, 1992.

21. P.H. LIN, H. TOBUSHI, K. TANAKA, T. HATTORI and M. MAKITA, *Pseudoelastic behaviour of TiNi shape memory alloy subjected to strain variations*, J. Intelligent Mats. Systems Structures, 5, 694–701, 1994.

22. Page 75 in Ref. 4.

DEPARTMENT OF MECHANICAL ENGINEERING,
SOUTHEAST UNIVERSITY, NANJING, CHINA,

DEPARTMENT OF MECHANICAL ENGINEERING,
AICHI INSTITUTE OF TECHNOLOGY, YAGUSA-CHO, TOYOTA, JAPAN,

DEPARTMENT OF AEROSPACE ENGINEERING,
TOKYO METROPOLITAN INSTITUTE OF TECHNOLOGY, ASAHIGAOKA, HINO, TOKYO, JAPAN

and

LABORATOIRE DE MÉCANIQUE APPLIQUÉE
UNIVERSITÉ DE FRANCHE-COMTÉ, ROUTE DE GRAY, BESANÇON CEDEX, FRANCE.

Received November 2, 1994.

Arch. Mech., 47, 2, pp. 295–335, Warszawa 1995

Boundary value problems for Poisson's equation in a multi-wedge – multi-layered region (*)

G.S. MISHURIS (RZESZÓW)

A METHOD TO SOLVE ELLIPTIC PROBLEMS for plane domains, represented by wedges and layers, is discussed and applied to Poisson's equations. Linear conditions of general form are prescribed on the exterior boundaries and all the interfaces except the one between the regions of different geometry (layers and wedges). The latter contact boundary is characterized by the condition of a given discontinuity of the function itself and its normal derivative. The essence of the method consists in combining the Fourier and Mellin transforms along the mentioned contact lines. This allows us to reduce the problem to the system of singular integral equations with fixed point singularities. The theory, developed by the author elsewhere, is applied to investigate the equations. The analysis is significantly simplified by incorporating the geometrical feature of the layers and wedges: they present chain-like systems. The results, concerning existence and properties of the solutions, are interpreted also in terms of their physical meaning. The numerical method to solve the systems of equations is presented.

Introduction

THE METHOD OF INTEGRAL TRANSFORMS is very effective in solving the linear boundary value problems in specific domains. So the Fourier transform for layered domains and the Mellin transform for wedges make it possible to solve the respective problems [21, 22, 23].

Previously the idea of using the Fourier and Mellin transforms simultaneously to solve some plane and Mode III problems of linear elasticity for layered media with a notch or, in particular case, a crack, was presented in [12, 13]. The notch (crack) was symmetric with respect to the normal to the layers, the interface boundary conditions were of the "ideal type", and there were not any sources.

In [14] the method was presented in a general form for a symmetric domain, when there are sources inside the domain, and jumps of the solution (normal derivative of the solution) along the interface boundaries. All of the problems were reduced to a class of singular equations (systems of singular equations) on a semi-axis with fixed point singularities in the neighbourhood of zero and at infinity. To this aim it was essential that the composition of sine or cosine Fourier and the Mellin transforms should be represented in the form of a product of the Mellin transform with modified argument and a certain function of the argument.

In [11] the conditions were obtained for solvability of the systems of integral equations, and convergence of the projective methods of finding their numerical

(*) Paper presented at 30th Polish Solid Mechanics Conference, Zakopane, September 5–9, 1994.

solutions was proved. Some additional results of that analysis without proofs are presented in [14]. As indicated in [12, 14], the process of the numerical approximation of the solutions is very stable.

For the cases when the domain was not symmetric, similar problems were solved in [12] for Mode III and the "ideal" type of contact condition only. In this way explicit form of interconnection formulae played an important role. The recurrent relations obtained did not contain simultaneously increasing and decreasing exponential terms, as it happened with "transfer matrix method". Extensive literature on such problems is reviewed in [9]. But in the cases when the contact conditions along the bimaterial interface are in a more general form (in comparison with the "ideal" contact), finding similar relations in an explicit form is a complicated problem. Moreover, for each type of the exterior boundary conditions it must be done separately.

In [9] it is proved that the "sweep method" is very effective and is free of the mentioned shortcomings. It makes it possible to build the algorithm to interconnect the solutions in neighbouring regions. The exterior boundary conditions define the conditions of the first step of the recurrent process. So it is considered in general scheme.

In the paper we show that the "sweep method" and the method of integral transforms from [14] make it possible to solve linear boundary value problems in combined domains with general form of the interior and exterior conditions along the boundaries. As an example, we consider the problem of Poisson's equation. It can be the problem of heat conduction, mass diffusion in solids, theory of consolidation [18], and the antiplane problem of linear fracture mechanics. We shall use the terminology of the last problem.

The domain under consideration is assumed to be a region of multi-layered – multi-wedge composite with notch, or, in a particular case, with a crack (Fig. 1).

We shall consider numerous combinations of exterior boundary conditions. Contact conditions along the common boundaries (interior boundary conditions) shall be defined in one of the following forms: $([u] - \tau_i \sigma_i)_{|\Gamma_i} = \delta u_i$, $[\sigma]_{|\Gamma_i} = \delta q_i$, – when the contact regions are layers, and $([u] - r\tau_j \sigma_j)_{|\Gamma_j} = \delta u_j$, $[\sigma]_{|\Gamma_j} = \delta q_j$, in the case of wedges. Here by $[f]_{|\Gamma_i}$ we denote a jump of a function f across the boundary Γ_i, u, σ are the displacement and traction vectors in the case of mechanical approach. These conditions generalize the usual "ideal" type of contact conditions obtained when $\tau_i, \tau_j = 0$. The mentioned formulae follow from conjugation conditions between two regions across thin intermediate domain [7]. It is clear that the geometry of the intermediate domain depends on the geometry of contact regions and can be either a thin layer or a thin wedge. So, in the case when we deal with Mode III for elastic homogeneous materials, the constants in the respective relations are of the form: $\tau_i = h_i^*/\mu_i^*$, $\tau_j = \phi_j^*/\mu_j^*$ and from the assumptions it follows that $\tau_i, \tau_j \ll 1$. Here μ_i^* is the shear modulus and h_i^*, ϕ_j^* are the respective geometric parameters of thin intermediate

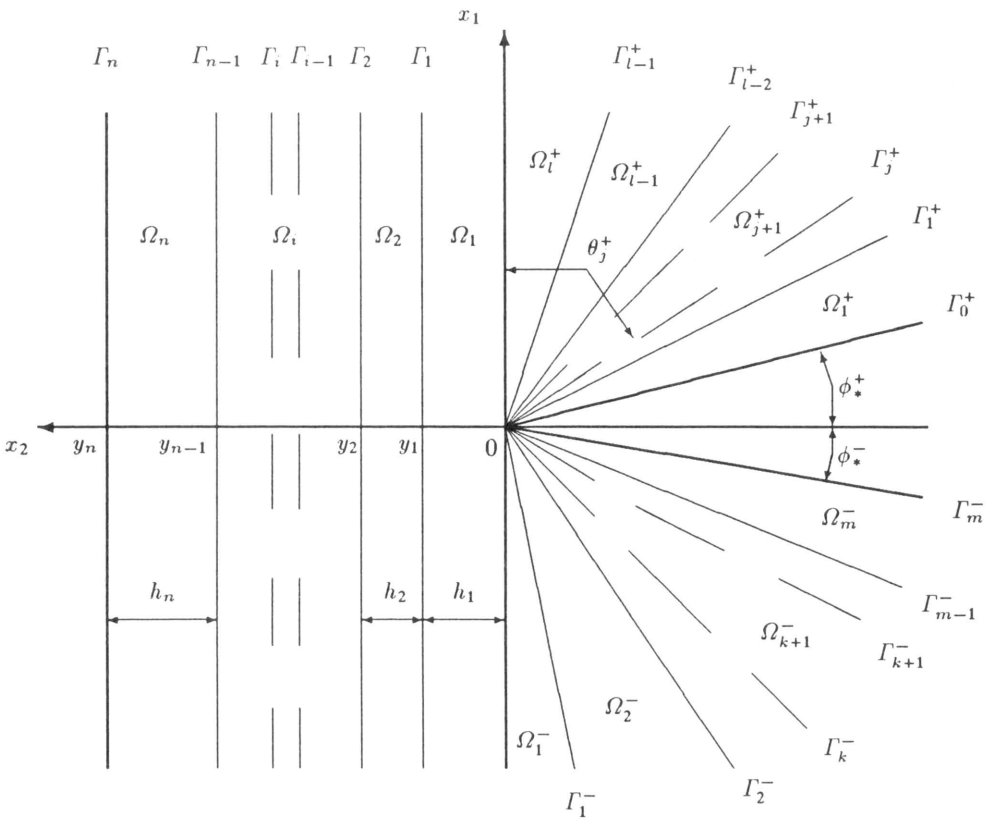

FIG. 1. The domain Ω under consideration.

domains. Furthermore, these conditions can be considered independently of the particular model of the thin interconnecting domain. Then the parameters can be interpreted as a measure of pliability of the adhesive.

On the interfaces between the different geometrical regions we shall assume the "ideal" type conditions only. This is because that type of conditions determines in an essential way the class of solutions of the problem. *A priori* estimates of the functions of this class play an important role in reducing the problem to the integral equations. For conditions of a more general form (for example as those noted above), the class of solutions of the problem is changed. That is why we cannot consider all types of conditions in a general scheme.

Formulation of the problem is presented in Sec. 1 of the paper. Using the results obtained in Appendix A by means of the sweep method, fitting of the Fourier and Mellin transforms along the common boundaries between the layers and wedges is made in Sec. 2. In the third section the problems, for which all of geometrical and mechanical parameters are symmetric with respect to the OX_2-axis, are reduced to the integral equations. The general case is considered in the next section. Analysis of the integral equations and the systems of the

equations, obtained in two last sections, is drawn in Appendix B. Theorems concerning solvability of the equations, asymptotics of their solutions and possibility of application of numerical methods are presented.

1. Problem formulation

Let us consider the infinite domain presented in Fig. 1 which consists of layer part $\Omega_L = \bigcup_{i=1}^{n} \Omega_i$ and two wedge parts $\Omega^+ = \bigcup_{j=1}^{l} \Omega_j^+$, $\Omega^- = \bigcup_{k=1}^{m} \Omega_k^-$. Here

$$\begin{aligned} \Omega_i &= \{(x_1, x_2) : x_1 \in \mathbb{R},\ x_2 \in (y_{i-1}, y_i)\}, && i = 1, 2, \ldots, n, \\ \Omega_j^+ &= \{(r, \theta) : r \in \mathbb{R}_+,\ \theta \in (\theta_{j-1}^+, \theta_j^+)\}, && j = 1, 2, \ldots, l, \\ \Omega_k^- &= \{(r, \theta) : r \in \mathbb{R}_+,\ \theta \in (\theta_{k-1}^-, \theta_k^-)\}, && k = 1, 2, \ldots, m. \end{aligned}$$

The boundaries of the regions we denote by

$$\begin{aligned} \Gamma_i &= \{(x_1, x_2) : x_1 \in \mathbb{R},\ x_2 = y_i\}, && i = 0, 1, 2, \ldots, n, \\ \Gamma_j^+ &= \{(r, \theta) : r \in \mathbb{R}_+,\ \theta = \theta_j^+\}, && j = 0, 1, 2, \ldots, l, \\ \Gamma_k^- &= \{(r, \theta) : r \in \mathbb{R}_+,\ \theta = \theta_k^-\}, && k = 0, 1, 2, \ldots, m. \end{aligned}$$

Moreover, $\Gamma_0 = \Gamma_l^+ \cup \Gamma_0^-$ and

$$\begin{aligned} 0 = y_0 < \ldots < y_i < y_{i+1} < \ldots < y_n \le \infty, &\qquad h_i = y_i - y_{i-1}, \\ -\pi = \theta_0^- < \ldots < \theta_k^- < \theta_{k+1}^- < \ldots < \theta_m^- = -\frac{\pi}{2} + \phi_*^-, &\qquad \phi_k^- = \theta_k^- - \theta_{k-1}^-, \\ -\frac{\pi}{2} + \phi_*^+ = \theta_0^+, \ldots < \theta_j^+ < \theta_{j+1}^+ < \ldots < \theta_l^+ = 0, &\qquad \phi_j^+ = \theta_j^+ - \theta_{j-1}^+. \end{aligned}$$

Further all values, referring to the layered part of the domain (Ω_L) will be denoted by index i, but the one referring to the wedges parts (Ω^+, Ω^-), will be marked with indices j, k.

We shall seek the function $u(x_1, x_2)$ which satisfies the Poisson equation (1.1) inside the corresponding regions Ω_i, Ω_j^+, Ω_k^-:

$$\begin{aligned} -\mu_i \Delta u_i &= W_i, && (x_1, x_2) \in \Omega_i, \\ -\mu_j^+ \Delta u_j^+ &= W_j^+, && (r, \theta) \in \Omega_j^+, \\ -\mu_k^- \Delta u_k^- &= W_k^-, && (r, \theta) \in \Omega_k^-, \end{aligned} \tag{1.1}$$

with certain positive constants μ_i, μ_j^+, μ_k^-.

Along the interior boundaries of the layered domain Ω_L the conditions hold:

$$\begin{aligned} \left(u_{i+1} - u_i - \mu_i \tau_i \frac{\partial}{\partial x_2} u_i\right)\Big|_{\Gamma_i} &= \delta u_i(x_1), && x_1 \in \mathbb{R}, \quad i = 1, 2, \ldots, n-1, \\ \frac{\partial}{\partial x_2}(\mu_{i+1} u_{i+1} - \mu_i u_i)\Big|_{\Gamma_i} &= \delta q_i(x_1), && x_1 \in \mathbb{R}. \end{aligned} \tag{1.2}$$

Analogous relations for the interior bounds of wedged domains $\Omega^{\pm}$ can be written in the form:

$$
\begin{aligned}
&\left(u_{j+1}^{+} - u_j^{+} - \mu_j^{+}\tau_j^{+}\frac{\partial}{\partial\theta}u_j^{+}\right)\Big|_{\Gamma_j^{+}} = \delta u_j^{+}(r), \quad r \in \mathbb{R}_+, \quad j = 1,2,\ldots,l-1,\\
&\frac{1}{r}\frac{\partial}{\partial\theta}(\mu_{j+1}^{+}u_{j+1}^{+} - \mu_j^{+}u_j^{+})\Big|_{\Gamma_j^{+}} = \delta q_j^{+}(r), \quad r \in \mathbb{R}_+;
\end{aligned} \tag{1.3}
$$

$$
\begin{aligned}
&\left(u_{k+1}^{-} - u_k^{-} - \mu_k^{-}\tau_k^{-}\frac{\partial}{\partial\theta}u_k^{-}\right)\Big|_{\Gamma_k^{-}} = \delta u_k^{-}(r), \quad r \in \mathbb{R}_+, \quad k = 1,2,\ldots,m-1,\\
&\frac{1}{r}\frac{\partial}{\partial\theta}(\mu_{k+1}^{-}u_{k+1}^{-} - \mu_k^{-}u_k^{-})\Big|_{\Gamma_k^{-}} = \delta q_k^{-}(r), \quad r \in \mathbb{R}_+,
\end{aligned} \tag{1.4}
$$

where τ_i, τ_j^{+}, $\tau_k^{-} \geq 0$ are certain constants.

Finally, the last of the interior conditions between the regions of different geometry (along the boundaries Γ_l^{+}, Γ_0^{-}) are "ideal", i.e.

$$
\begin{aligned}
(u_1 - u_l^{+})\big|_{\Gamma_l^{+}} &= \delta u^{+}(x_1),\\
\frac{\partial}{\partial x_2}(\mu_1 u_1 - \mu_l^{+}u_l^{+})\Big|_{\Gamma_l^{+}} &= \delta q^{+}(x_1), \qquad x_1 > 0.
\end{aligned} \tag{1.5}
$$

$$
\begin{aligned}
(u_1 - u_1^{-})\big|_{\Gamma_0^{-}} &= \delta u^{-}(x_1),\\
\frac{\partial}{\partial x_2}(\mu_1 u_1 - \mu_1^{-}u_1^{-})\Big|_{\Gamma_0^{-}} &= \delta q^{-}(x_1), \qquad x_1 < 0.
\end{aligned} \tag{1.6}
$$

Now we define the exterior boundary conditions for the domain Ω. So, on the wedge boundaries Γ_0^{+}, Γ_m^{-}, one of the following relations holds:

$$
\begin{aligned}
&\text{(a)} \qquad u_1^{+}\big|_{\Gamma_0^{+}} = \delta u_0^{+}(r), \qquad r \in \mathbb{R}_+,\\
&\text{(b)} \qquad \mu_1^{+}\frac{1}{r}\frac{\partial}{\partial\theta}u_1^{+}\big|_{\Gamma_0^{+}} = \delta q_0^{+}(r), \qquad r \in \mathbb{R}_+,
\end{aligned} \tag{1.7}
$$

$$
\begin{aligned}
&\text{(a)} \qquad u_m^{-}\big|_{\Gamma_m^{-}} = -\delta u_m^{-}(r), \quad r \in \mathbb{R}_+,\\
&\text{(b)} \qquad \mu_m^{-}\frac{1}{r}\frac{\partial}{\partial\theta}u_m^{-}\big|_{\Gamma_m^{-}} = -\delta q_m^{-}(r), \quad r \in \mathbb{R}_+.
\end{aligned} \tag{1.8}
$$

On the exterior boundary Γ_n we shall consider conditions (a), (b) analogous to (1.7), (1.8) and the relation (c):

$$
\begin{aligned}
&\text{(a)} \qquad u_n\big|_{\Gamma_n} = -\delta u_n(x_1), \quad x_1 \in \mathbb{R},\\
&\text{(b)} \qquad \mu_n\frac{\partial}{\partial x_2}u_n\big|_{\Gamma_n} = -\delta q_n(x_1), \quad x_1 \in \mathbb{R},\\
&\text{(c)} \qquad \lim_{x_2\to\infty} u_{n+1} = 0.
\end{aligned} \tag{1.9}
$$

In the case (c) we assume that the last region Ω_{n+1} is a half-plane. Then the condition $(1.9)_c$ means that the solution of the problem tends to zero both in the direction $x_2 \to \infty$ and $x_1 \to \infty$. Consequently, we have here nine different combinations of exterior conditions. The corresponding problems (1.1)–(1.6) with the boundary conditions (1.7)–(1.9) are denoted by problems $(\mathcal{J}^+, \mathcal{J}^-, \mathcal{J})$, where $(\mathcal{J}^+ = 1,2;\ \mathcal{J}^- = 1,2;\ \mathcal{J} = 1,2,3)$. Here the value of $\mathcal{J}^+$ is equal 1 (or 2) if the condition $(1.7)_a$ (or $(1.7)_b$) holds. In an analogous way one can define the values of $\mathcal{J}^-$, $\mathcal{J}$ from the conditions (1.8) and (1.9), respectively.

We assume that all the functions which appear in the equations and the boundary conditions are sufficiently smooth:

$$
\begin{gathered}
W_i \in \mathbf{C}(\overline{\Omega_i}), \qquad W_j^{\pm} \in \mathbf{C}(\overline{\Omega_i^{\pm}}), \\
\delta q_i \in \mathbf{C}^1(\overline{\mathbb{R}}), \qquad \delta q^+, \delta q^-, \delta q_j^{\pm} \in \mathbf{C}^1(\overline{\mathbb{R}_+}), \\
\delta u_i \in \mathbf{C}^2(\overline{\mathbb{R}}), \qquad \delta u^+, \delta u^-, \delta u_j^{\pm} \in \mathbf{C}^2(\overline{\mathbb{R}_+}), \\
\delta u_i, \delta u^+, \delta u^-, \delta u_j^{\pm} = O(r^{-2}), \qquad r \to \infty, \\
r\delta q_i, r\delta q^+, r\delta q^-, r\delta q_j^{\pm}, r^2 W_i, r^2 W_j^{\pm} = O(r^{-2}), \qquad r \to \infty, \\
\delta u^+, \delta u^-, \delta u_j^{\pm} = o(r^2), \qquad r \to 0.
\end{gathered} \tag{1.10}
$$

The assumptions concerning the defined functions are adopted in the forms (1.10) in order to have singularities of the solutions, connected with the interior properties of the problems only. In the opposite case (when the defined functions are not smooth and have any singularities) it is easy to find special solutions of the problems accounting for these singularities. Then, using the linearity of the problems, we can find their solution as a sum of two functions. The first one is this special solution, and the second function is the solution of the problem without any singularities in the right-hand sides of the equations and the boundary conditions.

We shall seek the regular solutions of the problems $(\mathcal{J}^+, \mathcal{J}^-, \mathcal{J})$ in a class of functions $\mathbf{LW}(\Omega)$ such that $u \in \mathbf{LW}(\Omega)$ if the following relations are true:

$$
\begin{aligned}
& u_{|_G} \in \mathbf{C}^2(G), \\
& u(r) = O(r^{-\gamma_1}), \qquad r\operatorname{grad} u(r) = O(r^{-\gamma_2}), \qquad r \to \infty, \\
& u(r) = u_* + O(r^{\gamma_0}), \qquad r\operatorname{grad} u(r) = O(r^{\gamma_0}), \qquad r \to 0.
\end{aligned} \tag{1.11}
$$

Here G denotes each region of Ω and γ_0, γ_1, γ_2 are certain constants such that $0 < \gamma_0 < 1$; $\gamma_1, \gamma_2 > 0$. Besides, in the cases of the first type boundary condition at least on one exterior boundary of the wedge $(\mathcal{J}^+\mathcal{J}^- < 4)$, additional relation holds:

$$
u_*(\mathcal{J}^+, \mathcal{J}^-, \mathcal{J}) = 0.
$$

REMARK 1. It can be shown that the solution of the problem $(\mathcal{J}^+, \mathcal{J}^-, \mathcal{J})$ from $\mathbf{LW}(\Omega)$ with the values of the parameters as above belongs to an energetic space of the corresponding linear boundary problem [16]. Therefore, the

problems in the class $\mathbf{LW}(\Omega)$ have unique solutions. The fact that $u_* = 0$ in the same problems follows from the corresponding boundary conditions and from the properties of the functions from $\mathbf{LW}(\Omega)$. Accurate values of the parameters $\gamma_0 = \gamma_0(\mathcal{J}^+, \mathcal{J}^-, \mathcal{J})$, $\gamma_1 = \gamma_1(\mathcal{J}^+, \mathcal{J}^-, \mathcal{J})$, $\gamma_2 = \gamma_2(\mathcal{J}^+, \mathcal{J}^-, \mathcal{J})$, $u_* = u_*(2, 2, \mathcal{J})$ will be obtained. Let us note that the value of γ_0 defines the order of singularity of grad $u(r)$ in the neighbourhood of zero, and plays an important role in physical applications [2].

2. Fitting of Fourier and Mellin transforms along Γ_0

Applying the Fourier and Mellin transforms to the equation (1.1) and to the exterior and interior boundary conditions (1.2)–(1.9) in respective domains and using the sweep method [9], we obtain the following relations between the transformations of unknown functions along the boundary Γ_0 (see Eqs. (A.22), (A.45), (A.46) in Appendix A):

$$\mathbf{u}_b^1(\lambda) = M_p(\lambda)(\overline{z}_+(\lambda) + \overline{z}_-(\lambda)) + m_p^+(\lambda) + m_p^-(\lambda), \tag{2.1}$$

$$\mathbf{v}_l^l(s) = M_q(s)(\tilde{z}_+(s+1) + \tilde{z}_-(s+1) - \Delta q_*(s)) + m_q(s), \tag{2.2}$$

$$\mathbf{w}_b^1(s) = M_r(s)(\tilde{z}_-(s+1) - \tilde{z}_+(s+1) + \Delta r_*(s)) + m_r(s), \tag{2.3}$$

where

$$\mathbf{u}_b^1(\lambda) = \overline{u}_1|_{\Gamma_0}, \qquad \mathbf{v}_l^l(s) = \tilde{u}_l^+|_{\Gamma_l^+}, \qquad \mathbf{w}_b^1(s) = \tilde{u}_1^-|_{\Gamma_0^-}$$

are the Fourier and Mellin transformations, defined in the usual way (A.2), (A.28). Functions M_p, $m_p^\pm$, M_q, m_q, M_r, m_r are obtained in Appendix A (see (A.23), (A.47)). Their behaviour depends essentially on the exterior boundary conditions (1.7)–(1.9) (see Lemma A.1, Lemma A.2).

The unknown odd and even functions z_-, z_+ appearing at the right-hand sides of the equations (2.1)–(2.3) are defined by the relation (A.12):

$$z_+(x_1) + z_-(x_1) = \mu_1 \frac{\partial}{\partial x_2} u_1|_{\Gamma_0}. \tag{2.4}$$

Now, we have the situation when equations (1.1) and all the interior and exterior boundary conditions (1.2)–(1.9) are satisfied, except $(1.5)_a$, $(1.6)_a$. Moreover, the contact condition $(1.5)_b$, $(1.6)_b$ are satisfied also owing to choice of the right-hand sides of the equations (2.2), (2.3), (where $\Delta q_*(s) = \widetilde{\delta q}^+(s+1)$, $\Delta r_*(s) = \widetilde{\delta q}^-(s+1)$, see (A.40), (A.44) in Appendix A).

So, once the functions z_+, z_- are known, all of the functions $u_i(x_1, x_2)$, $u_j^+(r, \theta)$, $u_k^-(r, \theta)$ will be calculated by the formulae (A.19)–(A.21), (A.37), (A.41) and the inverse Fourier and Mellin transforms.

Then the remaining conditions $(1.5)_a$, $(1.6)_a$ along the bounds Γ_0^-, Γ_l^+ are used to find the functions z_+, z_-, which (as it follows from the *a priori* assumptions (1.11)) must satisfy the conditions (A.24) (Corollary A.1 to Lemma A.1 from Appendix A).

The equations $(1.5)_a$, $(1.6)_a$ can be rewritten in the form:

$$u_1|_{\Gamma_l^+}(x_1) = (u_l^+ + \delta u^+)|_{\Gamma_l^+}(r), \qquad x_1 = r, \tag{2.5}$$

$$u_1|_{\Gamma_0^-}(x_1) = (u_1^- + \delta u^-)|_{\Gamma_0^-}(r), \qquad x_1 = -r. \tag{2.6}$$

We can represent the function u_1 in (2.5), (2.6) by the inverse Fourier transform

$$u_1(x_1) = \mathcal{F}^{-1}[\mathbf{u}_b^1](x_1),$$

or, taking into account (2.1) and parity of the functions M_p, $m_p^{\pm}$:

$$u_1(x_1) = 2\mathcal{F}_c^{-1}\left[M_p\overline{z}_+ + m_p^+\right](x_1) - 2i\mathcal{F}_s^{-1}\left[M_p\overline{z}_- + m_p^-\right](x_1), \tag{2.7}$$

where

$$\mathcal{F}_c^{-1}[u(\lambda);\ \lambda \to x_1] \equiv \int_0^\infty u(\lambda)\cos(\lambda x_1)\,d\lambda,$$

$$\mathcal{F}_s^{-1}[u(\lambda);\ \lambda \to x_1] \equiv \int_0^\infty u(\lambda)\sin(\lambda x_1)\,d\lambda,$$

are the sine and cosine Fourier transforms [21].

Replacing in (2.5), (2.6) the argument of x_1 by r and $-r$, respectively, and applying the Mellin transform (A.28) to both sides of the equations, we obtain

$$\begin{aligned} 2\mathcal{M}\mathcal{F}_c^{-1}[M_p\overline{z}_+ + m_p^+](s) - 2i\mathcal{M}\mathcal{F}_s^{-1}[M_p\overline{z}_- + m_p^-](s) &= \mathbf{v}_t^l + \Delta v_l, \\ 2\mathcal{M}\mathcal{F}_c^{-1}[M_p\overline{z}_+ + m_p^+](s) + 2i\mathcal{M}\mathcal{F}_s^{-1}[M_p\overline{z}_- + m_p^-](s) &= \mathbf{w}_b^l + \Delta w_0, \end{aligned} \tag{2.8}$$

where $\Delta w_0 = \mathcal{M}[\delta u^-](s)$, $\Delta v_l = \mathcal{M}[\delta u^+](s)$. Substituting $\mathbf{v}_t^l$, $\mathbf{w}_b^1$ from (2.2), (2.3) in the equations (2.8), they can be rewritten in the form:

$$\begin{aligned} 2\mathcal{M}\mathcal{F}_c^{-1}[M_p\overline{z}_+ + m_p^+](s) &= M_+(s)\widetilde{z}_-(s+1) + M_-(s)\widetilde{z}_+(s+1) + d_1(s), \\ 2i\mathcal{M}\mathcal{F}_s^{-1}[M_p\overline{z}_- + m_p^-](s) &= -M_-(s)\widetilde{z}_-(s+1) - M_+(s)\widetilde{z}_+(s+1) + d_2(s). \end{aligned} \tag{2.9}$$

Here we denote functions $M_\pm(s)$, $d_i(s)$, $(i = 1, 2)$ by

$$M_+(s) = \frac{1}{2}(M_q(s) + M_r(s)),$$

$$M_-(s) = \frac{1}{2}(M_q(s) - M_r(s)),$$
$$d_1(s) = \frac{1}{2}(M_r\Delta r_* - M_q\Delta q_* + m_r + m_q + \Delta v_l + \Delta w_0),$$
$$d_2(s) = \frac{1}{2}(M_r\Delta r_* + M_q\Delta q_* + m_r - m_q + \Delta w_0 - \Delta v_l).$$

As it follows from (1.11), Eqs. (2.9) hold, in general, in the strip $0 < \Re s < \gamma_1$. They constitute the system of two functional equations of functions $z_\pm(\lambda)$. We can conveniently consider the system in terms of the functions $\overline{z}_\pm(\lambda)$. To this aim we represent the unknown functions of the right-hand sides of the equations in the form

$$\begin{aligned} \widetilde{z}_+(s+1) &= 2\mathcal{M}\mathcal{F}_c^{-1}[\overline{z}_+](s+1), \\ \widetilde{z}_-(s+1) &= -2i\mathcal{M}\mathcal{F}_s^{-1}[\overline{z}_-](s+1). \end{aligned} \tag{2.10}$$

Let us note that the operators $\mathcal{M}\mathcal{F}_c^{-1}$, $\mathcal{M}\mathcal{F}_s^{-1}$ can be generated in the form of a product of one integral operator, the Mellin transform with modified argument, and certain functions of that argument. Namely, for any $0 < \alpha, \beta < 1$ the identities hold

$$\begin{aligned} \mathcal{M}\mathcal{F}_c^{-1}[u_+](s) &= \Gamma(s)\cos\frac{\pi s}{2}\mathcal{M}[u_+](1-s), \qquad 0 < \Re s < \beta, \\ \mathcal{M}\mathcal{F}_s^{-1}[u_-](s) &= \Gamma(s)\sin\frac{\pi s}{2}\mathcal{M}[u_-](1-s), \qquad -\alpha < \Re s < \beta. \end{aligned} \tag{2.11}$$

The relations (2.11) are obtained by integrating directly [19]. To do this it is necessary that functions $u_\pm$ summable on $\mathbb{R}_+$ should satisfy the estimates:

$$\begin{aligned} u_\pm(\lambda) &= o(\lambda^{-1+\beta}), \qquad \lambda \to 0, \\ u_\pm(\lambda) &= o(\lambda^{-1-\alpha}), \qquad \lambda \to \infty. \end{aligned} \tag{2.12}$$

Besides, the first equation from (2.11) can be extended to a wider strip than that assumed above. Really, it can be seen that the right-hand side of $(2.11)_1$ is an analytic function in the strip $-\alpha < \Re s < \beta$, maybe except one point $s = 0$. In that point it can have a simple pole, connected with the behaviour of gamma-function. From (2.12) and the properties of the Fourier transform it follows that

$$\mathcal{F}_c^{-1}[u_+] = \text{Const} + O(x^\alpha), \qquad x \to 0.$$

This fact makes it possible to extend analytically the left-hand side of Eq. $(2.11)_1$ to the whole strip $-\alpha < \Re s < \beta$.

As it follows from (A.24), the terms $[M_p\overline{z}_\pm + m_p^\pm](\lambda)$ satisfy exactly the conditions (2.12) with $\alpha = \gamma_0$ and $\beta = \min\{1, \gamma_1\}$. Consequently, the left-hand sides of the equations (2.9) can be reduced to the form

$$\begin{aligned} 2\mathcal{M}\mathcal{F}_c^{-1}[M_p\overline{z}_+ + m_p^+](s) &= 2\Gamma(s)\cos\frac{\pi s}{2}\mathcal{M}[M_p\overline{z}_+ + m_p^+](1-s), \\ 2i\mathcal{M}\mathcal{F}_s^{-1}[M_p\overline{z}_- + m_p^-](s) &= 2i\Gamma(s)\sin\frac{\pi s}{2}\mathcal{M}[M_p\overline{z}_- + m_p^-](1-s), \end{aligned} \tag{2.13}$$

where identities hold in the strip $-\gamma_0 < \Re s < \min\{1, \gamma_1\}$ and a simple pole in the point $s = 0$ is possible,

$$2\mathcal{M}\mathcal{F}_c^{-1}[M_p\overline{z}_+ + m_p^+](s) = \frac{1}{s}u_\star + O(1), \qquad s \to 0. \tag{2.14}$$

The identities (2.11) cannot be directly used to reduce the operators $\mathcal{M}\mathcal{F}_c^{-1}$, $\mathcal{M}\mathcal{F}_s^{-1}$ which appear in the right-hand sides of (2.9). The reason is that the arguments of the operators are situated in the wrong region and the conditions as (2.12) are not satisfied for the functions $z_\pm(\lambda)$. However, it can be shown that relations similar to (2.9) hold in this case also. Namely,

$$\begin{aligned} \mathcal{M}\mathcal{F}_c^{-1}[u_+](s+1) &= -\Gamma(s)\sin\frac{\pi s}{2}\mathcal{M}[u'_+](1-s), \\ \mathcal{M}\mathcal{F}_s^{-1}[u_-](s+1) &= \Gamma(s)\cos\frac{\pi s}{2}\mathcal{M}[u'_-](1-s), \end{aligned} \tag{2.15}$$

in the strip $-\alpha < \Re s < \beta$, when the following estimates are satisfied:

$$\begin{aligned} u_\pm(\lambda), \quad \lambda\frac{\partial}{\partial\lambda}u_\pm(\lambda) &= o(\lambda^{-\alpha}), && \lambda \to \infty, \\ u_-(\lambda), \quad \lambda\frac{\partial}{\partial\lambda}u_\pm(\lambda) &= o(\lambda^{\beta}), && \lambda \to 0, \\ u_+(\lambda) &= u_+(0) + o(\lambda^\beta), && \lambda \to 0. \end{aligned}$$

Then, by integrating by parts we can obtain the identities

$$\begin{aligned} \mathcal{M}\mathcal{F}_c^{-1}[u_+](s+1) &= -\Gamma(s+1)\sin\frac{\pi s}{2}\mathcal{M}[u^*_+](-s) + \frac{\pi}{2}u_+(0)\Gamma(s+1), \\ \mathcal{M}\mathcal{F}_s^{-1}[u_-](s+1) &= -\Gamma(s+1)\cos\frac{\pi s}{2}\mathcal{M}[u_-](-s). \end{aligned} \tag{2.16}$$

Here we choose the function of $u^*_+(\lambda)$ in the form

$$u^*_+(\lambda) = u_+(\lambda) - u_+(0)(1+\lambda^2)^{-1}, \tag{2.17}$$

such that the following relations are satisfied

$$u^*_+(\lambda) = O(\lambda^{\min\{\beta,2\}}), \quad \lambda \to 0, \qquad u^*_+(\lambda) = O(\lambda^{-\min\{\alpha,2\}}), \quad \lambda \to \infty.$$

It remains now to see that the conditions necessary to satisfy Eqs. (2.15) are identical with the estimates (A.24) for functions $z_\pm(\lambda)$ with $\alpha = \gamma_0$, $\beta = \gamma_2$. Hence, the system of functional equations (2.8) can be reduced to the following form:

$$\widehat{\mathbf{Y}}(s) = \mathbf{\Phi}(s)\widehat{\mathbf{Z}}(s) + F(s), \qquad -\gamma_0 < \Re s < \gamma_\infty, \tag{2.18}$$

where we introduce the symbols: $\widehat{u}(s) = \widetilde{u}(-s) = \mathcal{M}[u](-s)$, $d_*(s) = z_*^+ \pi \Gamma(s+1)$, $\gamma_\infty = \min\{1, \gamma_1, \gamma_2\}$ and

$$\mathbf{Z}(\lambda) = \begin{pmatrix} \overline{z}_+^*(\lambda) \\ i\overline{z}_-(\lambda) \end{pmatrix},$$

$$F(s) = \frac{\mu_1}{\Gamma(s)\sin \pi s} \begin{pmatrix} (d_1(s) + M_+ d_*(s)) \sin \dfrac{\pi s}{2} \\ (d_2(s) - M_- d_*(s)) \cos \dfrac{\pi s}{2} \end{pmatrix},$$

$$\mathbf{Y}(\lambda) = \mu_1 \begin{pmatrix} \lambda M_p \overline{z}_+(\lambda) + \lambda m_p^+ \\ i(\lambda M_p \overline{z}_-(\lambda) + \lambda m_p^-) \end{pmatrix},$$

$$\mathbf{\Phi}(s) = \mu_1 \begin{pmatrix} -sM_-(s)\mathrm{tg}\dfrac{\pi s}{2} & -sM_+(s) \\ sM_+(s) & sM_-(s)\mathrm{ctg}\dfrac{\pi s}{2} \end{pmatrix},$$

$$\overline{z}_+^*(\lambda) = \overline{z}_+(\lambda) - z_*^+(1+\lambda^2)^{-1}, \qquad z_+^*(x_1) = z_+(x_1) - z_*^+ \pi \exp(-|x_1|).$$

Here the constant $z_*^+ = z_+(0)$ is defined in (A.24), (A.49) for some types of the boundary conditions. We normalize the vector functions $F(s)$, $\mathbf{Y}(\lambda)$ and matrix function $\mathbf{\Phi}(s)$ by μ_1 such that the vector functions $\mathbf{Y}(\lambda)$, $\mathbf{Z}(\lambda)$ have similar dimensions. In such case the matrix function $\mathbf{\Phi}(s)$ has not any physical dimensionality.

A priori estimates (A.24) are true for the vector functions $\mathbf{Y}(\lambda)$, $\mathbf{Z}(\lambda)$ also. Therefore, the functions are analytic in the strips $-\gamma_0 < \Re s < \gamma_1$ and $-\gamma_0 < \Re s < \gamma_2$, respectively. Using Lemma A.1 of Appendix A and the equation (2.17) it can be shown that

$$\mathbf{Y}(\lambda) + \mathbf{Z}(\lambda) = O(\lambda^{-2}), \qquad \lambda \to \infty. \tag{2.19}$$

Taking this fact into account, we rewrite the equations (2.18) in the form

$$\left[\widehat{\mathbf{Y}} + \widehat{\mathbf{Z}}\right](s) = \mathbf{\Phi}_*(s)\widehat{\mathbf{Z}}(s) + F(s), \qquad \mathbf{\Phi}_*(s) = \mathbf{I} + \mathbf{\Phi}(s). \tag{2.20}$$

From (2.19) it follows that the left-hand side of (2.20) is an analytic vector function in the strip $-2 < \Re s < \gamma_\infty$, which is wider that the analiticity strips of $\mathbf{Y}(\lambda)$, $\mathbf{Z}(\lambda)$ separately.

To conclude, one can say that *a priori* estimates of the solution play an important role in "fitting" the integral transforms along boundary Γ_0.

3. Reduction of the problems in symmetric domain to integral equations

First of all let us consider the case which is of special interest, when the domain Ω and all the boundary conditions are symmetric with respect to OX_2-axis (see

Corollary A.2 from Appendix A). In that case $M_+(s) = 0$, $M_-(s) = M_q(s)$ and the system (2.20) splits up, what could be expected, into two equations ($i = 1, 2$)

$$\frac{1}{\Delta_j(s)} [\widehat{\mathbf{y}}_j + \widehat{\mathbf{z}}_j] (s) - \widehat{\mathbf{z}}_j(s) = \frac{1}{\Delta_j(s)} f_j(s). \tag{3.1}$$

Here y_j, z_j, f_j are the respective components of the vectors $\mathbf{Y}$, $\mathbf{Z}$, F, and $\Delta_j(s)$ – diagonal elements of the matrix function $\mathbf{\Phi}_*$ – are

$$\Delta_j(s, \mathcal{J}^+) = 1 + (-1)^j \mu_1 s M_q(s, \mathcal{J}^+)[\mathrm{tg}(\pi s/2)]^{3-2j}. \tag{3.2}$$

Equations (3.1) for $j = 1$ ($j = 2$) correspond to the problems $(1, 1, \mathcal{J})$ and $(2, 2, \mathcal{J})$ for $\mathcal{J} = 1, 2, 3$, in which all of the defined functions are symmetric (skew-symmetric) with respect to the OX_2-axis. In this way the solutions of the problems are even (odd) functions of argument x_1.

We denote the "symmetric" problems $(\mathcal{J}^+, \mathcal{J}^+, \mathcal{J})$ ($\mathcal{J}^+ = 1, 2$, $\mathcal{J} = 1, 2, 3$) by $\{1, \mathcal{J}^+, \mathcal{J}\}$, but the "skew-symmetric" problems $(\mathcal{J}^+, \mathcal{J}^+, \mathcal{J})$ by $\{2, \mathcal{J}^+, \mathcal{J}\}$. So, the parameter $j = 1, 2$ corresponds to the even or odd components of the solution of the initial problem $(\mathcal{J}^+, \mathcal{J}^+, \mathcal{J})$.

As it follows from Lemma A.2 (see Appendix A), $\Delta_j(it)$ are real, even functions, which are not equal to zero for all values of t. We denote by $\omega_\infty = \omega_\infty(j, \mathcal{J}^+)$ the zeros of the functions $\Delta_j(s)$ which are the nearest to the imaginary axis (inside the half-plane $\Re s > 0$). Taking into account the properties of the function $M_q(s)$ (Lemma A.2), it can be obtained that ω_∞ are real, and the inequality holds $0 < \omega_\infty < 2$. The values of ω_∞ depend on μ_1, geometric and elastic parameters of the wedges $\mu_k^\pm$, $\theta_k^\pm$, contact constants $\tau_k^\pm$ and the type of the exterior boundary conditions ($\mathcal{J}^+ = 1, 2$) along the wedge boundaries. At the same time the magnitudes of ω_∞ do not depend on any parameters (except μ_1) and on any interior and exterior boundary conditions inside the layered domain Ω_L. It can be also shown that

$$0 < \omega_\infty(1, 1), \quad \omega_\infty(2, 2) < 1; \qquad 1 < \omega_\infty(1, 2), \quad \omega_\infty(2, 1) < 2. \tag{3.3}$$

REMARK 2. It is easy to see that the transcendental functions $\Delta_j(it)$ are completely identical with the functions which are generated in the process of determining the stress singularities in the neighbourhood of the notch tip by the homogeneous solutions method [6]. In the cases when the number of the wedges is sufficiently large, to obtain these functions is a very complicated problem. In [1] it has been shown that the sweep method makes it possible to construct the effective algorithm to calculate zero points of these functions.

Returning to the equations (3.1), we note that the functions $\Delta_j^{-1}(s)$ are analytic in the strip $-\omega_\infty < \Re s < \omega_\infty$, but $f_j(s)$ can have one pole in the strip $-2 < \Re s < j$ in the point $s = 0$ only, and the estimates are true:

$$\Delta_1^{-1}(s) = 1 + O(s^2), \quad f_1(s) = O(s), \quad \Delta_2^{-1}(s), f_2(s) = O(1), \quad s \to 0, \tag{3.4}$$

in the case when the first type exterior boundary condition ($\mathcal{J}^+ = 1$) along wedge boundaries holds, and

$$
\begin{aligned}
\Delta_1^{-1}(s) &= \left(1 + \mu_1 \zeta_l^+ \frac{\pi}{2}\right)^{-1} + O(s^2), \\
f_1(s) &= \frac{\mu_1}{4s} \zeta_l^+ (\Xi_W - 2\pi z_*^+) + O(1), \\
\Delta_2^{-1}(s) &= \frac{-\pi s^2}{2\mu_1 \zeta_l^+} + O(s^4), \\
f_2(s) &= \frac{1}{2\pi s^2} \zeta_l^+ (\Xi_W^- - \Xi_W^+) + O(s^{-1}), \\
\Delta_2^{-1}(s) f_2(s) &= \frac{1}{4}(\Xi_W^+ - \Xi_W^-) + O(s), \qquad s \to 0,
\end{aligned}
\tag{3.5}
$$

for the second type ($\mathcal{J}^+ = 2$) one. Here $\Xi_W^{\pm}$ – principal vectors of all exterior forces, acting in the domains $\Omega_{\pm}$, $\Xi_W = \Xi_W^+ + \Xi_W^-$. Their concrete values and formula for constant ζ_l^+ are presented in Lemma A.1 and Lemma A.2 of Appendix A.

The left-hand sides of Eqs. (3.1) are analytic at $s = 0$. From the estimates (3.4), (3.5) it follows that the right-hand sides (3.1) can have a pole in the point $s = 0$ for the problems $\{1, 2, \mathcal{J}\}$, ($\mathcal{J} = 1, 2, 3$) only (i.e. in the cases when the normal derivatives of the solutions are defined along the exterior wedge boundaries and we seek even solutions of the problems). In order to exclude this situation it is necessary to assume that the relation

$$
\Xi_W - 2\pi z_*^+ = 0 \tag{3.6}
$$

holds. Besides, in the cases when we deal with the problems $\{1, 2, \mathcal{J}\}$ for $\mathcal{J} = 2, 3$, the constant z_*^+ is already determined in (A.24) and the necessary condition for solvability of the problem

$$
2\pi \Xi_L + \Xi_W^+ + \Xi_W^- = 0 \tag{3.7}
$$

follows immediately. These results are completely identical to the assertions of Remarks A.1, A.2 (Appendix A). Let us note that mechanical and mathematical sense of the condition (3.7) is evident. It means that the principal vector of all exterior forces must be equal to zero for the problems in which all of the exterior boundary conditions are of the second type only.

It is interesting to note that for the problems $\{2, 2, \mathcal{J}\}$, ($\mathcal{J} = 1, 2, 3$) the right-hand sides of Eqs. (3.1) are analytic at the point $s = 0$, in spite of the fact that the function $f_2(s)$ has a second order pole in this point.

In addition we introduce here the values of z_*^+, obtained in Appendix A:

$$z_*^+ = \begin{cases} \frac{1}{2\pi}\Xi_W, & \mathcal{J}^+ = \mathcal{J}^- = 2; \quad \mathcal{J} = 1,2,3, \\ -\Xi_L, & \mathcal{J} = 2,3; \quad \mathcal{J}^\pm = 1,2, \\ ?, & \text{for remaining problems.} \end{cases} \tag{3.8}$$

The unknown value of z_*^+ for the "symmetric" problem $\{1,1,1\}$ can be calculated by solving the respective integral equation only (see Appendix B).

The constant u_* can be obtained from the relation:

$$u_* = \frac{2}{\mu_1}(f_1(0) + \widehat{\mathbf{z}}_1(0)(\Delta_1(0) - 1)), \tag{3.9}$$

which connects it with the same integral measure of the solution $\mathbf{z}_1(\lambda)$ of the equation (3.1). Now, from (3.4) it follows that the condition $u_* = 0$ from (1.11) holds for the problems $\{1,1,\mathcal{J}\}$, ($\mathcal{J}$=1,2,3) automatically.

Further, rewriting the equations (3.1) in the form

$$\widehat{\mathbf{z}}_j(s) = \frac{1}{\Delta_j(s)}([\widehat{\mathbf{y}}_j + \widehat{\mathbf{z}}_j](s) - f_j(s)), \tag{3.10}$$

it is easy to see that the term inside the brackets is analytic in the strip $-2 < \Re s < \gamma_\infty$. Therefore, the functions $\widehat{\mathbf{z}}_j(s)$ and $\Delta_j^{-1}(s)$ have a common simple pole in the point $s = -\omega_\infty$. It makes it possible to calculate the value of the other parameter γ_0 in the definition of the functions of class $\mathbf{LW}(\Omega)$

$$\gamma_0 = \omega_\infty(j, \mathcal{J}^+), \tag{3.11}$$

and the constants in the main asymptotics term of the functions $\mathbf{z}_j(\lambda)$ at infinity

$$\begin{aligned} \mathbf{z}_j(\lambda) &= A_\infty^j \lambda^{-\omega_\infty} + o(\lambda^{-\omega_\infty^* + \varepsilon}), \qquad \lambda \to \infty, \\ A_\infty^j &= \frac{1}{\Delta_j'(-\omega_\infty)}([\widehat{\mathbf{y}}_j + \widehat{\mathbf{z}}_j](-\omega_\infty) - f_j(-\omega_\infty)). \end{aligned} \tag{3.12}$$

Here ω_∞^* ($\omega_\infty < \omega_\infty^*$) is the real part of zero of the function $\Delta_j(s, \mathcal{J}^+)$ such that in the strip $\omega_\infty < \Re s < \omega_\infty^*$ there are not any zeros of this function. Let us note that the constants A_∞^j in the first equation (3.12) can be defined as an integral measure of the solutions $\mathbf{z}_j(\lambda)$.

In order to reduce (3.1) to integral equations we use the estimate:

$$\Delta_j(s) = (1 + \mu_1/\mu_l^+) + O(\exp[-|\Im s|(\pi/2 - \phi_l^+)]), \quad |\Im s| \to \infty, \tag{3.13}$$

which follows from Lemma A.2. Then we can rewrite (3.1) in the equivalent form:

$$\left(\frac{1}{\Delta_j(s)} - \frac{\mu_l^+}{\mu_1 + \mu_l^+}\right)[\widehat{\mathbf{y}}_j + \widehat{\mathbf{z}}_j](s) = \frac{\mu_l^+}{\mu_1 + \mu_l^+}\left[\frac{\mu_1}{\mu_l^+}\widehat{\mathbf{z}}_j - \widehat{\mathbf{y}}_j\right](s) - \frac{1}{\Delta_j(s)}f_j(s).$$

Applying the inverse Mellin transform to both sides of the equations we obtain the relations:

$$\frac{\mu_l^+}{\mu_1+\mu_l^+}\left[\frac{\mu_1}{\mu_l^+}\mathbf{z}_j-\mathbf{y}_j\right](\lambda)-\int_0^\infty[\mathbf{y}_j+\mathbf{z}_j](\xi)\Psi_j(\lambda,\xi)\,d\xi$$

$$=-\frac{1}{2\pi i}\int_{-i\infty}^{i\infty}\frac{1}{\Delta_j(s)}f_j(s)\lambda^s\,ds, \tag{3.14}$$

$$\Psi_j(\lambda,\xi)=\frac{1}{2\pi i\xi}\int_{-i\infty}^{i\infty}\left(\frac{1}{\Delta_j(s)}-\frac{\mu_l^+}{\mu_1+\mu_l^+}\right)\left(\frac{\lambda}{\xi}\right)^s ds.$$

These equations contain two unknown functions $\mathbf{y}_j(\lambda)$, $\mathbf{z}_j(\lambda)$ which are related (see (2.18)) by the equations:

$$\begin{aligned}
\mathbf{y}_j(\lambda) &= \lambda\mu_1 M_p(\lambda)\mathbf{z}_j(\lambda)+h_z^j(\lambda),\\
\mathbf{z}_j(\lambda) &= (\lambda\mu_1 M_p(\lambda))^{-1}\mathbf{y}_j(\lambda)+h_y^j(\lambda),\\
h_z^1(\lambda) &= \mu_1(\lambda m_p^+(\lambda)+\lambda z_*^+(1+\lambda^2)^{-1}M_p(\lambda)),\\
h_z^2(\lambda) &= \lambda\mu_1 m_p^-(\lambda),\\
h_y^1(\lambda) &= -m_p^+(\lambda)(M_p(\lambda))^{-1}-z_*^+(1+\lambda^2)^{-1},\\
h_y^2(\lambda) &= -m_p^-(\lambda)(M_p(\lambda))^{-1},
\end{aligned} \tag{3.15}$$

where

$$\begin{aligned}
&h_z^1(\lambda),\ h_z^2(\lambda),\ h_y^1(\lambda),\ h_y^2(\lambda)=O(\lambda^{-2}), && \lambda\to\infty,\\
&h_y^2(\lambda)=O(\lambda),\quad h_y^1(\lambda)=O(\lambda), && \lambda\to 0,\quad \mathcal{J}=2,3,\\
&h_z^2(\lambda)=\begin{cases}O(\lambda^2), & \mathcal{J}=1,\\ O(\lambda), & \mathcal{J}=3,\end{cases}\ h_z^1(\lambda)=O(\lambda), && \lambda\to 0,\quad \mathcal{J}=1,3.
\end{aligned}$$

Eliminating from (3.14) one of the unknown functions, we can obtain the respective integral equations for the other one. Taking into account the behaviour of the functions $M_p(\lambda)$, $h_z^j(\lambda)$, $h_y^j(\lambda)$, elimination of the function $\mathbf{y}_j(\lambda)$ is suitable in the case ($\mathcal{J}=1$) when the boundary condition of the first type holds on the boundary Γ_n. In the case ($\mathcal{J}=2$), when the second boundary condition is satisfied, it is convenient to eliminate the function $\mathbf{z}_j(\lambda)$. As regards the third boundary condition $(1.9)_c$, any of these functions can be eliminated, because their behaviour is of a similar character.

The respective integral equations are written in the form

$$\begin{aligned}
&\mathcal{A}_Z^j(\mathcal{J}^+,\mathcal{J})\,\mathbf{z}_j=\mathbf{g}_Z^j,\quad j=1,2,\quad \mathcal{J}^+=1,2,\quad \mathcal{J}=1,3,\\
&\mathcal{A}_Y^j(\mathcal{J}^+,\mathcal{J})\,\mathbf{y}_j=\mathbf{g}_Y^j,\quad j=1,2,\quad \mathcal{J}^+=1,2,\quad \mathcal{J}=2,3.
\end{aligned} \tag{3.16}$$

Here the integral operators $\mathcal{A}^j_Z(\mathcal{J}^+,\mathcal{J})$, $\mathcal{A}^j_Y(\mathcal{J}^+,\mathcal{J})$ are defined by the relations

$$[\mathcal{A}^j_{Z(Y)}(\mathcal{J}^+,\mathcal{J})\mathbf{u}](\lambda) \equiv \mathbf{u}(\lambda) + \int_0^\infty K_{Z(Y)}(\lambda,\xi)\Psi_j(\lambda,\xi)\mathbf{u}(\xi)d\xi, \tag{3.17}$$

where the functions of the kernels of the operators and right-hand sides of Eqs. (3.16) are obtained in the following forms:

$$K_Z(\lambda,\xi) = \frac{\mu_1+\mu_l^+}{\mu_1}\,\frac{1+\mu_1\xi M_p(\xi)}{\lambda\mu_l^+ M_p(\lambda)-1},$$

$$K_Y(\lambda,\xi) = \frac{\mu_1+\mu_l^+}{\mu_1}\,\frac{\mu_1+(\xi M_p(\xi))^{-1}}{\mu_l^+-(\lambda M_p(\lambda))^{-1}},$$

$$\mathbf{g}^j_Z(\lambda) = \frac{\mu_1+\mu_l^+}{\mu_1}\,\frac{1}{\lambda\mu_l^+ M_p(\lambda)-1} \times\left(\frac{1}{2\pi i}\int_{-i\infty}^{i\infty}\lambda^s\frac{1}{\Delta_j(s)}f_j(s)\,ds-[\mathcal{N}h^j_Z](\lambda)\right), \tag{3.18}$$

$$\mathbf{g}^j_Y(\lambda) = \frac{\mu_1+\mu_l^+}{\mu_l^+-(\lambda M_p(\lambda))^{-1}} \times\left(\frac{1}{2\pi i}\int_{-i\infty}^{i\infty}\lambda^s\frac{1}{\Delta_j(s)}f_j(s)\,ds-[\mathcal{N}h^j_Y](\lambda)+h^j_Y(\lambda)\right).$$

The integral operator $\mathcal{N}$ in (3.18) has a similar form to the operators from (3.17)

$$[\mathcal{N}u](\lambda) \equiv \frac{\mu_l^+}{\mu_1+\mu_l^+}u(\lambda) + \int_0^\infty \Psi_j(\lambda,\xi)u(\lambda)\,d\xi. \tag{3.19}$$

In addition, let us note that the definition of the functional spaces in which the integral equations are considered and the analysis of the equations is presented below in the first subsection of Appendix B. Theorems concerning solvability of the equations and possibility of using numerical methods are proved. Values of the other unknown parameter γ_∞ of class $\mathbf{LW}(\Omega)$ and the value of z_*^+ for the "symmetric" problem $\{1,1,1\}$ are determined.

4. Reduction of the problems to the systems of the integral equations (general case)

The system of functional equations (2.20) is reduced to the system of integral equations in a similar way. First of all, denote by $\nu_\infty(\mathcal{J}^+,\mathcal{J}^-)$ the zero of the

function

$$\Delta(s,\mathcal{J}^+,\mathcal{J}^-) = \det\Phi_* = (1-\mu_1 sM_-(s)\mathrm{tg}(\pi s/2)) \times(1+\mu_1 sM_-(s)\mathrm{ctg}(\pi s/2)) + (\mu_1 sM_+(s))^2,$$

which is the nearest to the imaginary axis (such that $\Re s \geq 0$). From the estimates obtained in Lemma A.2, it can be shown that $\nu_\infty(\mathcal{J}^+,\mathcal{J}^-) \in \mathbb{R}_+$, $0 < \nu_\infty(\mathcal{J}^+,\mathcal{J}^-) < 1$ and the following lemma holds:

LEMMA. In region $|\Re s| < \nu_\infty(\mathcal{J}^+,\mathcal{J}^-)$, there exists a matrix function $\Phi_*^{-1}(s)$ inverse to Φ_* which satisfies the estimates:

1) $\Phi_*^{-1}(s) = \chi_+\mathbf{I} + \chi_-\mathbf{E}\,\mathrm{tg}(\pi s/2) + \Phi_{**}(s)$;
$\Phi_{**}(s) = O(\exp(-\varepsilon|\Im s|)), \quad |\Im s| \to \infty$;

2) $\Phi_*^{-1}(s) = \mathbf{I} + O(s), \quad s \to 0,$ for the problems $(1,1,\mathcal{J})$, $\mathcal{J} = 1,2,3$ and
$\Phi_*^{-1}(s) = \left(1 + \dfrac{\pi\mu_1\zeta_1^-\zeta_l^+}{\zeta_l^+ + \zeta_1^-}\right)^{-1}\begin{pmatrix} 1 & \delta s \\ -\delta s & 0 \end{pmatrix} + O(s^2), \quad s \to 0,$ for remaining problems $(\mathcal{J}^+,\mathcal{J}^-,\mathcal{J})$; $\mathcal{J}^+,\mathcal{J}^- = 1,2$; $\mathcal{J}^+\mathcal{J}^- > 1$, $\mathcal{J} = 1,2,3$.

Here the values of the constants ζ_l^+, ζ_1^- in the Subsec. 2 for $\mathcal{J}^+ = 2$, $\mathcal{J}^- = 2$ are defined in Lemma A.2 of Appendix A, but in the cases $\mathcal{J}^+ = 1$ ($\mathcal{J}^- = 1$) we suppose that $\zeta_l^+ = 0$ ($\zeta_1^- = 0$) and the other constants can be calculated by the relations:

$$\varpi_- = 1 + \mu_1(\mu_1^-)^{-1}, \qquad \varpi_+ = 1 + \mu_1(\mu_l^+)^{-1}, \qquad \varepsilon = \min\{\phi_l^+,\phi_1^-\},$$

$$\lambda_\pm = \frac{\varpi_- \pm \varpi_+}{\varpi_-^2 + \varpi_+^2}, \qquad \mathbf{E} = \begin{pmatrix} 0 & 1 \\ -1 & 0 \end{pmatrix}, \qquad \delta = \frac{\pi}{2}\frac{\zeta_l^+ - \zeta_1^-}{\zeta_l^+ + \zeta_1^-}.$$

Let us note that the function $\Delta(s,\mathcal{J}^+,\mathcal{J}^-) = \det\Phi_*(s)$ has in interval $(0,2)$ at least two real zeros. Moreover, for the symmetric problems considered in the previous section, the function $\Delta(s,\mathcal{J}^+,\mathcal{J}^-) = \Delta_1(s,\mathcal{J}^+)\Delta_2(s,\mathcal{J}^+)$ $(\mathcal{J}^+ = \mathcal{J}^-)$ has two zeros $\omega_\infty(1,\mathcal{J}^+)$ and $\omega_\infty(2,\mathcal{J}^+)$. Then $\nu_\infty(\mathcal{J}^+,\mathcal{J}^+) = \min\{\omega_\infty(1,\mathcal{J}^+), \omega_\infty(2,\mathcal{J}^+)\}$

Taking into account the results of the Lemma, rewrite the systems of the fuctional equatons (2.20) in an equivalent form inside the strip $|\Re s| < \nu_\infty(\mathcal{J}^+,\mathcal{J}^-)$

$$\Phi_*^{-1}(s)\left[\hat{\mathbf{Y}} + \hat{\mathbf{Z}}\right](s) - \Phi_*^{-1}(s)F(s) = \hat{\mathbf{Z}}(s). \tag{4.1}$$

As it follows from Lemma A.2 and the estimates (A.24), the vector functions $\Phi_*^{-1}(s)[\hat{\mathbf{Y}}+\hat{\mathbf{Z}}](s)$ and $\hat{\mathbf{Z}}(s)$ are analytic in the strips $-2 < \Re s < \gamma_\infty$ and $-\gamma_0 < \Re s < \gamma_\infty$, respectively. However, the vector function $\Phi_*^{-1}(s)F(s)$ can have, in

general, a pole at the point $s = 0$ in the cases of the second type boundary condition at least on one boundary of wedge. Moreover, the components of $F(s)$ can be represented in the forms:

$$f_1(s) = \frac{\mu_1}{4s}\left((\zeta_l^+\Upsilon_\Xi^+ + \zeta_1^-\Upsilon_\Xi^-) + s(\zeta_l^+\Upsilon_\Theta^+ + \zeta_1^-\Upsilon_\Theta^-)\right) + O(s), \quad s \to 0,$$

$$f_2(s) = \frac{\mu_1}{2\pi s^2}\left((\zeta_1^-\Upsilon_\Xi^- - \zeta_l^+\Upsilon_\Xi^+) + s(\zeta_1^-\Upsilon_\Theta^- - \zeta_l^+\Upsilon_\Theta^+)\right) + O(1), \quad s \to 0,$$

where we denote $\Upsilon_\Xi^\pm = \Xi_W^\pm - \pi z_*^+$, $\Upsilon_\Theta^\pm = \Theta_W^\pm + \pi z_*^+$, but constants $\Xi_W^\pm$, $\Theta_W^\pm$ are defined in Lemma A.2. Then the necessary condition of regularity of $\mathbf{\Phi}_*^{-1}(s)F(s)$ in this point is to choose the value of z_*^+ as it is in the relation (3.8). For the problems $(1,1,1)$, $(1,2,1)$ the vector function $\mathbf{\Phi}_*^{-1}(s)F(s)$ has no pole for any values of z_*^+. Moreover, in the cases of the first type boundary conditions on one boundary of the wedge ($\mathcal{J}^+\mathcal{J}^- < 4$, $\mathcal{J} = 1,2,3$), it can be shown that the relation $u_*(\mathcal{J}^+, \mathcal{J}^-, \mathcal{J}) = 0$ (see (1.11)) holds immediately.

In a similar way as in the previous section it can be asserted that a pole of the vector function $\widehat{\mathbf{Z}}(s)$ in half-plane $\Re s < 0$ coincides with the zero of the function $\Delta(s, \mathcal{J}^+, \mathcal{J}^-)$ which is the nearest to the imaginary axis, i.e.

$$\gamma_0 = \nu_\infty(\mathcal{J}^+, \mathcal{J}^-). \tag{4.2}$$

If this zero is simple, then the main term in asymptotics of the solution of the system (4.1) has the form

$$\mathbf{Z}(\lambda) = \mathbf{\Lambda}_\infty \lambda^{-\nu_\infty} + O(\lambda^{-\nu_\infty^*}), \qquad \lambda \to \infty. \tag{4.3}$$

Here $\nu_\infty < \nu_\infty^* < 2$ is the real part of a zero of the function $\Delta(s, \mathcal{J}^+, \mathcal{J}^-)$ such that there are not any zeros of this function in the strip $\nu_\infty < \Re s < \nu_\infty^*$. Moreover, the vector $\mathbf{\Lambda}_\infty$ can be calculated as an integral measure of $\mathbf{Z}(\lambda)$ by the relation

$$\mathbf{\Lambda}_\infty = \frac{1}{\dfrac{\partial}{\partial s}\det \mathbf{\Phi}_*(s)|_{s=-\nu_\infty}} \times \lim_{s \to -\nu_\infty} \det \mathbf{\Phi}_*(s)\mathbf{\Phi}_*^{-1}(s)\left(\left[\widehat{\mathbf{Y}} + \widehat{\mathbf{Z}}\right](-\nu_\infty) - F(-\nu_\infty)\right). \tag{4.4}$$

Further, rewrite the system (4.1), taking into account the results of Lemma

$$\mathbf{\Phi}_{**}(s)\left[\widehat{\mathbf{Y}} + \widehat{\mathbf{Z}}\right](s) + \left[\chi_+\widehat{\mathbf{Y}} + (\chi_+ - 1)\widehat{\mathbf{Z}}\right](s) + \chi_-\operatorname{tg}\frac{\pi s}{2}\mathbf{E}\left[\widehat{\mathbf{Y}} + \widehat{\mathbf{Z}}\right](s) = \mathbf{\Phi}_*^{-1}(s)F(s).$$

Applying to this equation the inverse Mellin transform we obtain

$$[\chi_+\mathbf{Y} + (\chi_+ - 1)\mathbf{Z}](\lambda) + \int_0^\infty \Psi(\lambda,\xi)[\mathbf{Y}+\mathbf{Z}](\xi)\,d\xi \tag{4.5}$$
$$-\frac{2}{\pi}\chi_-\mathbf{E}\int_0^\infty [\mathbf{Y}+\mathbf{Z}](\xi)\frac{\lambda\,d\xi}{\lambda^2-\xi^2} = \frac{1}{2\pi i}\int_{-i\infty}^{i\infty}\lambda^s\Phi_*^{-1}(s)F(s)\,ds,$$

where homogeneous matrix function $\Psi(\lambda,\xi)$ of degree -1 is defined by the relation

$$\Psi(\lambda,\xi) = \frac{1}{2\pi i\xi}\int_{-i\infty}^{i\infty}\Phi_{**}(s)\left(\frac{\lambda}{\xi}\right)^s ds.$$

The relations between the vector functions $\mathbf{Y}$ and $\mathbf{Z}$ can be written in the form:

$$\mathbf{Y} = \lambda\mu_1 M_p(\lambda)\mathbf{Z} + H_Z, \quad \mathcal{J} = 1,3; \qquad \mathbf{Z} = (\lambda\mu_1 M_p(\lambda))^{-1}\mathbf{Y} + H_Y, \quad \mathcal{J} = 2,3,$$

where the components of the vector functions $H_Z(\lambda)$, $H_Y(\lambda)$ and the respective estimates are presented in (3.15).

Using a similar line of reasoning as before, the systems of integral equations

$$\begin{aligned}\mathcal{B}_Z(\mathcal{J}^+,\mathcal{J}^-,\mathcal{J})\mathbf{Z} &= \mathcal{G}_Z, \qquad \mathcal{J} = 1,2,\\ \mathcal{B}_Y(\mathcal{J}^+,\mathcal{J}^-,\mathcal{J})\mathbf{Y} &= \mathcal{G}_Y, \qquad \mathcal{J} = 2,3,\end{aligned} \tag{4.6}$$

can be found. Here

$$[\mathcal{B}_{Z(Y)}\mathbf{u}](\lambda) = \mathbf{u}(\lambda) + \int_0^\infty K_{Z(Y)}(\lambda,\xi)\Psi(\lambda,\xi)\mathbf{u}(\xi)\,d\xi$$
$$-\frac{2}{\pi}\chi_-\mathbf{E}\int_0^\infty K_{Z(Y)}(\lambda,\xi)\mathbf{u}(\xi)\frac{\lambda\,d\xi}{\lambda^2-\xi^2},$$

but the functions $K_{Z(Y)}(\lambda,\xi)$ and the vector functions $\mathcal{G}_{Z(Y)}(\lambda)$ are calculated by the relations

$$\begin{aligned}K_Z(\lambda,\xi) &= \frac{1+\mu_1\xi M_p(\xi)}{\lambda\mu_l^+ M_p(\lambda)\chi_+ + \chi_+ - 1},\\ K_Y(\lambda,\xi) &= \frac{1+(\mu_1\xi M_p(\xi))^{-1}}{(\chi_+-1)(\lambda\mu_1 M_p(\lambda))^{-1}+\chi_+},\end{aligned} \tag{4.7}$$

(4.7) [cont.]
$$\mathcal{G}_Z(\lambda) = \frac{1}{\lambda\mu_l^+ M_p(\lambda)\chi_+ + \chi_+ - 1} \times \left(\frac{1}{2\pi i} \int_{-i\infty}^{i\infty} \lambda^s \mathbf{\Phi}_*^{-1}(s) F(s)\, ds - [\mathcal{L}H_Z](\lambda) \right),$$

$$\mathcal{G}_Y(\lambda) = \frac{1}{(\chi_+ - 1)(\lambda\mu_1^+ M_p(\lambda))^{-1} + \chi_+} \times \left(\frac{1}{2\pi i} \int_{-i\infty}^{i\infty} \lambda^s \mathbf{\Phi}_*^{-1}(s) F(s) ds - [\mathcal{L}H_Y](\lambda) + H_Y(\lambda) \right).$$

Besides, the operator $\mathcal{L}$ is defined by the equation

$$[\mathcal{L}\mathbf{u}](\lambda) = \chi_+ \mathbf{u}(\lambda) + \int_0^\infty \mathbf{\Psi}(\lambda, \xi)\mathbf{u}(\xi)\, d\xi - \frac{2}{\pi}\chi_- \mathbf{E} \int_0^\infty \mathbf{u}(\xi) \frac{\lambda\, d\xi}{\lambda^2 - \xi^2}.$$

Let us note here an important difference of the systems of integral equations (4.6) in comparison with the equations (3.16). Namely, as $\mathcal{A}^j_{Z(Y)}(\mathcal{J}^+, \mathcal{J})$ in (3.17) are the operators with the fixed point singularities only, the operators $\mathcal{B}_{Z(Y)}(\mathcal{J}^+, \mathcal{J}^-, \mathcal{J})$ from (4.1) include also the usual moving singularity with the kernel of the same type as $(\lambda - \xi)^{-1}$, in the case when $\chi_- \neq 0$.

The systems of integral equations are investigated below in the second subsection of Appendix B. The values of the other unknown parameter γ_∞ of class $\mathbf{LW}(\Omega)$ and the value of z_*^+ for the problem (1,1,1) and (1,2,1) are obtained.

Appendix A

A.1. Sweep method in the layered regions

Applying to Eqs. (1.1) the Fourier transform inside each of the layered domains Ω_i, the transformations of the solutions are obtained in the form [21]

(A.1)
$$\overline{u_i}(\lambda, x) = C_1^i(\lambda) e^{|\lambda| x_2} + C_2^i(\lambda) e^{-|\lambda| x_2} + \frac{1}{\mu_i |\lambda|} \int_{y_{i-1}}^{x_2} \overline{W_i}(\lambda, \xi) \operatorname{sh}[(\xi - x_2)|\lambda|]\, d\xi,$$

where the Fourier transform is defined in an usual way

(A.2)
$$\overline{u}(\lambda, x) = \mathcal{F}[u(x_1, x_2); x_1 \to \lambda] \equiv \frac{1}{2\pi} \int_{-\infty}^{\infty} \exp(i\lambda x_1) u(x_1, x_2) dx_1.$$

Following [9], denote functions

$$\begin{aligned} \mathbf{p}_t^i(\lambda) &= \mu_i \frac{\partial}{\partial x_2}\overline{u}_i|_{\Gamma_i}, \qquad \mathbf{u}_t^i(\lambda) = \overline{u}_i|_{\Gamma_i}, \\ \mathbf{p}_b^i(\lambda) &= \mu_i \frac{\partial}{\partial x_2}\overline{u}_i|_{\Gamma_{i-1}}, \qquad \mathbf{u}_b^i(\lambda) = \overline{u}_i|_{\Gamma_{i-1}}, \quad i = 1, 2, \ldots, n. \end{aligned} \tag{A.3}$$

From *a priori* estimates (1.11) of functions of class $\mathbf{LW}(\Omega)$ and from the properties of the Fourier transform it can be shown that the functions defined above must satisfy the relations

$$\begin{aligned} [\mathbf{u}_{t(b)}^i(\lambda)]_+ &= \begin{cases} O(\lambda^{\gamma_1 - 1}), & 0 < \gamma_1 < 1, \\ O(\ln(\lambda)), & \gamma_1 = 1, \\ \text{Const} + O(\lambda^{\gamma_1 - 1}), & \gamma_1 > 1, \quad \lambda \to 0, \end{cases} \\ [\mathbf{u}_{t(b)}^i(\lambda)]_- &= O(\lambda^{\gamma_1 - 1}), \qquad \lambda \to 0, \end{aligned}$$

$$[\mathbf{p}_{t(b)}^i(\lambda)]_+ = \text{Const} + O(\lambda^{\gamma_2}), \qquad [\mathbf{p}_{t(b)}^i(\lambda)]_- = O(\lambda^{\gamma_2}), \quad \lambda \to 0, \tag{A.4}$$

$$\lambda \frac{\partial}{\partial \lambda}\mathbf{p}_{t(b)}^i(\lambda) = O(\lambda^{\gamma_2}), \qquad \lambda \to 0, \quad i = 1, 2, \ldots, n,$$

$$\lambda \mathbf{u}_{t(b)}^i,\ \lambda \mathbf{u}_t^1,\ \mathbf{p}_{t(b)}^i,\ \mathbf{p}_t^1,\ \lambda \frac{\partial}{\partial \lambda}\mathbf{p}_{t(b)}^i,\ \lambda \frac{\partial}{\partial \lambda}\mathbf{p}_t^1 = O(\lambda^{-2}), \quad \lambda \to \infty, \quad i = 2, 3, \ldots, n,$$

$$\lambda \mathbf{u}_b^1(\lambda),\ \mathbf{p}_b^1(\lambda),\ \lambda \frac{\partial}{\partial \lambda}\mathbf{p}_b^1(\lambda) = O(\lambda^{-\gamma_0}), \qquad \lambda \to \infty.$$

Here by $[\mathbf{f}(\lambda)]_\pm$ we understand the even (odd) component of a function $\mathbf{f}$ and the constants in (A.4) are different, in general.

Substituting the relations (A.1) in (A.3) and eliminating the functions $C_1^i(\lambda)$, $C_2^i(\lambda)$, we obtain the relations between functions $\mathbf{u}_{t(b)}^i$ and $\mathbf{p}_{t(b)}^i$ in the form

$$\begin{aligned} \mathbf{u}_t^i &= R_{tt}^i \mathbf{p}_t^i + R_{tb}^i \mathbf{p}_b^i + u_{t0}^i, \\ \mathbf{u}_b^i &= R_{bt}^i \mathbf{p}_t^i + R_{bb}^i \mathbf{p}_b^i + u_{b0}^i, \qquad i = 1, 2, \ldots, n, \end{aligned} \tag{A.5}$$

where coefficients are calculated by the equations

$$\begin{aligned} R_{tt}^i(\lambda) &= -R_{bb}^i(\lambda) = \frac{1}{\mu_i \lambda}\operatorname{cth}(\lambda h_i), \quad R_{bt}^i(\lambda) = -R_{tb}^i(\lambda) = \frac{1}{\mu_i \lambda \operatorname{sh}(\lambda h_i)}, \\ u_{t(b)0}^i &= \frac{1}{\mu_i \lambda \operatorname{sh}(\lambda h_i)} \int_{y_{i-1}}^{y_i} \overline{W_i}(\lambda, \xi) \operatorname{ch}[\lambda(\xi - y_{b(t)})]\, d\xi, \quad y_b = y_{i-1}, \quad y_t = y_i. \end{aligned} \tag{A.6}$$

Now, apply the Fourier transform to the interior contact conditions along the boundaries Γ_i, $i = 1, 2, \ldots, n-1$. The corresponding equations can be written in

terms of the functions defined above $\mathbf{u}^i_{t(b)}$, $\mathbf{p}^i_{t(b)}$

$$\begin{aligned} \mathbf{u}^{i+1}_b - \mathbf{u}^i_t - \tau_i \mathbf{p}^i_t &= \Delta u_i, \\ \mathbf{p}^{i+1}_b - \mathbf{p}^i_t &= \Delta p_i, \qquad i = 1, 2, ..., n-1. \end{aligned} \tag{A.7}$$

Here $\Delta u_i(\lambda) = \mathcal{F}[\delta u_i](\lambda)$, $\Delta p_i(\lambda) = \mathcal{F}[\delta q_i](\lambda)$ are the Fourier transformations of the known functions.

As it has been shown in [9], the relations (A.5) and (A.7) make it possible to eliminate the unknown functions, either $\mathbf{u}^i_{t(b)}$ or $\mathbf{p}^i_{t(b)}$, and to obtain formulas for the remaining one. Substitute (A.5) in (A.7), then two systems of the difference equations $(A.8)_a$ and $(A.8)_b$ for the unknown functions $\mathbf{p}^i_{t(b)}$ are obtained

$$\begin{aligned} &\text{(a)} \quad A^i_p \mathbf{p}^{i-1}_t - C^i_p \mathbf{p}^i_t + B^i_p \mathbf{p}^{i+1}_t + F^i_{pt} = 0, \qquad i = 2, 3, ..., n-1, \\ &\text{(b)} \quad A^i_p \mathbf{p}^i_b - C^i_p \mathbf{p}^{i+1}_b + B^i_p \mathbf{p}^{i+2}_b + F^i_{pb} = 0, \qquad i = 1, 2, ..., n-2, \end{aligned} \tag{A.8}$$

where

$$\begin{aligned} A^i_p &= -R^i_{tb}, \qquad C^i_p = \tau_i + R^i_{tt} - R^{i+1}_{bb}, \qquad B^i_p = R^{i+1}_{bt}, \\ F^i_{bp} &= u^{i+1}_{b0} - u^i_{t0} - \Delta u_i + (R^i_{tt} + \tau_i)\Delta p_i - R^{i+1}_{bt}\Delta p_{i+1}, \\ F^i_{pt} &= u^{i+1}_{b0} - u^i_{t0} - \Delta u_i + R^{i+1}_{bb}\Delta p_i - R^i_{tb}\Delta p_{i+1}. \end{aligned} \tag{A.9}$$

They are equivalent to each other and are identical in the case when all of the jump functions Δp_i are equal to zero.

In order to solve any of these systems of difference equations it is necessary to have exterior boundary ("initial" in this sense) conditions on the first and the last surfaces of the package of layers. On the boundary Γ_n one of the conditions (1.9) is defined. Apply the Fourier transform to this boundary condition; then, taking into account (A.3), (A.5) it can be written in a form similar to (A.8)

$$A^n_p \mathbf{p}^{n-1}_t - C^n_p \mathbf{p}^n_t + F^n_{pt} = 0, \tag{A.10}$$

where the functions A^n_p, C^n_p, F^n_{pt} are defined for each type of the conditions $(1.9)_1$, $(1.9)_2$, $(1.9)_3$

$$\begin{aligned} &\text{(a)} \quad (\mathcal{J} = 1) \quad A^n_p = -R^n_{tb}, \quad C^n_p = \tau_n + R^n_{tt}, \\ &\qquad\qquad\qquad\quad F^n_{pt} = -\Delta u_n - u^n_{t0} - R^n_{tb}\Delta p_{n-1}, \\ &\text{(b)} \quad (\mathcal{J} = 2) \quad A^n_p = 0, \quad C^n_p = 1, \quad F^n_{pt} = -\Delta p_n, \\ &\text{(c)} \quad (\mathcal{J} = 3) \quad A^n_p = -R^n_{tb}, \quad C^n_p = \tau_n + R^n_{tt} + \frac{1}{|\lambda|\mu_{n+1}}, \end{aligned} \tag{A.11}$$

$$F_{pt}^n = -\Delta u_n - u_{t0}^n - R_{tb}^n \Delta p_{n-1} - \frac{1}{|\lambda|\mu_{n+1}} \left(\Delta p_n - \int_{y_n}^{\infty} \overline{W_{n+1}}(\lambda, \xi) e^{-|\lambda|\xi} d\xi \right).$$

Let us note that the relation (A.10) corresponding to $(1.9)_3$ is obtained by passage to the limit $x_2 \to \infty$ in (A.5), taking into account the boundary condition (A.7) for $i = n$. This fact makes it possible to consider this condition in a common scheme. Moreover, from $(A.11)_c$ it is possible to obtain the conditions: (a) (passing to the limit $\mu_{n+1} \to \infty$) or (b) (for $\tau_n = 0$ and $\mu_{n+1} \to 0$), respectively. In the case when $\tau_n \neq 0$ and $\mu_{n+1} \to 0$, the boundary condition is represented in the form $(u + \tau_n \mathbf{grad} u)_{|\Gamma_n} = f(x_1)$. However, these passages to the limit are not possible, in general. That is because the limit boundary value problem is, as a rule, the singular perturbation of initial value boundary problem. It will be clear from the analysis of the symbols of the respective integral operators.

In order to close the system of difference equations (A.8) it is necessary to have the second boundary condition along boundary Γ_0. This condition is absent (the solution along Γ_0 is not known and is connected with the solutions inside the wedge regions Ω_l^+, Ω_0^-). To eliminate this fact, let us assume that the condition has the form

$$z(x_1) = \mu_1 \frac{\partial}{\partial x_2} u_1|_{\Gamma_0}, \tag{A.12}$$

with some unknown function $z(x_1)$. Then the missing relation can be written in the form

$$-C_p^0 \mathbf{p}_b^1 + B_p^0 \mathbf{p}_b^2 + F_{pb}^0 = 0, \tag{A.13}$$

where

$$C_p^0 = 1, \qquad B_p^0 = 0, \qquad F_{pb}^0 = \overline{z}_+(\lambda) + \overline{z}_-(\lambda).$$

Here we present unknown function $z(x_1)$ as a sum of even and odd functions $z_+(x_1)$, $z_-(x_1)$.

As one could expect, the boundary conditions (A.10) and (A.13) are prescribed for different functions $\mathbf{p}_b^i$, $\mathbf{p}_l^i$, respectively. In order to solve any of the systems of difference equations $(A.8)_a$, $(A.8)_b$, these conditions must be rewritten in terms of common-type functions. So, Eq. (A.13) can be presented in the form

$$-C_p^0 \mathbf{p}_t^0 + B_p^0 \mathbf{p}_t^1 + F_{pt}^0 = 0, \tag{A.14}$$

where C_p^0, B_p^0 are defined above, $F_{pt}^0 = F_{pb}^0$ and function $\mathbf{p}_t^0$ is defined by the relation similar to $(A.7)_2$

$$\mathbf{p}_t^0 = \mathbf{p}_b^1, \tag{A.15}$$

with

$$\Delta p_0 = 0. \tag{A.16}$$

Now, the system of difference equation $(A.8)_a$ with the boundary conditions (A.10), (A.14) can be solved by the sweep method. Following [9], define the auxiliary functions

$$\alpha_p^n = (C_p^n)^{-1} A_p^n, \qquad \beta_p^n = (C_p^n)^{-1} F_{pt}^n, \tag{A.17}$$

and in the next steps

$$\begin{aligned} \alpha_p^i &= (C_p^i - B_p^i \alpha_p^{i+1})^{-1} A_p^i, \\ \beta_p^i &= (C_p^i - B_p^i \alpha_p^{i+1})^{-1} (F_{pt}^i + B_p^i \beta_p^{i+1}), \quad i = n-1, n-2, ..., 2, 1. \end{aligned} \tag{A.18}$$

The solutions of this problem are in the form:

$$\mathbf{p}_t^0 = \beta_p^0 = \overline{z}_+(\lambda) + \overline{z}_-(\lambda), \tag{A.19}$$

$$\mathbf{p}_t^i = \alpha_p^i \mathbf{p}_t^{i-1} + \beta_p^i, \qquad i = 1, 2, ..., n. \tag{A.20}$$

If the functions $z_+(x_1), z_-(x_1)$ are known, then the values of the functions $\mathbf{p}_t^i$ will be found from (A.19), (A.20). Moreover, the values of $\mathbf{p}_b^i$ and the values of $\mathbf{u}_{b(t)}^i$ can be obtained from $(A.7)_2$ and (A.5), respectively. Corresponding relations are

$$\begin{aligned} \mathbf{u}_t^i &= D_{pt}^i \mathbf{p}_t^i + d_{pt}^i, \qquad i = 1, 2, ..., n, \\ \mathbf{u}_b^i &= D_{pb}^i \mathbf{p}_t^i + d_{pb}^i, \qquad i = 1, 2, ..., n-1, \end{aligned} \tag{A.21}$$

where

$$\begin{aligned} D_{pt}^i &= R_{tt}^i + R_{tb}^i (\alpha_p^i)^{-1}, \qquad d_{pt}^i = u_{t0}^i + R_{tt}^i (\Delta p_{i-1} - (\alpha_p^i)^{-1} \beta_p^i), \\ D_{pb}^i &= R_{bt}^i + R_{bb}^i (\alpha_p^i)^{-1}, \qquad d_{pb}^i = u_{b0}^i + R_{bb}^i (\Delta p_{i-1} - (\alpha_p^i)^{-1} \beta_p^i). \end{aligned}$$

Further, we shall need the relation between the functions $\mathbf{u}_b^1$, $\mathbf{p}_b^1 (= \mathbf{p}_t^0)$, defined along the exterior boundary Γ_0 (with respect to the layered domain)

$$\mathbf{u}_b^1 = M_p \mathbf{p}_b^1 + m_p = M_p(\lambda)(\overline{z}_+(\lambda) + \overline{z}_-(\lambda)) + m_p, \tag{A.22}$$

where functions M_p, m_p are in the form

$$\begin{aligned} M_p &= R_{bt}^1 \alpha_p^1 + R_{bb}^1, \qquad m_p = u_{b0}^1 + R_{bt}^1 \beta_p^1. \\ & m_p(\lambda) = m_p^+(\lambda) + m_p^-(\lambda). \end{aligned} \tag{A.23}$$

The relations (A.22), (A.23) will be necessary in order to satisfy the contact conditions along Γ_0.

LEMMA A.1. Functions M_p, $m_p^{\pm}$ belong to $\mathbf{C}^{\infty}(\mathbb{R}_+)$ and satisfy the following estimates:

1) $$|\lambda| M_p(\lambda) = -\frac{1}{\mu_1} + M_p^*(\lambda);$$
$$M_p^*(\lambda) = \exp(-2|\lambda| h_1)\left[\frac{2}{\mu_1} + O\left(\exp\left(-|\lambda| \min_{2\le j\le n} h_j\right)\right)\right], \quad |\lambda| \to \infty;$$

2) $$m_p^{\pm}(\lambda) = o(\exp(-|\lambda| h_1)), \quad |\lambda| \to \infty;$$

3) $$M_p(\lambda) = -\begin{cases} \eta_1 + O(\lambda^2), & \mathcal{J} = 1 \\ \lambda^{-2}\zeta_1 + O(1), & \mathcal{J} = 2, \quad \lambda \to 0; \\ \dfrac{1}{|\lambda|\mu_{n+1}} + O(1), & \mathcal{J} = 3 \end{cases}$$

4) $$m_p^+(\lambda) = -\left\{\begin{array}{ll} 0, & \mathcal{J} = 1 \\ \lambda^{-2}\zeta_1 \Xi_1^n, & \mathcal{J} = 2 \\ \dfrac{1}{|\lambda|\mu_{n+1}} \Xi_1^{n+1}, & \mathcal{J} = 3 \end{array}\right\} + O(1), \quad \lambda \to 0;$$

$$m_p^-(\lambda) = -\left\{\begin{array}{ll} 0, & \mathcal{J} = 1 \\ \lambda^{-1}\zeta_1 \Theta_1^n, & \mathcal{J} = 2 \\ \dfrac{\operatorname{sgn}(\lambda)}{\mu_{n+1}} \Theta_1^{n+1}, & \mathcal{J} = 3 \end{array}\right\} + O(\lambda), \quad \lambda \to 0;$$

5) $M_p(\lambda) < 0$ for $\lambda \in \mathbb{R}$ and all $\mathcal{J}(= 1, 2, 3)$.

Here the constants ζ_i, Ξ_i^n, Ξ_i^{n+1}, η_i, Θ_i^n, Θ_i^{n+1} $(i = 1, 2, \ldots, n)$ are defined by the equations

$$\eta_i = \sum_i^n \frac{h_j}{\mu_j} + \sum_i^{n-1} \tau_j, \qquad \Xi_i^n = \sum_{i-1}^n \Delta p_j(0) + \sum_i^n \int_{y_{j-1}}^{y_j} \overline{W_j}(0, \xi)\, d\xi,$$

$$\zeta_i = \left(\sum_i^n \mu_j h_j\right)^{-1}, \qquad \Theta_i^n = \sum_{i-1}^n \Delta p_j'(0) + \sum_i^n \int_{y_{j-1}}^{y_j} \overline{W}_j'(0, \xi)\, d\xi,$$

$$\Theta_i^{n+1} = \Theta_i^n + \int_{y_n}^{\infty} \overline{W}_j'(0, \xi)\, d\xi, \qquad \Xi_i^{n+1} = \Xi_i^n + \int_{y_n}^{\infty} \overline{W}_{n+1}(0, \xi)\, d\xi.$$

Symbol $'$ denotes the derivative of the function with respect to λ. We do not present here the proof of Lemma A.1 taking into account the volume of the paper and a technical character of the proof.

COROLLARY A.1. From (A.4) and Lemma A.1 *a priori* estimates of the unknown functions z_+, z_- can be obtained

$$
\begin{gathered}
\overline{z}_\pm(\lambda), \quad \lambda\frac{\partial}{\partial\lambda}\overline{z}_\pm(\lambda) = O(\lambda^{-\gamma_0}), \quad \lambda \to \infty, \\
\overline{z}_+(\lambda) = z_*^+ + O(\lambda^{\gamma_2^+}), \quad \lambda\frac{\partial}{\partial\lambda}\overline{z}_\pm(\lambda) = O(\lambda^{\gamma_2^\pm}), \quad \lambda \to 0, \\
\overline{z}_-(\lambda) = z_*^-\lambda^{\gamma_2^-} + O(\lambda^{\gamma_2^-+\varepsilon}), \quad \lambda \to 0, \\
\lambda\left(M_p(\lambda)\overline{z}_+(\lambda) + m_p^+\right) = O(\lambda^{\min\{1,\gamma_1^+\}}), \quad \lambda \to 0, \\
\lambda\left(M_p(\lambda)\overline{z}_-(\lambda) + m_p^-\right) = O(\lambda^{\gamma_1^-}), \quad \lambda \to 0, \\
\lambda\left(M_p(\lambda)\overline{z}_\pm(\lambda) + m_p^\pm\right) = O(\lambda^{\gamma_0}), \quad \lambda \to \infty,
\end{gathered}
\tag{A.24}
$$

where

$$
\begin{gathered}
z_*^+ = -\Xi_1^n, \quad z_*^- = -\Theta_1^n, \quad \gamma_2^+ = \gamma_1^+ + 1, \quad \gamma_2^- = 1, \quad \gamma_1^- = 2, \quad \text{for } \mathcal{J} = 2, \\
z_*^+ = -\Xi_1^{n+1}, \quad z_*^- = -\Theta_1^{n+1}, \quad \gamma_2^+ = \gamma_1^+, \quad \gamma_2^- = 1, \quad \gamma_1^- = 2, \quad \text{for } \mathcal{J} = 3, \\
1 + \gamma_2^\pm = \gamma_1^\pm, \qquad \gamma_2^+ \le 2, \qquad \gamma_2^- \le 1, \quad \text{for } \mathcal{J} = 1.
\end{gathered}
$$

Note that the values of the constant $z_*^\pm$ in the case $\mathcal{J} = 1$ are unknown as yet and will be obtained below. Besides, even and odd components of the solution decrease at infinity in a different way (the respective exponents are $\gamma_1^\pm$, $\gamma_2^\pm$). Constant u_* from (1.11) can be calculated by the equation

$$
u_*(2,2,\mathcal{J}) = 2\int_0^\infty \left(M_p(\lambda)\overline{z}_+(\lambda) + m_p^+(\lambda)\right)\,d\lambda. \tag{A.25}
$$

Moreover, in the cases of the first type boundary conditions at least on one boundary of the wedge ($\mathcal{J}^+\mathcal{J}^- < 4$), the additional relation (1.11) is satisfied

$$
\int_0^\infty \left(M_p(\lambda)\overline{z}_+(\lambda) + m_p^+(\lambda)\right)\,d\lambda = 0. \tag{A.26}
$$

A.2. Sweep method in the wedge regions

Applying the Mellin transform to equations (1.1) inside the respective regions, the transformations of the solutions are presented in the form

$$
\begin{aligned}
\widetilde{u}_j^\pm(s,\theta) = {} & A_j^\pm(s)\cos(s\theta) + B_j^\pm(s)\sin(s\theta) \\
& + \frac{1}{\mu_j^\pm s}\int_{\theta_{j-1}^\pm}^{\theta} \widetilde{W}_j^\pm(s+2,\phi)\sin[(\phi-\theta)s]\,d\phi.
\end{aligned}
\tag{A.27}
$$

Here and elsewhere the Mellin transform is defined in an usual way [21]

$$\widetilde{u}(s,\theta) = \mathcal{M}[u(r,\theta);\, r \to s] \equiv \int_0^\infty u(r,\theta) r^{s-1}\, dr. \tag{A.28}$$

Further, determine the functions as in (A.3)

$$\begin{aligned} \mathbf{q}_t^j(s) &= \mu_j^+ \frac{\partial}{\partial\theta}\widetilde{u}_j^+|_{\Gamma_j^+}, \qquad \mathbf{v}_t^j(s) = \widetilde{u}_j^+|_{\Gamma_j^+}, \\ \mathbf{q}_b^j(s) &= \mu_j^+ \frac{\partial}{\partial\theta}\widetilde{u}_j^+|_{\Gamma_{j-1}^+}, \qquad \mathbf{v}_b^j(s) = \widetilde{u}_j^+|_{\Gamma_{j-1}^+}, \quad j = 1,2,...,l; \end{aligned} \tag{A.29}$$

$$\begin{aligned} \mathbf{r}_t^k(s) &= \mu_k^- \frac{\partial}{\partial\theta}\widetilde{u}_k^-|_{\Gamma_k^-}, \qquad \mathbf{w}_t^k(s) = \widetilde{u}_k^-|_{\Gamma_k^-}, \\ \mathbf{r}_b^k(s) &= \mu_k^- \frac{\partial}{\partial\theta}\widetilde{u}_k^-|_{\Gamma_{k-1}^-}, \qquad \mathbf{w}_b^k(s) = \widetilde{u}_k^-|_{\Gamma_{k-1}^-}, \quad i = 1,2,...,m. \end{aligned} \tag{A.30}$$

From the properties of the Mellin transform it follows that the functions $\mathbf{q}_{b(t)}^j(s)$, $\mathbf{r}_{b(t)}^k(s)$ are analytical in the strip $-\gamma_0 < \Re s < \gamma_2$. However, the functions $\mathbf{w}_{b(t)}^k(s)$, $\mathbf{v}_{b(t)}^j(s)$ are analytical, in general, in domain $0 < \Re s < \gamma_1$ only. They can have a common simple pole at the point $s = 0$. Besides, the functions

$$\mathbf{v}_{t(b)}^j(s) - \frac{1}{s}u_*, \qquad \mathbf{w}_{t(b)}^k(s) - \frac{1}{s}u_* = O(1), \quad s \to 0, \tag{A.31}$$

are analytical in the whole strip $-\gamma_0 < \Re s < \gamma_1$. All those functions tend to zero along the imaginary axis inside the respective domains.

Similar reasoning as in (A.5) shows that the relations

$$\begin{aligned} \mathbf{v}_t^j &= P_{tt}^j \mathbf{q}_t^j + P_{tb}^J \mathbf{q}_b^j + v_{t0}^j, \\ \mathbf{v}_b^j &= P_{bt}^j \mathbf{q}_t^j + P_{bb}^j \mathbf{q}_b^j + v_{b0}^j, \qquad j = 1,2,...,l; \end{aligned} \tag{A.32}$$

$$\begin{aligned} \mathbf{w}_t^k &= Q_{tt}^k \mathbf{r}_t^k + Q_{tb}^k \mathbf{r}_b^k + w_{t0}^k, \\ \mathbf{w}_b^k &= Q_{bt}^k \mathbf{r}_t^k + Q_{bb}^k \mathbf{r}_b^k + w_{b0}^k, \qquad k = 1,2,...,m, \end{aligned} \tag{A.33}$$

between the transformations of the boundary functions hold also in the wedge regions. Here the coefficients are found by the formulae:

$$\begin{aligned} P_{tt}^j(s) &= -R_{bb}^j(s) = -\frac{1}{\mu_j^+ s}\operatorname{ctg}(s\phi_j^+), \\ P_{bt}^j(s) &= -P_{tb}^j(s) = -\frac{1}{\mu_j^+ s \sin(s\phi_j^+)}, \end{aligned} \tag{A.34}$$

(A.34) [cont.]
$$v^j_{t(b)0} = \frac{1}{\mu^+_j s \sin(s\phi^+_j)} \int\limits_{\theta^+_{j-1}}^{\theta^+_j} \widetilde{W}^+_j(s+2,\phi) \times \cos[s(\phi - \theta^+_{b(t)})]\, d\phi, \quad \theta^+_b = \theta^+_{j-1}, \quad \vartheta^+_t = \theta^+_j,$$
$$Q^k_{tt}(s) = -Q^k_{bb}(s) = -\frac{1}{\mu^-_k s} \operatorname{ctg}(s\phi^-_k),$$
$$Q^k_{bt}(s) = -Q^k_{tb}(s) = -\frac{1}{\mu^-_k s \sin(s\phi^-_k)},$$
$$w^k_{t(b)0} = \frac{1}{\mu^-_k s \sin(s\phi^-_k)} \int\limits_{\theta^-_{k-1}}^{\theta^-_k} \widetilde{W}^-_k(s+2,\phi) \times \cos[s(\phi - \theta^-_{b(t)})]\, d\phi, \quad \theta^-_b = \theta^-_{k-1}, \quad \vartheta^-_t = \theta^-_k.$$

Now, rewrite the interior boundary conditions,

(A.35)
$$\begin{aligned} \mathbf{v}^{j+1}_b - \mathbf{v}^j_t - \tau^+_j \mathbf{q}^j_t &= \Delta v_j, \\ \mathbf{q}^{j+1}_b - \mathbf{q}^j_t &= \Delta q_j, \quad j = 1,2,\ldots,l-1; \\ \mathbf{w}^{k+1}_b - \mathbf{w}^k_t - \tau^-_k \mathbf{r}^k_t &= \Delta w_k, \\ \mathbf{r}^{k+1}_b - \mathbf{r}^k_t &= \Delta r_k, \quad k = 1,2,\ldots,m-1, \end{aligned}$$

where the functions

(A.36)
$$\begin{aligned} \Delta v_j(s) &= \mathcal{M}[\delta u^+_j](s), \\ \Delta q_j(s) &= \mathcal{M}[\delta q^+_j](s+1), \\ \Delta w_k(s) &= \mathcal{M}[\delta u^-_k](s), \\ \Delta r_k(s) &= \mathcal{M}[\delta q^-_k](s+1), \end{aligned}$$

are the Mellin transforms of the respective functions.

Then the net result for wedge domain Ω^- is in a similar form as (A.19), (A.20):

(A.37)
$$\begin{aligned} \mathbf{r}^0_t &= \mathbf{r}^1_b = \tilde{z}_-(s+1) - \tilde{z}_+(s+1) + \Delta r_*(s), \\ \mathbf{r}^k_t &= \alpha^k_r \mathbf{r}^{k-1}_t + \beta^k_r, \\ \mathbf{w}^k_t &= D^k_{rt} \mathbf{r}^k_t + d^k_{rt}, \\ \mathbf{w}^k_b &= D^k_{rb} \mathbf{r}^k_t + d^k_{rb}, \qquad k = 1,\ldots,m. \end{aligned}$$

All the relations necessary to calculate the coefficients of (A.37) are given below.

$$
\begin{aligned}
\alpha_r^m &= (C_r^m)^{-1} A_r^m, \qquad \beta_r^m = (C_r^m)^{-1} F_{rt}^m, \\
\alpha_r^k &= (C_r^k - B_r^k \alpha_r^{k+1})^{-1} A_r^k, \\
\beta_r^k &= (C_r^k - B_r^k \alpha_r^{k+1})^{-1} (F_{rt}^k + B_r^k \beta_r^{k+1}), \\
D_{rt}^k &= Q_{tt}^k + Q_{tb}^k (\alpha_r^k)^{-1}, \qquad d_{rt}^k = w_{t0}^k + Q_{tt}^k (\Delta r_{k-1} - (\alpha_r^k)^{-1} \beta_r^k), \\
D_{rb}^k &= Q_{bt}^k + Q_{bb}^k (\alpha_r^k)^{-1}, \qquad d_{rb}^k = w_{b0}^k + Q_{bb}^k (\Delta r_{k-1} - (\alpha_r^k)^{-1} \beta_r^k), \\
A_r^k &= -Q_{tb}^k, \qquad C_r^k = \tau_k^- + Q_{tt}^k - Q_{bb}^{k+1}, \qquad B_r^k = Q_{bt}^{k+1}, \\
F_{rb}^k &= w_{b0}^{k+1} - w_{t0}^k - \Delta w_k + (Q_{tt}^k + \tau_k^-) \Delta r_k - Q_{bt}^{k+1} \Delta r_{k+1}, \\
F_{rt}^k &= w_{b0}^{k+1} - w_{t0}^k - \Delta w_k + Q_{bb}^{k+1} \Delta r_k - Q_{tb}^k \Delta r_{k+1}, \\
\Delta r_*(s) &= \mathcal{M}[\delta q^-](s+1), \qquad k = m-1, m-2, \ldots, 2, 1.
\end{aligned}
\tag{A.38}
$$

The constants at the first step of the sweep method are defined by one of the boundary conditions (1.8)

$$
\begin{aligned}
A_r^m &= \begin{Bmatrix} -Q_{tb}^m \\ 0 \end{Bmatrix}, \qquad C_r^m = \begin{Bmatrix} Q_{tt}^m \\ 1 \end{Bmatrix}, \\
F_{rt}^m &= \begin{Bmatrix} -\Delta w_m - w_{to}^m - Q_{tb}^m \Delta r_{m-1} \\ -\Delta r_m \end{Bmatrix}, \quad \mathcal{J}^- = 1, \quad \mathcal{J}^- = 2.
\end{aligned}
\tag{A.39}
$$

The last boundary condition along the boundary Γ_0^- follows from (1.4_2) and from the assumption (A.12):

$$
C_r^0 = 1, \quad B_r^0 = 0, \quad \Delta r_0 = 0, \quad F_{rt}^0 = \tilde{z}_-(s+1) - \tilde{z}_+(s+1) + \Delta r_*. \tag{A.40}
$$

In an analogous way, the relations are obtained for the wedge regions Ω^+

$$
\begin{aligned}
\mathbf{q}_b^{l+1} &= \mathbf{q}_t^l = \tilde{z}_-(s+1) + \tilde{z}_+(s+1) - \Delta q_*(s), \\
\mathbf{q}_b^j &= \alpha_q^j \mathbf{q}_b^{j+1} + \beta_q^j, \\
\mathbf{v}_t^j &= D_{qt}^j \mathbf{q}_b^j + d_{qt}^j, \\
\mathbf{v}_b^j &= D_{qb}^j \mathbf{q}_q^j + d_{qb}^j, \quad j = l, 2, \ldots, 1,
\end{aligned}
\tag{A.41}
$$

where the necessary coefficients are in the form:

$$
\begin{aligned}
\alpha_q^1 &= (C_q^m)^{-1} B_q^0, \qquad \beta_q^1 = (C_q^0)^{-1} F_{qb}^0, \\
\alpha_r^{j+1} &= (C_r^j - A_r^j \alpha_r^j)^{-1} B_r^j, \\
\beta_q^{j+1} &= (C_q^j - A_q^j \alpha_q^j)^{-1} (F_{qb}^j + A_q^j \beta_q^j), \\
D_{qt}^j &= P_{tb}^j + P_{tt}^j (\alpha_q^j)^{-1}, \quad d_{qt}^j = v_{t0}^j - P_{tt}^j (\Delta q_j - (\alpha_q^j)^{-1} \beta_q^j),
\end{aligned}
\tag{A.42}
$$

(A.42) [cont.]
$$D^j_{qb} = P^j_{bt} + P^j_{bb}(\alpha^j_q)^{-1}, \quad d^j_{qb} = v^j_{b0} - P^j_{bt}(\Delta q_j - (\alpha^j_q)^{-1}\beta^j_q),$$
$$A^j_q = -P^j_{tb}, \qquad C^j_q = \tau^+_j + P^j_{tt} - P^{j+1}_{bb}, \qquad B^j_q = P^{j+1}_{bt},$$
$$F^j_{qb} = v^{j+1}_{b0} - v^j_{t0} - \Delta v_j + (P^j_{tt} + \tau^+_j)\Delta q_j - P^{j+1}_{bt}\Delta q_{j+1},$$
$$F^j_{qt} = v^{j+1}_{b0} - v^j_{t0} - \Delta v_j + P^{j+1}_{bb}\Delta q_j - P^j_{tb}\Delta q_{j+1},$$
$$\Delta q_*(s) = \mathcal{M}[\delta q^+](s+1), \qquad j = 1, 2, ..., l-1.$$

The exterior boundary conditions (with respect to package of wedges Ω^+) follow from (1.7), (1.3_2) and the assumption (A.12)

(A.43)
$$C^0_q = \begin{Bmatrix} P^1_{bb} \\ 1 \end{Bmatrix}, \qquad B^0_q = \begin{Bmatrix} -P^1_{bt} \\ 0 \end{Bmatrix},$$
$$F^0_{qb} = \begin{Bmatrix} \Delta v_0 - v^1_{bo} + P^1_{bb}\Delta q_1 \\ \Delta q_0 \end{Bmatrix}, \quad \mathcal{J}^+ = 1, \quad \mathcal{J}^+ = 2;$$

(A.44) $$C^l_q = 1, \quad A^l_q = 0, \quad \Delta q_l = 0, F^l_{qt} = \tilde{z}_+(s+1) + \tilde{z}_-(s+1) - \Delta q_*.$$

Now, the relations similar to (A.22) can be found which relate the transformations of functions $z_\pm(x_1)$ along the boundaries Γ^-_0, Γ^+_l and the solutions inside the wedges nearest to the layered domain

(A.45) $$\mathbf{v}^l_t = M_q\mathbf{q}^{l+1}_b + m_q = M_q(\tilde{z}_+(s+1) + \tilde{z}_-(s+1) - \Delta q_*(s)) + m_q,$$

(A.46) $$\mathbf{w}^1_b = M_r\mathbf{r}^0_t + m_r = M_r(\tilde{z}_-(s+1) - \tilde{z}_+(s+1) + \Delta r_*(s)) + m_r,$$

where

(A.47)
$$M_q(s) = P^l_{tb}\alpha^l_q + P^l_{tt}, \qquad m_q(s) = v^l_{t0} + P^l_{tb}\beta^l_q,$$
$$M_r(s) = Q^1_{bt}\alpha^1_r + Q^1_{bb}, \qquad m_r(s) = w^1_{b0} + Q^1_{bt}\beta^1_r,$$

LEMMA A2. Functions M_q, M_r and m_q, m_r are analytical (maybe except one point $s = 0$) in the strips $|\Re s| < \min\{\pi/\phi^\pm_j\}$ and $|\Re s| < \min\{2, \pi/\phi^\pm_j\}$, respectively, and the following estimates hold:

1)
$$sM_q(s) = -(\mu^+_l)^{-1}\mathrm{ctg}(\phi^+_l s) + M^*_q(s),$$
$$sM_r(s) = (\mu^-_1)^{-1}\mathrm{ctg}(\phi^-_1 s) + M^*_r(s),$$
$$M^*_q(s) = O(\exp(-|\Im s|\phi^+_l)), \quad |\Im s| \to \infty,$$
$$M^*_r(s) = O(\exp(-|\Im s|\phi^-_1)), \quad |\Im s| \to \infty;$$

2)
$$M_q(s) = \begin{Bmatrix} \eta_+ + O(s^2), & \mathcal{J}^+ = 1 \\ -s^{-2}\zeta^+_l + O(1), & \mathcal{J}^+ = 2 \end{Bmatrix}, \quad s \to 0,$$
$$M_r(s) = \begin{Bmatrix} -\eta_- + O(s^2), & \mathcal{J}^- = 1 \\ s^{-2}\zeta^-_1 + O(1), & \mathcal{J}^- = 2 \end{Bmatrix}, \quad s \to 0;$$

3) $$m_q(s) = o(|s|^{-1}\exp(-|\Im(s)|\phi_l^+)), \qquad |\Im(s)| \to \infty,$$
$$m_r(s) = o(|s|^{-1}\exp(-|\Im(s)|\phi_1^-)), \qquad |\Im(s)| \to \infty;$$

4) $$m_q(s) = \left\{ \begin{array}{ll} 0, & \mathcal{J}^+ = 1 \\ s^{-2}\zeta_l^+\Xi_l^+ + s^{-1}\zeta_l^+\Theta_l^+, & \mathcal{J}^+ = 2 \end{array} \right\} + O(1), \quad s \to 0,$$
$$m_r(s) = \left\{ \begin{array}{ll} 0, & \mathcal{J}^- = 1 \\ s^{-2}\zeta_1^-\Xi_1^- + s^{-1}\zeta_1^-\Theta_1^-, & \mathcal{J}^- = 2 \end{array} \right\} + O(1), \quad s \to 0;$$

5) $M_q(s), M_r(s)$ are even functions, but $M_q(it), M_r(it)$ are real and different from zero along the imaginary axis, i.e.:
$M_q(it), -M_r(it) > 0, \quad t \in \overline{\mathbb{R}}$.

Here the constants are calculated by the geometric and mechanical parameters:

$$\zeta_j^+ = \left(\sum_1^j \mu_i^+\phi_i^+\right)^{-1}, \qquad \eta_+ = \sum_1^l \phi_j^+(\mu_j^+)^{-1} + \sum_1^{l-1}\tau_j^+,$$

$$\zeta_k^- = \left(\sum_k^m \mu_i^-\phi_i^-\right)^{-1}, \qquad \eta_- = \sum_1^m \phi_k^-(\mu_k^-)^{-1} + \sum_1^{m-1}\tau_k^-,$$

$$\Xi_j^+ = \sum_0^j \Delta q_i(0) + \sum_1^j \int_{\theta_{i-1}^+}^{\theta_i^+} \widetilde{W}_i^+(2,\phi)\,d\phi,$$

$$\Xi_k^- = \sum_{k-1}^m \Delta r_i(0) + \sum_k^m \int_{\theta_{i-1}^-}^{\theta_i^-} \widetilde{W}_i^-(2,\phi)\,d\phi,$$

$$\Theta_j^+ = \sum_0^j \Delta q_i'(0) + \sum_1^j \int_{\theta_{i-1}^+}^{\theta_i^+} \frac{\partial}{\partial s}\widetilde{W}_i^+(2,\phi)\,d\phi,$$

$$\Theta_k^- = \sum_{k-1}^m \Delta r_i'(0) + \sum_k^m \int_{\theta_{i-1}^-}^{\theta_i^-} \frac{\partial}{\partial s}\widetilde{W}_i^-(2,\phi)\,d\phi.$$

COROLLARY A.2. Let us assume that the following statements hold:

1. The domain Ω is symmetric with respect to the OX_2-axis ($m = l$, $\phi_j^+ = \phi_{m-j+1}^-$).

2. The constants of the equations (1.1) and of the interior boundary conditions (1.3), (1.4) are identical for the corresponding wedges ($\mu_j^+ = \mu_{m-j+1}^-$, $\tau_j^+ = \tau_{m-j}^-$).

3. The types of the exterior boundary conditions along the boundaries of wedges are identical ($\mathcal{J}^+ = \mathcal{J}^-$);

then the identity is true

$$M_q(s) = -M_r(s).$$

REMARK A.1. The following relation is necessary to solve the problems $(2, 2, \mathcal{J})$ $\mathcal{J} = 2, 3$ in class $\mathbf{LW}(\Omega)$

$$2\pi\Xi_L + \Xi_W^+ + \Xi_W^- = 0. \tag{A.48}$$

REMARK A.2. The asymptotics of the solution of the problem $(2, 2, 1)$ is

$$\overline{z}_+(\lambda) = \frac{1}{2\pi}\Xi_W + O(\lambda^{\gamma_2}), \qquad \lambda \to 0. \tag{A.49}$$

Then the value of the constant z_*^+ in *a priori* estimates (A.24) can be corrected. Here the following notations are introduced:

$$\begin{aligned} \Xi_L &= \left\{ \begin{matrix} \Xi_1^n, & \mathcal{J} = 2 \\ \Xi_1^{n+1}, & \mathcal{J} = 3 \end{matrix} \right\}, \qquad \Xi_W = \Xi_W^+ + \Xi_W^-, \\ \Xi_W^+ &= \Xi_l^+ + \Delta q_*(0), \qquad \Xi_W^- = \Xi_1^- + \Delta r_*(0). \end{aligned} \tag{A.50}$$

The proofs of the Remarks follow from the fact that the functions $\mathbf{v}_t^l(s)$, $\mathbf{w}_b^1(s)$ can have a simple pole at the point $s = 0$ only.

Appendix B

In this section the singular integral equations (3.16) and the systems of equations (4.1) obtained in the Secs. 3, 4 are investigated. Theory of the systems of equations for the operators with the fixed point singularities have been obtained in [11, 14] in Banach spaces of summable functions with a weight. It is based on the theory of the integral Wiener–Hopf type operators which have been constructed in [4, 5, 8]. The same integral equations with fixed and moving singularities are considered in [3, 20]. But those results can be not applied to the systems (4.6). We investigate more accurately Eqs. (3.16) in order to derive similar results for the systems of equations.

B.1. The analysis of singular equations (3.16)

Denote by $\mathbf{L}^{p,\alpha,\beta}(\mathbb{R}_+)$ the Banach space of functions p-summable on $\mathbb{R}_+$ with a weight. The norm of the space is determined as follows

$$\|u\|^{p,\alpha,\beta} = \left(\int_0^\infty |u(\xi)|^p \rho_{\alpha,\beta}^p(\xi) \xi^{-1}\, d\xi \right)^{1/p}, \quad \rho_{\alpha,\beta}(\xi) = \left\{ \begin{matrix} \xi^\alpha, & \xi \in (0,1), \\ \xi^\beta, & \xi \in (1,\infty). \end{matrix} \right. \tag{B.1}$$

Besides, by $\mathbf{W}_{(l)}^{p,\alpha,\beta}(\mathbb{R}_+)$ we denote the space of functions having distributional derivatives $u^{(j)}$ up to the order l, with the norm

$$\|u\|_{(l)}^{p,\alpha,\beta} = \sum_{j=0}^{l} \|u^{(j)}\|^{p,\alpha+j,\beta+j}.$$

Let us note that the space $\mathbf{W}_{(l)}^{p,\alpha,\beta}(\mathbb{R}_+)$ is not the usual Sobolev space [10]. Moreover, the asymptotics of the functions from $\mathbf{W}_{(l)}^{p,\alpha,\beta}(\mathbb{R}_+)$ and the asymptotics of their derivatives are related in a specific way. It is evident that $\mathbf{L}^{p,\alpha-h,\beta+h} \subset \mathbf{L}^{p,\alpha,\beta}$, $\mathbf{W}_{(l)}^{p,\alpha,\beta} \subset \mathbf{L}^{p,\alpha,\beta}$, for any $h > 0$, $l \in \mathbf{N}$, though the embeddings are not compact.

Taking into account the results of Lemmas A.1, A.2 it can be obtained that for any $\varepsilon > 0$, $1 \le p < \infty$, $m \in \mathbf{N}$, $\alpha > -\min\{1, \omega_\infty(j, \mathcal{J}^+)\}$, $\lambda, \xi \in \mathbb{R}_+$ and for a certain $C \in \mathbb{R}_+$ the relations hold

$$\begin{aligned} &K_Z, K_Y \in \mathbf{C}^\infty(\overline{\mathbb{R}}_+^2), \quad |K_Z(\lambda,\xi)|,\ |K_Y(\lambda,\xi)| \le C\exp(-\xi h_1), \\ &\Psi_j(\cdot,1) \in \mathbf{W}_{(m)}^{1,-\omega_\infty+\varepsilon,\omega_\infty-\varepsilon}(\mathbb{R}_+), \quad \mathcal{G}_Z^j, \mathcal{G}_Y^j \in \mathbf{W}_{(m)}^{p,\alpha,\omega_\infty-\varepsilon}(\mathbb{R}_+). \end{aligned} \tag{B.2}$$

Further we can rewrite *a priori* estimates (A.24) for the unknown functions $\mathbf{z}_j$, $\mathbf{y}_j$ in terms of Banach spaces, using the definition (B.1). Namely, for $\varepsilon > 0$ it must be true that

$$\mathbf{z}_j,\ \mathbf{y}_j \in \mathbf{W}_{(1)}^{1,-\gamma_\infty+\varepsilon,\gamma_0-\varepsilon}(\mathbb{R}_+), \tag{B.3}$$

where $\gamma_0 = \omega_\infty$, but γ_∞ is unknown in this time constant. From [14] it follows that it is natural to look for the solutions of the equations (3.16) in the spaces $\mathbf{L}^{p,\alpha,\beta}(\mathbb{R}_+)$. Taking this fact into account, assume the weaker condition than (B.3)

$$\mathbf{z}_j,\ \mathbf{y}_j \in \mathbf{L}^{p,-\gamma_\infty+\varepsilon,\omega_\infty-\varepsilon}(\mathbb{R}_+). \tag{B.4}$$

REMARK B.1. Let the solutions of the equations (3.16) exist in the spaces (B.4). Then from [14] and the relations (B.2) it follows immediately that those solutions belong to the spaces $\mathbf{W}_{(m)}^{p,-\gamma_\infty+\varepsilon,\omega_\infty-\varepsilon}(\mathbb{R}_+)$ for any $m \in \mathbf{N}$. Therefore, the conditions (B.3) and (B.4) are equivalent to Eqs. (3.16).

Basing on [14] and relations (B.2) it can be obtained that symbols of the operators $\mathcal{A}_Z^j(\mathcal{J}^+, \mathcal{J})$, $\mathcal{A}_Y^j(\mathcal{J}^+, \mathcal{J})$ (3.17) in the spaces $\mathbf{L}^{p,\alpha,\beta}(\mathbb{R}_+)$ ($1 \le p < \infty$, $\alpha > -\gamma_\infty$, $\beta < \gamma_\infty$) are defined by the equations:

$$\begin{aligned} \mathbf{a}_Z^j(\alpha - it, \mathcal{J}^+, \mathcal{J}) &= 1 + K_Z(0,0)\tilde{\Psi}_j(\alpha - it, 1), \\ \mathbf{a}_Y^j(\alpha - it, \mathcal{J}^+, \mathcal{J}) &= 1 + K_Y(0,0)\tilde{\Psi}_j(\alpha - it, 1), \end{aligned} \tag{B.5}$$

where $\widetilde{\Psi}_j(s,1) \equiv \mathcal{M}[\Psi_j(\cdot,1)](s)$. After some algebra it follows that

$$
\begin{aligned}
\mathbf{a}_Z^j(s,\mathcal{J}^+,1) &= \frac{\mu_l^+ + \mu_1}{\mu_1}(1 - \Delta_j^{-1}(s)),\\
\mathbf{a}_Y^j(s,\mathcal{J}^+,2) &= \frac{\mu_l^+ + \mu_1}{\mu_l^+}\Delta_j^{-1}(s),\\
\mathbf{a}_Z^j(s,\mathcal{J}^+,3) &= \mathbf{a}_Y^j(s,\mathcal{J}^+,3) = \frac{(\mu_l^+ + \mu_1)\mu_{n+1}}{\mu_1(\mu_{n+1} + \mu_l^+)}\\
&\qquad \times \left(1 + \left(\frac{\mu_1}{\mu_{n+1}} - 1\right)\Delta_j^{-1}(s)\right).
\end{aligned}
\tag{B.6}
$$

REMARK B.2. Symbols of the operators $\mathcal{A}_Z^j(\mathcal{J}^+,3)$ and $\mathcal{A}_Y^j(\mathcal{J}^+,3)$ are identical, and the respective equations (3.16) are isometrically equivalent. Then it is sufficient to investigate one of them only. Moreover, when $\mu_1 = \mu_{n+1}$, these symbols are constants. Therefore, the respective operators $\mathcal{A}_Z^j(\mathcal{J}^+,3)$ and $\mathcal{A}_Y^j(\mathcal{J}^+,3)$ are of the Fredholm type. Taking into account Remark 1, it follows that the equations (3.16) in this case have unique solutions in the spaces defined above and we shall not consider this case ($\mu_1 = \mu_{n+1}$, $\mathcal{J} = 3$) below.

Denote by $\omega_0(j,\mathcal{J}^+,\mathcal{J})$, ($\mathcal{J} = 1,3$) and $\omega_0(j,\mathcal{J}^+,2)$ the zeros of the functions $\mathbf{a}_Z^j(s,\mathcal{J}^+,\mathcal{J})$, ($\mathcal{J} = 1,3$) and $\mathbf{a}_Y^j(s,\mathcal{J}^+,2)$, respectively, which are the nearest to the imaginary axis (inside the half-plane $\Re s \geq 0$). It can be shown that

$$
\begin{aligned}
&\omega_0(2,1,1) = \omega_0(2,2,1) = \omega_0(1,1,2) = \omega_0(1,2,2) = 1,\\
&\omega_0(1,2,1) = \omega_0(2,1,2) = 2,\\
&0 < \omega_0(j,\mathcal{J}^+,3) < \omega_\infty(j,\mathcal{J}^+) < 1, \qquad \mu_1 < \mu_{n+1},\\
&0 < \omega_0(j,\mathcal{J}^+) < \omega_\infty(j,\mathcal{J}^+,3) < 1, \qquad \mu_1 > \mu_{n+1},
\end{aligned}
\tag{B.7}
$$

and all these zeros are simple. Moreover, the zeros $\omega_0(j,\mathcal{J}^+,3)$ are placed in the same regions as $\omega_\infty(j,\mathcal{J}^+)$ (see (3.3)). The other zeros are double, and

$$\omega_0(1,1,1) = \omega_0(2,2,2) = 0.$$

Besides, for the problems {1,1,1} and {2,2,2} there are simple zeros $\omega_0^* = 2$ of the functions $\mathbf{a}_Z^1(s,1,1)$, $\mathbf{a}_Y^2(s,2,2)$ in the strip $\omega_0 < \Re s \leq 2$ only.

Thus the problems $\{j,\mathcal{J}^+,\mathcal{J}\}$ are divided into two groups, depending on the values of the respective zeros $\omega_0(j,\mathcal{J}^+,\mathcal{J})$.

Now consider the first situation when $\omega_0(j,\mathcal{J}^+,\mathcal{J}) > 0$. If it is assumed that $\alpha = 0$, then the symbols $\mathbf{a}_Z^j(it,\mathcal{J}^+,\mathcal{J})$, $\mathbf{a}_Y^j(it,\mathcal{J}^+,\mathcal{J})$ of the respective operators are real, even functions, which are not equal to zero along the imaginary axis ($t \in \overline{\mathbb{R}}$). Therefore, their indices are equal to zero [8] for all $|\alpha| < \omega_0(j,\mathcal{J}^+,\mathcal{J})$

$$\kappa = -\operatorname{ind}\mathbf{a}_Z^j(\alpha - it,\mathcal{J}^+,\mathcal{J}) = -\operatorname{ind}\mathbf{a}_Y^j(\alpha - it,\mathcal{J}^+,\mathcal{J}) = 0. \tag{B.8}$$

Moreover, in the cases when $\omega_0(j, \mathcal{J}^+, \mathcal{J}) > 0$, the values of the constant z_*^+ have been already obtained (3.8). Then the right-hand sides of the equations (3.16) are known functions. So, we can present the following:

THEOREM B.1. *Let* $1 \le p < \infty$, $m \in \mathbf{N}$, $\omega_0(j, \mathcal{J}^+, \mathcal{J}) > 0$, $\beta < \omega_\infty(j, \mathcal{J}^+)$, $\beta - \alpha \ge 0$, $-\min\{1, \omega_0(j, \mathcal{J}^+, \mathcal{J}), \omega_\infty(j, \mathcal{J}^+)\} < \alpha < \omega_0(j, \mathcal{J}^+, \mathcal{J})$, *then*

1. The operators $\mathcal{A}_Z^j(\mathcal{J}^+, \mathcal{J})$, $\mathcal{A}_Y^j(\mathcal{J}^+, \mathcal{J})$ *in the spaces* $\mathbf{L}^{p,\alpha,\beta}(\mathbb{R}_+)$ *are normally solvable with the indices* $\kappa = 0$;

2. There exist unique solutions of the equations (3.16) *from* $\mathbf{W}_{(m)}^{p,\alpha,\beta}(\mathbb{R}_+) \subset \mathbf{L}^{p,\alpha,\beta}(\mathbb{R}_+)$;

3. The respective "truncated" equations (3.16):

$$\mathbf{u}_R(\lambda) + \int_{1/R}^{R} K_{Z(Y)}(\lambda, \xi)\Psi_j(\lambda, \xi)\mathbf{u}_R(\xi)\, d\xi = \mathbf{g}_{Z(Y)}^j(\lambda), \quad \lambda \in \left(\frac{1}{R}, R\right),$$

have unique solutions $u_R \in \mathbf{L}^p(R^{-1}, R)$, *beginning from a certain* $R > 1$. *After extending the function* u_R *through zero to the entire axis* $(\widetilde{u}_R)$, *it converges for* $R \to \infty$ *to the solution of the equation* (3.16) *with respect to norm of the space* $\mathbf{L}^{p,\alpha,\beta}(\mathbb{R}_+)$ *and the estimate holds*

$$\|\mathbf{u} - \widetilde{u}_R\|^{p,\alpha,\beta} = o(R^{-\delta}), \qquad R \to \infty; \qquad \delta = \min\{\omega_\infty - \beta, \alpha + \omega_\infty\};$$

4. Galerkin method for the equation (3.16) *with respect to the set of functions* $\phi_n^{\alpha,\beta} = \phi_n \rho_{\alpha,\beta}^{-1}$:

$$\text{(B.9)} \qquad \begin{aligned} \phi_n(\lambda) &= \left\{ \begin{array}{cc} \sqrt{2}\,\lambda\, \Lambda_n(-2\ln\lambda), & 0 < \lambda < 1; \\ 0, & 1 < \lambda < \infty, \end{array} \right\} \quad n = 0, 1, 2, \ldots, \\ \phi_n(\lambda) &= -\phi_{-n-1}(\lambda^{-1}), \qquad n = -1, -2, -3, \ldots, \end{aligned}$$

is valid in Hilbert space $\mathbf{L}^{2,\alpha,\beta}(\mathbb{R}_+)$. *Here* $\Lambda_n(t)$, $(n = 0, 1, 2, \ldots)$ *are normed Laguerre polynomials* [4];

5. The solutions of Eqs. (3.16) *have the asymptotics expansion in the neighbourhood of zero in the form*

$$\mathbf{u}(\lambda) = O(\lambda^{\gamma_\infty}), \qquad \lambda \to 0, \qquad \gamma_\infty = \min\{1, \omega_0(j, \mathcal{J}^+, \mathcal{J})\},$$

and at infinity the asymptotics are defined by the relation (3.12).

Let us here note that the "truncated" equation is not singular but a Fredholm type equation. Besides, from Theorem B.1 all the parameters in the definition of class $\mathbf{LW}(\Omega)$ are found. Solving numerically the Eqs. (3.16), the approximate solutions of the initial (symmetric) boundary value problems $\{j, \mathcal{J}^+, \mathcal{J}\}$ can be obtained as well as the asymptotics of the solutions in the neighbourhood of zero

and at infinity by the relations (3.9), (3.12). Note, that the constants u_*, Λ^j_∞, which play an important role in applications, can be calculated as *integral measure* of the approximate solutions of the Eqs. (3.16) by the relations (3.9), (3.12). Then the optimal parameters of the spaces $\mathbf{L}^{p,\alpha,\beta}(\mathbb{R}_+)$ can be selected in order to obtain the maximal degree of convergence of approximate solutions to the exact one. Namely, to calculate the value of u_* it is enough to take $\alpha = \beta = 0$, because u_* depends on the norm of the solution $\|z_1\|^{1,0,0}$ in a linear way. To calculate the values of Λ^j_∞, only the respective parameters must be in the form $\alpha = -\beta = \omega_\infty(j, \mathcal{J}^+)$. Similar integral relations as (3.9) and (3.12) can be obtained for the constants in the asymptotics 4 (Theorem B.1), near the point $\lambda = 0$ from the functional equations (3.1) passing to the limit $s \to \omega_0$.

Now, consider the integral equations (3.16) for the remaining problems {1,1,1} and {2,2,2} for which $\omega_0(1,1,1) = \omega_0(2,2,2) = 0$. In these cases it can be shown that

$$\kappa = -\operatorname{ind} \mathbf{a}^1_Z(\alpha - it, 1, 1) = -\operatorname{ind} \mathbf{a}^2_Y(\alpha - it, 2, 2) = \left\{ \begin{array}{ll} 1, & 0 < \alpha < 2 \\ -1, & -2 < \alpha < 0 \end{array} \right\},$$

in the spaces $\mathbf{L}^{p,\alpha,\beta}(\mathbb{R}_+)$. However, the constant z^+_* is defined for the problem {2,2,2} only. As regards the problem {1,1,1} the right-hand side of Eq. (3.16) (see (3.18)) can be represented in the form: $\mathbf{g}^1_Z(\lambda) = g_1(\lambda) + z^+_* \, g_2(\lambda)$, where the functions g_1, g_2 are bounded in the neighbourhood of zero. Let us note that this representation is true for all the problems, of course, but the respective functions are not bounded near the point $\lambda = 0$. So, the following theorem can be formulated:

THEOREM B.2. *Let* $1 \le p < \infty$, $-2 < \alpha < 0$, $\beta < \omega_\infty$, $\beta - \alpha \ge 0$, $m \in \mathbf{N}$, *then*

1. The operator $\mathcal{A}^1_Z(1,1)$ *in the spaces* $\mathbf{L}^{p,\alpha,\beta}(\mathbb{R}_+)$ *is normally solvable with the index* $\kappa = -1$;

2. There exists a unique value of z^+_* *for which the equation* (3.16) *has a solution* $\mathbf{z}_1$ *in the spaces* $\mathbf{L}^{p,\alpha,\beta}(\mathbb{R}_+)$;

3. This solution is unique and its asymtotics is in the form

$$\mathbf{z}_1(\lambda) = O(\lambda^2), \qquad \lambda \to 0,$$

but at infinity it is defined by the relation (3.12).

Let us note that the equation (3.16) cannot be numerically solved directly as in Theorem B.1. To this aim the equation must be regularized (see [4]). Then the equation obtained has a unique solution for any right-hand sides (for any values of z^+_*). But the condition (A.26), which automatically holds for equation (3.16), is not true for the regularized equation, in general. It makes it possible to calculate from (A.26) the sought value of z^+_*. Namely, the regularized equation can be solved with the right-hand sides of g_1 and g_2, separately. Then the solution of (3.16) is a linear combination of those solutions, so that the relation (A.26) is true.

For problem $\{2,2,2\}$ we can prove

THEOREM B.3. *Let* $1 \le p < \infty$, $-1 < \alpha < 0$, $\beta < \omega_\infty$, $\beta - \alpha \ge 0$, $m \in \mathbf{N}$, *then*

1. The operator $\mathcal{A}^2_{Y'}(2,2)$ *in the spaces* $\mathbf{L}^{p,\alpha,\beta}(\mathbb{R}_+)$ *is normally solvable with the index* $\kappa = -1$;

2. There exists a unique solution of the equation (3.16) $\mathbf{y}_2$ *in the spaces* $\mathbf{L}^{p,\alpha,\beta}(\mathbb{R}_+)$;

3. The asymptotics of the solution has the form

$$\mathbf{y}_2(\lambda) = O(\lambda), \qquad \lambda \to 0,$$

and at infinity it is defined by the relation (3.12).

Similarly to Theorem B.2, Eq. (3.16) cannot be numerically solved directly and a regularization of the equation is necessary. Then the unique solution will be found, because the value of z_*^+ is already known. In this case the relation (A.48) is the usual necessary condition for solvability of the boundary value problem, and the condition of "orthogonality" of the right-hand side of the integral equation (3.16) to the kernel of conjugate operator. Besides, the value of u_* can be calculated from the relation (A.25).

In the spaces $\mathbf{L}^{p,\alpha,\beta}(\mathbb{R}_+)$ for the values of the parameter $\alpha > 0$, the following theorem can be proved:

THEOREM B.4. *Let* $1 \le p < \infty$, $0 < \alpha < 2$, $\beta < \omega_\infty$, $\beta - \alpha \ge 0$, $m \in \mathbf{N}$, *then*

1. The operators $\mathcal{A}^1_Z(1,1)$, $\mathcal{A}^2_{Y'}(2,2)$ *in the spaces* $\mathbf{L}^{p,\alpha,\beta}(\mathbb{R}_+)$ *are normally solvable with the indices* $\kappa = 1$;

2. Homogeneous equations $\mathcal{A}^1_Z(1,1)\mathbf{u} = 0$, $\mathcal{A}^2_{Y'}(2,2)\mathbf{u} = 0$ *have unique nontrivial solutions* $\mathbf{u} \in \mathbf{L}^{p,\alpha,\beta}(\mathbb{R}_+)$ *which belong to all the spaces* $\mathbf{W}^{p,\alpha,\beta}_{(m)}(\mathbb{R}_+)$ $(\mathbf{u} \in \bigcap \mathbf{W}^{p,\alpha,\beta}_{(m)}(\mathbb{R}_+))$;

3. The asymptotic expansions of the solutions in the neighbourhood of zero are:

$$\mathbf{u}(\lambda) = B\ln(\lambda) + C + O(\lambda^2), \qquad \lambda \to 0$$

but at infinity the relations (3.12) *will be satisfied as before.*

Let us note that nontrivial solutions of the respective homogeneous boundary problems play an important role in asymptotic methods [17]. Taking this fact into account, theorems are proved in [15] which make it possible to find these nontrivial solutions numerically. However, in order to obtain the solutions of the homogeneous boundary value problem by the respective nontrivial solution of integral equation, it is necessary to use generalized integral transforms [24], and, therefore, it is necessary to justify the analysis of the paper also in the spaces of distributions.

B.2. The analysis of the systems of singular equations (4.6)

As before, it is easy to see that for any $\varepsilon > 0$, $1 \le p < \infty$, $m \in \mathbf{N}$, $\alpha > -\min\{1, \nu_\infty(\mathcal{J}^+, \mathcal{J}^-)\}$,

$$\Psi_{ij}(\cdot\,,1) \in \mathbf{W}^{1,-\nu_\infty+\varepsilon,\nu_\infty-\varepsilon}_{(m)}(\mathbb{R}_+), \qquad \mathcal{G}^j_Z, \mathcal{G}^j_{Y'} \in \mathbf{W}^{p,\alpha,\nu_\infty-\varepsilon}_{(m)}(\mathbb{R}_+), \tag{B.10}$$

where Ψ_{ij}, $\mathcal{G}_Z^j$, $\mathcal{G}_Y^j$ $(i,j=1,2)$ are the components of the matrix function $\boldsymbol{\Psi}$ and the vector functions $\mathcal{G}_Z$, $\mathcal{G}_Y$, respectively. For functions $K_{Z(Y)}$ the relations (3.18) are true.

The solutions of the systems of integral equations (4.6) will be sought in the spaces

$$\mathbf{Z},\mathbf{Y}\in\mathbf{L}_2^{p,-\gamma_\infty+\varepsilon,\nu_\infty-\varepsilon}(\mathbb{R}_+). \tag{B.11}$$

Using a similar line of resoning as before, it can be shown that the solutions will belong to the spaces $\mathbf{W}_{(1),2}^{1,-\gamma_\infty+\varepsilon,\nu_\infty-\varepsilon}(\mathbb{R}_+)$, so that the *a priori* estimates (A.24) will be satisfied. Here by $\mathbf{X}_2$ we denote the Banach space of the vector functions with components from $\mathbf{X}$, the norm of which is defined in the usual way.

First of all consider the cases when $\chi_-=0$, i.e. $\mu_1^-=\mu_l^+$. Then the symbols $\mathbf{B}_{Z(Y)}$ of the operators $\mathcal{B}_{Z(Y)}(\mathcal{J}^+,\mathcal{J}^-,\mathcal{J})$ from (4.6) in the spaces $\mathbf{L}_2^{p,\alpha,\beta}(\mathbb{R}_+)$ $(\alpha>-\gamma_\infty,\ \beta<\nu_\infty)$ are

$$\mathbf{B}_{Z(Y)}(\alpha-it,\mathcal{J}^+,\mathcal{J}^-,\mathcal{J})=\mathbf{I}+K_{Z(Y)}(0,0)\widetilde{\boldsymbol{\Psi}}(\alpha-it,1), \tag{B.12}$$

or, after some calculations, they can be rewritten in the form

$$\begin{aligned}
&\mathbf{B}_Z(s,\mathcal{J}^+,\mathcal{J}^-,1)=(1-\chi_+)^{-1}\boldsymbol{\Phi}_*^{-1}(s)(\boldsymbol{\Phi}_*(s)-\mathbf{I}),\\
&\mathbf{B}_Z(s,\mathcal{J}^+,\mathcal{J}^-,3)=\mathbf{B}_Y(s,\mathcal{J}^+,\mathcal{J}^-,3)\\
&\qquad=\left(1-\chi_+\left(1-\frac{\mu_1}{\mu_{n+1}}\right)\right)^{-1}\boldsymbol{\Phi}_*^{-1}(s)\left(\boldsymbol{\Phi}_*(s)-\left(1-\frac{\mu_1}{\mu_{n+1}}\right)\mathbf{I}\right),\\
&\mathbf{B}_Y(s,\mathcal{J}^+,\mathcal{J}^-,2)=\chi_+^{-1}\boldsymbol{\Phi}_*^{-1}(s).
\end{aligned}$$

Note that the operator $\mathcal{B}_Z(\mathcal{J}^+,\mathcal{J}^-,3)$ is isometrically equivalent to $\mathcal{B}_Y(\mathcal{J}^+,\mathcal{J}^-,3)$ and all the conclusions of Remark B.2 hold also in the present case.

Denote by $\nu_0(\mathcal{J}^+,\mathcal{J}^-,2)$, $\nu_0(\mathcal{J}^+,\mathcal{J}^-,\mathcal{J})$, $(\mathcal{J}=1,3)$ the zeros of the determinants of the matrix functions $\mathbf{B}_Y(s,\mathcal{J}^+,\mathcal{J}^-,2)$ and $\mathbf{B}_Z(s,\mathcal{J}^+,\mathcal{J}^-,\mathcal{J})$ $(\mathcal{J}=1,3)$, respectively, which are the nearest to the imaginary axis (inside half-plane $\Re s\geq 0$). It can be shown that

$$\begin{aligned}
&\nu_0(2,2,1)=\nu_0(1,1,2)=1,\\
&0<\nu_0(\mathcal{J}^+,\mathcal{J}^-,3)<\nu_\infty(\mathcal{J}^+,\mathcal{J}^-)<1, \qquad \mu_1<\mu_{n+1},\\
&0<\nu_\infty(\mathcal{J}^+,\mathcal{J}^-)<\nu_0(\mathcal{J}^+,\mathcal{J}^-,3)<1, \qquad \mu_1>\mu_{n+1},
\end{aligned} \tag{B.13}$$

and all zeros are simple. For other problems

$$\nu_0(1,1,1)=\nu_0(1,2,1)=\nu_0(1,2,2)=\nu_0(2,2,2)=0,$$

and their multiplicities are equal to two. As before, the problems are divided into two groups depending on the values of the respective zeros.

Consider the first group (of the problems for which $\nu_0(\mathcal{J}^+, \mathcal{J}^-, \mathcal{J}) > 0$). Then it is easy to see that for all values of $|\alpha| < \nu_0(\mathcal{J}^+, \mathcal{J}^-, \mathcal{J})$ the indices of the respective operators are equal to zero:

$$\text{(B.14)} \qquad \mathcal{K} = -\operatorname{ind} \det \mathbf{B}_{Z(Y)}(\alpha - it, \mathcal{J}^+, \mathcal{J}^-, \mathcal{J}) = 0, \quad |\alpha| < \nu_0(\mathcal{J}^+, \mathcal{J}^-, \mathcal{J}).$$

However, when we deal with the systems of integral equations it is not enough to calculate only the indices of the operators in order to investigate their solvability. In this case, the partial indices κ_j, $(j = 1, 2)$ play also an important role [5]. In order to obtain the values of κ_j, $(j = 1, 2)$ note that the real parts of the symbols (B.13) (for $s = it$, $t \in \mathbb{R}$) are diagonal matrices with the components

$$\text{(B.15)} \qquad \mathbf{b}_j(s, \mathcal{J}^+, \mathcal{J}^-, \mathcal{J}) = \frac{1}{\vartheta - \chi_+} \left(\vartheta - \frac{\Delta^*_{3-j}(s)}{\det \mathbf{\Phi}_*(s)} \right),$$

where $\vartheta = \vartheta(\mathcal{J})$ are $\vartheta(1) = 1$, $\vartheta(2) = 0$, $\vartheta(3) = (1 - \mu_1/\mu_{n+1})^{-1}$, and

$$\Delta^*_j(s, \mathcal{J}^+, \mathcal{J}^-) = 1 + (-1)^j \mu_1 s M_+(s, \mathcal{J}^+, \mathcal{J}^-) \left(\operatorname{tg} \frac{\pi s}{2} \right)^{3-2j}.$$

Let us note that for the symmetric problems $\{j, \mathcal{J}^+, \mathcal{J}\}$ investigated above $\Delta^*_j(s, \mathcal{J}^+, \mathcal{J}^+) = \Delta_j(s, \mathcal{J}^+)$.

Taking into account the properties of the functions $\Delta^*_j(s, \mathcal{J}^+, \mathcal{J}^-)$, which follow from Lemma A.2, it can be shown that

$$1 \le \Delta^*_1(it, \mathcal{J}^+, \mathcal{J}^-) \le \varpi_- + \varpi_+ \le \Delta^*_2(it, \mathcal{J}^+, \mathcal{J}^-) \le \infty,$$

and $\mathbf{b}_j(it, \mathcal{J}^+, \mathcal{J}^-, \mathcal{J})$ are real even functions such that $\mathbf{b}_j(it, \mathcal{J}^+, \mathcal{J}^-, \mathcal{J}) \neq 0$ for all $t \in \overline{\mathbb{R}}$. Then $\operatorname{ind} \mathbf{b}_j(it, \mathcal{J}^+, \mathcal{J}^-, \mathcal{J}) = 0$ and the symbols of the operators are definite matrix functions [5] and, hence, all their left and right partial indices are equal to zero [5].

THEOREM B.5. *Let* $1 \le p < \infty$, $m \in \mathbf{N}$, $\nu_0(\mathcal{J}^+, \mathcal{J}^-, \mathcal{J}) > 0$, $\beta < \nu_\infty(\mathcal{J}^+, \mathcal{J}^-)$, $\beta - \alpha \ge 0$, $-\min\{1, \nu_0(\mathcal{J}^+, \mathcal{J}^-, \mathcal{J}), \nu_\infty(\mathcal{J}^+, \mathcal{J}^-)\} < \alpha < \nu_0(\mathcal{J}^+, \mathcal{J}^-, \mathcal{J})$, *then there exists a certain value* $\varepsilon > 0$ *such that for all* $|\chi_-| < \varepsilon$:

1. The operators $\mathcal{B}_{Z(Y)}(\mathcal{J}^+, \mathcal{J}^-, \mathcal{J})$, *in the spaces* $\mathbf{L}_2^{p,\alpha,\beta}(\mathbb{R}_+)$ *are normally solvable, moreover, their indices and all partial indices are equal to zero.*

2. There exist the unique solutions of the systems of equations (4.6) *from* $\mathbf{W}^{p,\alpha,\beta}_{(m),2}(\mathbb{R}_+) \subset \mathbf{L}_2^{p,\alpha,\beta}(\mathbb{R}_+)$.

3. Galerkin method for the systems of equation (4.6) *in Hilbert space* $\mathbf{L}_2^{2,\alpha,\beta}(\mathbb{R}_+)$ *converges by the set of the functions* (B.9) *with vector coefficients.*

4. The asymptotics of the solutions of systems (4.6) *in the neighbourhood of zero is in the form*

$$\mathbf{u}(\lambda) = O(\lambda^{\gamma_\infty}), \qquad \lambda \to 0, \qquad \gamma_\infty = \min\{1, \nu_0(\mathcal{J}^+, \mathcal{J}^-, \mathcal{J})\},$$

and at infinity the asymptotics are defined by the relations (4.3), (4.4).

Now, consider the systems (4.6) for the problems when $\nu_0(\mathcal{J}^+, \mathcal{J}^-, \mathcal{J}) = 0$. It can be shown that in these cases depending on the value $\pm\alpha > 0$ ($|\alpha| < \nu_0(\mathcal{J}^+, \mathcal{J}^-, \mathcal{J})$)

$$\mathcal{K} = -\text{ind det } \mathbf{B}_{Z(Y)}(\alpha - it, \mathcal{J}^+, \mathcal{J}^-, \mathcal{J}) = \pm 1.$$

Observe that for problems (1,2,2), (2,2,2) the values of z_*^+ are known and

$$\kappa_1 = -\text{ind } \mathbf{b}_1(\alpha - it, 1, 2, 2) = -\text{ind } \mathbf{b}_1(\alpha - it, 1, 2, 2) = 0,$$
$$\kappa_2 = -\text{ind } \mathbf{b}_2(\alpha - it, 2, 2, 2) = -\text{ind } \mathbf{b}_2(\alpha - it, 1, 2, 2) = \pm 1.$$

For the problems (1,1,1) and (1,2,1) it can be shown that

$$\kappa_1 = -\text{ind } \mathbf{b}_1(\alpha - it, 1, 1, 1) = -\text{ind } \mathbf{b}_1(\alpha - it, 1, 2, 1) = \pm 1,$$
$$\kappa_2 = -\text{ind } \mathbf{b}_2(\alpha - it, 1, 1, 1) = -\text{ind } \mathbf{b}_2(\alpha - it, 1, 2, 1) = 0.$$

Moreover, in the last cases we can represent the right-hand side (4.6) in the same form as before $\mathcal{G}_Z = \mathcal{G}_1 + z_*^+ \mathcal{G}_2$, where values of z_*^+ are unknown. Then the vector functions $\mathcal{G}_1$ and $\mathcal{G}_2$ are bounded in the neighbourhood of zero.

Taking into account the volume of the paper, we do not present here the three other theorems concerning the systems of equations, which are similar to Theorems B.2 – B.4.

The proofs of Theorem B.1 – B.5 follow immediately from the investigations of the operators and the results [11, 14]. However, in [11, 14] the operators with fixed point singularities were considered only. Therefore, we can prove the conclusions of Theorem B.5 (and the other ones, which are not formulated) under stronger assumptions ($\chi_- = 0$). Then the stability of the index and the partial indices of the operator with respect to small perturbations of the operator norm [4] is used to prove the theorems for values of $|\chi_-| < \varepsilon$.

Acknowledgment

The author is grateful to Professor A.M. LINKOV for his suggestions to problem formulation and numerous helpful remarks.

References

1. V.G. BLINOVA and A.M. LINKOV, *A method to derive the main asymptotic terms near the tips of elastic wedges* [in Russian], Vestn., St Petersb. Univ., Ser 1, **2**, 8, 69–72, 1992.
2. G.P. CHEREPANOV, *Fracture mechanics of composite materials* [in Russian], Nauka, Moscow 1983.
3. R.V. DUDUCHAVA, *Integral equations of convolution with discontinuous symbols, singular integral equations with fixed singularities and their applications to problems of mechanics* [in Russian], Tr. Tbilis. Mat. Inst, A.N. Gruz. SR, 10, 135, 1979.
4. I.C. GOHBERG and N.A. FELDMAN, *Equations in convolutions and projectional methods of their solutions* [in Russian], Nauka, Moscow 1971.

5. I.C. GOHBERG and M.G. KREIN, *Systems of integral equations on semi-axis with kernels dependent on the difference of the arguments* [in Russian], Usp. Mat. Nauk, **13**, 2, 3–72, 1958.
6. A.I. KALANDIYA, *Mathematical method of two-dimensional elasticity*, "Mir", Moscow 1973.
7. G.S. KIT and M.G. KRIVTSUN, *Plane thermoelasticity problems for bodies with cracks* [in Russian], "Naukova Dumka", Kiev 1983.
8. M.G. KREIN, *Integral equations on semi-axis with kernels dependent on the difference of the arguments* [in Russian], Usp. Mat. Nauk, **13**, 5, 3–120, 1958.
9. A.M. LINKOV and N. FILIPPOV, *Difference equations approach to the analysis of layered systems*, Mecchanica, 26, 195–209, 1991.
10. H. MARCINKOWSKA, *Distributions, Sobolev spaces, differential equations* [in Polish], PWN, Warszawa 1993.
11. G.S. MISHURIS, *On a class of matrix integral equations* [in Russian], VINITI, Nr 637384, 1984.
12. G.S. MISHURIS, *Applications of the integral transforms in problems of elastic solids with notches* [in Russian], Ph.D. Thesis, stored at VINITI, Nr 0485004348, 174, 1985.
13. G.S. MISHURIS, *A plane problem of elasticity theory for a layered medium with semi-infinite crack perpendicular to the boundary between the layers* [in Russian], Studies in Elasticity and Plasticity, Leningrad Univ. Publ., 15, 82–96, 1986.
14. G.S. MISHURIS and Z.S. OLESIAK, *On boundary value problems in fracture of elastic composites*, EJAM, **6**, 1995.
15. G. MISHURIS, *On nontrivial solution of one singular integral equation*, Zesz. Nauk. Politech. Rzeszowskiej, Matematyka, **16**, 119–130, 1994.
16. N.F. MOROZOV, *Mathematical problems of the crack theory* [in Russian], "Nauka", Moscow, 255, 1984.
17. S.A. NAZAROV, *Introduction to asymptotic methods of the theory of elasticity* [in Russian], Izd. Leningrad Univ., Leningrad 1983.
18. W. NOWACKI and Z.S. OLESIAK, *Thermodiffusion in solid bodies* [in Polish], 272, Polish Scientific Publishers (PWN), Warszawa 1991.
19. A.P. PRUDNIKOV, YU.A. BRYCHKOV and O.U. MARICHEV, *Integrals and series. Elementary functions. Tables* [in Russian], Nauka, Moscow 1981.
20. D. PRZEWORSKA-ROLEWICZ, *Equations with transformed argument. An algebraic approach*, Elsevier Publ., Amsterdam 1973.
21. C.J. TRANTER, *Integral transforms in mathematical physics*, Methuen, London; J. Wiley and Sons, New York 1951.
22. I.N. SNEDDON, *The use of integral transforms*, McGraw-Hill, Inc., New York 1977.
23. YA.S. UFLYAND, *Integral transforms in problems of the theory of elasticity*, Translated from the Russian edition: Izd. Ak. Nauk SSSR, Moscow-Leningrad 1967.
24. A.H. ZEMANIAN, *Generalized integral transformations*, John Wiley and Sons, Inc., New York 1969.

DEPARTMENT OF MATHEMATICS,
RZESZÓW UNIVERSITY OF TECHNOLOGY, RZESZÓW.

Received September 21, 1994.

Arch. Mech., 47, 2, pp. 337–351, Warszawa 1995

Combined plastic simple waves in a thin-walled tube (*)

H.V. NGUYEN (WARSZAWA)

CONSTITUTIVE RELATIONS for adiabatic rate-independent materials processes with combined isotropic-linear hardening finite deformations are used to study the problem of a thin-walled cylindrical tube subject to combined longitudinal and torsional impact at one end. The effect of transversal inertia is disregarded but that of transversal motion is taken into account. Influence of the plastic spin on the problem is discussed. A numerical solution for stress trajectories of simple adiabatic waves is provided.

1. Introduction

THE PROPAGATION OF WAVES in a thin-walled tube at small strains and rotations have been studied by CLIFTON [2] for isotropic hardening, and by LIPKIN and CLIFTON [6] for kinematic hardening. GOEL and MALVERN [4] proposed a method accounting for the combined effects of isotropic and kinematic hardening laws. TING [17] obtained solutions for all possible combinations of discontinuous loading, and explicit simple wave solution for linear work-hardening materials. The endochronic theory of plasticity was used by HAN-CHIN WU and HSUAN-CHI LIN [22] to obtain the simple wave solution. Adiabatic simple waves were investigated by RANIECKI [16], PODOLAK and RANIECKI [15], where the effects of energy dissipation on the velocity and profile of simple waves were analyzed. Isothermal and adiabatic simple waves in a thin-walled tube at finite strains were studied by NGUYEN in [19]. It was shown that the differences between the isothermal and adiabatic slow wave velocities may be considerably great. In those works, the radial motion and lateral inertia effects were neglected, and two wave velocities were established: fast wave velocity c_f and slow wave velocity c_s, satisfying the inequality

$$c_s \leq c_2 \leq c_f \leq c_1 .$$

Here $c_1 = \sqrt{E/\varrho_0}$ denotes the velocity of longitudinal elastic wave, and $c_2 = \sqrt{\mu/\varrho_0}$ – the velocity of transversal elastic wave.

We consider in this paper a thin-walled cylindrical tube subject to a suddenly applied, combined longitudinal and torsional stress (or motion) at one end of the tube, on the basis of the constitutive equations derived in [20, 21]. The effect of transversal inertia is disregarded but that of transversal motion is taken into account. The latter appears to be important in the case of finite strain, see for example NOWACKI [10, 11].

(*) Paper presented at 30th Polish Solid Mechanics Conference, Zakopane, September 5–9, 1994.

2. Kinematics of the combined tension-torsion loading of a thin-walled tube

Consider a thin-walled tube with wall thickness H formed so that, prior to deformation, the cross-section is circular with radius A measured to the midpoint of the wall. The position of material in the tube is given by cylindrical polar coordinates R, Θ, Z in the undeformed configuration. During the deformation, the mean radius and thickness of the tube are a and h, respectively, and the ring of material originally at Z rotates by angle $\omega = sZ/A$ about the Z axis and moves to the axial position $z = (1 + L)Z$. Here the angle of twist per unit undeformed length of the tube is s/A, and the strain L is the change in length of the tube per unit undeformed length. Denote by r, ϕ, z the cylindrical coordinates in the current configuration; the motion is given by equations of the form

$$
\begin{aligned}
r &= \frac{h}{H}(R - A) + a, \\
\phi &= \Theta + \frac{sZ}{A} = \Theta + \omega, \\
z &= (1 + L)Z.
\end{aligned}
\tag{2.1}
$$

During this motion the undeformed elementary length vector $d\mathbf{X}$ becomes the deformed element $d\mathbf{x} = \mathbf{F}\,d\mathbf{X}$, where $\mathbf{F}$ is the deformation gradient.

From (2.1) we can find the components of the velocity gradient. In cylindrical polar coordinates, in the current configuration, they are:

$$
\mathbf{V} = \dot{\mathbf{F}}\,\mathbf{F}^{-1} = \begin{pmatrix} \dfrac{\dot{h}}{h} & -\dfrac{\dot{s}\,Z}{A} & 0 \\ \dfrac{\dot{s}\,Z}{A} & \dfrac{\dot{a}}{a} & \dfrac{r\,\dot{s}}{A(1+L)} \\ 0 & 0 & \dfrac{\dot{L}}{1+L} \end{pmatrix} = \begin{pmatrix} \dfrac{\partial v_r}{\partial r} & -\dfrac{v_\varphi}{r} & 0 \\ \dfrac{\partial v_\varphi}{\partial r} & \dfrac{v_r}{r} & \dfrac{\partial v_\varphi}{\partial z} \\ 0 & 0 & \dfrac{\partial v_z}{\partial z} \end{pmatrix},
\tag{2.2}
$$

where v_r, v_φ, v_z are the physical components of the particle velocity vector in the cylindrical coordinates. The tube is assumed to be sufficiently thin, so that the deformation due to twisting and extension can be regarded to be homogeneous across the wall, and it may be calculated as the deformation of the midsurface of the wall. The deformation rate and the spin rate are now given by:

$$
\mathbf{D} = \begin{pmatrix} \dfrac{\partial v_r}{\partial r} & 0 & 0 \\ 0 & \dfrac{v_r}{r} & \dfrac{1}{2}\dfrac{\partial v_\varphi}{\partial z} \\ 0 & \dfrac{1}{2}\dfrac{\partial v_\varphi}{\partial z} & \dfrac{\partial v_z}{\partial z} \end{pmatrix}
\tag{2.3}
$$

and

$$\boldsymbol{\omega} = \begin{pmatrix} 0 & -\frac{v_\varphi}{r} & 0 \\ \frac{v_\varphi}{r} & 0 & \frac{1}{2}\frac{\partial v_\varphi}{\partial z} \\ 0 & -\frac{1}{2}\frac{\partial v_\varphi}{\partial z} & 0 \end{pmatrix}. \tag{2.4}$$

Due to the axial symmetry, the equation of continuity has the form

$$\dot{\beta} = \beta \operatorname{div} \mathbf{v} = \beta \left(\frac{\partial v_r}{\partial r} + \frac{v_r}{r} + \frac{\partial v_z}{\partial z} \right), \tag{2.5}$$

where $\beta = \varrho_0/\varrho$, ϱ_0 and ϱ are the density in the undeformed and deformed configuration, respectively.

3. Formulation of basic equations

Let the tension applied to the tube be $2\pi a h \sigma$, and let the torque be $2\pi a^2 h \tau$. Assume that the tube wall is sufficiently thin so that the stress state is homogeneous, and thus the Cauchy stress has three nonzero components

$$\sigma_{zz} = \sigma \qquad \text{and} \qquad \sigma_{z\varphi} = \sigma_{\varphi z} = \tau .$$

The equations of motion are reduced to:

$$\begin{aligned} \dot{v}_r &= \frac{v_\varphi^2}{r}, \\ \frac{\partial \tau}{\partial z} &= \varrho \, \dot{v}_\varphi + \frac{\varrho}{r} v_\varphi v_r, \\ \frac{\partial \sigma}{\partial z} &= \varrho \, \dot{v}_z . \end{aligned} \tag{3.1}$$

Constitutive relations for an adiabatic process for rate-independent materials with combined isotropic-kinematic hardening at moderate pressures, when the thermal expansion, the heat of elastic deformation and the heat of internal rearrangement are neglected (as discussed in [21]), are of the form

$$\overset{\nabla}{\mathbf{T}} = \beta \, \mathbf{L}\mathbf{D} - \frac{3 \, \mathrm{j} \mu \beta \, \mathbf{D} \cdot (\overline{\mathbf{T}} - \boldsymbol{\Pi})}{\sigma_Y^2 \, \mathcal{H}} \left[(\overline{\mathbf{T}} - \boldsymbol{\Pi}) + \mathbf{P} \right], \tag{3.2}$$

$$\mathrm{j} = \begin{cases} 1 \text{ if } f = 0 \quad \text{and} \quad \mathbf{D} \cdot (\overline{\mathbf{T}} - \boldsymbol{\Pi}) \geq 0, \\ 0 \text{ if } f = 0 \quad \text{and} \quad \mathbf{D} \cdot (\overline{\mathbf{T}} - \boldsymbol{\Pi}) < 0 \quad \text{or} \quad f < 0. \end{cases}$$

Here $\mathbf{T} = \beta\boldsymbol{\sigma}$, $\overset{\nabla}{\mathbf{T}} = \dot{\mathbf{T}} - \boldsymbol{\omega}\mathbf{T} + \mathbf{T}\boldsymbol{\omega}$ is the Zaremba-Jaumann rate, $\overline{\mathbf{T}}$ is the deviatoric part of $\mathbf{T}$, $\mathbf{L}$ is the fourth order tensor of elastic moduli, μ is the Lamé constant and f is the Huber-Mises yield criterion

$$f = \frac{3}{2}(\overline{\mathbf{T}} - \boldsymbol{\Pi}) \cdot (\overline{\mathbf{T}} - \boldsymbol{\Pi}) - \sigma_Y^2(\vartheta, \alpha) = 0. \tag{3.3}$$

Here σ_Y is the yield stress in simple tension, ϑ is the temperature, and α corresponds to the size of the yield surface

$$\dot{\alpha} = (\overline{\mathbf{T}} - \boldsymbol{\Pi}) \cdot \mathbf{D}^p. \tag{3.4}$$

The shift of the yield surface is represented here by the back stress $\boldsymbol{\Pi}$, for which the evolution law has the form of linear kinematic hardening

$$\overset{\nabla}{\boldsymbol{\Pi}} = c\,\mathbf{D}^p, \tag{3.5}$$

where c = const and $\mathbf{D}^p$ is the plastic rate of deformation. The change in the temperature is described by

$$\varrho_0 c_v \dot{\vartheta} = (1 - \pi)(\overline{\mathbf{T}} - \boldsymbol{\Pi}) \cdot \mathbf{D}^p. \tag{3.6}$$

α_v is volumetric thermal expansion and c_v is specific heat at constant volume; the first term on the right-hand side of (3.6) represents the rate of energy dissipation and, therefore, $\pi < 1$. For numerous metals π takes the value from the interval 0.02 to 0.1 [8]. In Eq. (3.2) $\mathcal{H}$ is the hardening function

$$\mathcal{H} = 1 + \frac{c}{2\mu\beta} + \frac{1}{6\mu\beta}\frac{\partial(\sigma_Y^2)}{\partial\alpha} + \frac{(1-\pi)}{6\mu\beta\varrho_0 c_v}\frac{\partial(\sigma_Y^2)}{\partial\vartheta},$$

and tensor $\mathbf{P}$ is obtained by expressing the term $(\boldsymbol{\omega}^p\mathbf{T} - \mathbf{T}\boldsymbol{\omega}^p)$ as a function of $\mathbf{D}^p$, where $\boldsymbol{\omega}^p$ is the plastic spin [21]. Adopt the following form for the plastic spin [3, 7, 12–14]

$$\boldsymbol{\omega}^p = \eta\,(\boldsymbol{\Pi}\mathbf{D}^p - \mathbf{D}^p\boldsymbol{\Pi}), \tag{3.7}$$

where η may depend on the invariants of $\mathbf{D}^p$ and $\boldsymbol{\Pi}$. In ONAT [12], DAFALIAS [3] and LORET [7] η was taken as a constant to provide the non-oscillatory solution. The derivation of the relation for η, based on the analysis of simple shear problem was given and verified in the papers of PAULUN and PĘCHERSKI [13, 14].

In the case of moderate pressures, $\beta = 1$ and the fundamental equations of our problem can be derived from the kinematical and constitutive relations. Thus we have

$$\begin{aligned}
&\frac{\partial v_\varphi}{\partial t} + v_z\frac{\partial v_\varphi}{\partial z} - \frac{1}{\varrho_0}\frac{\partial\tau}{\partial z} = 0,\\
&\frac{\partial v_z}{\partial t} + v_z\frac{\partial v_z}{\partial z} - \frac{1}{\varrho_0}\frac{\partial\sigma}{\partial z} = 0,\\
&\frac{\partial\vartheta}{\partial t} + v_z\frac{\partial\vartheta}{\partial z} - \frac{\mathrm{j}(1-\pi)}{\varrho_0 c_v\mathcal{H}}\Psi = 0,
\end{aligned} \tag{3.8}$$

(3.8) [cont.]

$$\frac{\partial \sigma}{\partial t} + v_z \frac{\partial \sigma}{\partial z} + \frac{E\tau}{2\mu} \frac{\partial v_\varphi}{\partial z} - E \frac{\partial v_z}{\partial z} + \mathrm{j}\, f^{(\sigma)} \Psi = 0,$$

$$\frac{\partial \tau}{\partial t} + v_z \frac{\partial \tau}{\partial z} - \left(\mu + \frac{\sigma}{2}\right) \frac{\partial v_\varphi}{\partial z} + \mathrm{j}\, f^{(\tau)} \Psi = 0,$$

$$\frac{\partial (\ln h)}{\partial t} + v_z \frac{\partial (\ln h)}{\partial z} + \frac{\tau}{2\mu} \left(1 - \frac{E}{2\mu}\right) \frac{\partial v_\varphi}{\partial z} - \left(1 - \frac{E}{2\mu}\right) \frac{\partial v_z}{\partial z} - \mathrm{j}\, f^{(h)} \Psi = 0,$$

$$\frac{\partial (\ln a)}{\partial t} + v_z \frac{\partial (\ln a)}{\partial z} + \frac{\tau}{\mu} \left(1 - \frac{E}{4\mu}\right) \frac{\partial v_\varphi}{\partial z} - \left(1 - \frac{E}{2\mu}\right) \frac{\partial v_z}{\partial z} + \mathrm{j}\, f^{(a)} \Psi = 0,$$

$$\frac{\partial \Pi}{\partial t} + v_z \frac{\partial \Pi}{\partial z} + \mathrm{j}\, f^{(p)} \Psi = 0,$$

$$\frac{\partial \Pi_{23}}{\partial t} + v_z \frac{\partial \Pi_{23}}{\partial z} - \mathrm{j}\, f^{(23)} \Psi = 0,$$

where E is Young's modulus; Π, Π_{23} are the non-zero components of the back stress $\mathbf{\Pi}$,

$$\Psi = \psi_1 \frac{\partial v_z}{\partial z} + \psi_2 \frac{\partial v_\varphi}{\partial z} - \psi_3 \left(\frac{\partial \ln h}{\partial t} + v_z \frac{\partial \ln h}{\partial z}\right) - \psi_4 \left(\frac{\partial \ln a}{\partial t} + v_z \frac{\partial \ln a}{\partial z}\right), \tag{3.9}$$

and

$$\begin{aligned}
f^{(\sigma)} &= \frac{3E}{2\sigma_Y^2 \mathcal{H}} \left(\psi_1 - \frac{\eta\tau}{\mu} \psi_5\right), \\
f^{(\tau)} &= \frac{3\mu}{\sigma_Y^2 \mathcal{H}} \left(\psi_2 + \frac{\eta\sigma}{2\mu} \psi_5\right), \\
f^{(h)} &= \frac{3}{\sigma_Y^2 \mathcal{H}} \left[\frac{\psi_4}{2} - \left(1 - \frac{E}{4\mu}\right) \psi_1 + \frac{\eta\tau}{2\mu} \left(1 - \frac{E}{2\mu}\right) \psi_5\right], \\
f^{(a)} &= \frac{3}{\sigma_Y^2 \mathcal{H}} \left[\frac{\psi_4}{2} - \frac{\psi_1}{2} - \frac{\eta\tau}{\mu} \left(1 - \frac{E}{4\mu}\right) \psi_5\right], \\
f^{(p)} &= \frac{3c}{4\sigma_Y^2 \mathcal{H}} (\psi_4 - \psi_1), \\
f^{(23)} &= \frac{3c}{2\sigma_Y^2 \mathcal{H}} \psi_2,
\end{aligned} \tag{3.10}$$

with

$$\begin{aligned}
\psi_1 &= \left(\frac{2\sigma}{3} - \Pi\right), \qquad \psi_2 = (\tau - \Pi_{23}), \\
\psi_3 &= \left(\frac{\sigma}{3} - 2\Pi\right), \qquad \psi_4 = \left(\frac{\sigma}{3} + \Pi\right), \\
\psi_5 &= \sigma \Pi_{23}.
\end{aligned}$$

In the equation (3.8) we have

$$\mathrm{j} = \begin{cases} 1 & \text{if } f = \dfrac{3}{2}\left(\psi_1^2 + 2\psi_2^2 + \psi_3^2 + \psi_4^2\right) - \sigma_Y^2 \\ & \quad = \sigma^2 + 9\Pi^2 - 3\sigma\Pi + 3(\tau - \Pi_{23})^2 - \sigma_Y^2 = 0, \\ & \text{and } \Psi \geq 0, \\ 0 & \text{if } f = 0 \text{ and } \Psi < 0 \text{ or } f < 0, \end{cases}$$

and

$$\mathcal{H} = 1 + \frac{c}{2\mu} + \frac{1}{6\mu}\frac{\partial(\sigma_Y^2)}{\partial\alpha} + \frac{(1-\pi)}{6\mu\varrho_0 c_v}\frac{\partial(\sigma_Y^2)}{\partial\vartheta}.$$

The system of nine equations (3.8) is a quasi-linear, non-symmetric and homogeneous system of partial differential equations for nine unknowns. It can be rewritten in the form

$$\mathbf{A}\frac{\partial \mathbf{U}(z,t)}{\partial z} + \mathbf{B}\frac{\partial \mathbf{U}(z,t)}{\partial t} = 0, \qquad \mathbf{U} = \begin{pmatrix} v_\varphi \\ v_z \\ \vartheta \\ \sigma \\ \tau \\ \ln h \\ \ln a \\ \Pi \\ \Pi_{23} \end{pmatrix}. \tag{3.11}$$

The characteristic speeds W are the roots of the determinantal equation $|\mathbf{A} - W\mathbf{B}| = 0$ (see, for example, NOWACKI [9]), where $\mathbf{A}$ is the matrix of coefficients of z-derivatives, and $\mathbf{B}$ is the matrix of coefficients of the time derivatives. Expansion of this determinant gives us the equation

$$X^3\left(\mathcal{M}X^2 + \mathcal{N}X + \mathcal{P}\right) = 0, \tag{3.12}$$

with

$$X = \varrho_0(W - v_z)^2 = \varrho_0\Omega^2. \tag{3.13}$$

Here Ω is the local velocity (with respect to the material at the time t),

$$\begin{aligned} \mathcal{M} &= 1 + \mathrm{j}\psi_3 f^{(h)} - \mathrm{j}\psi_4 f^{(a)}, \\ \mathcal{N} &= -\left[E + \left(\mu + \frac{\sigma}{2}\right)\right]\mathcal{M} + \mathrm{j}\frac{E}{2\mu}\psi_1 f^{(\sigma)} + \mathrm{j}\psi_6 f^{(\tau)}, \\ \mathcal{P} &= E\mathcal{M}\left(\mu + \frac{\sigma}{2}\right) - \mathrm{j}\frac{E}{2\mu}\left(\mu + \frac{\sigma}{2}\right)\psi_1 f^{(\sigma)} - \mathrm{j}E\psi_7 f^{(\tau)}, \end{aligned} \tag{3.14}$$

and

$$\psi_6 = \psi_2 + \frac{\tau}{2\mu}\left(1 - \frac{E}{2\mu}\right)\psi_3 + \frac{\tau}{\mu}\left(1 - \frac{E}{4\mu}\right)\psi_4,$$

$$\psi_7 = \psi_2 + \frac{\tau}{2\mu}(\psi_1 + \psi_4). \tag{3.15}$$

Equation (3.12) has the trivial solution $X = 0$ and two solutions of the quadratic part $X_{1,2}$. The greater X_f is called the velocity of the fast wave, and the smaller X_s – the velocity of the slow wave. In the limiting cases when j=0 (the region of elastic deformation or of elastic unloading), we deduce from the equation (3.12) that

$$X_f = \varrho_0 \Omega_f{}^2 = E,$$

$$X_s = \varrho_0 \Omega_s{}^2 = \mu + \frac{\sigma}{2} \tag{3.16}$$

as in [19]. The discriminant Δ of (3.12), after some algebraic manipulations, takes the form

$$\Delta = \left\{\left[E - \left(\mu + \frac{\sigma}{2}\right)\right]\mathcal{M} - \mathrm{j}\frac{E}{2\mu}\psi_1 f^{(\sigma)} + \mathrm{j}\psi_6 f^{(\tau)}\right\}^2 + 2\mathrm{j}\frac{E}{\mu}\psi_1\psi_6 f^{(\sigma)} f^{(\tau)} + 4\mathrm{j}E\mathcal{M} f^{(\tau)}(\psi_7 - \psi_6). \tag{3.17}$$

When the ratios of stress/elastic moduli are small as compared to unity and can be neglected in (3.15), we have $\psi_6 = \psi_7 = \psi_2$ and thus the plastic spin does not play important role, see [3,21]; then we can show that

$$\Delta = \left[(E - \mu)\mathcal{M} - \mathrm{j}\frac{E}{2\mu}\psi_1 f^{(\sigma)} + \mathrm{j}\psi_2 f^{(\tau)}\right]^2 + \mathrm{j}\left(\frac{E\psi_1\psi_2}{\sigma_Y^2 \mathcal{H}}\right)^2 > 0. \tag{3.18}$$

The system of equation (3.8) is now hyperbolic. These results, in the case of small deformations, reduce to those of [4].

We can eliminate $\ln h$ and $\ln a$ from the system (3.8). Using Eqs. $(3.8)_{6,7}$, they can be expressed in terms of $\dfrac{\partial v_\varphi}{\partial z}$ and $\dfrac{\partial v_z}{\partial z}$. Determinant of these two equations is $\mathcal{M}$. Assuming that $\mathcal{M} \neq 0$ and eliminating $\ln h$ and $\ln a$ from (3.9) leads to

$$\Psi^* = \frac{1}{\mathcal{M}}\left(\frac{E}{2\mu}\psi_1 \frac{\partial v_z}{\partial z} + \psi_6 \frac{\partial v_\varphi}{\partial z}\right). \tag{3.19}$$

Now the system (3.8) assumes the form

$$\begin{aligned}
\frac{\partial v_\varphi}{\partial t} + v_z \frac{\partial v_\varphi}{\partial z} - \frac{1}{\varrho_0}\frac{\partial \tau}{\partial z} &= 0,\\
\frac{\partial v_z}{\partial t} + v_z \frac{\partial v_z}{\partial z} - \frac{1}{\varrho_0}\frac{\partial \sigma}{\partial z} &= 0,\\
\frac{\partial \vartheta}{\partial t} + v_z \frac{\partial \vartheta}{\partial z} - \frac{\mathrm{j}(1-\pi)}{\varrho_0 c_v \mathcal{H}}\Psi^* &= 0,
\end{aligned}$$

$$\begin{aligned}
\frac{\partial \sigma}{\partial t} + v_z \frac{\partial \sigma}{\partial z} + \frac{E\tau}{2\mu}\frac{\partial v_\varphi}{\partial z} - E\frac{\partial v_z}{\partial z} + \mathrm{j} f^{(\sigma)}\Psi^* &= 0,\\
\frac{\partial \tau}{\partial t} + v_z \frac{\partial \tau}{\partial z} - \left(\mu + \frac{\sigma}{2}\right)\frac{\partial v_\varphi}{\partial z} + \mathrm{j} f^{(\tau)}\Psi^* &= 0,
\end{aligned} \tag{3.20}$$

$$\begin{aligned}
\frac{\partial \Pi}{\partial t} + v_z \frac{\partial \Pi}{\partial z} + \mathrm{j} f^{(p)}\Psi^* &= 0,\\
\frac{\partial \Pi_{23}}{\partial t} + v_z \frac{\partial \Pi_{23}}{\partial z} - \mathrm{j} f^{(23)}\Psi^* &= 0,
\end{aligned}$$

where

$$\mathrm{j} = \begin{cases} 1 & \text{if } f = 0 \text{ and } \Psi^* \geq 0,\\ 0 & \text{if } f = 0 \text{ and } \Psi^* < 0 \text{ or } f < 0. \end{cases}$$

4. Special cases

In the particular case of torsional loading $\sigma = \Pi = 0$ we obtain from $(3.20)_2$ $v_z = \text{const} = 0$, and from (3.10) we have

$$\psi_1 = \psi_3 = \psi_4 = \psi_5 = 0, \qquad \psi_2 = \psi_6 = \tau - \Pi_{23},$$

$$f^{(\sigma)} = f^{(h)} = f^{(a)} = f^{(2)} = f^{(3)} = 0, \qquad f^{(\tau)} = \frac{3\mu\psi_2}{\sigma_Y^2 \mathcal{H}} \qquad f^{(23)} = -\frac{3c\psi_2}{2\sigma_Y^2 \mathcal{H}},$$

so the system (3.20) takes now the following form:

$$\begin{aligned}
\frac{\partial v_\varphi}{\partial t} - \frac{1}{\varrho_0}\frac{\partial \tau}{\partial z} &= 0,\\
\frac{\partial \vartheta}{\partial t} - \frac{\mathrm{j}(1-\pi)(\tau - \Pi_{23})}{\varrho_0 c_v \mathcal{H}}\frac{\partial v_\varphi}{\partial z} &= 0,\\
\frac{\partial \tau}{\partial t} - \mu\left(1 - \frac{\mathrm{j}}{\mathcal{H}}\right)\frac{\partial v_\varphi}{\partial z} &= 0,\\
\frac{\partial \Pi_{23}}{\partial t} - \frac{\mathrm{j}c}{2\mathcal{H}}\frac{\partial v_\varphi}{\partial z} &= 0,
\end{aligned} \tag{4.1}$$

where

$$\mathrm{j} = \begin{cases} 1 & \text{if } f = (\tau - \Pi_{23})^2 - \tau_Y{}^2 \equiv \bar{\sigma}_e^2 - \tau_Y{}^2 = 0 \text{ and } (\tau - \Pi_{23}) \dfrac{\partial v_\varphi}{\partial z} \geq 0, \\ 0 & \text{if } f = 0 \text{ and } (\tau - \Pi_{23}) \dfrac{\partial v_\varphi}{\partial z} < 0 \text{ or } f < 0. \end{cases}$$

Here $\bar{\sigma}_e$ is the reduced effective stress, and τ_Y is the yield stress in pure shear ($\tau_Y = \sigma_Y/\sqrt{3}$ according to the von Mises yield criterion).

When longitudinal loading is considered, we have $\tau = \Pi_{23} = 0$ and the first equation of (3.20) gives $v_\varphi = \text{const} = 0$. The system (3.20) now becomes

$$\begin{aligned} \frac{\partial v_z}{\partial t} + v_z \frac{\partial v_z}{\partial z} - \frac{1}{\varrho_0} \frac{\partial \sigma}{\partial z} &= 0, \\ \frac{\partial \vartheta}{\partial t} + v_z \frac{\partial \vartheta}{\partial z} - \frac{\mathrm{j}(1-\pi)}{\varrho_0 c_v \mathcal{H}} \Psi^* &= 0, \\ \frac{\partial \sigma}{\partial t} + v_z \frac{\partial \sigma}{\partial z} - E \frac{\partial v_z}{\partial z} + \mathrm{j} f^{(\sigma)} \Psi^* &= 0, \\ \frac{\partial \Pi}{\partial t} + v_z \frac{\partial \Pi}{\partial z} + \mathrm{j} f^{(p)} \Psi^* &= 0, \end{aligned} \tag{4.2}$$

where

$$\Psi^* = \frac{E}{2\mu\mathcal{M}} \psi_1 \frac{\partial v_z}{\partial z}, \qquad f^{(\sigma)} = \frac{3E}{2\sigma_Y^2 \mathcal{H}} \psi_1, \qquad f^{(p)} = -\frac{3c}{4\sigma_Y^2 \mathcal{H}} \psi_3.$$

The terms of the plastic spin do not participate in (4.1) and (4.2). It is involved, however, in the equations of combined longitudinal-torsional loading problems. So, the effect of combined loading intensifies the influence of the plastic spin. This conclusion shows the need for futher study in this direction.

5. Simple wave solutions

For the field equations of rate-independent elastic-plastic non-conductors there exist solutions which depend on z and t only via the dependence on a single independent variable, say $\xi(z,t)$. This allows us to convert the partial differential equations obtained before into ordinary differential equations with respect to the new variables. It is shown that the surface $\xi = \text{const}$ coincides with the surface of an ordinary plastic wave [16]. The travelling planes on which the state variable are constant are called simple waves. By combining various simple waves it is possible to find explicit solutions of a certain class of boundary values problems [1]. We find now the particular solution $\mathbf{U} = \mathbf{U}[\xi(z,t)]$ of the system (3.20). Note that

$$\frac{\partial \mathbf{U}}{\partial z} = \frac{d\mathbf{U}}{d\xi} \frac{\partial \xi}{\partial z} = \mathbf{U}' \frac{\partial \xi}{\partial z}, \qquad \frac{\partial \mathbf{U}}{\partial t} = \frac{d\mathbf{U}}{d\xi} \frac{\partial \xi}{\partial t} = \mathbf{U}' \frac{\partial \xi}{\partial t}, \tag{5.1}$$

where we have denoted $\frac{d\mathbf{U}}{d\xi} = \mathbf{U}'$. The system of equation (3.20) then becomes

$$
\begin{aligned}
v'_\varphi \dot{\xi} - \frac{1}{\varrho_0}\tau' \xi_{,z} &= 0, \\
v'_z \dot{\xi} - \frac{1}{\varrho_0}\sigma' \xi_{,z} &= 0, \\
\vartheta' \dot{\xi} - \frac{\mathrm{j}(1-\pi)}{\varrho_0 c_v \mathcal{H}}\Psi^* &= 0,
\end{aligned}
$$

$$
\begin{aligned}
\sigma' \dot{\xi} + \frac{E\tau}{2\mu} v'_\varphi \xi_{,z} - E v'_z \xi_{,z} + \mathrm{j} f^{(\sigma)} \Psi^* &= 0, \\
\tau' \dot{\xi} - \left(\mu + \frac{\sigma}{2}\right) v'_\varphi \xi_{,z} + \mathrm{j} f^{(\tau)} \Psi^* &= 0,
\end{aligned}
\tag{5.2}
$$

$$
\begin{aligned}
\Pi' \dot{\xi} + \mathrm{j} f^{(p)} \Psi^* &= 0, \\
\Pi'_{23} \dot{\xi} - \mathrm{j} f^{(23)} \Psi^* &= 0,
\end{aligned}
$$

where we have denote, for example, $v'_\varphi = \frac{dv_\varphi}{d\xi} \ldots$, $\dot{\xi} = \frac{d\xi}{dt}$, $\xi_{,z} = \frac{\partial \xi}{\partial z}$ and

$$
\begin{aligned}
\Psi^* &= \frac{1}{\mathcal{M}} \left(\frac{E}{2\mu} \psi_1 v'_z \xi_{,z} + \psi_6 v'_\varphi \xi_{,z} \right), \\
&= \alpha v'_z \xi_{,z} + \beta v'_\varphi \xi_{,z} .
\end{aligned}
\tag{5.3}
$$

Let us multiply $(5.2)_{1,2}$ by $\xi_{,z}$ and $(5.2)_{5-8}$ by $\dot{\xi}$; substitute the first two equations into the remainder, taking into account the following relation (see [16, 18])

$$
\dot{\xi} = -\Omega \sqrt{\xi_{,z}\, \xi_{,z}} \, . \tag{5.4}
$$

Then v'_φ and v'_z can be eliminated from (5.2) and we obtain this set of equations

$$
\begin{pmatrix}
X & -\frac{\mathrm{j}(1-\pi)}{\varrho_0 c_v \mathcal{H}}\alpha & -\frac{\mathrm{j}(1-\pi)}{\varrho_0 c_v \mathcal{H}}\beta & 0 & 0 \\
0 & X - E + \mathrm{j} f^{(\sigma)} \alpha & \frac{E\tau}{2\mu} + \mathrm{j} f^{(\sigma)} \beta & 0 & 0 \\
0 & \mathrm{j} f^{(\tau)} \alpha & X - \left(\mu + \frac{\sigma}{2}\right) + \mathrm{j} f^{(\tau)} \beta & 0 & 0 \\
0 & \mathrm{j} f^{(p)} \alpha & \mathrm{j} f^{(p)} \beta & X & 0 \\
0 & -\mathrm{j} f^{(23)} \alpha & -\mathrm{j} f^{(23)} \beta & 0 & X
\end{pmatrix}
\begin{pmatrix}
\vartheta' \\ \sigma' \\ \tau' \\ \Pi' \\ \Pi'_{23}
\end{pmatrix}
= 0.
\tag{5.5}
$$

Here X, α, β have been defined in (3.13) and (5.3), and

$$\mathrm{j} = \begin{cases} 1 & \text{if } f = 0 \text{ and } \alpha\sigma' + \beta\tau' \geq 0, \\ 0 & \text{if } f = 0 \text{ and } \alpha\sigma' + \beta\tau' < 0 \text{ or } f < 0. \end{cases}$$

6. Numerical example

The temperature-dependent, strain rate-sensitive material of the tube is described by the power-law constitutive equation of the form

$$\tau = \begin{cases} \mu\gamma & \text{for } \gamma < \gamma^e, \\ \tau_0 \vartheta^q (\dot{\gamma})^m \gamma^n = \mathrm{T}\vartheta^q \gamma^n & \text{for } \gamma \geq \gamma^e, \end{cases} \tag{6.1}$$

where temperature ϑ is in °C, γ is shear strain, $\dot{\gamma}$ is strain rate in s^{-1} and $\gamma = \gamma^e + \gamma^p$ with γ^e and γ^p being the elastic and plastic part of shear, respectively. Numerical values of constants in (6.1) are taken from the paper of K.A HARTLEY *et al.* [5]. These material parameters were evaluated from the least squares fit of the experimental results made on tubular specimens of AISI 1018 cold-rolled steel (CRS), at a nominal strain rate of the order of $10^3 s^{-1}$. The resulting values and material parameters are presented in the following tables:

Chemical composition (weight percent)				
Material	C	Mn	P	S
1018 CRS	0.18	0.71	0.020	0.022

Material parameters of 1018CRS	
q	−0.38
n	0.015
m	0.019
τ_0	436 MPa
$\dot{\gamma}$	1200 s^{-1}
T	498.87 MPa
γ^e	0.026
μ	15384.6 MPa
ϱ_0	7900 kg/m^3
c_v	500 J/kg°C

Let us consider the posssible stress trajectories in the plane $\sigma - \tau$ connected with simple waves. Combined simple waves are described by the following equations:

$$X\frac{d\vartheta}{d\sigma} = \frac{1-\pi}{\varrho_0 c_v \mathcal{H}}\left(\alpha + \beta\frac{d\tau}{d\sigma}\right), \tag{6.2}$$

$$\frac{d\tau}{d\sigma} = -\frac{X - E + f^{(\sigma)}\alpha}{\frac{E\tau}{2\mu} + f^{(\sigma)}\beta},$$

(6.2) [cont.]
$$X\frac{d\Pi}{d\sigma} = -f^{(p)}\left(\alpha + \beta\frac{d\tau}{d\sigma}\right),$$
$$X\frac{d\Pi_{23}}{d\sigma} = f^{(23)}\left(\alpha + \beta\frac{d\tau}{d\sigma}\right).$$

Thus, the stress trajectories for fast ($X = X_f$) and also for slow ($X = X_s$) waves are the solutions of the first order differential equation $(6.2)_2$. The results of calculations, made according to the Runge–Kutta method using the material properties for CRS 1018, are shown in graphical form. We have taken the equation for plastic spin from the paper of PAULUN and PĘCHERSKI [14]. In Figs. 1 and 2 are plotted the stress trajectories for fast and slow waves in two cases: when the

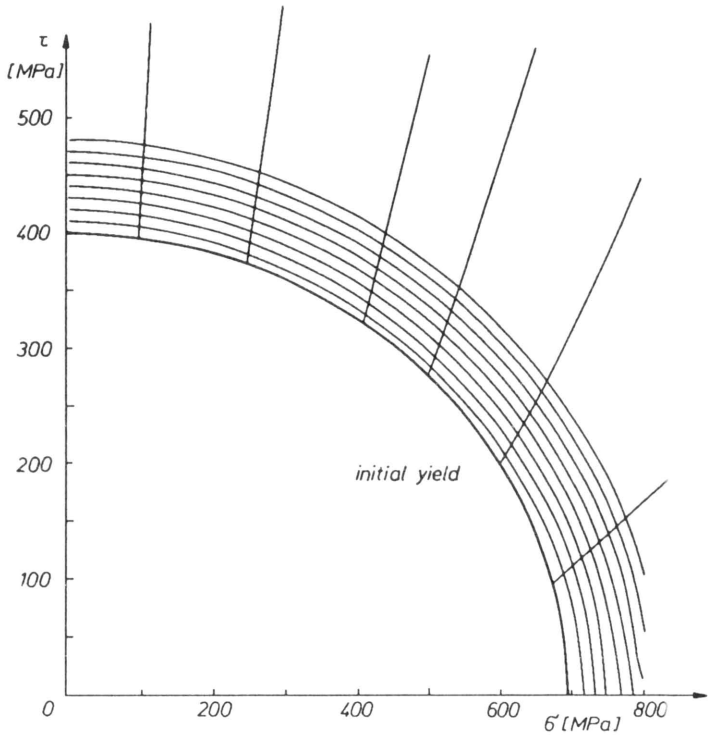

FIG. 1. Adiabatic stress trajectories, no plastic spin.

terms containing the plastic spin are present or not. Analysis of these makes it possible to draw several conclusions. The trajectories for fast and slow waves are not orthogonal as in the case of small deformations. No substantial differences may be observed between the stress trajectories for fast waves in these two cases, but there exists an essential difference what may be seen from the figures for slow waves. In the case when the plastic spin is present, the stress trajectories have a maximum and then decrease.

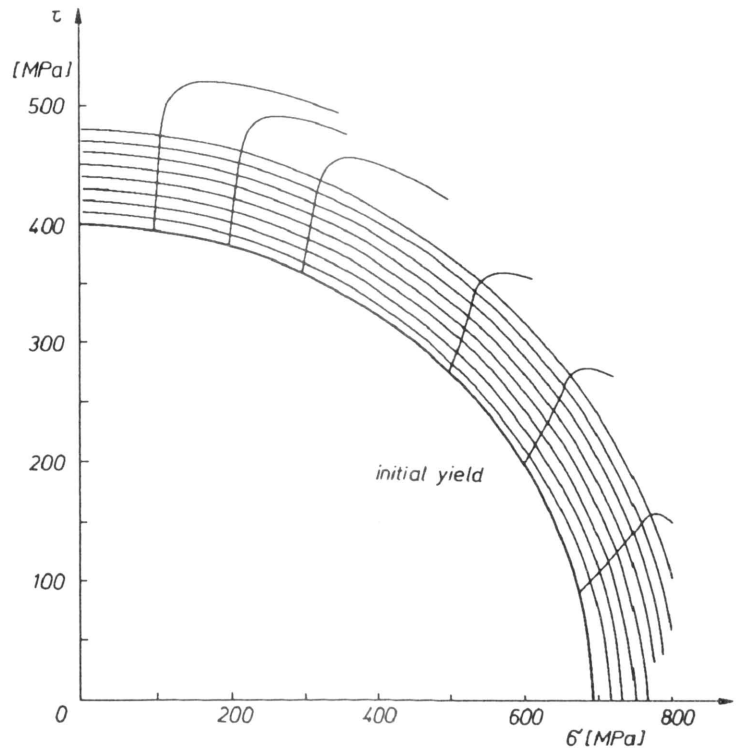

FIG. 2. Adiabatic stress trajectories, with plastic spin.

7. Conclusions

In the paper, thin-walled cylindrical tubes subject to combined longitudinal and torsional impact at one end are considered. The effects of transversal motion are taken into account. We have shown that the plastic spin has a large influence on the problems of combined loading. Using a numerical example we can see that the adiabatic stress trajectories for fast waves are very "close" in two cases: on account of the terms of plastic spin or without these terms. For slow waves an essential difference occurs. Moreover, calculations show that the velocities of slow waves tend to zero faster in the case when the terms containing the plastic spin are present (see Fig. 3).

By combining segments of the fast and slow wave trajectories we can find the solutions of a certain class of boundary-value problems. The method presented here cannot be used in the cases of arbitrary boundary conditions; it may be applied only in the case of constant stresses at the boundary of the tube. The method of solution of the initial-boundary value problem was discussed by CLIFTON [2].

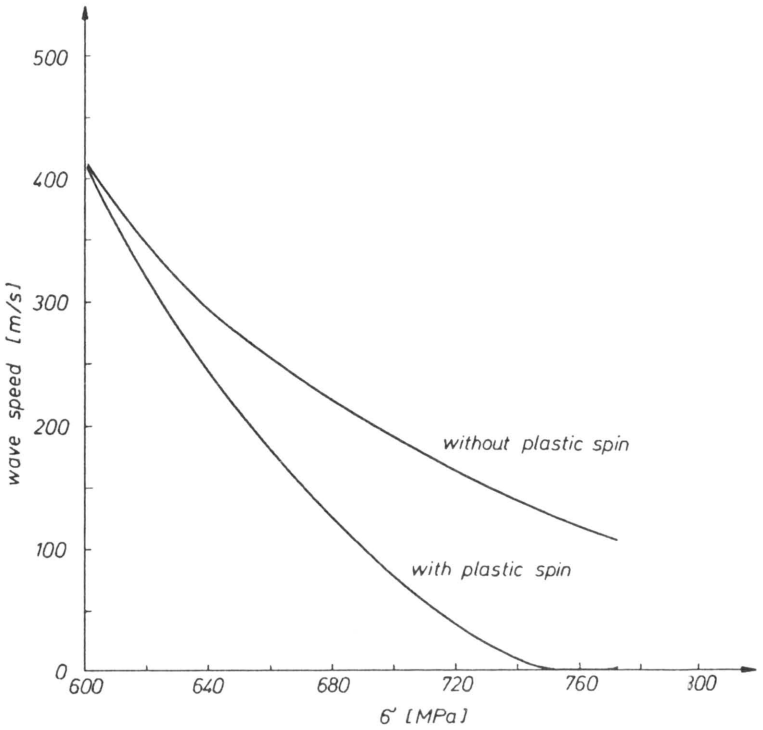

FIG. 3. Slow wave velocity vs. stress.

Acknowledgements

This paper is based on the work developed in the course of research carried out under the grant No. 3 1014 9101 "Thermomechanics of defects and phase changes in the materials" sponsored by the KBN Research Committee, Poland, for which the author is grateful.

References

1. H.H. BLEICH and I. NELSON, *Plane waves in an elastic-plastic half-space due to combined surface pressure and shear*, J. Appl. Mech., **33**, 1, 149–158, 1966.
2. R.T. CLIFTON, *An analysis of combined longitudinal and torsional waves in a thin-valled tube*, [in:] Fifth U.S. Nat. Congr. of Appl. Mech. Proceedings ASME, pp. 465–480, 1966.
3. Y.F. DAFALIAS, *The plastic spin concept and a simple illustration of its role in finite plastic transformations*, Mech. Materials, 3, 223–233, 1984.
4. R.P. GOEL and L.E. MALVERN, *Biaxial plastic simple waves with combined kinematic and isotropic hardening*, J. Appl. Mech., **37**, 1100–1106, 1970.
5. K.A. HARTLEY, J. DUFFY and R.H. HAWLEY, *Measurement of the temperature profile during shear band formation in steels deforming at high strain rates*, J. Mech. Phys. Solids., **35**, 3, 283–301, 1986.
6. J. LIPKIN and R.J. CLIFTON, *An experimental study of combined longitudinal and torsonal plastic waves in a thin-walled tube*, [in:] Proc. 12th Int. Congr. Appl. Mech., pp. 292–304, 1968.

7. B. LORET, *On the effects of plastic rotation in the finite deformation of anisotropic elastoplastic materials*, Mech. Materials, 2, 287–304, 1983.
8. Z. MRÓZ and B. RANIECKI, *On the uniqueness problem in coupled thermoplasticity*, Int. J. Engng. Sci., **14**, 211–221, 1976.
9. W.K. NOWACKI, *Stress waves in non-elastic solids*, Pergamon Press, 1978.
10. W.K. NOWACKI, *Thermal effects in dynamic plasticity, numerical solution and experimental investigations (thermographic-infrared detection)*, J. de Physique, **46**, 8, 113–119, 1985.
11. W.K. NOWACKI and T. KURCYK, *Sur le champ des températures en thermoélastoviscoplasticité finie*, J. de Méc. Thé. et App., pp. 109–124, (Numéro Spécial) 1982.
12. E.T. ONAT, *Shear flow of kinematically hardening rigid-plastic materials*, [in:] Mechanics of material behaviour, G.J. DVORAK and R.T. SHIELD [Eds.], pp. 311–324, Elsevier, 1984.
13. J.E. PAULUN and R. PĘCHERSKI, *On the application of the plastic spin concept for the description of anisotropic hardening in finite deformation plasticity*, Int. J. Plasticity, 3, 303–314, 1987.
14. J.E. PAULUN and R. PĘCHERSKI, *On the relation for plastic spin*, Arch. Appl. Mech., **62**, 376–385, 1992.
15. K. PODOLAK and B. RANIECKI, *A note on the influence of energy dissipation on the propagation of elastic-plastic waves*, Arch. Mech., **28**, 625–634, 1976.
16. B. RANIECKI, *Ordinary waves in inviscid plastic media*, [in:] Mechanical Waves in Solids, J. MANDEL and L. BRUN [Eds.], pp. 157–219, CISM 22, Springer, Udine 1976.
17. T.C.T. TING, *The initiation of combined stress waves in a thin-walled tube due to impact loadings*, Int. J. Solids Struct., **8**, 269–293, 1972.
18. NGUYEN HUU VIEM, *Isothermal and adiabatic acceleration waves in an elastic-plastic medium at finite deformations* [in Polish], PhD Thesis, IFTR – Pol. Acad. Sci., Prace IPPT Nr 34, 1984.
19. NGUYEN HUU VIEM, *Isothermal and adiabatic simple waves in a thin-walled tube*, Arch. Mech., **37**, 4-5, 449–464, 1985.
20. NGUYEN HUU VIEM, *Constitutive equations for finite deformations of elastic-plastic metallic solids with induced anisotropy*, Arch. Mech., **44**, 5-6, 585–594, 1992.
21. NGUYEN HUU VIEM, *Isothermal and adiabatic flow laws of metallic elastic-plastic solids at finite strains and propagation of acceleration waves*, Arch. Mech., **44**, 5-6, 595–602, 1992.
22. HAN CHIN WU and HSUAN CHI LIN, *Combined plastic waves in a thin-walled tube* Int. J. Solids Struct., **10**, 903–917, 1974.

POLISH ACADEMY OF SCIENCES
INSTITUTE OF FUNDAMENTAL TECHNOLOGICAL RESEARCH, WARSZAWA.

Received October 28, 1994.

Arch. Mech., 47, 2, pp. 353–377, Warszawa 1995

A gradient plasticity approach to finite element predictions of soil instability (*)

J. PAMIN (1) and R. DE BORST (2) (DELFT)

A DRUCKER-PRAGER gradient plasticity theory is applied in finite element simulation of two-dimensional localization problems in geomaterials. The gradient-dependent theory preserves well-posedness of the governing equations in presence of material instability and prevents a spurious mesh sensitivity of numerical results. An internal length scale incorporated in the theory determines the width of shear bands. Assuming weak satisfaction of the yield condition, a family of mixed finite elements is developed, in which plastic strains are interpolated with C^1-continuity in addition to the standard discretization of the displacements. Instabilities in a biaxially compressed specimen and in a slope under an increasing gravity load are simulated.

1. Introduction

FAILURE OF LOOSE and cemented granular materials like soil and rock is often accompanied by a sudden transition from a uniform deformation field into a number of localized *shear bands*. Although they are called sometimes slip planes, they have a small but finite thickness. Soil and rock specimens exhibit also a gradual degradation of stiffness with the increase of deformation and, beyond a certain level of straining, even a decrease of the load-carrying capacity called *softening*. The phenomena of *strain localization* and *softening* are closely related [1]. In simple terms, material heterogeneity induces strongly nonlinear stress-strain and volume change relations, and a local weakness of the material triggers strain localization. As a result of the inhomogeneous deformations, a softening response at the structural level is observed.

Localization can be considered as an instability in the macroscopic constitutive description of inelastic deformation [2]. Within the classical continuum theory, this kind of instability is associated with discontinuities in the strain-rate field, which, under static loading conditions, coincides with the *loss of ellipticity* of the governing partial differential equations. The acoustic tensor singularity condition [2, 3] gives the critical value of the hardening modulus, for which the bifurcation into a discontinuous strain-rate field is possible, and the direction of the discontinuity plane.

At a continuum level softening is modelled by means of a descending relation between stresses and strains (strain softening), which introduces the *material*

(*) Paper presented at 30th Polish Solid Mechanics Conference, Zakopane, September 5–9, 1994.

(1) On leave from Cracow University of Technology, Faculty of Civil Engineering.

(2) Also at Eindhoven University of Technology, Faculty of Mechanical Engineering.

instability mentioned before [4]. It has been shown that, under the assumption of small displacement gradients, the loss of material stability is a necessary condition for the loss of ellipticity [5]. Some constitutive relations for frictional materials are nonsymmetric, for instance, plasticity models do not obey the normality postulate, which may also lead to violation of material stability. In this case localization may be encountered even for a hardening model [2] and may occur prior to the limit load [6].

The loss of ellipticity may thus be induced by softening or non-associated plastic flow or a combination of the two effects. A meaningful prediction of the post-critical behaviour is impossible within the classical continuum theory, since the loss of ellipticity implies the *loss of well-posedness* of the rate boundary value problem [7]. Localization of deformation in a set of measure zero then ensues, which loses physical sense in the continuum description, since it predicts total failure without energy dissipation. As a result, numerical solutions exhibit a spurious discretization sensitivity.

The problem of mechanical representation of localized deformation can also be interpreted as follows. As long as the deformation of a soil/rock mass is almost uniform, the characteristic size of material heterogeneity is very small compared to the wave length of the deformation mode. However, the classical model fails to predict the real behaviour if the wave length of the deformation mode is comparable to the characteristic size of material heterogeneity, e.g. during localization in a shear band [8].

A natural solution is to enhance, or to *regularize*, the continuum description. There exist a few methods to regularize the governing equations [7]. They all include a so-called internal length scale that defines the width of the shear bands. In this contribution the elasto-plastic continuum description is enhanced by making the yield function dependent on the Laplacian of an equivalent strain measure [9–12]. This non-local theory is thought to reflect the micro-mechanical changes in an inhomogeneous material during failure processes. Due to the gradient dependence, the consistency condition, which governs the plastic flow, becomes a partial differential equation. To solve this equation, it is cast in a weak form and the plastic strain field is discretized in addition to the usual discretization of the displacement field.

The purpose of this paper is to examine the *gradient plasticity* approach for shear band formation in geomaterials. The assumptions of static loading and small deformations are adopted. We will limit our consideration to the non-associated Drucker–Prager model, which includes the dilatancy and non-normality of the plastic flow. In the first part of the paper we summarize the theory and the algorithm of finite element computations. In the second part, the Drucker–Prager gradient plasticity model and two special finite elements are used to solve an example of localized deformations in a plane strain sample in biaxial compression and in an embankment under an increasing gravity load.

2. Drucker–Prager gradient plasticity

Firstly, we summarize the rate boundary value problem of gradient plasticity (cf. [11, 12]). We introduce the displacement vector $\mathbf{u} = (u_x, u_y, u_z)$, the strain tensor in a vector form $\boldsymbol{\varepsilon} = (\varepsilon_{xx}, \varepsilon_{yy}, \varepsilon_{zz}, \gamma_{xy}, \gamma_{yz}, \gamma_{zx})$ and the stress tensor in a vector form $\boldsymbol{\sigma} = (\sigma_{xx}, \sigma_{yy}, \sigma_{zz}, \sigma_{xy}, \sigma_{yz}, \sigma_{zx})$. Under the assumption of small deformations and static loading we have the following equations for an elasto-plastic body occupying a volume V (Fig. 1):

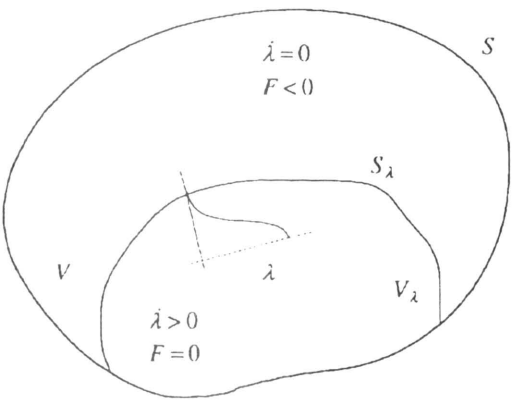

FIG. 1. Idealization of an elastic-plastic body.

$$\mathbf{L}^T \dot{\boldsymbol{\sigma}} + \dot{\mathbf{b}} = 0, \tag{2.1}$$

$$\dot{\boldsymbol{\varepsilon}} = \mathbf{L}\,\dot{\mathbf{u}}\,, \tag{2.2}$$

$$\dot{\boldsymbol{\sigma}} = \mathbf{D}^e(\dot{\boldsymbol{\varepsilon}} - \dot{\lambda}\,\mathbf{m}), \tag{2.3}$$

where superimposed dots denote the derivatives with respect to time, and the superscript T is the transpose symbol. In the above equations $\mathbf{L}$ is a differential operator matrix, $\mathbf{b}$ is a body-force vector and $\mathbf{D}^e$ is the elastic stiffness matrix. Eq. (2.3) contains the definition of the plastic strain-rate vector, called the flow rule:

$$\dot{\boldsymbol{\varepsilon}}^p = \dot{\lambda}\,\mathbf{m}, \qquad \mathbf{m} = \frac{\partial G}{\partial \boldsymbol{\sigma}}, \tag{2.4}$$

in which $\dot{\lambda}$ is a plastic multiplier and $\mathbf{m}$ defines the direction of the plastic flow. The vector $\mathbf{m}$ may be derived from a plastic potential function G.

The gradient dependence is included solely in the definition of the yield function F

$$F = F(\boldsymbol{\sigma}, \kappa, \nabla^2\kappa), \tag{2.5}$$

in which κ is an invariant plastic strain measure (the hardening parameter). Together with Eqs. (2.1)–(2.3) the Kuhn-Tucker conditions

$$\dot{\lambda} \geq 0, \qquad F \leq 0, \qquad \dot{\lambda} F = 0 \tag{2.6}$$

must be fulfilled. To complete the rate boundary value problem we specify the standard static and kinematic boundary conditions on complementary parts of the body surface S:

$$\dot{\boldsymbol{\Sigma}} \boldsymbol{\nu}_s = \dot{\mathbf{t}}, \qquad \dot{\mathbf{u}} = \dot{\mathbf{u}}_s, \tag{2.7}$$

where $\dot{\boldsymbol{\Sigma}}$ is the stress tensor in a matrix form, $\boldsymbol{\nu}_s$ denotes the outward normal to the surface S and $\mathbf{t}$ is the boundary traction vector. It is noted that with the motion equation instead of the equilibrium equation (2.1) and with additional initial conditions, an initial value problem of gradient plasticity can be formulated for dynamic loading [13].

The gradient dependence of the yield function makes the plastic consistency condition $\dot{F} = 0$ become a differential equation:

$$\left(\frac{\partial F}{\partial \boldsymbol{\sigma}}\right)^T \dot{\boldsymbol{\sigma}} + \frac{\partial F}{\partial \kappa} \dot{\kappa} + \frac{\partial F}{\partial \nabla^2 \kappa} \nabla^2 \dot{\kappa} = 0. \tag{2.8}$$

We introduce the gradient of the yield function $\mathbf{n}$:

$$\mathbf{n} = \frac{\partial F}{\partial \boldsymbol{\sigma}}, \tag{2.9}$$

the (variable) hardening modulus h:

$$h(\kappa, \nabla^2 \kappa) = -\frac{\dot{\kappa}}{\dot{\lambda}} \frac{\partial F}{\partial \kappa}, \tag{2.10}$$

and the gradient influence variable g:

$$g(\kappa) = \frac{\dot{\kappa}}{\dot{\lambda}} \frac{\partial F}{\partial \nabla^2 \kappa}, \tag{2.11}$$

which is assumed to be a function of κ only. We can now write Eq. (2.8) in the form:

$$\mathbf{n}^T \dot{\boldsymbol{\sigma}} - h \dot{\lambda} + g \nabla^2 \dot{\lambda} = 0. \tag{2.12}$$

For softening the modulus h is negative and the additional variable g is positive. In the simplest case h and g are constants (softening is linear). For $g = 0$ the classical flow theory of plasticity is retrieved. The consistency condition is then a

nonlinear algebraic equation, from which the plastic multiplier can be determined locally. The problem of solving Eq. (2.12), which is essentially valid in the plastic part of the body V_λ (Fig. 1), is characteristic for the present theory.

In this paper we use a finite element discretization to solve simultaneously the two coupled equations of equilibrium and plastic consistency. For this purpose we assume a weak satisfaction of the consistency condition and discretize the plastic strain field, in addition to the standard discretization of the displacements [9, 11]. This aspect will be further discussed in the remainder of the paper.

Secondly, we present the Drucker-Prager gradient plasticity model. We adopt constant values of the friction and dilatancy angles, and only the cohesion exhibits softening and gradient-dependence, which results in isotropy of the model. In the context of the *critical state* models [14], the Drucker-Prager theory is capable of describing the behaviour of geomaterials in the *supercritical* (softening) regime, but is inadequate in the *subcritical* (hardening) regime, where a cap is necessary to allow for yielding at high confining pressures. The Drucker-Prager yield function for gradient-dependent plasticity can be written as follows:

$$F = \sqrt{3J_2} + \alpha p - \beta \bar{c}_g(\kappa, \nabla^2 \kappa), \tag{2.13}$$

where J_2 is the second invariant of the deviatoric stress tensor, $p = \frac{1}{3}(\sigma_{xx} + \sigma_{yy} + \sigma_{zz})$ is the hydrostatic pressure, α and β are functions of the internal friction angle ϕ:

$$\alpha = \frac{6 \sin \phi}{3 - \sin \phi}, \qquad \beta = \frac{6 \cos \phi}{3 - \sin \phi}, \tag{2.14}$$

and $\bar{c}_g$ is a gradient-dependent measure of the cohesion. Introducing a matrix $\mathbf{P}$ and a vector $\boldsymbol{\Pi}$, defined as

$$\mathbf{P} = \begin{bmatrix} 2/3 & -1/3 & -1/3 & 0 & 0 & 0 \\ -1/3 & 2/3 & -1/3 & 0 & 0 & 0 \\ -1/3 & -1/3 & 2/3 & 0 & 0 & 0 \\ 0 & 0 & 0 & 2 & 0 & 0 \\ 0 & 0 & 0 & 0 & 2 & 0 \\ 0 & 0 & 0 & 0 & 0 & 2 \end{bmatrix}, \qquad \boldsymbol{\Pi} = \begin{bmatrix} 1/3 \\ 1/3 \\ 1/3 \\ 0 \\ 0 \\ 0 \end{bmatrix}, \tag{2.15}$$

the yield function takes the form:

$$F = \left(\frac{3}{2}\boldsymbol{\sigma}^T \mathbf{P} \boldsymbol{\sigma}\right)^{1/2} + \alpha \boldsymbol{\Pi}^T \boldsymbol{\sigma} - \beta \bar{c}_g(\kappa, \nabla^2 \kappa), \tag{2.16}$$

so that the gradient to the yield function equals

$$\mathbf{n} = \frac{3\mathbf{P}\boldsymbol{\sigma}}{2\left(\frac{3}{2}\boldsymbol{\sigma}^T \mathbf{P} \boldsymbol{\sigma}\right)^{1/2}} + \alpha \boldsymbol{\Pi}. \tag{2.17}$$

For non-associated plasticity we define the plastic potential function and its gradient in a similar fashion:

$$G = \sqrt{3J_2} + \tilde{\alpha} p, \tag{2.18}$$

$$\mathbf{m} = \frac{3\mathbf{P}\boldsymbol{\sigma}}{2\left(\frac{3}{2}\boldsymbol{\sigma}^T\mathbf{P}\boldsymbol{\sigma}\right)^{1/2}} + \tilde{\alpha}\boldsymbol{\Pi}, \tag{2.19}$$

where $\tilde{\alpha}$ is a function of the dilatancy angle ψ similar to the definition of α in Eq. (2.14). To determine the relation between $\dot{\kappa}$ to $\dot{\lambda}$ we use the strain-hardening hypothesis:

$$\dot{\kappa} = \left(\frac{2}{3}\dot{\varepsilon}^p_{ij}\dot{\varepsilon}^p_{ij}\right)^{1/2} = \left[\frac{2}{3}\left(\dot{\boldsymbol{\varepsilon}}^p\right)^T\mathbf{Q}\,\dot{\boldsymbol{\varepsilon}}^p\right]^{1/2}, \tag{2.20}$$

with $\mathbf{Q} = \mathrm{diag}[1,1,1,1/2,1/2,1/2]$. Substituting the plastic strain-rate vector $\dot{\boldsymbol{\varepsilon}}^p = \dot{\lambda}\,\mathbf{m}$ into Eq. (2.20) and observing that $\mathbf{PQP} = \mathbf{P}$ and $\mathbf{PQ}\boldsymbol{\Pi} = \mathbf{0}$, we obtain:

$$\dot{\kappa} = \eta\,\dot{\lambda}\,, \qquad \eta = \left(1 + \frac{2}{9}\tilde{\alpha}^2\right)^{1/2}. \tag{2.21}$$

According to the definitions in Eqs. (2.10) and (2.11) we have:

$$h = \eta\beta\frac{\partial\bar{c}_g}{\partial\kappa}\,, \qquad g = -\eta\beta\frac{\partial\bar{c}_g}{\partial\nabla^2\kappa}\,. \tag{2.22}$$

For linear softening $\bar{c}_g$ can be written as:

$$\bar{c}_g = c_y + \frac{h}{\eta\beta}\kappa - \frac{g}{\eta\beta}\nabla^2\kappa \tag{2.23}$$

with constant h and g and with the initial value of the cohesion c_y. For nonlinear softening the cohesion changes according to:

$$\bar{c}_g = \bar{c}(\kappa) - \frac{g(\kappa)}{\eta\beta}\nabla^2\kappa\,, \tag{2.24}$$

and the softening modulus is calculated as:

$$h = \eta\beta\frac{\partial\bar{c}(\kappa)}{\partial\kappa} - \frac{\partial g(\kappa)}{\partial\kappa}\nabla^2\kappa. \tag{2.25}$$

The important advantage of the Drucker–Prager yield function is its smoothness, since the presence of singular edges on the yield surface poses a difficulty for the gradient plasticity algorithm [12]. In fact the Drucker–Prager yield surface also possesses a vertex at the cross-section with the hydrostatic axis. From Eq. (2.13) we calculate that at the vertex $p = \bar{c}_g\mathrm{ctg}\,\phi$. It is assumed here that the stress points in large triaxial tension, which would fall in the vertex regime $p > \bar{c}_g\mathrm{ctg}\,\phi$, are not admitted.

3. Algorithm and finite elements

An incremental formulation of the above boundary value problem gives rise to residual terms, which make a stress update necessary. The evolution of the elastic-plastic boundary within a loading step must be also considered.

In order to derive an incremental-iterative algorithm [11, 12], we require a weak satisfaction of the equilibrium condition

$$\int_V \delta \mathbf{u}^T \left(\mathbf{L}^T \boldsymbol{\sigma}_{j+1} + \mathbf{b}_{j+1} \right) dV = 0 \tag{3.1}$$

and the yield condition

$$\int_V \delta\lambda F \left(\boldsymbol{\sigma}_{j+1}, \kappa_{j+1}, \nabla^2 \kappa_{j+1} \right) dV = 0 \tag{3.2}$$

at the end of iteration $j+1$ of the current loading step, where δ denotes a variation of a quantity. Unlike in the classical plasticity algorithms, the latter condition is also satisfied in a weak sense and is only fulfilled when convergence is achieved.

Equation (3.1) can be modified using integration by parts and the standard boundary conditions $(2.7)_1$, and decomposing $\boldsymbol{\sigma}_{j+1}$ as $\boldsymbol{\sigma}_j + d\boldsymbol{\sigma}$, where d indicates an increment, i.e. the difference between the values of a variable at the end of iteration $j+1$ and iteration j:

$$\int_V \delta \boldsymbol{\varepsilon}^T \, d\boldsymbol{\sigma} \, dV = \int_V \delta \mathbf{u}^T \mathbf{b}_{j+1} \, dV + \int_S \delta \mathbf{u}^T \mathbf{t}_{j+1} \, dS - \int_V \delta \boldsymbol{\varepsilon}^T \boldsymbol{\sigma}_j \, dV. \tag{3.3}$$

Using the incremental form of the relationship between the stress and the elastic strain vector

$$d\boldsymbol{\sigma} = \mathbf{D}^e (d\boldsymbol{\varepsilon} - d\lambda \mathbf{m}), \tag{3.4}$$

we obtain the following integral equation:

$$\int_V \delta \boldsymbol{\varepsilon}^T \mathbf{D}^e (d\boldsymbol{\varepsilon} - d\lambda \mathbf{m}) \, dV = \int_V \delta \mathbf{u}^T \mathbf{b}_{j+1} \, dV + \int_S \delta \mathbf{u}^T \mathbf{t}_{j+1} \, dS - \int_V \delta \boldsymbol{\varepsilon}^T \boldsymbol{\sigma}_j \, dV. \tag{3.5}$$

We observe that this equation does not depend explicitly on the Laplacian of the plastic multiplier and has a form similar to the incremental equilibrium equations used for classical plasticity.

The yield function F in Eq. (3.2) is developed in a Taylor series around $(\boldsymbol{\sigma}_j, \kappa_j, \nabla^2 \kappa_j)$ and truncated after the linear terms:

$$F(\boldsymbol{\sigma}_{j+1}, \kappa_{j+1}, \nabla^2 \kappa_{j+1}) = F(\boldsymbol{\sigma}_j, \kappa_j, \nabla^2 \kappa_j) + \left(\frac{\partial F}{\partial \boldsymbol{\sigma}} \right)^T \Bigg|_j d\boldsymbol{\sigma} + \frac{\partial F}{\partial \kappa} \Bigg|_j d\kappa + \frac{\partial F}{\partial \nabla^2 \kappa} \Bigg|_j \nabla^2 (d\kappa), \tag{3.6}$$

where $d\kappa = \kappa_{j+1} - \kappa_j$. With the definitions (2.9)–(2.11) we obtain the following form of Eq. (3.6):

$$F(\boldsymbol{\sigma}_{j+1}, \kappa_{j+1}, \nabla^2\kappa_{j+1}) = F(\boldsymbol{\sigma}_j, \kappa_j, \nabla^2\kappa_j) + \mathbf{n}^T d\boldsymbol{\sigma} - h\, d\lambda + g\nabla^2(d\lambda), \tag{3.7}$$

which after substitution into Eq. (3.2) gives the following integral equation:

$$\int_{V_\lambda} \delta\lambda \left[\mathbf{n}^T \mathbf{D}^e\, d\boldsymbol{\varepsilon} - (h + \mathbf{n}^T \mathbf{D}^e \mathbf{m})\, d\lambda + g\nabla^2(d\lambda)\right] dV = -\int_{V_\lambda} \delta\lambda F(\boldsymbol{\sigma}_j, \kappa_j, \nabla^2\kappa_j) dV. \tag{3.8}$$

The values of $\mathbf{n}$, $\mathbf{m}$, h and g on the left-hand side of Eq. (3.8) are determined at the end of iteration j, i.e. for the state defined by $(\boldsymbol{\sigma}_j, \kappa_j, \nabla^2\kappa_j)$. If the same mesh is used for both the equilibrium and yield condition, i.e. if integrals over the whole volume V appear in Eqs. (3.2) and (3.8), either the admissible $\delta\lambda$ must vanish or we must enforce $F = 0$, $\mathbf{n} = \mathbf{0}$ and $d\lambda = 0$ in the elastic part of the body.

In the residual terms on the right-hand side of Eqs. (3.5) and (3.8) the stress $\boldsymbol{\sigma}_j$ appears. It is determined using the standard elastic predictor-plastic corrector algorithm (backward Euler type) at each integration point which is in a plastic state:

$$\boldsymbol{\sigma}_j = \boldsymbol{\sigma}_0 + \mathbf{D}^e \Delta\boldsymbol{\varepsilon}_j - \Delta\lambda_j \mathbf{D}^e \mathbf{m}_j\,, \tag{3.9}$$

where $\boldsymbol{\sigma}_0$ is the stress state at the end of the previous (converged) load increment, and Δ denotes a total increment (from state 0 to iteration j). The values of κ_j and $\nabla^2\kappa_j$ are also updated using total increments. This necessitates the use of so-called algorithmic consistent stiffness matrix $\mathbf{H}$ (instead of the elastic stiffness $\mathbf{D}^e$) in the tangent operator, otherwise the quadratic convergence rate of Newton's algorithm is not preserved [12]. Since the vector $\mathbf{m}_j$ is known only after the mapping in Eq. (3.9), it is approximated by the gradient calculated for the "trial" stress:

$$\boldsymbol{\sigma}_t = \boldsymbol{\sigma}_0 + \mathbf{D}^e \Delta\boldsymbol{\varepsilon}_j\,. \tag{3.10}$$

To decide whether an elastic point enters the plastic regime, or whether a plastic point begins elastic unloading, the trial value of the yield function F_t is calculated at each integration point:

$$F_t = F(\boldsymbol{\sigma}_t, \overline{\sigma}_g(\kappa_j, \nabla^2\kappa_j)), \tag{3.11}$$

where the gradient-dependent yield strength is determined as follows:

$$\overline{\sigma}_g = \overline{\sigma}(\kappa_j) - g(\kappa_j)\nabla^2\lambda_j\,. \tag{3.12}$$

An integration point is assumed to be in the plastic state when $F_t > 0$ and in the elastic state when $F_t < 0$. In the elastic elements $\lambda = 0$, so that for spreading of the plastic zone it is important that the numerical solution should allow for $\nabla^2\lambda > 0$ at the elastic-plastic boundary. The gradient-dependent yield strength $\overline{\sigma}_g$ is then reduced as a result of the plastic process in the neighbourhood.

In the integral equations (3.5) and (3.8) there appear at most first-order derivatives of the displacements and second-order derivatives of the plastic multiplier. Therefore, the discretization of the displacement field $\mathbf{u}$ requires C^0-continuous interpolation functions $\mathbf{N}$ and the discretization of the plastic multiplier λ requires C^1-continuous shape functions $\mathbf{h}$:

$$\mathbf{u} = \mathbf{N}\mathbf{a}, \qquad \lambda = \mathbf{h}^T\boldsymbol{\Lambda}, \tag{3.13}$$

where $\mathbf{a}$ is a nodal displacement vector and $\boldsymbol{\Lambda}$ denotes a vector of nodal degrees of freedom for the plastic multiplier field. It is noted that the left-hand side of Eq. (3.8) can be modified using integration by parts to decrease the order of the differential operator and to symmetrize the ensuing matrix operator. However, the dependence of the yield function on the Laplacian of the plastic strain measure is essential for the progressive plastification and for the determination of the non-standard residual forces on the right-hand side of Eq. (3.8), which necessitates C^1-continuous interpolation functions. To be able to use C^0-continuous shape functions, it is necessary to introduce the first derivatives of the plastic multiplier as independent, interpolated variables and add a penalty constraint to the formulation [12].

According to the linear kinematic relation (3.2), the discretization of strains has the form:

$$\boldsymbol{\varepsilon} = \mathbf{B}\mathbf{a}, \qquad \mathbf{B} = \mathbf{L}\mathbf{N}. \tag{3.14}$$

Introducing a vector $\mathbf{p}$ which contains the Laplacians of the shape functions in $\mathbf{h}$, we obtain the discretization formula for the Laplacian of the plastic multiplier:

$$\nabla^2\lambda = \mathbf{p}^T\boldsymbol{\Lambda}. \tag{3.15}$$

Substitution of the identities (3.13)–(3.15) in Eq. (3.5) gives the discretized equilibrium condition:

$$\delta\mathbf{a}^T \int_V \left[\mathbf{B}^T\mathbf{D}^e\mathbf{B}\,d\mathbf{a} - \mathbf{B}^T\mathbf{D}^e\mathbf{m}\mathbf{h}^T\,d\boldsymbol{\Lambda}\right] dV = \delta\mathbf{a}^T \int_V \mathbf{N}^T\mathbf{b}_{j+1}dV + \delta\mathbf{a}^T \int_S \mathbf{N}^T\mathbf{t}_{j+1}dS - \delta\mathbf{a}^T \int_V \mathbf{B}^T\boldsymbol{\sigma}_j\,dV. \tag{3.16}$$

Substitution of Eqs. (3.13)$_2$, (3.14) and (3.15) in Eq. (3.8) gives the discretized yield condition:

$$\delta\boldsymbol{\Lambda}^T \int_V \left[-\mathbf{h}\mathbf{n}^T\mathbf{D}^e\mathbf{B}\,d\mathbf{a} + (h + \mathbf{n}^T\mathbf{D}^e\mathbf{m})\mathbf{h}\mathbf{h}^T\,d\boldsymbol{\Lambda} - g\mathbf{h}\mathbf{p}^T\,d\boldsymbol{\Lambda}\right] dV = \delta\boldsymbol{\Lambda}^T \int_V F(\boldsymbol{\sigma}_j, \kappa_j, \nabla^2\kappa_j)\mathbf{h}\,dV. \tag{3.17}$$

Equations (3.16) and (3.17) must hold for any admissible variation of $\delta\mathbf{a}$ and $\delta\boldsymbol{\Lambda}$, so that we obtain the following set of algebraic equations [11]:

$$\begin{bmatrix} \mathbf{K}_{aa} & \mathbf{K}_{a\lambda} \\ \mathbf{K}_{\lambda a} & \mathbf{K}_{\lambda\lambda} \end{bmatrix} \begin{bmatrix} d\mathbf{a} \\ d\boldsymbol{\Lambda} \end{bmatrix} = \begin{bmatrix} \mathbf{f}_e + \mathbf{f}_a \\ \mathbf{f}_\lambda \end{bmatrix}, \tag{3.18}$$

with the elastic stiffness matrix

$$\mathbf{K}_{aa} = \int_V \mathbf{B}^T\mathbf{D}^e\mathbf{B}\,dV, \tag{3.19}$$

the off-diagonal matrices:

$$\mathbf{K}_{a\lambda} = -\int_V \mathbf{B}^T\mathbf{D}^e\mathbf{m}\mathbf{h}^T\,dV, \qquad \mathbf{K}_{\lambda a} = -\int_V \mathbf{h}\mathbf{n}^T\mathbf{D}^e\mathbf{B}\,dV, \tag{3.20}$$

the nonsymmetric gradient-dependent matrix:

$$\mathbf{K}_{\lambda\lambda} = \int_V \left[(h + \mathbf{n}^T\mathbf{D}^e\mathbf{m})\mathbf{h}\mathbf{h}^T - g\mathbf{h}\mathbf{p}^T\right] dV, \tag{3.21}$$

the external force vector and the vector of nodal forces equivalent to internal stresses:

$$\mathbf{f}_e = \int_V \mathbf{N}^T\mathbf{b}_{j+1}\,dV + \int_S \mathbf{N}^T\mathbf{t}_{j+1}\,dS, \qquad \mathbf{f}_a = -\int_V \mathbf{B}^T\boldsymbol{\sigma}_j\,dV, \tag{3.22}$$

respectively, and the vector of residual forces emerging from the weak fulfilment of the yield condition:

$$\mathbf{f}_\lambda = \int_V F(\boldsymbol{\sigma}_j, \lambda_j, \nabla^2\lambda_j)\mathbf{h}\,dV. \tag{3.23}$$

The matrix $\mathbf{K}_{\lambda\lambda}$ is nonsymmetric due to the gradient-dependence, even if the associated flow rule is considered ($\mathbf{m} = \mathbf{n}$).

Since we have a higher-order continuum formulation, the problem of additional boundary conditions for the plastic multiplier field must be addressed. The boundary conditions, derived from the variational principle for gradient plasticity [9], have the form:

$$\delta\, d\lambda = 0 \qquad \text{or} \qquad (\nabla\, d\lambda)^T \boldsymbol{\nu}_\lambda = 0. \tag{3.24}$$

For the present formulation the condition $(3.24)_2$ is automatically satisfied on the evolving elastic-plastic boundary (internal part of S_λ). However, one of the conditions (3.24) must be enforced on the surface of the body S if the tangent operator in Eq. (3.18) does not possess a sufficient rank for elastic elements.

We will consider the actual problem of a structure which is initially elastic and then, due to an inhomogeneous stress distribution, exhibits a partial plastification. If all elements are elastic, we have $\mathbf{K}_{\lambda a} = \mathbf{0}$ since the gradient vectors $\mathbf{m}$ and $\mathbf{n}$ are set to zero. Then we obtain from Eq. (3.18) the classical set of equations in $d\mathbf{a}$

$$\mathbf{K}_{aa}\, d\mathbf{a} = \mathbf{f}_e + \mathbf{f}_a \tag{3.25}$$

and the additional set of equations in $d\boldsymbol{\Lambda}$

$$\mathbf{K}^e_{\lambda\lambda}\, d\boldsymbol{\Lambda} = \mathbf{f}_\lambda\,. \tag{3.26}$$

For the elastic state we have $F < 0$ and we set the residual forces $\mathbf{f}_\lambda$ to zero. Equation (3.26) then yields the desired solution $d\boldsymbol{\Lambda} = \mathbf{0}$ if the global matrix $\widehat{\mathbf{K}}^e$ is non-singular after the element assembly and, if necessary, after the introduction of boundary conditions for the $\boldsymbol{\Lambda}$ degrees of freedom.

If plastic elements appear in the structure, we have $\mathbf{f}_\lambda \neq \mathbf{0}$ in elastic elements adjacent to the plastic zone and we compute non-zero $d\boldsymbol{\Lambda}$ from Eq. (3.26). The C^1-continuous finite elements have the feature, that these nodal values of plastic multiplier $d\boldsymbol{\Lambda}$ yield $d\lambda \approx 0$ and $\nabla^2(d\lambda) > 0$ at the integration points. As a result, the yield strength $\overline{\sigma}_g = \overline{\sigma} - g\nabla^2\lambda$ is reduced and new elastic elements can enter the plastic regime.

To avoid singularity of the tangent operator for elastic elements, the hardening modulus h in Eq. (3.21) is initially set equal to Young's modulus E. The gradient term may be neglected in the matrix $\mathbf{K}^e_{\lambda\lambda}$ for elastic elements (its inclusion only slightly influences the results). Using numerical integration the matrix $\mathbf{K}^e_{\lambda\lambda}$ is then determined as:

$$\mathbf{K}^e_{\lambda\lambda} = \sum_{ip=1}^{np} E\mathbf{h}_{ip}\mathbf{h}^T_{ip} V_{ip}\,, \tag{3.27}$$

where V_{ip} is a volume contribution of an integration point. The rank of submatrix $\mathbf{K}^e_{\lambda\lambda}$ should be examined in order to determine the number of integration points and additional boundary conditions necessary to avoid spurious zero-energy modes for the plastic multiplier field.

A high-order integration scheme and too many additional boundary conditions for the plastic multiplier field may lead to overconstrained plastic flow and may have a negative influence on the accuracy of finite element predictions. Since the yield condition may be conceived as a differential constraint to the equilibrium condition of a nonlinear solid, the number of constraints for the plastic multiplier field must be limited, otherwise the solution will be inaccurate or locked (just as it happens for some standard elements in the incompressible limit). In other words, we have a two-field theory similar to the mixed formulation with independent displacement and pressure interpolation, and a proper constraint ratio should be satisfied by the Λ degrees of freedom.

Figure 2 presents two gradient plasticity elements used in this study for plane strain configurations. Element R32EG employs quadratic serendipity interpolation of displacements, and uses bi-Hermitian shape functions for the plastic strain field and 2×2 Gauss integration. This element is the most robust of gradient plasticity elements [12] due to the special qualities of the integration stations (BARLOW points [15]), at which higher-order accuracy of the derivatives of the interpolated fields is obtained and the yield condition is satisfied exactly upon convergence. As alluded to in the preceding, the matrix $\mathbf{K}^e_{\lambda\lambda}$ requires additional constraints, which can be introduced by extra boundary conditions for derivatives of λ. For an arbitrary assembly, the conditions $\Lambda_n = 0$ and $\Lambda_{xy} = 0$ on the whole model boundary exactly supply the required number of constraints. Element T21EG has quadratic interpolation of displacements and cubic interpolation of λ, which is based on a non-conforming plate bending triangle [16]. The element has Λ_x and Λ_y degrees of freedom, but it does not fulfil the continuity requirements for λ_n on its boundary. Integration with 3 Gauss points is used, as well as 3 Hammer points at midsides of the triangle. Neither of these schemes is optimal, since return mapping to the inside of the yield locus is observed ($F_{ip} < 0$) and stress oscillations are found. Additional boundary conditions $\Lambda_n = 0$ are necessary to prevent the existence of non-zero λ modes in elastic elements.

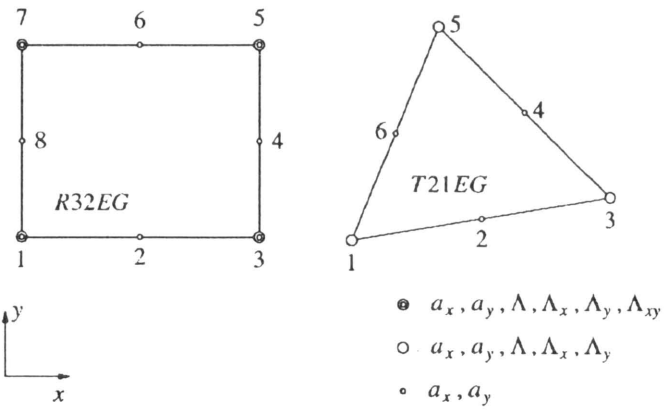

FIG. 2. Gradient plasticity elements: C^1-continuous rectangle and non-conforming triangle.

4. Applications in geomechanics

4.1. Shear layer

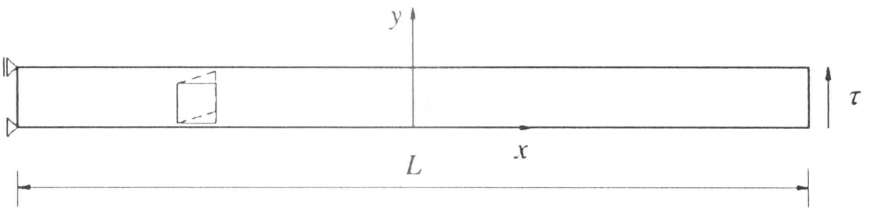

FIG. 3. Shear layer.

To illustrate the regularization introduced by the gradient-dependence we solve the one-dimensional problem of an infinite shear layer (Fig. 3). Introducing the notation $\tau = \sigma_{xy}$ and $\gamma = \varepsilon_{xy}$, the elastic constitutive relation for this case can be written as:

$$\tau = G\gamma^e , \tag{4.1}$$

where G is the shear modulus. For the plastic regime we consider the yield function of Eq. (2.13)

$$F = \sqrt{3}\,\tau - \beta \bar{c}_g \tag{4.2}$$

and we assume the case of volume-preserving plastic flow ($\tilde{\alpha} = 0$). Equation $(2.21)_2$ then gives $\eta = 1$ and Eq. (2.23) provides the following gradient-dependent evolution of the cohesion with a linear softening rule:

$$\bar{c}_g = c_y + \frac{h}{\beta}\kappa - \frac{g}{\beta}\frac{d^2\kappa}{dx^2} . \tag{4.3}$$

The hardening parameter can be calculated from Eq. (2.20) as:

$$\dot{\kappa} = \frac{\dot{\gamma}^p}{\sqrt{3}} \tag{4.4}$$

and both $h < 0$ and $g > 0$ are constant.

For this problem an analytical solution can be derived similar to that presented in [11] for a bar in pure tension. We solve the differential equation (4.3) rewritten as:

$$l^2\frac{d^2\kappa}{dx^2} + \kappa = \frac{\beta(\bar{c}_g - c_y)}{h} , \tag{4.5}$$

where a new parameter

$$l = \sqrt{-\frac{g}{h}} , \tag{4.6}$$

the internal length scale of our gradient-enhanced continuum, has been introduced. We notice that for Eq. (4.6) to make sense, g must be positive. Assuming a symmetric distribution of plastic strains with respect to the y-axis (Fig. 3), the solution of Eq. (4.5) is derived as:

$$\kappa = A\cos(x/l) + \frac{\beta(\bar{c}_g - c_y)}{h}. \tag{4.7}$$

We consider the evolution of the elasto-plastic process, so that Eq. (4.7) is differentiated with respect to "time":

$$\dot{\kappa} = \dot{A}\cos(x/l) + \frac{\beta\,\dot{\bar{c}}_g}{h}. \tag{4.8}$$

We assume that the plastic strains localize near the centre of the layer in a zone $(-w/2,\ w/2)$, so that w is the width of the shear band. Using the boundary condition $\dot{\kappa} = 0$ on the elastic-plastic boundary $x = \pm w/2$ we obtain

$$\dot{\kappa} = \frac{\beta\,\dot{\bar{c}}_g}{h}\left[1 - \frac{\cos(x/l)}{\cos(w/2l)}\right]. \tag{4.9}$$

The derivation has so far been general for any one-dimensional stress state. Now we return to the pure shear case and use the rate form of Eq. (4.1), the consistency condition

$$\dot{F} = \sqrt{3}\,\dot{\tau} - \beta\,\dot{\bar{c}}_g = 0, \tag{4.10}$$

Eq. (4.4) and Eq. (4.9) to determine the total shear strain rate:

$$\dot{\gamma} = \dot{\gamma}^e + \dot{\gamma}^p = \frac{\dot{\tau}}{G} + \frac{3\,\dot{\tau}}{h}\left[1 - \frac{\cos(x/l)}{\cos(w/2l)}\right]. \tag{4.11}$$

Assuming the position of the supports as in Fig. 3, we calculate the transverse velocity at the right-end of the layer $\dot{\nu}_r$:

$$\dot{\nu}_r = \int_{-L/2}^{L/2} \dot{\gamma}^e dx + \int_{-w/2}^{w/2} \dot{\gamma}^p dx = \frac{L\,\dot{\tau}}{G} + \frac{3\,\dot{\tau}}{h}[w - 2l\tan(w/2l)]. \tag{4.12}$$

The ratio of the velocity and the shear stress rate then equals

$$\frac{\dot{\nu}_r}{\dot{\tau}} = \frac{L}{G} + \frac{3}{h}[w - 2l\tan(w/2l)]. \tag{4.13}$$

To find the most critical equilibrium path we look for a value of w giving an aperiodic solution with the steepest descending branch. Therefore we require

$$\frac{d(\dot{\nu}_r/\dot{\tau})}{dw} = 0, \tag{4.14}$$

which results in the equation

$$\cos^2(w/2l) = 1. \tag{4.15}$$

This equation has the smallest non-trivial solution $w/2l = \pi$, so that

$$w = 2\pi l \tag{4.16}$$

with the length scale l defined by Eq. (4.6). The width of the localization zone is thus fully determined by the model parameters h and g. Substituting Eq. (4.16) into Eq. (4.13) and dividing by L gives a ratio of the average strain rate and the stress rate:

$$\frac{\dot{\nu}_r/L}{\dot{\tau}} = \frac{1}{G} + \frac{6\pi}{h}\frac{l}{L}. \tag{4.17}$$

We observe that the post-peak response is governed by the ratio l/L, which means that a size effect is incorporated in the model. The increase of the structural size L with constant l results in a more brittle behaviour.

In numerical simulations the shear layer in Fig. 3 has been discretized using 20 and 80 rectangular elements. Linear dependence relations for the relevant degrees of freedom have been added to prevent bending. The length of the layer is $L = 100\,\text{mm}$, the shear modulus $G = 10000\,\text{N/mm}^2$, Poisson's ratio $\nu = 0$, the friction angle $\phi = 0°$ ($\beta = 2.0$), the initial value of the cohesion $c_y = 1\,\text{N/mm}^2$, the softening modulus $h = -0.2G$. To trigger localization, the centre 10 mm of the layer have been assigned a 10% smaller value for c_y.

Figures 4 and 5 compare the finite element predictions for three values of the internal length: $l = 2.5$, 5 and 10 mm. The gradient influence coefficients are calculated from Eq. (4.6) as $g = 12500$, 50000 and 200000 N, respectively. The load-displacement diagrams in Fig. 4 show, that as long as all the points in the structure remain in the softening regime, the results for the two meshes with 20 and 80 elements are practically the same. The inclinations of the post-peak branches are close to the analytical values: $-\Delta\tau/\Delta\nu_r = 73.74, 26.94, 11.87\,[\text{N/mm}^3]$ for $l = 2.5$, 5 and 10 mm, respectively. When the strain in the centre elements leaves the softening branch, the load-displacement diagrams bend upwards and the localization zone broadens. This behaviour is a result of the fact that the softening modulus h goes to zero in the centre elements and g is kept constant, so that the internal length l locally increases to infinity. In this regime the calculations are stable provided the discretization used is dense enough. In Fig. 4

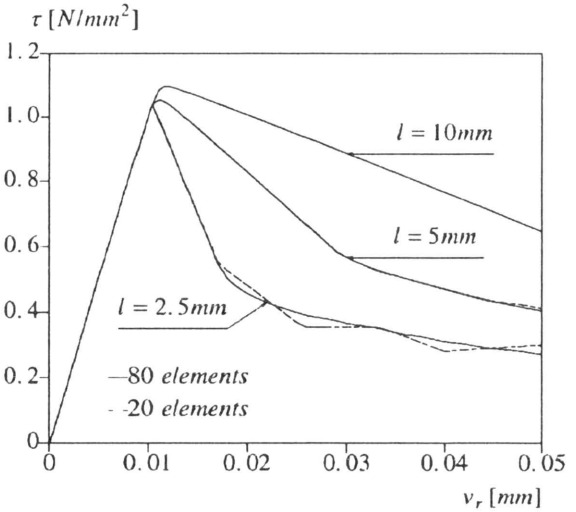

FIG. 4. Computed relations between the shear stress and the lateral displacement at the right-hand end of the shear layer.

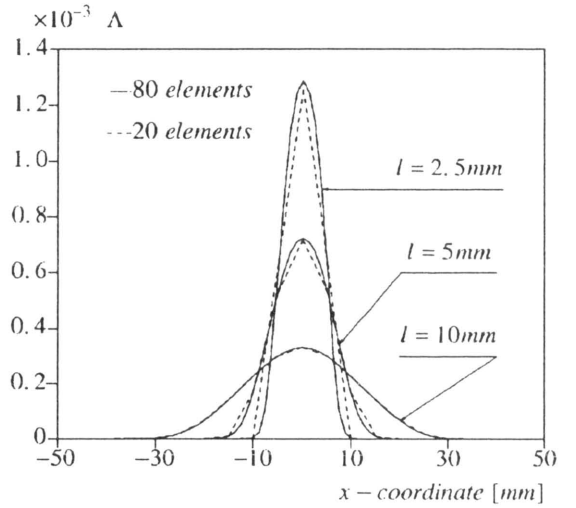

FIG. 5. Distribution of plastic multiplier along the layer for two discretizations and three values of the internal length ($v_r = 0.025$ mm).

the results for both meshes are similar for the larger internal length values, but for $l = 2.5$ mm and the coarse mesh oscillations are observed. From Fig. 4 it is visible that the approach is capable of simulating the size effect, since the ratio l/L governs the response in the post-peak regime.

In Fig. 5 the distribution of nodal values of the plastic multiplier is plotted and only a slight mesh sensitivity is observed. The diagrams prove that the length parameter l determines the width of localization zone, which is close to the ana-

lytical value $w = 2\pi l$. Only for $l = 2.5\,\text{mm}$ the width of the localization zone is broader than $w = 15.7\,\text{mm}$, since for $\nu_r = 0.025\,\text{mm}$ softening has already been exhausted in the centre of the layer.

4.2. Biaxial compression

We investigate the standard plane strain biaxial compression test [17] using gradient-dependent Drucker-Prager plasticity. The test configuration has the following dimensions: $B = 60\,\text{mm}$ and $H = 120\,\text{mm}$ (Fig. 6). The bottom of the specimen is smooth and rigid, the load is applied at the top and all nodes along the upper edge are constrained to have the same vertical displacements. The material data are: elastic shear modulus $G = 1000\,\text{N/mm}^2$, Poisson's ratio $\nu = 0.2$, initial cohesion $c_y = 1\,\text{N/mm}^2$, constant softening modulus $\partial\bar{c}/\partial\kappa = -0.025G$ and friction angle $\phi = 30°$. First, we analyze the case of associated plastic flow ($\bar{\alpha} = \alpha$). According to Eq. (2.21) $\eta \approx 1.149$ and according to Eq. $(2.22)_2$, the softening modulus $h \approx -0.060G$. An internal length scale $l = 4\,\text{mm}$ is assumed and the gradient coefficient is calculated from Eq. (4.6) as $g \approx 955\,\text{N}$. Three discretizations have been used: 6×12, 12×24 and 24×48 elements R32EG.

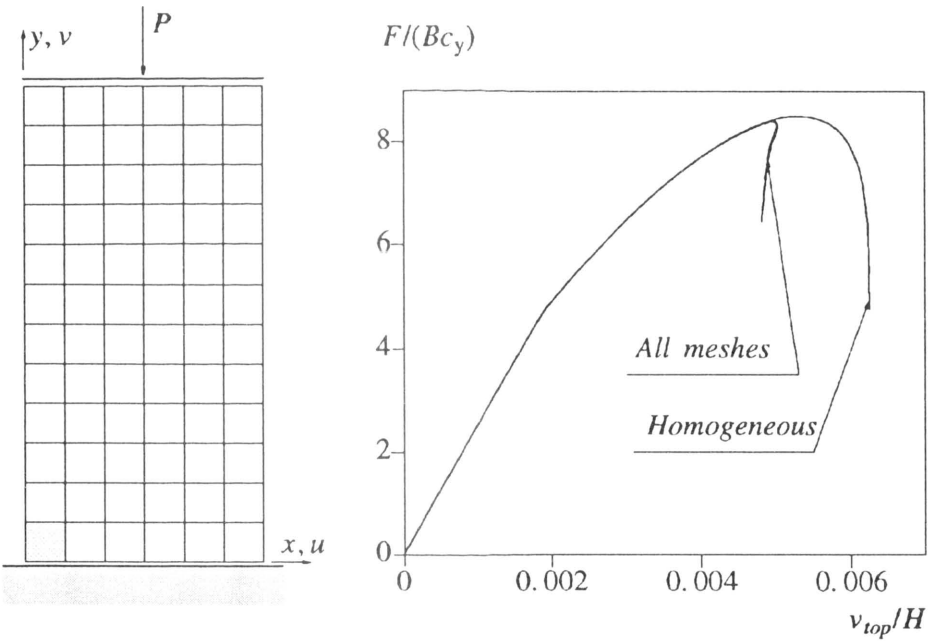

FIG. 6. Test configuration (with imperfection in the bottom left-hand corner) and load-displacement diagram for the associated plasticity case.

To follow an equilibrium path associated with the localized deformation mode, one or more slightly weaker spots (imperfections) can be introduced in the model. The bifurcation problem is then transferred into a limit problem and the imperfections initiate a localized deformation pattern. In our example an imperfect

zone with 10% smaller c_y is introduced in the bottom left-hand corner (Fig. 6). Calculations are performed under arc-length control.

Figure 6 presents the relative load versus relative displacement diagrams for the case of homogeneous deformations, which is obtained without inserting imperfections, and for the gradient plasticity model (all meshes). The pressure-dependence of the yield function causes an initial stress build-up and hardening behaviour, despite the cohesion softening. The whole specimen shows an almost uniform plastic flow and a shear band-type localization is impossible at the onset of plastification. This behaviour agrees with the fact that for this stress state the acoustic tensor singularity condition [2, 3] gives a critical value of the softening modulus, which is much smaller than the value used in our calculations.

At a load level $F/(Bc_y) \approx 8.4$ a bulging localization mode emerges as shown in Fig. 7. The results obtained for the gradient-dependent continuum using the three meshes are almost identical also in the post-critical regime.

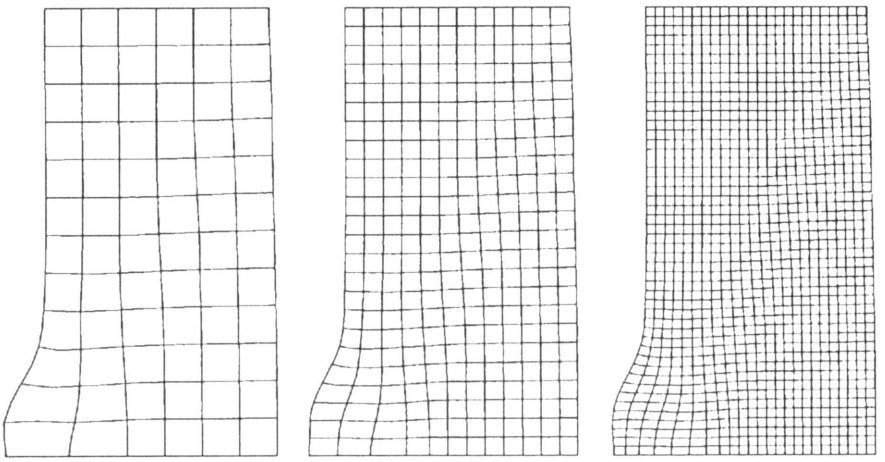

FIG. 7. Incremental deformations of the gradient-dependent model at $F/(Bc_y) = 7.3$.

During the plastic process the relations between the stress components change and the critical value of the softening modulus increases. While at the onset of instability the analytical expression from [3] gives $h_{\mathrm{cr}} \approx -0.13G$, which is smaller than the input data, so that shear-band formation is impossible, in the post-critical regime the bulging mode promotes a shear-band mode (Fig. 8).

Next, we consider the non-associated plasticity case. The test data are the same as before with the exception of the dilatancy angle ψ, which is now equal to zero (volume preserving plastic flow). The value the softening modulus is $h \approx -0.052G$ and the gradient constant is $g \approx 831\,\mathrm{N}$. Calculations are now performed under displacement control.

The load-displacement curves for the three discretizations are shown in Fig. 9, under homogeneous and inhomogeneous deformations. In this figure the shear band obtained for classical, gradient-independent plasticity ($l = 0$) has also been

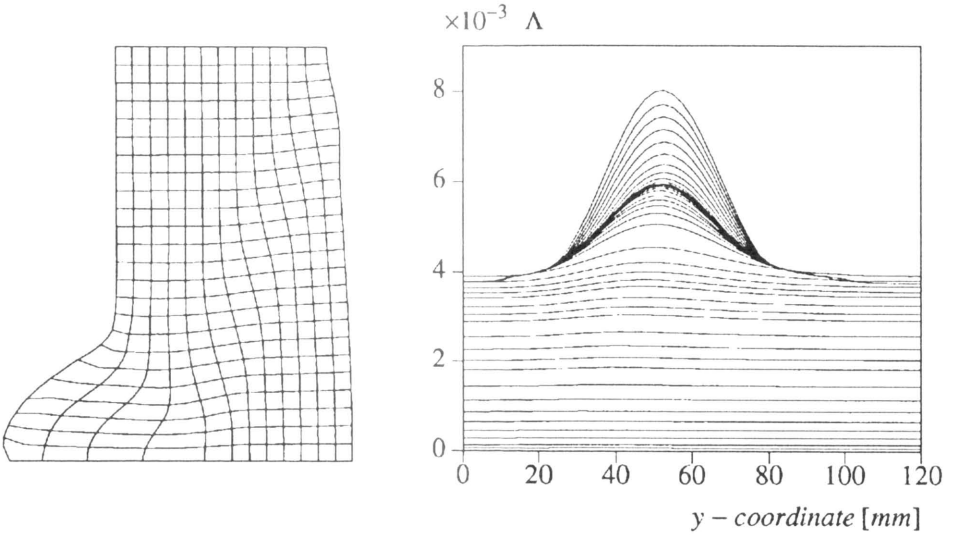

FIG. 8. Emergence of a shear band in presence of the bulging mode. Incremental displacements of the medium mesh at $F/(Bc_y) = 6.4$ (left) and the evolution of the plastic multiplier distribution along the vertical symmetry axis (right).

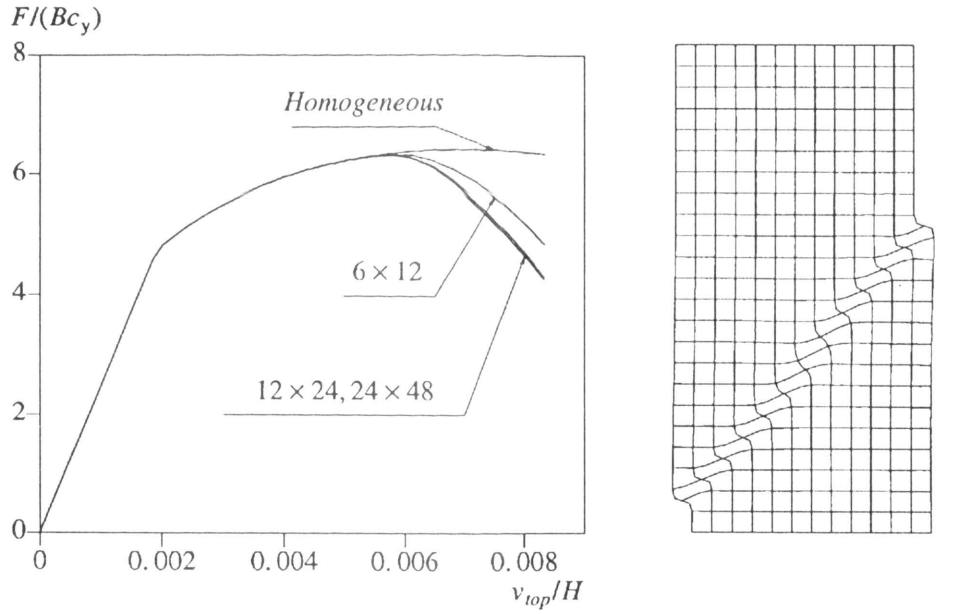

FIG. 9. Load-displacement diagram for the non-associated plasticity case and the incremental deformations of the gradient-independent model for the medium mesh.

plotted. It shows how in the classical continuum the gradient-independent finite elements attempt to predict localization in a discrete plane. The shear band width converges to the smallest value admitted by the discretization. For other meshes

completely different solutions are computed in the post-critical regime. On the other hand, the gradient-dependent model removes the spurious mesh sensitivity. Although the response for the coarse mesh is a bit too stiff, it is almost the same for the medium and fine mesh. The shear band width is practically the same for all meshes (Fig. 10). Even though we now analyze a biaxial stress state, the relation $w = 2\pi l$, derived for the one-dimensional case in the previous section, gives a good approximation of the shear band width.

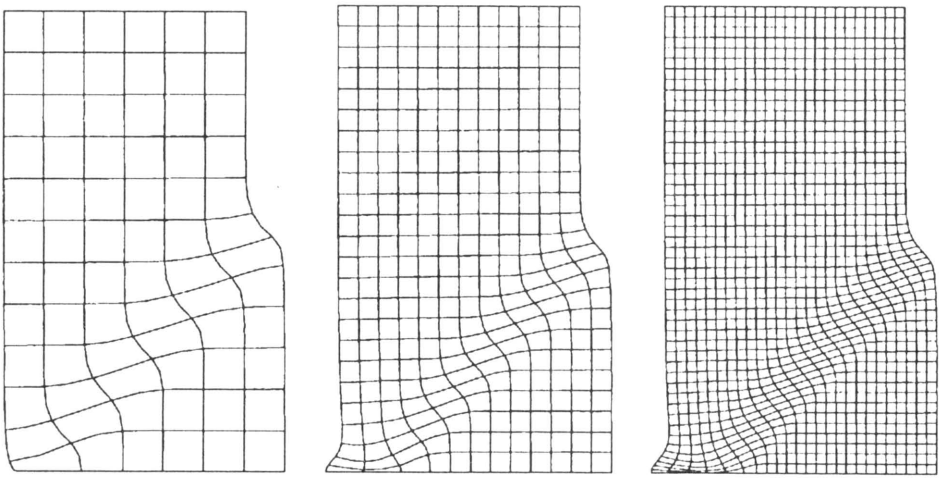

FIG. 10. Incremental deformations of the gradient-dependent model at $v_{\text{top}}/H = 0.0083$.

The non-associated plasticity model results in a more ductile and less stable behaviour than the associated model. At the onset of plastification localization is impossible ($h_{\text{cr}} \approx -0.427G$ according to [3]), but at the onset of numerically predicted shear banding the analytical value of the critical hardening modulus is already positive ($h_{\text{cr}} \approx 0.03G$ according to [3]).

4.3. Slope stability

Figure 11 shows two configurations used for the analysis of soil mass stability under an increasing gravity load. On the left we present a slope with an inclination of 45° (cf. [18]), and on the right a vertical embankment. In both cases the lower edge is fixed and the right edge is supported in the horizontal direction.

The material data are based on [18]: Young's modulus $E = 2 \cdot 10^8\,\text{N/m}^2$, Poisson's ratio $\nu = 0.25$, initial cohesion $c_y = 2000\,\text{N/m}^2$, friction angle $\phi = 20°$, dilatancy angle $\psi = 10°$. The soil density $\rho = 1000\,\text{kg/m}^3$ is adopted. The linear softening rate for cohesion is $\partial\bar{c}/\partial\kappa = -0.01G$. The strain hardening hypothesis gives $\eta = \dot{\kappa} \,/\, \dot{\lambda} \approx 1.015$ and the softening modulus $h \approx -0.060G$. The results for two internal length scales $l = 0.02\,\text{m}$ and $l = 0.04\,\text{m}$ are compared (the gradient constants are $g \approx 688\,\text{N}$ and $g \approx 2752\,\text{N}$, respectively).

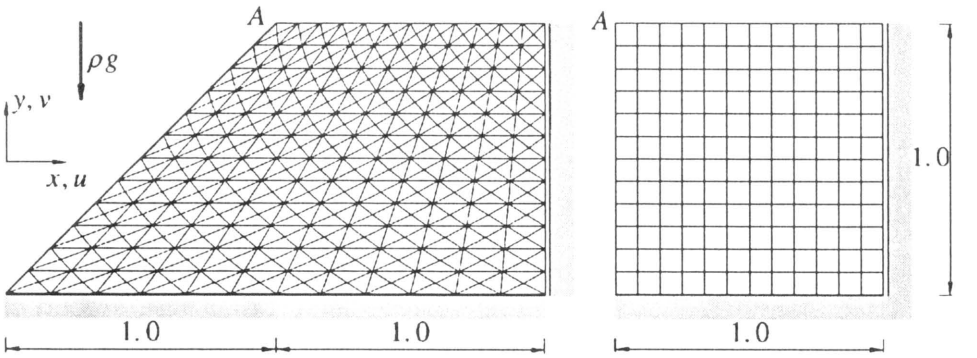

FIG. 11. Inclined and vertical embankment models (dimensions in m).

For the first configuration we use two crossed-diagonal meshes with $12 \times 12 \times 4$ and $24 \times 24 \times 4$ six-noded triangles T21EG with 3 integration points. For the second configuration we use three discretizations with 12×12, 24×24 and 48×48 eight-noded elements R32EG with a 2×2 integration scheme. The calculations are performed under the arc-length or single displacement control. In the latter case the vertical displacement of point A is the controlling parameter (cf. Fig. 11).

We begin the discussion with the vertical embankment. Figure 12 presents the calculated relations between the gravity load factor and the vertical displacement of point A obtained using the Drucker–Prager gradient plasticity model. When the gravity load reaches the level 0.6, the first plastic points occur in the bottom left-hand corner of the embankment. A shear band then gradually extends towards the upper edge and a softening response follows.

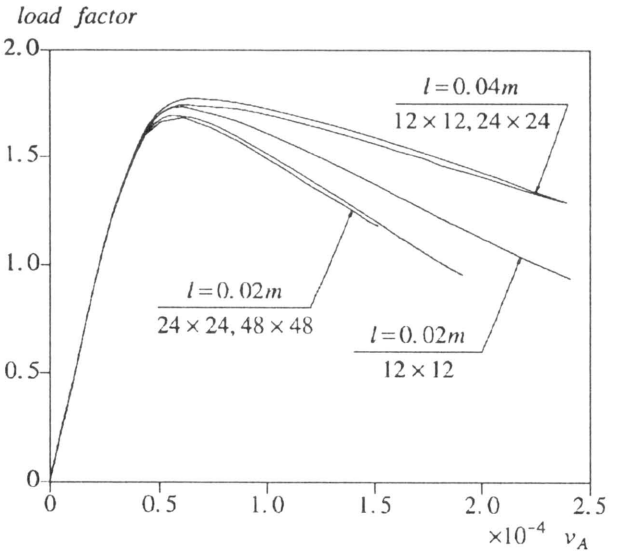

FIG. 12. Mesh sensitivity of load-displacement diagrams for the vertical embankment and gradient plasticity elements R32EG.

Figure 13 presents the incremental displacements at the final load level for the smaller internal length $l = 0.02\,\mathrm{m}$. It is observed that the medium and fine mesh produce almost identical results. A too stiff response is found in Fig. 12 for the coarse mesh (12×12 elements). The shear band width defined by the assumed internal length is close to the smallest possible size that can be reproduced by this mesh. Therefore the representation is insufficient, while for the larger internal length $l = 0.04\,\mathrm{m}$ the coarse and medium meshes give already similar results. Figure 14 illustrates the dependence of the shear band width w on the assumed value of the internal length l. As for the biaxial compression test, a good correspondence is found with the analytical relation $w = 2\pi l$ derived for the pure shear case.

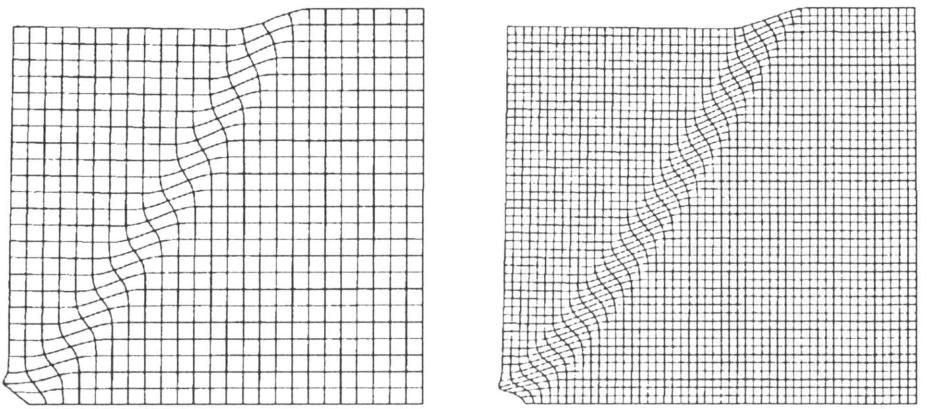

FIG. 13. Incremental deformation patterns for the medium and fine mesh ($l = 0.02\,\mathrm{m}$).

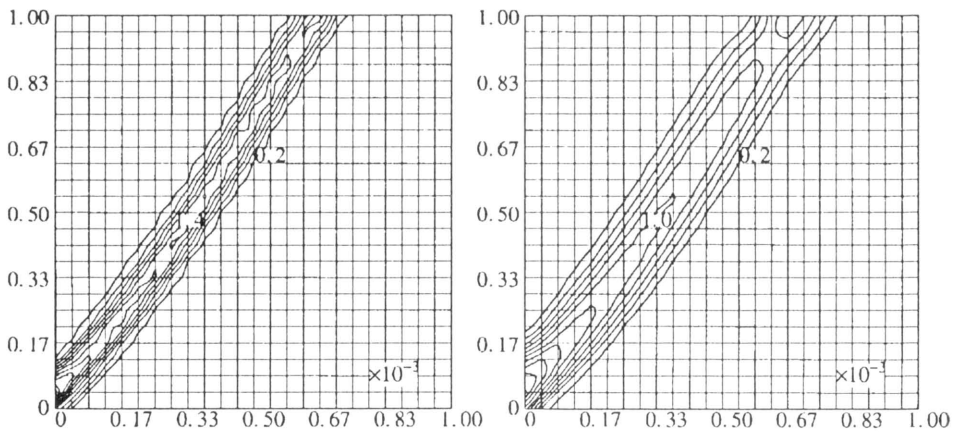

FIG. 14. Contour plots of equivalent plastic strain for $l = 0.02\,\mathrm{m}$ (left) and $l = 0.04\,\mathrm{m}$ (right).

Next, we analyze the stability of the slope in Fig. 11. In the gradient plasticity calculations the length scale $l = 0.04\,\mathrm{m}$ is used. Figure 15 presents the load-displacement diagrams. With the increase of the dead-weight (at the load

factor value 1.8), the compressed soil mass starts to plastify at the bottom of the embankment. The plastic zone then gradually expands upwards and at the peak-load a shear band forms, along which a part of the soil mass slides down.

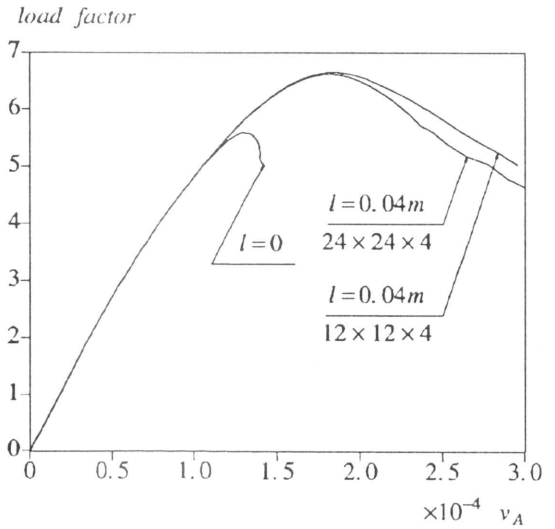

FIG. 15. Classical versus gradient plasticity solutions for the slope stability problem in terms of gravity load factor and vertical displacement at point A.

Calculations for classical softening plasticity case ($l = 0$) fail soon after the formation of the shear band. The gradient plasticity algorithm gives a more stable behaviour. The peak-load is higher and the response is more ductile when the gradient terms are included. The results for both analyzed meshes are close, but not the same (Fig. 15).

Figure 16 presents the final incremental deformations for the gradient plasticity case and $24 \times 24 \times 4$ element mesh. The expected smoothing effect is observed and the curved shear band has the width of several elements. Figure 17 compares

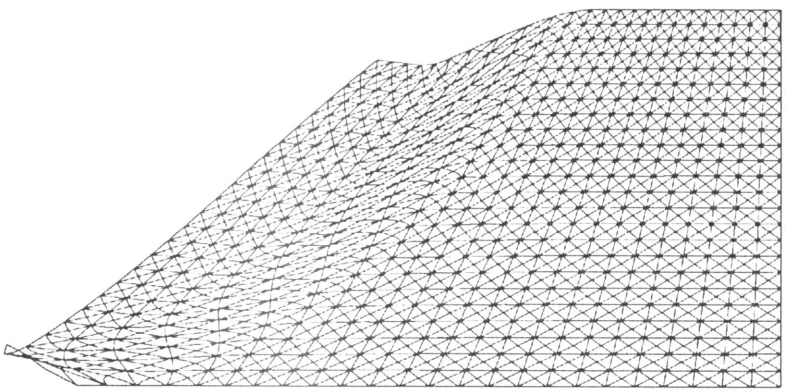

FIG. 16. Incremental deformation pattern for the finest mesh ($24 \times 24 \times 4$ elements T21EG) and $l = 0.04$ m.

the contour plots of the equivalent plastic strain obtained for the two analyzed discretizations. The strains are slightly more localized for the fine mesh, but the shear band width $w \approx 0.25\,\mathrm{m}$ is well reproduced.

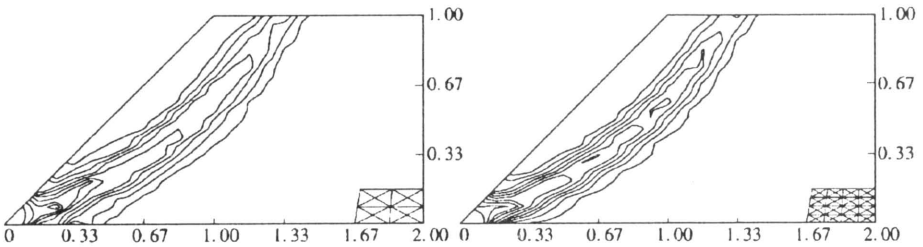

FIG. 17. Contour plots of equivalent plastic strain for two discretizations ($l = 0.04\,\mathrm{m}$).

1. Conclusions

The employed gradient plasticity theory, which incorporates a yield function dependent on higher-order spatial derivatives of a plastic strain measure, preserves ellipticity of the governing equations in the post-critical regime. Therefore, the boundary value problem for a softening continuum remains well-posed. An internal length scale is present in the theory and determines the width of the shear localization bands. Therefore, the results of finite element simulations are almost insensitive to the mesh refinement.

The fundamental feature of the used algorithm is a weak (and not pointwise) satisfaction of the yield condition, which is coupled with a weak equilibrium condition. The dependence of the yield function on the Laplacian of the plastic strain measure induces the necessity of C^1-continuous interpolation of the plastic strain field in the incremental formulation. A C^1-continuous rectangular element and a non-conforming triangular element have been implemented and applied in some soil instability problems.

The results have shown that the gradient plasticity models may be successfully applied in the numerical simulation of localization phenomena in frictional materials. The Drucker–Prager flow theory with a gradient-dependent softening cohesion is an example of a plasticity formulation that can be employed for prediction of various instability modes in overconsolidated soils. A further investigation of advanced elasto-plastic models like the Cam-clay model [14] with the gradient localization limiter is necessary. The experimental determination of the internal length scale for various geomaterials is also of primary importance.

2. Acknowledgements

The calculations have been carried out with the DIANA finite element code of TNO Building and Construction Research. The financial support of the Commis-

sion of the European Communities through the Brite-Euram program (project BE-3275) is gratefully acknowledged.

References

1. H.E. READ and G.A. HEGEMIER, *Strain softening of rock, soil and concrete. A review article*, Mech. Mater., **3**, 271–294, 1984.
2. J.W. RUDNICKI and J.R. RICE, *Conditions for the localization of deformation in pressure-sensitive dilatant materials*, J. Mech. Phys. Solids, **23**, 371–394, 1975.
3. K. RUNESSON, N.S. OTTOSEN and D. PERIĆ, *Discontinuous bifurcations of elastic-plastic solutions at plane stress and plane strain*, Int. J. Plasticity, **7**, 99–121, 1991.
4. G. MAIER and T. HUECKEL, *Nonassociated and coupled flow rules of elastoplasticity for rock-like materials*, Int. J. Rock Mech. Min. Sci. & Geomech. Abstr., **16**, 77–92, 1979.
5. K.J. WILLAM and G. ETSE, *Failure assessment of the extended Leon model for plain concrete*, [in:] Proc. Second Int. Conf. Computer Aided Analysis and Design of Concrete Structures, N. BIĆANIĆ *et al.* [Eds.], Pineridge Press, Swansea, 851–870, 1990.
6. P.A. VERMEER and R. DE BORST, *Non-associated plasticity for soils, concrete and rock*, Heron, **29**, 3, 1984.
7. R. DE BORST, L.J. SLUYS, H.-B. MÜHLHAUS and J. PAMIN, *Fundamental issues in finite element analyses of localization of deformation*, Engng. Comput., **10**, 99–121, 1993.
8. H.-B. MÜHLHAUS, R. DE BORST and E.C. AIFANTIS, *Constitutive models and numerical analyses for inelastic materials with microstructure*, [in:] Proc. Seventh Conf. Int. Assoc. Comp. Methods and Advances in Geomechanics, G. BEER *et al.* [Eds.], Balkema, Rotterdam, 377–385, 1991.
9. H.-B. MÜHLHAUS and E.C. AIFANTIS, *A variational principle for gradient plasticity*, Int. J. Solids Structures, **28**, 845–857, 1991.
10. I. VARDOULAKIS and E.C. AIFANTIS, *A gradient flow theory of plasticity for granular materials*, Acta Mech., **87**, 197–217, 1991.
11. R. DE BORST and H.-B. MÜHLHAUS, *Gradient-dependent plasticity: Formulation and algorithmic aspects*, Int. J. Num. Meth. Engng., **35**, 521–539, 1992.
12. J. PAMIN, *Gradient-dependent plasticity in numerical simulation of localization phenomena*, Dissertation, Delft University of Technology, Delft 1994.
13. L.J. SLUYS, R. DE BORST and H.-B. MÜHLHAUS, *Wave propagation, localization and dispersion in a gradient -dependent medium*, Int. J. Solids Structures, **30**, 1153–1171, 1993.
14. A. GENS and D.M. POTTS, *Critical state models in computational geomechanics*, Engng. Comput., **5**, 178–197, 1988.
15. J. BARLOW, *Optimal stress locations in finite element model*, Int. J. Num. Meth. Engng., **10**, 243–251, 1976.
16. O.C. ZIENKIEWICZ and R.L. TAYLOR, *The finite element method*, fourth edition, Vol. 2, Chapter 1, McGraw-Hill, London 1991.
17. R. DE BORST, *Numerical methods for bifurcation analysis in geomechanics*, Ing.-Arch., **59**, 160–174, 1989.
18. M. ORTIZ, Y. LEROY and A. NEEDLEMAN, *A finite element method for localized failure analysis*, Comp. Meth. Appl. Mech. Engng., **61**, 189–214, 1987.

DELFT UNIVERSITY OF TECHNOLOGY,
FACULTY OF CIVIL ENGINEERING, DELFT, THE NETHERLANDS.

Received September 14, 1994.

Arch. Mech., 47, 2, pp. 379–390, Warszawa 1995

A strategy for determining the equilibrium shape of an inclusion (*)

I. SCHMIDT and D. GROSS (DARMSTADT)

A METHOD IS proposed for determinig the equilibrium shape of a single coherent three-dimensional precipitate with an arbitrary selfstrain ("eigenstrain"). Using an explicit expression for the elastic driving force, the method allows for general anisotropy of both the matrix and the inclusion material. Boundary integral techniques are employed to solve the corresponding problem of linear elasticity. Examples in two dimensions for isotropic, orthotropic and completely anisotropic matrix materials are given. It is found, that various equi-axial equilibrium shapes are possible without taking the interfacial energy into consideration.

1. Introduction

THE MORPHOLOGY OF inhomogeneities in a material is, in addition to the properties of the different phases, of great importance for the overall material behaviour and, thus, for the engineering applications. It is well established that the thermodynamic forces which determine the morphology, are due to minimization of interface- and elastic strain energy contributions [1, 2]. The simplest case where their influence can be studied, is that of a single second phase particle (inclusion), being coherently embedded in an infinitely extended matrix phase. Here the state of stress arises from the adjustment of the mismatching crystal lattices along the interface (but there might as well be present external or thermal loads or body forces).

The influence of the particle shape on the strain energy and the problem of finding the equilibrium shape, that minimizes the interface- and/or strain energy of the system has been widely investigated, using different assumptions and simplifications [2–5, 7]. These works, as well as experimental studies, have recently been reviewed [6]. The most common simplification is to constrain the inclusion shape to be within a certain family of geometric shapes, such as ellipsoids, cubes or plates. Though ROITBURD and KAGANOVA [3] showed that, in special cases, an ellipsoid indeed can be an equilibrium shape, these simplifications are primarily due to the difficulty in determining the elastic strain energy of an arbitrarily shaped inclusion. For the same reason, equal elastic moduli in the inclusion and the matrix are often assumed [2, 5, 7]. However, these approaches have been successful in predicting e.g. habit planes of plate-like particles [2], but failed to describe other experimentally observed morphologies.

(*) Paper presented at 30th Polish Solid Mechanics Conference, Zakopane, September 5–9, 1994.

VOORHEES *et al.* [7] investigated the temporal evolution of a particle, for the first time without placing restrictions on its shape and assuming the particle evolution to take place by diffusion of mass. They incorporated an isotropic interface energy density but neglected the difference in elastic moduli of the phases.

Bearing in mind Roitburd's result that the equilibrium shape is a sphere, when the inclusion is elastically harder than the matrix, whereas it is a plate in the opposite case, it seems worthwile to study the influence of the inhomogeneity on the equilibrium shape alone. In this paper we present a strategy to determine equilibrium shapes of inclusions without any *a priori* assumptions. Unlike that of VOORHEES *et al.* [7], our approach allows for inhomogeneous inclusions and complete anisotropy of both the matrix and the inclusion material.

First we describe the state of stress in a two-phase system and give an expression for the elastic energy stored in it. We define the term "equilibrium shape" and give the necessary condition to determine it. Next we specify this condition and give a generally valid expression for the elastic driving force, which is then used to set up an iteration scheme. Boundary integral techniques are used here to compute the elastic field of the inclusion, in order to formulate the whole problem on the inclusion boundary.

2. Problem formulation

The state of stress accompanying a misfitting, inhomogeneous inclusion $\mathcal{B}$ of a given shape, embedded in an infinitely extended matrix, can be modelled as an eigenstrain problem in the framework of linear elasticity [8]. In absence of body forces and external loads, the governing equations are as follows:

$$\sigma_{ij,j} = 0, \tag{2.1}$$

$$\sigma_{ij} = C_{ijkl}\varepsilon^{\mathrm{el}}_{kl}, \tag{2.2}$$

$$C_{ijkl} = \begin{cases} C^{\mathrm{in}}_{ijkl} & \mathbf{x} \in \mathcal{B}, \\ C^{\mathrm{out}}_{ijkl} & \mathbf{x} \notin \mathcal{B}, \end{cases} \tag{2.3}$$

$$\varepsilon^{\mathrm{el}}_{ij} = \begin{cases} \varepsilon_{ij} - \varepsilon^{0}_{ij} & \mathbf{x} \in \mathcal{B}, \\ \varepsilon_{ij} & \mathbf{x} \notin \mathcal{B}, \end{cases} \tag{2.4}$$

$$\varepsilon_{ij} = \frac{1}{2}(u_{i,j} + u_{j,i}). \tag{2.5}$$

Here σ_{ij} are the Cauchy stresses, u_i the displacements, $\varepsilon_{ij}, \varepsilon^{\mathrm{el}}_{ij}$ the components of the total and elastic strain tensor, respectively, and $C^{\mathrm{in/out}}_{ijkl}$ are components of the elastic constant tensor inside and outside the inclusion, respectively. ε^{0}_{ij} denote components of the spatially constant inelastic transformation- (or "eigen"-) strain

tensor, measuring the difference in the crystal lattices of the two phases. Of course, all tensor components refer to the same (Cartesian) coordinate system.

It can be seen from elementary considerations [8] (Appendix A1), that the elastic strain energy associated with this state of stress is given by

$$\Pi = -\frac{1}{2}\varepsilon^0_{ij}\int_{\mathcal{B}} \sigma_{ij}dV\,. \tag{2.6}$$

Neglecting the interfacial energy contribution, Π represents the total potential energy of the system. Consequently, the equilibrium shape $\partial\mathcal{B}$ of the inclusion will be such that it extremizes Π under the constraint that the volume of $\mathcal{B}$ should be constant:

$$V_{\mathcal{B}} = \int_{\mathcal{B}} dV = V_0\,. \tag{2.7}$$

Employing the Lagrange multiplier method, the equivalent problem is to find the shape $\partial\mathcal{B}$ that extremizes the functional

$$\Pi^*(\partial\mathcal{B}) = -\frac{1}{2}\varepsilon^0_{ij}\int_{\mathcal{B}} \sigma_{ij}dV - \lambda(V_0 - \int_{\mathcal{B}} dV), \tag{2.8}$$

where λ is an undetermined constant and the σ_{ij} satisfy the set of equations (2.1)–(2.5). Hence, the necessary condition for equilibrium in the inclusion shape is

$$\delta\Pi^* = 0, \tag{2.9}$$

where δ denotes the variation of the inclusion shape $\partial\mathcal{B}$.

3. Interface equilibrium, generalized force

Since the elastic constant and the eigenstrain tensor suffer a jump across the interface, $\partial\mathcal{B}$ represents a discontinuity surface for the field quantities. However, the interfacial tractions must be continuous, and in the case of a coherent interface the same holds for the displacements [8]. Denoting the jump of some quantity, say, A by $[\![A]\!] = A^{\text{out}} - A^{\text{in}}$, this reads:

$$[\![u_i]\!] = 0, \tag{3.1}$$

$$[\![\sigma_{ij}]\!]\,n_j = 0. \tag{3.2}$$

It follows from (3.1), that the displacement derivative tangential to the interface $\partial\mathcal{B}$ must also be continuous, and therefore the jump of the displacement gradient must be of the form

$$[\![u_{i,j}]\!] = \gamma_i n_j\,, \tag{3.3}$$

where $\mathbf{n}$ is the unit outward normal to $\partial\mathcal{B}$ and γ_i are proportionality constants, which can be determined from Eq. (3.2). With this result, all the jump quantities can be expressed in terms of the displacement gradient on the interface (see Appendix A2). We will make use of this later on.

ESHELBY [9] showed that the variation of elastic energy due to a small migration δs of a discontinuity surface in direction normal to it can be written as an integral along this discontinuity surface (any share of the interface migration, that is tangential to the interface, does not contribute to the change in energy):

$$\delta \Pi = -\int_{\partial\mathcal{B}} \delta s \underbrace{n_k [\![P_{kj}]\!] n_j}_{f_n} \, dA, \tag{3.4}$$

where

$$P_{kj} = W\delta_{jk} - \sigma_{ij} u_{i,k} \tag{3.5}$$

are components of Eshelby's energy-momentum tensor. f_n is work-conjugate to the normal displacement s (Fig. 1) and can therefore be interpreted as a generalized normal force acting on the interface. This quantity is a convenient measure for the tendency of the interface to move in or against the normal direction.

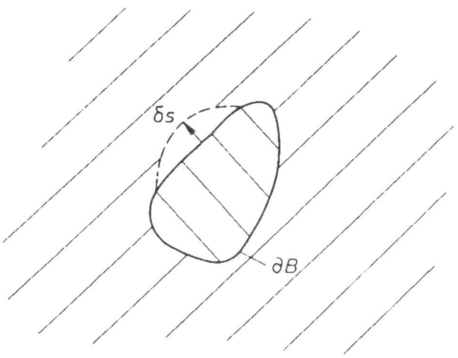

FIG. 1. Migration of the inclusion boundary.

The variation of the inclusion volume is $\delta V_{\mathcal{B}} = \int_{\mathcal{B}} \delta s \, dA$, and thus Eq. (2.9) now reads:

$$\delta \Pi^* = \delta \Pi + \lambda \delta V_{\mathcal{B}} = -\int_{\partial\mathcal{B}} \delta s (f_n - \lambda) dA = 0,$$

Since $\lambda = \text{const}$, it follows, that the necessary condition for interface equilibrium is

$$f_n = \text{const} \qquad \text{on} \quad \partial\mathcal{B}. \tag{3.6}$$

Because of its great importance in the problem, it is useful to give a more detailed expression for the generalized force f_n, which eventually displays the

influence of the different problem parameters more clearly: taking into account the continuity (3.2) of the surface tractions $\mathbf{t}$ and the fact that $\mathbf{n}$ is a unit vector, f_n can be written as [9]

$$f_n = [\![W]\!] - t_i [\![u_{i,k}]\!] n_k .$$

As mentioned before, all the jump quantities can be expressed in terms of the displacement gradient adjacent to the interface inside the inclusion. Thus also the jump in W can be given in that way, and a tedious calculation yields

$$f_n = -\frac{1}{2}\left\{C^{\text{in}}_{ijpq}\varepsilon^0_{pq} - [\![C_{ijpq}]\!]u_{p,q}\right\} n_j \Omega^{-1}_{ik}(\mathbf{n}) n_l \left\{C^{\text{in}}_{klrs}\varepsilon^0_{rs} - [\![C_{klrs}]\!]u_{r,s}\right\} + \frac{1}{2}u_{i,j}C^{\text{out}}_{ijkl}u_{k,l} - \frac{1}{2}(u_{i,j} - \varepsilon^0_{ij})C^{\text{in}}_{ijkl}(u_{k,l} - \varepsilon^0_{kl}), \tag{3.7}$$

where $\Omega^{-1}_{ik}(\mathbf{n})$ denotes components of the inverse of $\Omega_{ik}(\mathbf{n}) = C^{\text{out}}_{ijkl} n_j n_l$.

Apart from being lengthy, expression (3.7) is also fairly general: It gives the elastic driving force for the evolution of a three-dimensional, inhomogeneous inclusion of arbitrary shape and holds for arbitrary anisotropy of both the matrix and the inclusion material. Unfortunately, the displacement gradient enters into f_n, which involves the solution of the transmission problem (2.1)–(2.5). Therefore one needs to know the entire inclusion shape to evaluate f_n at one point of the surface.

4. Iteration scheme

Let it be supposed now that the $u_{i,j}$ are available for any given inclusion shape. For an arbitrary shape $\partial\mathcal{B}_k$, Eq. (3.7) then gives the distribution of the generalized force along the interface. In view of (3.4), a migration of the interface $\partial\mathcal{B}_k$ in the direction of its normal by Δs, must lead to a decrease in Π^*, if Δs:

- has the same sign as f_n: e.g. $\Delta s \propto f_n$,
- is sufficently small compared to some characteristic length (e.g. the cubic root of the inclusion volume): $\Delta s \ll (V_{\mathcal{B}_k})^{1/3}$,
- leaves the inclusion volume unchanged: $\int_{\partial\mathcal{B}_k} \Delta s \, dA = 0$.

Allow the interface to move actually in that manner ($\partial\mathcal{B}_k \to \partial\mathcal{B}_{k+1}$), then $\Pi^*_{k+1} < \Pi^*_k$ for sure. For the new inclusion shape $\partial\mathcal{B}_{k+1}$ so constructed, the above reasoning is just the same, and thus, repeated application of the described procedure must lead to a (local) minimum in the total potential energy.

5. Boundary-integral approach

In each step of the iteration scheme, the computation of the generalized force requires the knowledge of the displacement gradient at the interface. Here we

employ boundary-integral techniques to compute the latter. In doing so, we take advantadge of the possibility to formulate the whole problem on the interface, which reduces the dimension of the problem by one. From now on we restrict ourselves to the two-dimensional problem, assuming a state of plane strain in the two-phase system (i.e. the inclusion has the shape of an infinitely extended cylinder, the shape of the cross-section of which is what we are looking for). This is just to spare some work - we emphasize, that the $3D$ problem can be treated in the same way.

Viewing the matrix and the inclusion as two separate bodies, we have two integral equations which relate boundary values of the *elastic* displacements and surface tractions: One describing the outer domain problem of the matrix, and one for the inner domain problem of the inclusion [10]. Since $\partial\mathcal{B}$ is a common boundary of the two domains, inserting the transition conditions (3.1), (3.2) yields a set of two integral equations for the unkown displacements and tractions on the boundary of the inclusion:

$$
\begin{aligned}
c_{ij}(S)\, u_j(S) &= \int_{\partial\mathcal{B}} G_{ij}^{\text{out}}(S,S')\, t_j(S')\, dS' - \int_{\partial\mathcal{B}} T_{ij}^{\text{out}}(S,S',\vec{n})\, u_j(S')\, dS', \\
c_{ij}(S)\,[u_j(S) - u_j^0(S)] &= \int_{\partial\mathcal{B}} G_{ij}^{\text{in}}(S,S')\, t_j(S')\, dS' \\
&\quad - \int_{\partial\mathcal{B}} T_{ij}^{\text{in}}(S,S',\vec{n})\,[u_j(S') - u_j^0(S')]\, dS'.
\end{aligned}
\tag{5.1}
$$

Here the common notation is used: $G_{ij}^{\text{in/out}}, T_{ij}^{\text{in/out}}$ are the fundamental solutions for the displacements and tractions of inclusion and matrix material, respectively. In the two-dimensional case they are available in a closed form for arbitrary anisotropy [11]. u_j^0 denotes the inelastic displacement associated with the eigenstrain ε_{ij}^0 and for a smooth surface $c_{ij} = \frac{1}{2}\delta_{ij}$ (otherwise c_{ij} are known functions of the corner angle). S denotes the arc length on the contour.

Evaluating Hooke's law (2.2) on the boundary and using the knowledge of the tangential displacement derivative, the desired total strain ε_{kl} can be obtained from the solution of (5.1) through

$$
\begin{aligned}
C_{ijkl}^{\text{in}} n_j \varepsilon_{kl} &= t_i + C_{ijkl}^{\text{in}} n_j \varepsilon_{kl}^0, \\
m_k m_l \varepsilon_{kl} &= \frac{du_i}{dS} m_i
\end{aligned}
\tag{5.2}
$$

with m_k being the unit vector tangent to the contour.

Equations (3.6), (3.7) together with (5.1), (5.2) represent a set of equations which determine the equilibrium shape $\partial\mathcal{B}$.

6. Numerical procedure

The numerical solution of (5.1) poses no problem, it is managed in the customary way [10]: Using isoparametric linear elements, the evaluation of the discretized form of (5.1) at the nodes amounts to an algebraic system for the nodal values of **u** and **t**. After obtaining the strains from (5.2), where the tangential derivative is approximated by the difference quotient, the generalized force is evaluated at each node through (3.7). The nodal points are then moved in normal direction according to the value of f_n. The procedure is repeated until either the variation of f_n along the interface is sufficiently small, or the elastic energy starts to increase again.

7. Results

In what follows the coordinate axes are chosen to coincide with the principal directions of the eigenstrain tensor ε^0_{ij}, which is thus characterized by its two principal values ε^0_1, ε^0_2. The equilibrium shape turns out to be quite sensitive to

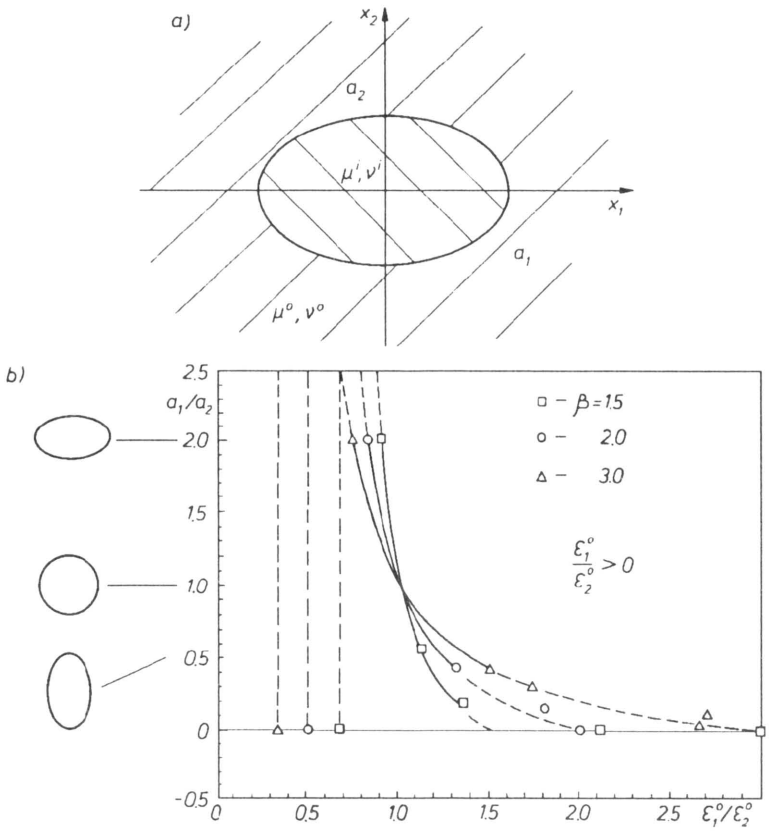

FIG. 2. a) Equilibrium shape for $\det(\varepsilon_{ij}) < 0$. b) Ellipse aspect ratio vs. ratio of principal transformation strains.

the ratio of the latter, and therefore Figs. 2, 3 depict aspect ratios against the ratio of principal strains. Furthermore, the inclusion material is taken to be isotropic, having a shear modulus μ^i and a Poisson's ratio ν^i.

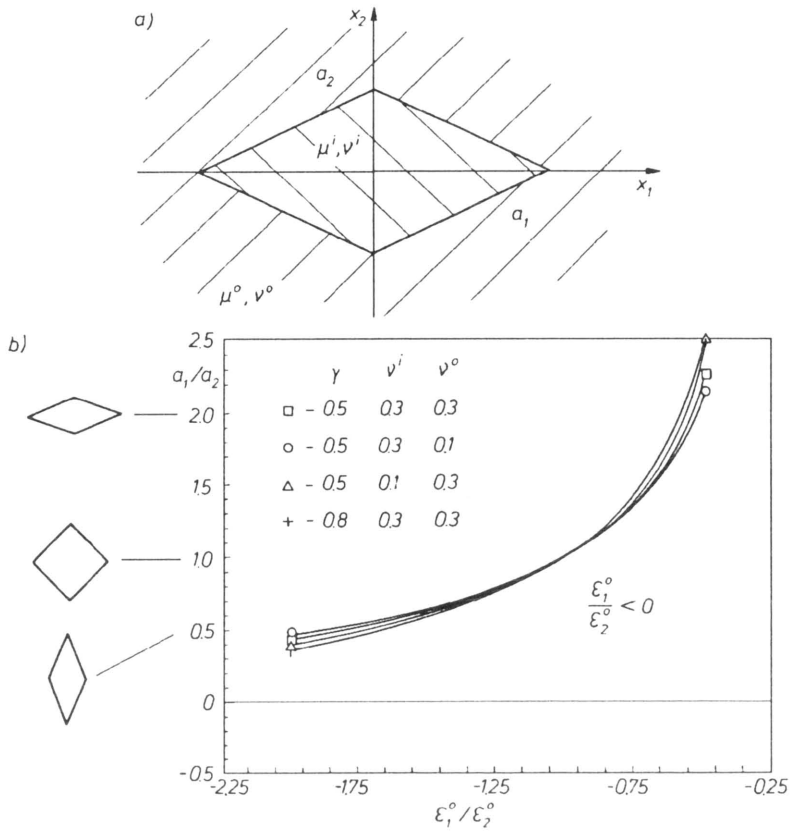

FIG. 3. a) Equilibrium shape for $\det(\varepsilon_{ij}) < 0$. b) Rhombohedron-aspect ratio vs. ratio of principal transformation strains.

If also the matrix material is isotropic, then an ellipse is an equilibrium shape, if its principal axes coincide with the principal directions of ε_{ij}^0 (Fig. 2a). As was shown by ROITBURD [3], the aspect ratio of the ellipse (which completely characterizes the shape) is given by

$$\frac{a_1}{a_2} = \frac{\beta - \varepsilon_1^0/\varepsilon_2^0}{\beta\varepsilon_1^0/\varepsilon_2^0 - 1} \qquad \text{where} \qquad \beta = \frac{1 - \nu^i\gamma}{(1 - \nu^i)\gamma}, \qquad \gamma = \frac{\mu^o}{\mu^i}.$$

This serves as a test for the numerical procedure: In Fig. 2b the dashed lines are the exact results, whereas solid lines show our numerical results. The vertical lines indicate the beginning of the interval for which equilibrium ellipses are possible (because $a_1/a_2 > 0$, it follows that $1/\beta < \varepsilon_1^0/\varepsilon_2^0 < \beta$). Ellipses were found regardless of the starting shape, which indicates that they are unique solutions representing a global minimum.

Qualitatively different results are obtained for $\varepsilon_1^0/\varepsilon_2^0 < 0$, that is, if the determinant of the eigenstrain tensor is negative (for example pure shear). In that case the equilibrium shape develops sharp corners and turns out to be a rhombohedron, the principal axes of which again are identical to the coordinate axes (Fig. 3a). Here the dependence of the aspect ratio on the material parameters is not so pronounced and the curves roughly follow $\varepsilon_2^0/\varepsilon_1^0$ (Fig,3b). Regardless of any material parameters, the curves pass through $a_1/a_2 = 1$ for $\varepsilon_1^0/\varepsilon_2^0 = -1$, i.e for a transformation strain which is a pure shear, the equilibrium shape is a square.

In the case of an orthotropic matrix material and $\varepsilon_1^0/\varepsilon_2^0 > 0$, the equilibrium shape is no longer an ellipse (Fig. 4): for dilatational eigenstrains the result is a "flattened" circle. The curvature of this contour has a minimum at points,

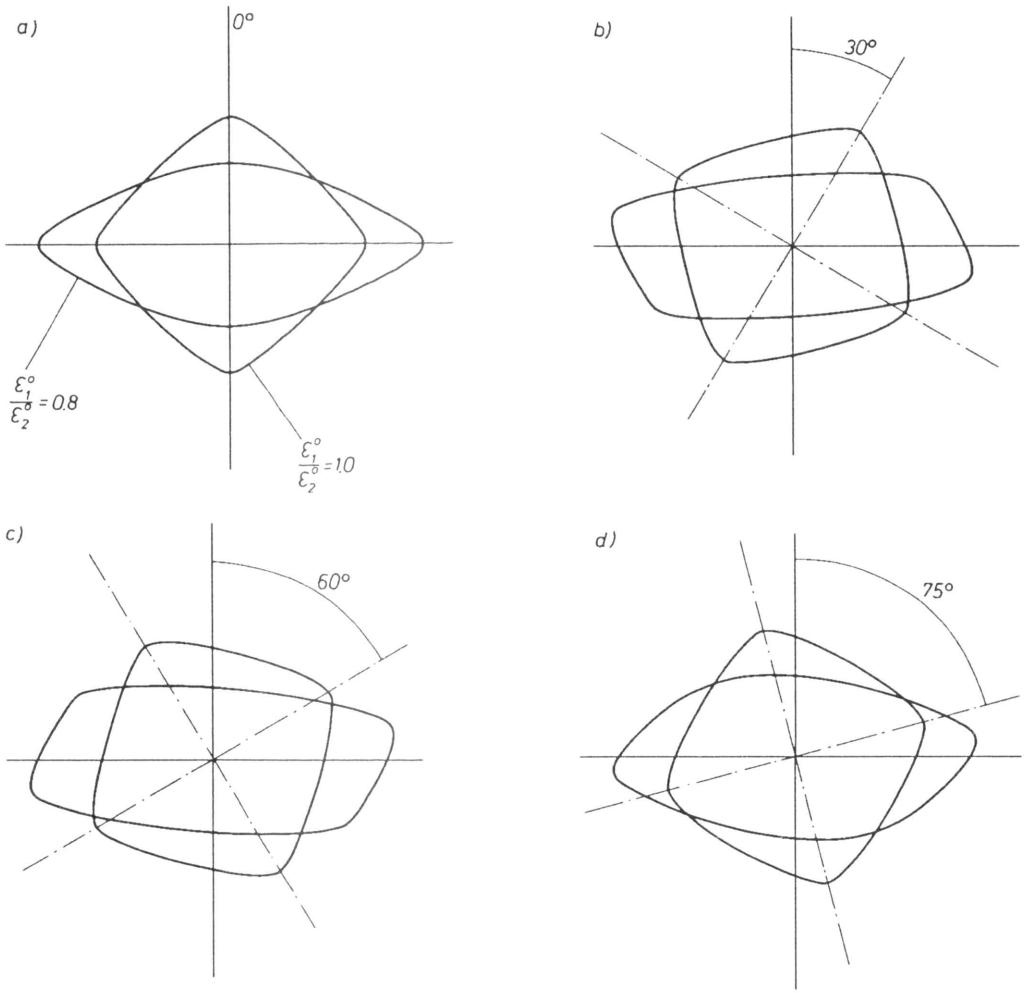

FIG. 4. Equilibrium shapes for rotated matrix anisotropy.

where its tangent coincides with the direction, in which the matrix material exhibits a minimum in Young's modulus. Conversely, points of maximum curvature correspond to directions of maximum Young's modulus. The degree of anisotropy is taken to be $A = 2c_{44}/(c_{11} - c_{22}) = 0.6$, and $\mu^{in}/c_{44} = 1.7$.

Apart from the principal directions of the matrix material for non-dilatational eigenstrains, a second characteristic direction, namely that of the principal axes of ε^0_{ij}, enters the problem. Therefore the result depends of course on the angle between the two. Figure 4 shows the equilibrium shapes for rotated matrix anisotropy and two different values of $\varepsilon^0_1/\varepsilon^0_2$. Apparently the shapes for non-dilatational eigenstrains can be obtained from that for the dilatational eigenstrains, by simply stretching (shrinking) the coordinate axes (i.e. an area-conserving transformation $x' = xg$, $y' = y/g$). The same is true for all the other results shown here: ellipses can be obtained from a circle in that way, as well as rhombohedrons can from a square.

Surprisingly, the matrix anisotropy does not change the type of equilibrium shape for $\varepsilon^0_1/\varepsilon^0_2 < 0$. The result is still a rhombohedron and, consequently, its aspect ratio is completely independent of the anisotropy direction.

For a matrix material of complete anisotropy, the equilibrium shape loses its four-fold symmetry (but retains point symmetry). Again the aforementioned connexion between curvature and Young's modulus can be obsereved (Fig. 5). But this time the two directions of maximum Young's moduli are not perpendicular to each other, and curvature – as well as maxima/minima of the Young's modulus – have different values.

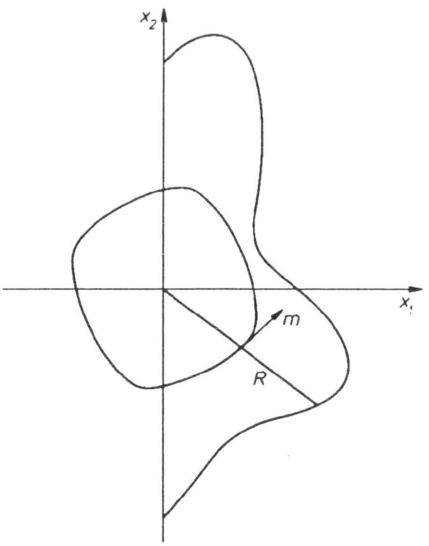

FIG. 5. Variation of Young's modulus and equilibrium shape for dilatational eigenstrains and completely anisotropic matrix material. (R is Young's modulus of the matrix material in direction m).

8. Conclusions

A strategy for determining the equilibrium shapes of inclusions has been presented, using a generally valid expression for the elastic driving force. It is applicable for 3D inhomogeneous inclusions with arbitrary anisotropy of both the matrix and the inclusion material.

Equi-axial (i.e. not plate-like) equilibrium shapes are possible without taking into account interfacial energy. Apart from the material parameters, they depend only on the ratio of the principal values of the transformation strain tensor. Two different types of equilibrium shapes have been found: One is ellipse-like (having neither sharp corners nor flat sides) and appears for $\det(\varepsilon_{ij}) > 0$, that is, if the transformation shear is in some sense smaller than the stretch: $\varepsilon_{xy}^2 < \varepsilon_x \varepsilon_y$. The other type is a rhombohedron, occuring for $\det(\varepsilon_{ij}) < 0$. To our knowledge, this is a new result. For dilatational eigenstrains the curvature of the contour seems to be a monotonic function of Young's modulus in the direction tangential to the contour in that point. This makes sense, because in that case the matrix experiences essentially a stretching in direction of the tangent to the contour. Therefore it is energetically favourable for the contour to "pass very quickly" through an area, where its tangent is close to a direction of maximum Young's modulus of the matrix material. This is achieved by increasing the curvature in that area. Equilibrium shapes for non-dilatational eigenstrains can be obtained by simply stretching/shrinking the shape for the dilatational ones, which does not qualitatively change the type of the shape.

Appendix

A.1

Let $\mathcal{D}$ and $\mathcal{B}$ be the space occupied by the matrix and the inclusion material, respectively. Then the elastic strain energy of the system is

$$\begin{aligned} \Pi &= \frac{1}{2} \int_{\mathcal{D}+\mathcal{B}} \sigma_{ij} \varepsilon_{ij}^{\mathrm{el}} dV \\ &= \frac{1}{2} \int_{\mathcal{D}} \sigma_{ij} u_{i,j} dV + \frac{1}{2} \int_{\mathcal{B}} \sigma_{ij} (u_{i,j} - \varepsilon_{ij}^0) dV \\ &= \frac{1}{2} \int_{\mathcal{D}+\mathcal{B}} \sigma_{ij} u_{i,j} dV - \frac{1}{2} \int_{\mathcal{B}} \sigma_{ij} \varepsilon_{ij}^0 dV. \end{aligned}$$

Integrating by parts, the first integral becomes:

$$\frac{1}{2} \int_{\mathcal{D}+\mathcal{B}} \sigma_{ij,j} u_i \, dV + \frac{1}{2} \int_{\partial(\mathcal{D}+\mathcal{B})} \sigma_{ij} n_j u_i \, dV = 0 + 0.$$

Thus

$$\Pi = -\frac{1}{2}\varepsilon^0_{ij}\int_{\mathcal{B}}\sigma_{ij}\,dV.$$

A.2

Inserting Hooke's law (2.2),(2.3) into (3.2) gives

$$\begin{aligned}[\![\sigma_{ij}]\!]n_j &= (\sigma^{\text{out}}_{ij} - \sigma^{\text{in}}_{ij})n_j \\ &= \{C^{\text{out}}_{ijkl}(u^{\text{in}}_{k,l} + [\![u_{k,l}]\!]) - C^{\text{in}}_{ijkl}(u^{\text{in}}_{k,l} - \varepsilon^0_{kl})\}n_j \\ &= \{[\![C_{ijkl}]\!]u^{\text{in}}_{k,l} + C^{\text{in}}_{ijkl}\varepsilon^0_{kl} + C^{\text{out}}_{ijkl}[\![u_{k,l}]\!]\}n_j = 0.\end{aligned}$$

Using (3.3) this becomes

$$\Omega_{ik}\gamma_k = \{[\![C_{ijkl}]\!]u^{\text{in}}_{k,l} + C^{\text{in}}_{ijkl}\varepsilon^0_{kl}\}n_j\,,$$

where

$$\Omega_{ik}(\mathbf{n}) = C^{\text{out}}_{ijkl}n_j n_l\,.$$

This is a set of algebraic equations to determine γ_i.

References

1. F.R.N. NABARRO, *The influence of elastic strain on the shape of particles segregating in alloys*, Proc. Phys. Soc. London, **52**, 1940.
2. A.G. KHACHATURYAN and V.N. HAIRAPETYAN, *Theory of structural phase transformations in solids*, Wiley, New York 1983.
3. I.M. KAGANOVA and A.L. ROITBURD, *Equilibrium between elastically interacting phases*, Sov. Phys. JETP, **67**, 6, 1988.
4. I.M. KAGANOVA and A.L. ROITBURD, *An anisotropic crystalline inclusion in an isotropic matrix*, Sov. Phys. Crystallogr., **34**, 5, 1989.
5. W.C. JOHNSON and J.W. CAHN, *Elastically induced shape bifurcations of inclusions*, Acta Met. Mat., **32**, 11, 1984.
6. W.C. JOHNSON and P.W. VOORHEES, Solid St. Phenomena, **23**, 87, 1992.
7. P.W. VOORHEES, G.B. MCFADDEN and W.C. JOHNSON, *On the morphological developement of second-phase particles in elastically stressed solids*, Acta Met. Mat., **40**, 11, 1992.
8. T. MURA, *Micromechanics of defects in solids*, Martinus Nijhoff, Dordrecht 1987.
9. J.D. ESHELBY, *Energy relations and the energy-momentum tensor in continuum mechanics*, Inelastic Behaviour of Solids, McGraw-Hill, 1970.
10. J. RIZZO and D.J. SHIPPY, *A formulation and solution procedure for the general non homogeneous elastic inclusion problem*, Int. J. Solids Structures, **4**, 1968.
11. F.J. RIZZO and D.J. SHIPPY, *A method for stress determination in plane anisotropic elastic bodies*, J. Composite Materials, **4**, 1970.

INSTITUT FUER MECHANIK, TH DARMSTADT, GERMANY.

Received November 15, 1994.

Arch. Mech., 47, 2, pp. 391–403, Warszawa 1995

Some numerical results for a viscoplastic softening problem (*)

I. SULICIU (BUCHAREST)

Dedicated to Morton E. Gurtin
on the occasion of his sixtieth birthday

WE ANALYZE the possibility to model strain localization by a Sokolovskii - Malvern type viscoplastic constitutive equation with a quasi-static curve which is descending on its last part. A stable and accurate numerical scheme is used in a program which can automatically switch from a dynamic to a quasi-static solution if necessary. The dependence of the strain localization on the applied (relatively small) engineering strain rate and on a material parameter called dynamic factor is studied. It is found that for large dynamic factor and/or small engineering strain rate, the descending part of the stress-strain relation does not appear at all.

1. Introduction

WE DISCUSS in this paper the possibility to describe the strain localization by means of a viscoplastic constitutive equation of Sokolovskii - Malvern type [1–3] which has along the quasi-static curve, a portion (usually the final one) of negative slope. We shall focus our attention here on a one-dimensional problem of a bar subjected to a process of deformation which is usually met in a strain-controlled experiment. Thus we shall consider that the bar has one end fixed and the other end is moving with a small constant velocity which will correspond to a global small strain rate thought of being well in the quasi-static range.

As it was shown in [8], the presence of a negative slope on the quasi-static curve together with the presence of inertia in the balance law of momentum may transform a very slow quasi-static process into a dynamic one, leading to very large strains distributed over a very short portion of a bar; this process is called strain localization.

There are discussions if there may exist stress-strain curves with negative slopes and, when they exist, if they have a "real physical meaning". For the existence of such curves with negative slopes we refer the reader to [16, pp. 577–578], where the experimental results of Elam from 1938 are reproduced, and to [7], where the stress-strain loops for Ni-Ti shape memory alloy are presented. We do not discuss here the "real physical meaning" of such curves (as they are allowed by the second law of thermodynamics, for instance), instead we assume that they exist and examine the consequences of such an assumption.

(*) Paper presented at 30th Polish Solid Mechanics Conference, Zakopane, September 5–9, 1994.

The presence of the descending portion on the end of the quasi-static curve of a viscoplastic model is also the main factor for an isothermal strain localization process in other studies (see [19]). The isothermal model discussed in [19] originates in the experimental study of Ludwik (see [16, §4.24]) used also by Prandtl (see [22, ch. 3 §1]) which may also be written as

$$\sigma = \sigma_E(\dot{\varepsilon}_p^m + \dot{\varepsilon}_o),$$

where $\dot{\varepsilon}_p$ is the plastic strain rate and $\dot{\varepsilon}_o$ is a constant which may be thought of as a lower limit for the strain rate at which the curve $\sigma = \dot{\varepsilon}_o \sigma_E(\varepsilon)$ for $\varepsilon > 0$ is obtained. Since the study in [19] is applied to rather large strain rates (being of order of 10^3/sec as those obtained in the experiments [20]), one may take $\dot{\varepsilon}_p^m + \dot{\varepsilon}_o \approx \dot{\varepsilon}_p^m$. Applying the same procedure as SOKOLOVSKII and MALVERN did (see [1–2] and also [22, Ch. 3, §1]), one can easily arrive at a semilinear constitutive equation of the form $(2.1)_3$, as

$$\dot{\varepsilon}_p = \left(\frac{\sigma - \dot{\varepsilon}_o \sigma_E(\varepsilon)}{\sigma_E(\varepsilon)} \right)^{1/m}.$$

In contrast to other studies, here we treat the entire problem as a dynamic problem consisting of a hyperbolic system of equations (2.1) to which we add initial-boundary data appropriate to a quasi-static strain-controlled experiment. The viscoplastic constitutive equation makes the stress and strain distribution spatially homogeneous and the particle velocity linear along the bar, after a certain interval of time. That distribution is maintained as long as the strain remains in the stable part of the quasi-static curve. When the strain moves out of the stable interval, depending on the applied strain rate and the magnitude of material parameters of the model, the process becomes again dynamic and a strain localization leading to the decrease of stress (and to the fracture) begins. The computational program we use here switches from the dynamic solution to the quasi-static solution and back to the dynamic one if necessary.

For different theoretical and experimental results referring to strain localization in metals see [17–20], and in geological materials – see [21]. For a relevant discussion on an important number of facts, experimentally put into evidence, which resemble a good part of our numerical experiments, see [17] and also [20].

We do not discuss here the influence of thermomechanical coupling on the strain localization, we refer the interested reader to [17–20] and especially to [18], where a detailed discussion concerning thermal softening and the influence of thermal conductivity for several popular viscoplastic models is given.

2. Preliminaries

We consider a bar which has initially the length L and mass density ϱ. The motion of the bar is governed by a system of partial differential equations re-

sulting from the balance laws of mass, momentum and a semilinear viscoplastic constitutive equations. The system is

$$\frac{\partial \varepsilon}{\partial t} - \frac{\partial v}{\partial X} = 0, \qquad \varrho \frac{\partial v}{\partial t} - \frac{\partial \sigma}{\partial X} = 0, \qquad \frac{\partial \sigma}{\partial t} - E_D \frac{\partial \varepsilon}{\partial t} = G(\varepsilon, \sigma). \tag{2.1}$$

The entries in Eqs. (2.1) have the following meanings: t is time, $X \in [0, L]$ is a spatial coordinate along the bar, the unknown functions are (v, σ, ε) = (particle velocity, stress, strain), $E_D > 0$ is the dynamic Young's modulus and $G(\varepsilon, \sigma)$ is a relaxation function.

We consider here a simple Sokolovskii–Malvern viscoplastic model ([1–2], see also [3] Ch. 2) for $\varepsilon \geq 0$, $\sigma \geq 0$, with a quasi-static curve, $\sigma = \sigma_E(\varepsilon)$ sometimes also called elastic-plastic boundary of the model. The function $G(\varepsilon, \sigma)$ in $(2.1)_3$ has the following form

$$G(\varepsilon, \sigma) = -k \begin{cases} \sigma - \sigma_E(\varepsilon), & \text{if } \sigma \geq \sigma_E(\varepsilon), \quad \varepsilon \geq 0, \\ 0, & \text{if } 0 \leq \sigma \leq \sigma_E(\varepsilon), \quad \varepsilon \geq 0. \end{cases} \tag{2.2}$$

We remind the reader (see also [4]) that a constitutive equation of the form $(2.1)_3$ is called viscoplastic if the set where $G(\varepsilon, \sigma) = 0$ contains a closure of an open set, and it is termed viscoelastic if that set is a single curve of the form $\sigma = \sigma_E(\varepsilon)$ (say). Notice the similarity and the difference between this viscoplastic model $(2.1)_3$+(2.2) and the viscoelastic one given by the same constitutive equation $(2.1)_3$, but with

$$G(\varepsilon, \sigma) = G_v(\varepsilon, \sigma) = -k(\sigma - \sigma_E(\varepsilon)) \tag{2.3}$$

used to describe the pseudoelastic behavior of shape memory alloys (see [5, 6] and the references given there).

For the sake of simplicity we assume here that the function $\sigma_E(\varepsilon)$ is of the following simplified form

$$\sigma_E(\varepsilon) = \begin{cases} E\varepsilon & \text{for } 0 \leq \varepsilon \leq \varepsilon_Y = \sigma_Y / E, \\ \sigma_Y - M(\varepsilon - \varepsilon_Y) & \text{for } \varepsilon_Y \leq \varepsilon. \end{cases} \tag{2.4}$$

with $0 < E < E_D$ and $M > 0$. In other words, we may say that the quasi-static curve is linear elastic (with the static Young's modulus E) up to the yield point $(\varepsilon_Y, \sigma_Y)$, then it softens, with the slope M for strains exceeding the yield value. We use (2.4) for illustrative purpose only, however it may be of some practical use in modelling incomplete phase transformations in Fe-based shape memory alloys of the type discussed in [7]. It seems that that material, in a certain temperature range, may break long before the entire specimen has passed from austenitic to martensitic phase.

To the system (2.1) with $G(\varepsilon, \sigma)$ given by (2.2) and $\sigma_E(\varepsilon)$ given by (2.4) we add the initial-boundary data

$$\begin{aligned} (v, \sigma, \varepsilon)(X, 0) &= (v_o, \sigma_o, \varepsilon_o)(X), \qquad X \in [0, L], \\ v(0, t) &= 0, \qquad v(L, t) = v^L(t), \qquad t \geq 0 \end{aligned} \tag{2.5}$$

to get a well-posed initial-boundary value problem for this system.

We remind that a problem is well-posed in the sense of Hadamard if: 1) it has a solution, 2) the existing solution is unique, and 3) it is stable in the sense that it depends continuously on the input data.

Since the curve $(\varepsilon, \sigma = \sigma_E(\varepsilon))$ given by (2.4) has a negative slope for $\varepsilon > \varepsilon_Y$, the solution of the initial-boundary value problem (2.1)+(2.2)+(2.4–2.5) may not be asymptotically stable. This is the mathematical fact which will allow us to describe at least qualitatively (due to the simplicity of the constitutive equation) the known phenomenon of strain localization.

The proof of the above assertion follows from the Fourier's analysis, in the same way as it was done in [8] for the viscoelastic model. Indeed, taking $v^L(t) \equiv 0$ in (2.5) and the initial data such that

$$\varepsilon_Y < \varepsilon_o(X), \qquad \sigma_E(\varepsilon_o(X)) < \sigma_o(X), \qquad X \in [0, L], \tag{2.6}$$

the problem (2.1)+(2.2)+(2.4–2.5) becomes linear in a time interval, i.e., as long as $\sigma(X,t) > \sigma_E(\varepsilon(X,t))$ and we can apply Fourier's method to solve that problem. For arbitrary initial data in (2.5) and verifying (2.6), the solution in strain will contain terms of the form

$$\begin{gathered} \sum_n A_n e^{\lambda_n t} \cos(\alpha_n X), \\ 0 < \lambda_1 < \ldots < \lambda_n < \cdot < \lambda_\infty = \frac{kM}{E_D}, \qquad \alpha_n \propto n\pi/L \end{gathered} \tag{2.7}$$

and thus if not all $A_n = 0$ (see [8] for a detailed discussion in a similar context), then we may get strain localization. The material constant λ_∞ was called in [6] "dynamic factor" since there its increase led to a more pronounced local dynamic behaviour during the phase transition. Here we expect that the increase of λ_∞ will lead to a faster and sharper strain localization. One purpose of this work is to test numerically the validity of this possibility.

In the class of the solutions of the problem (2.1)+(2.2)+(2.4–2.5) we have the quasi-static solution

$$\begin{aligned} v(X,t) &= \dot{\varepsilon}_e X, \quad \varepsilon(X,t) = \varepsilon_e(t) = \dot{\varepsilon}_e t, \\ \sigma(X,t) &= \overline{\sigma}(t), \qquad \dot{\varepsilon}_e = \text{const.} > 0, \end{aligned} \tag{2.8}$$

where $\overline{\sigma}$ is determined in our case, as the solution of

$$\dot{\overline{\sigma}} - E_D \dot{\varepsilon}_e = G(\dot{\varepsilon}_e t, \overline{\sigma}) = -k(\overline{\sigma} - \sigma_E(\dot{\varepsilon}_e t)), \qquad \overline{\sigma}(0) = 0. \tag{2.9}$$

Here ε_e is the engineering strain defined as the ratio of the actual length $\ell(t)$ of the bar by its initial value L minus one, and $\dot{\varepsilon}_e$ is the engineering strain rate. The curve $(\dot{\varepsilon}_e t, \overline{\sigma}(t))$, $t \geq 0$ almost coincides with $\sigma = \sigma_E(\varepsilon)$ for small $\dot{\varepsilon}_e$ when plotted on the same graph.

If the initial data in (2.5) are small deviations from $(0,0,0)$ and $v^L(t) = \dot{\varepsilon}_e L$ with $\dot{\varepsilon}_e$ small enough, then one can show both theoretically (see [8]) and numerically (see [5, 6, 9, 10] for numerical experiments related to the present ones) that the solution of the problem (2.1)+(2.2)+(2.4–2.5) tends in time to the quasi-static solution (2.8) for t large enough but smaller than $t_Y = \varepsilon_Y / \dot{\varepsilon}_e$. For strains $\varepsilon(X,t)$ exceeding ε_Y, the solution (2.8) looses its asymptotical stability and very small deviations from its spatially homogeneous form may lead to strain localization.

Numerically, in a slow process which starts well below the yield point, we may get sometimes the homogeneous solution (2.8), but most of the time we get localization (for large λ_∞) even due to the computer rounding of variables, which makes the computed solution deviate from (2.8) for $\varepsilon(t) > \varepsilon_Y$. In order to get boundary data $v^L(t)$ closer to a strain-controlled laboratory experiment we take it as a slight variation in time (about 0.1%) around a constant $\dot{\varepsilon}_e L$ (see next section). In this way the quasi-static solution (2.8) is no longer obtained for larger λ_∞.

The viscoplastic constitutive equation (2.1)+(2.2)+(2.4) may be thought of as a regularization of the rate-independent plastic constitutive equation

$$\dot{\sigma} = \begin{cases} E_D\,\dot{\varepsilon} & \text{if} \quad \begin{cases} 0 < \sigma < \sigma_E(\varepsilon), & 0 < \varepsilon < \varepsilon_M, \\ \text{or} \\ \sigma = \sigma_E(\varepsilon) \text{ and } \dot{\varepsilon} \leq 0 \end{cases} \\ \sigma'_E(\varepsilon)\,\dot{\varepsilon} & \text{if} \quad \sigma = \sigma_E(\varepsilon) \text{ and } \dot{\varepsilon} > 0, \end{cases} \tag{2.10}$$

where

$$\varepsilon_M = \left(1 + \frac{E}{M}\right)\varepsilon_Y, \qquad \sigma'_E(\varepsilon) = \begin{cases} E & \text{if } \varepsilon \in [0, \varepsilon_Y], \\ -M & \text{if } \varepsilon \in (\varepsilon_Y, \varepsilon_M). \end{cases} \tag{2.11}$$

We have restricted our discussion to the strain interval $[0, \varepsilon_M]$ with $\sigma_E(\varepsilon_M) = 0$, for obvious reasons.

If we restrict our initial data (2.5) so that

$$0 \leq \varepsilon_o(X) \leq \varepsilon_M, \qquad 0 \leq \sigma_o(X) \leq \sigma_E(\varepsilon_o(X)), \qquad X \in [0, L], \tag{2.12}$$

i.e., so that the initial data are in the elastic domain or on the plastic boundary of the rate-independent model, then the same input data can be used for both the rate-dependent problem (2.1)+(2.2)+(2.4–2.5)+(2.12) and rate-independent one $(2.1)_{1,2}$+(2.10)+(2.5)+(2.12), and the two solutions can be compared in energy [13], whenever the rate-independent one exists. For the rate-independent problem $(2.1)_{1,2}$+(2.10)+(2.5)+(2.12) one can show that there are initial data verifying (2.12) and $\varepsilon_o(X) > \varepsilon_Y$ such that any of the three conditions of the well-posedness of the problem in the sense of Hadamard is violated (see also [8]).

As mentioned before, the rate-dependent model leads to well-posedness of the initial-boundary value problem, but the solution is no longer asymptotically

stable over the whole strain interval. This loss of stability is more pronounced for higher dynamic factor $\lambda_\infty = kM/E_D$. In order to be sure we get a stable and accurate numerical scheme which is able to catch the above loss of stability, we have performed an energetic study of the method of characteristics for both the first and second approximation.

As a requirement of the second law of thermodynamics we build a free energy [4], then use that free energy together with the balance laws and constitutive equation to construct an energy identity and a total energy function [11]. These results are then used to obtain different estimates of the behaviour of the solution in rate-type viscoelasticity with monotone equilibrium curve [11] or non-monotone equilibrium curve [12], or in rate-type viscoplasticity with monotone or non-monotone "quasi-static curve" [13]. For an isolated body problem [11–13], one simple property equivalent to the second law of thermodynamics is that the total energy cannot increase in time. As a stability criterion for the numerical method of characteristics when applied to an isolated body problem, it was required that an appropriate discrete form of the total energy should verify the same non-increasing property [5, 14]. As a result we get here that the first approximation of the numerical method of characteristics is stable if and only if the time integration step h verifies the inequality

$$h \leq h'_m = \frac{2}{k}, \tag{2.13}$$

and a sufficient condition for the stability of the second approximation is

$$h \leq h''_m = \frac{2}{k} \frac{E_D}{E_D + M}, \tag{2.14}$$

which in fact are the same restrictions on the time integration steps as those obtained in [5].

We should point out again that the above conclusions are drawn for isolated body problems, but as before [5, 14] they are to be taken into consideration for non-isolated body problems as our problem is (since $v^L(t)$ is taken here most of the time as $\dot{\varepsilon}_e L$), since their violation leads to numerical instabilities. The accuracy of the numerical scheme may be tested as in [5] and in the following numerical experiments the necessary steps are taken into account.

3. Numerical experiments

As we mentioned before, we do not propose here a specific model which can describe the behaviour of a given material, we rather want to study the influence of an existing negative slope on the quasi-static curve in a viscoplastic constitutive equation of Sokolovskii–Malvern type [1–3]. Therefore we shall take as an example the numerical entries of a Cu-Zn-Al alloy as in [6, 15] but assuming

that the martensitic phase cannot be reached before the material breaks. Thus we put

$$\begin{aligned} &\varrho = 3.1 \times 10^3 \text{ Kg/m}^3, \qquad E = 11.7 \text{ GPa}, \qquad E_D = 20 \text{ GPa}, \\ &M = 0.6 \text{ GPa}, \qquad \varepsilon_Y = 0.01, \qquad L = 22 \text{ mm}, \qquad \varepsilon_2 = 0.2. \end{aligned} \tag{3.1}$$

Here ε_2 has the meaning of a maximum local strain which is reached by the specimen before the program which plots $\varepsilon = \varepsilon(X,t)$ is stopped.

We know from the remarks in the previous section that the material parameter λ_∞ defined in (2.7) may play an important role in the way the strain localization phenomenon takes place. We shall vary it over several orders of magnitude by varying the Maxwell's viscosity coefficient k in the interval $[1 \times 10^4,\ 1 \times 10^6]$/sec, but we may keep fixed the material parameters in the list (3.1).

Since we want to simulate a strain-controlled experiment with an engineering strain rate $\dot{\varepsilon}_e$ in the quasi-static range, we take the initial-boundary data in (2.5) as

$$\begin{aligned} &(v_o, \sigma_o, \varepsilon_o)(X) = (0,0,0), \qquad X \in [0, L], \\ &v^L(t) = \dot{\varepsilon}_e L(1 + 0.001 \times \sin(Ct)), \qquad \dot{\varepsilon}_e \in [1 \times 10^{-3}, 50]/\text{sec}, \end{aligned} \tag{3.2}$$

where $C = \sqrt{E_D/\varrho}$ is the sound speed. The above small deviation from a constant strain rate is intended to simulate the fact that a perfectly constant end velocity of the specimen is not usually realized. As we shall see, this fact will play an important role in strain localization, especially for large λ_∞.

We treat our problem dynamically, i.e., we do not neglect the accelerations even when $\dot{\varepsilon}_e$ is very small. We do that in order to be able to catch the non-homogeneous strain distribution, the strain concentration and localization, when they occur.

Due to the fact that the model is viscoplastic the "impact" problem (3.2) is transformed, for large k and small $\dot{\varepsilon}_e$, into a quasi-static one and its solution tends to the spatially homogeneous solution (2.8) as long as $\varepsilon(X,t) \in [0, \varepsilon_Y)$. We take into account this property in our numerical integration scheme (see also [6]) to switch back and forth, as appropriate, from a dynamic to a quasi-static solution. We treat the problem dynamically if the strain ε_i at one net point X_i, $i = 0, \ldots, N$ exceeds ε_Y or the stress variation $\sum_0^{N-1} |\sigma_{i+1} - \sigma_i|$ exceeds a certain given value, otherwise we use the quasi-static solution (2.8).

In Figs. 1, 2, 3 we plot stress-strain relations for different engineering strain rates $\dot{\varepsilon}_e$ for $\lambda_\infty = 3 \times 10^4$/sec, 3×10^3/sec, 3×10^2/sec. We plot here the local stress-strain relations $\sigma(0,t) \sim \varepsilon(0,t)$ and $\sigma(L,t) \sim \varepsilon(L,t)$, as well as the stress at $X = L$ versus engineering strain, i.e., $\sigma(L,t) \sim \varepsilon_e(t)$. The part of the stress-strain relation for t in the interval $[0, t_Y = \varepsilon_Y/\dot{\varepsilon}_e]$ practically coincides with the quasi-static curve $\sigma = \sigma_E(\varepsilon) = E\varepsilon$, $\varepsilon \in [0, \varepsilon_Y]$ even for $\varepsilon_e = 50$/sec of Fig. 1 or $\dot{\varepsilon}_e = 5$/sec of Fig. 3. When $\varepsilon_e(t)$ exceeds ε_Y, a fast process of strain

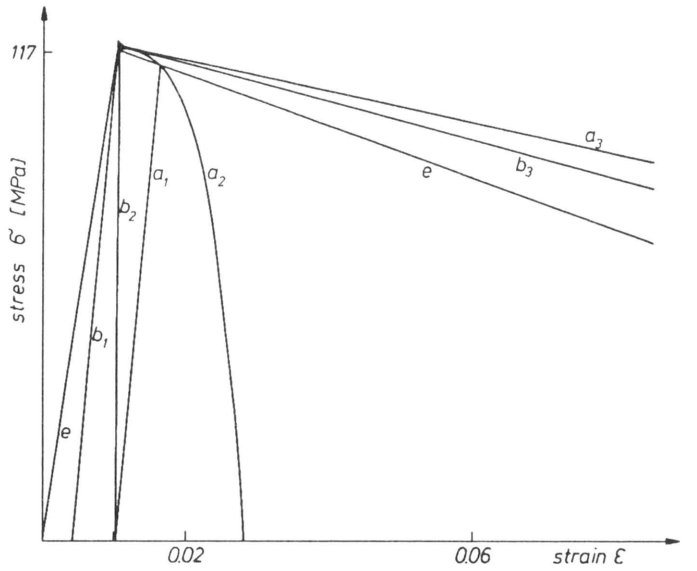

FIG. 1. Stress-strain curves for $k = 1 \times 10^6$/sec and different engineering strain rates $\dot{\varepsilon}_e$.
$M = 6 \times 10^8$ Pa, $E = 1.17 \times 10^{10}$ Pa, $E_D = 2 \times 10^{10}$ Pa, $\varepsilon_Y = 0.01$; $e : \sigma = \sigma_E(\varepsilon)$,
for $\dot{\varepsilon}_e = 0.5$/sec — $b_1 : \sigma \div \varepsilon$ at $X = 0$, $b_2 : \sigma \div \varepsilon_e$, $b_3 : \sigma \div \varepsilon$ at $X = L$;
for $\dot{\varepsilon}_e = 50$/sec — $a_1 : \sigma \div \varepsilon$ at $X = 0$, $a_2 : \sigma \div \varepsilon_e$, $a_3 : \sigma \div \varepsilon$ at $X = L$.

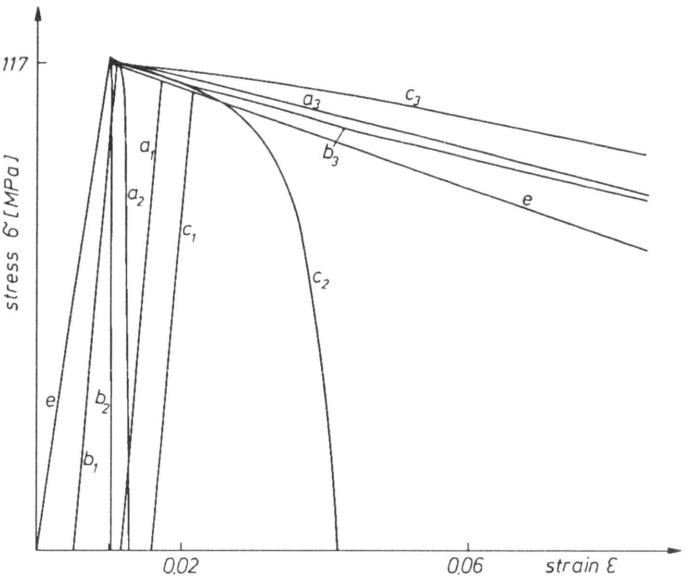

FIG. 2. Stress-strain curves for $k = 1 \times 10^5$/sec and different engineering strain rates $\dot{\varepsilon}_e$.
$M = 6 \times 10^8$ Pa, $E = 1.17 \times 10^{10}$ Pa, $E_D = 2 \times 10^{10}$ Pa, $\varepsilon_Y = 0.01$; $e : \sigma = \sigma_E(\varepsilon)$,
for $\dot{\varepsilon}_e = 0.05$/sec — $b_1 : \sigma \div \varepsilon$ at $X = 0$, $b_2 : \sigma \div \varepsilon_e$, $b_3 : \sigma \div \varepsilon$ at $X = L$;
for $\dot{\varepsilon}_e = 0.5$/sec — $a_1 : \sigma \div \varepsilon$ at $X = 0$, $a_2 : \sigma \div \varepsilon_e$, $a_3 : \sigma \div \varepsilon$ at $X = L$;
for $\dot{\varepsilon}_e = 5$/sec — $c_1 : \sigma \div \varepsilon$ at $X = 0$, $c_2 : \sigma \div \varepsilon_e$, $c_3 : \sigma \div \varepsilon$ at $X = L$.

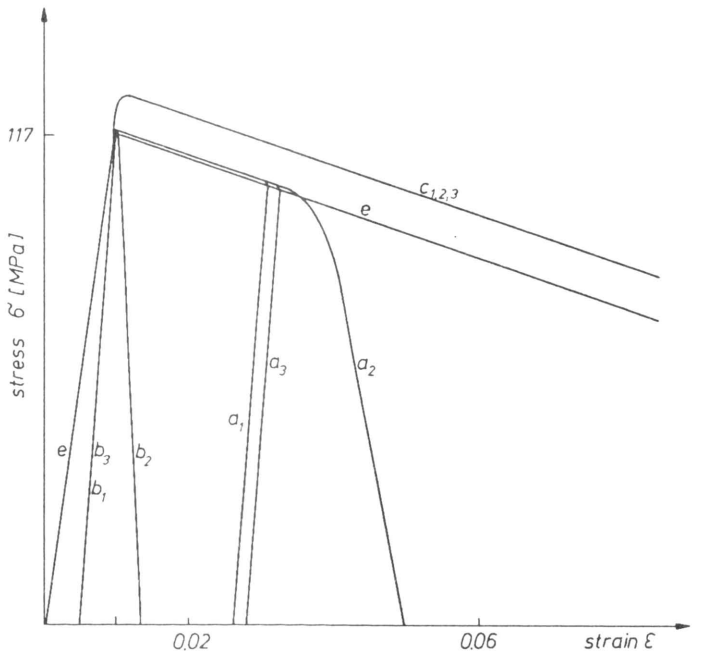

FIG. 3. Stress-strain curves for $k = 1 \times 10^4$/sec and different engineering strain rates $\dot{\varepsilon}_e$.
$M = 6 \times 10^8$ Pa, $E = 1.17 \times 10^{10}$ Pa, $E_D = 2 \times 10^{10}$ Pa, $\varepsilon_Y = 0.01$; $e : \sigma = \sigma_E(\varepsilon)$,
for $\dot{\varepsilon}_e = 0.01$/sec — $b_1 : \sigma \div \varepsilon$ at $X = 0$, $b_2 : \sigma \div \varepsilon_e$, $b_3 : \sigma \div \varepsilon$ at $X = L$;
for $\dot{\varepsilon}_e = 0.5$/sec — $a_1 : \sigma \div \varepsilon$ at $X = 0$, $a_2 : \sigma \div \varepsilon_e$, $a_3 : \sigma \div \varepsilon$ at $X = L$;
for $\dot{\varepsilon}_e = 5$/sec — $c_{1,2,3} : \sigma \div \varepsilon$ at $X = 0$ and $X = L$, $\sigma \div \varepsilon_e$.

localization – depending on the strain rate $\dot{\varepsilon}_e$ and on the viscosity coefficient k – is generated. A small part of the specimen is suffering large and fast deformations, while the rest of the specimen is unloaded (see also Figs. 4 – 7).

In Figs. 4 – 7 we plot strain ε versus distance $X \in [0, L]$ and time t measured in L/C (which is the time necessary for the wave to travel the length L of the specimen). One can see that the Figs. 1, 2, 3 and Figs. 4, 6, 7 correspond to each other in a certain way. Thus in the Fig. 4 we plot the strain distribution in time along the bar for the same strain rate $\dot{\varepsilon}_e = 50$/sec as are the stress-strain relations a_1, a_2, a_3 of Fig. 1. The same kind of relations between the Fig. 2 $\sim$ Fig. 6 and Fig. 3 $\sim$ Fig. 7 hold.

The Fig. 5 and Fig. 7 are $\varepsilon = \varepsilon(X, t)$ plots at the same engineering strain rate $\dot{\varepsilon}_e = 0.01$, but λ_∞ is by two orders of magnitude larger in Fig. 5 than in Fig. 7. We see that strain becomes more localized with the increase in λ_∞ while the unloading becomes sharper.

Concerning the position along the bar where the strain localization is produced, we did not observe any rules, i.e., it may appear anywhere along the bar. Thus in Fig. 3 the strain localization was produced somewhere inside the bar for both strain rates $\dot{\varepsilon}_e = 0.5$/sec, $\dot{\varepsilon}_e = 0.01$/sec; while for the strain rate

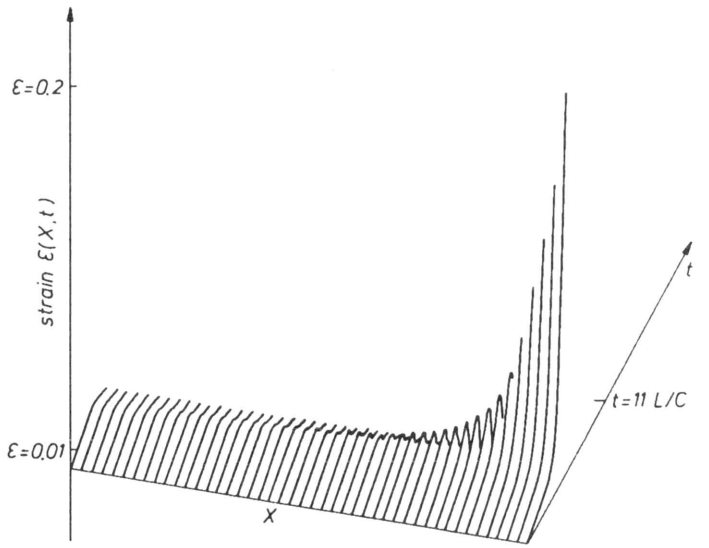

FIG. 4. Strain versus time and distance for $k = 1 \times 10^6$/sec and $\dot{\varepsilon}_e = 50$/sec. $M = 6 \times 10^8$ Pa, $E = 1.17 \times 10^{10}$ Pa, $E_D = 2 \times 10^{10}$ Pa, $\varepsilon_Y = 0.01$, $\varepsilon_e = 0.0199$.

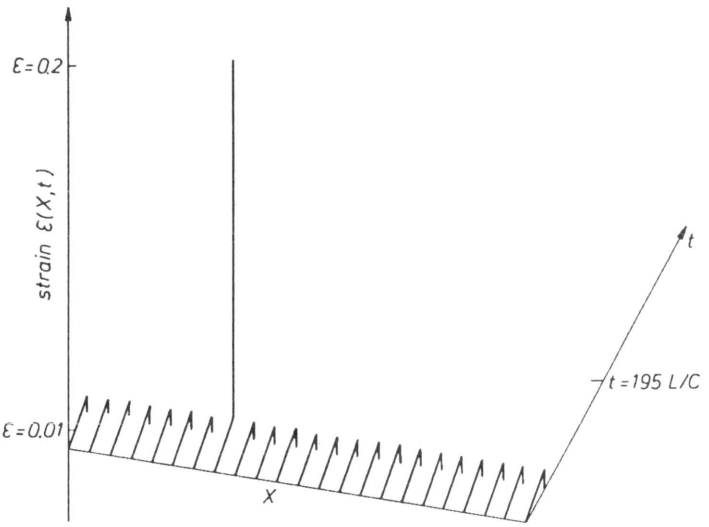

FIG. 5. Strain versus time and distance for $k = 1 \times 10^6$/sec and $\dot{\varepsilon}_e = 0.01$/sec. $M = 6 \times 10^8$ Pa, $E = 1.17 \times 10^{10}$ Pa, $E_D = 2 \times 10^{10}$ Pa, $\varepsilon_Y = 0.01$, $\varepsilon_e = 0.01$.

$\dot{\varepsilon}_e = 5$/sec the bar deformed homogeneously down to zero stress. Figures 1 and 2 show strain localization at $X = L$, while Fig. 7 gives it somewhere in the middle, even if its λ_∞ is the same as in Fig. 1.

We also notice that the Fig. 1 to Fig. 3 show that the increase in k (or λ_∞) has about the same effect on the strain localization as the decrease in the strain

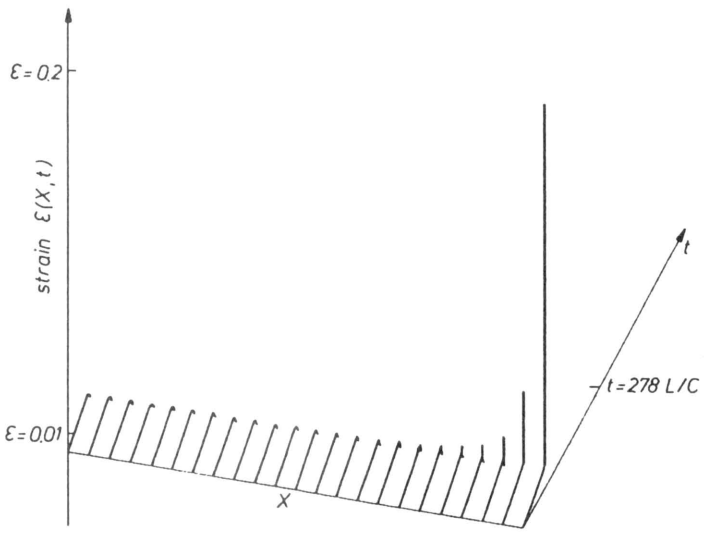

FIG. 6. Strain versus time and distance for $k = 1 \times 10^5$/sec and $\dot{\varepsilon}_e = 0.5$/sec. $M = 6 \times 10^8$ Pa, $E = 1.17 \times 10^{10}$ Pa, $E_D = 2 \times 10^{10}$ Pa, $\varepsilon_Y = 0.01$, $\varepsilon_e = 0.0124$.

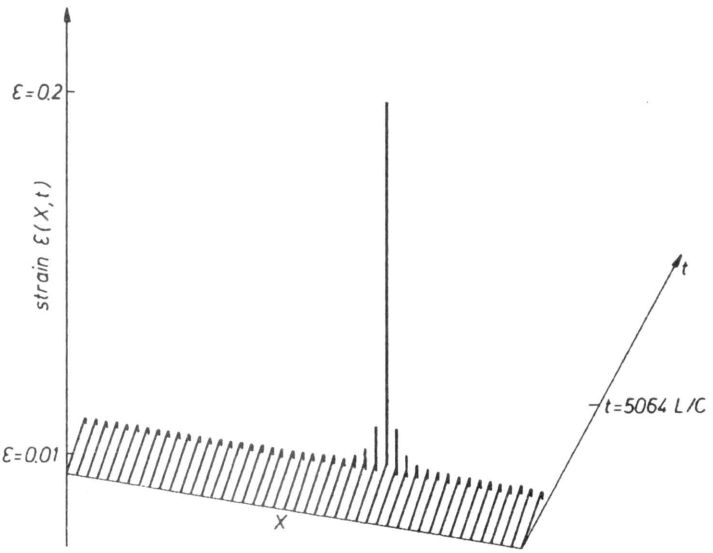

FIG. 7. Strain versus time and distance for $k = 1 \times 10^4$/sec and $\dot{\varepsilon}_e = 0.01$/sec. $M = 6 \times 10^8$ Pa, $E = 1.17 \times 10^{10}$ Pa, $E_D = 2 \times 10^{10}$ Pa, $\varepsilon_Y = 0.01$, $\varepsilon_e = 0.0109$.

rate $\dot{\varepsilon}_e$. One may find a certain kind of justification if one looks closely at the formula (2.7) of the asymptotic growth. Indeed, we may think of the following equivalence of exponential growth

$$\exp(\lambda_n t) \sim \exp(\lambda_\infty t) = \exp\left[(kM/(\dot{\varepsilon}_e E_D))\,\varepsilon_e\right] \tag{3.3}$$

if we take into account formula (2.7) and $(2.8)_2$. Thus for $\varepsilon_e > \varepsilon_Y$ and fixed M and E_D, the exponent in the above formula will increase with the increase of k or decrease of $\dot{\varepsilon}_e$, leading to a more pronounced strain localization.

We also mention that the decrease in strain rate below those shown in Figs. 1–3 for the lines b_1, b_2, b_3 will lead to the same curves, the only difference which may occur is the position of the strain localization.

As an overall conclusion from the numerical experiments shown in Figs. 1–7 one can assert that for k large enough and/or small enough $\dot{\varepsilon}_e$, the existence of the decreasing part at the end of the quasi-static curve $\sigma = \sigma_E(\varepsilon)$ is not observed at all. This observation which comes mainly from the instability properties of the quasi-static curve may explain why in laboratory measurement the descending part of a stress-strain curve is not so often encountered.

References

1. V. V. SOKOLOVSKII, *The propagation of elastic-viscoplastic waves in bars* [in Russian], Dokl. Akad. Nauk SSSR, **60**, pp. 775–778, 1948; Prikl. Mat. Mekh., **12**., pp. 261–280, 1948.
2. L.E. MALVERN, *The propagation of longitudinal waves of plastic deformation in a bar of a material exhibiting a strain rate effect*, J. Appl. Mech., **18**, pp. 203–208, 1951; *Plastic wave propagation in a bar of a material exhibiting a strain rate effect*, Q. Appl. Math., **8**, pp. 405–411, 1951.
3. N. CRISTESCU and I. SULICIU, *Viscoplasticity*, Nijhoff, The Hague 1982.
4. M.E. GURTIN, W.O. WILLIAMS and I. SULICIU, *On rate-type constitutive equations and the energy of viscoelastic and viscoplastic materials*, Int. J. Solids Structures, **16**, pp. 607–617, 1980.
5. M. MIHĂILESCU-SULICIU and I. SULICIU, *Stable numerical solution to a dynamic problem for a softening material*, Mech. Reas. Comm., **20**, pp. 475–480, 1993.
6. C. FĂCIU and I. SULICIU, *A Maxwellian model for pseudoelastic materials*, Scripta Metall., to appear 1994.
7. K. TANAKA, F. NISHIMURA and H. TOBUSHI, *Transformation conditions and subloops in a Fe-based shape memory alloy after incomplete transformations induced by thermomechanical loads*, 30th Polish Solid Mech. Conference, Zakopane, September 5–9, 1994. See also: *Transformation start lines in NiTi and Fe-based shape memory alloys after incomplete transformations induced by mechanical and/or thermal loads*, Mech. Materials, **15**, to appear, 1994.
8. I. SULICIU, *Some stability-instability problems in phase transitions modelled by piece-wise linear elastic or viscoelastic constitutive equations*, Int. J. Engng. Sci., **30**, pp. 483–494, 1992.
9. C. FĂCIU, *Numerical aspects in modelling phase transitions by rate-type constitutive equations*, Int. J. Engng. Sci., **29**, pp. 1103–1119, 1991.
10. C. FĂCIU, *Stress-induced phase transformations in rate-type viscoelasticity*, Journal de Physique IV, **C4**, 101–106, 1991.
11. I. SULICIU, *Some energetic properties of smooth solutions in rate-type viscoelasticity*, Int. J. Non-Linear Mech., **19**, pp. 525–544, 1984.
12. C. FĂCIU and M. MIHĂILESCU-SULICIU, *The energy in one-dimensional rate-type semi-linear viscoelasticity*, Int. J. Solids Structures, **23**, pp. 1505–1520, 1987.
13. I. SULICIU and M. ŞABAC, *Energy estimates in one-dimensional rate-type viscoplasticity*, J. Math. Anal. Appl., **131**, pp. 354–372, 1988.
14. M. MIHĂILESCU-SULICIU and I. SULICIU, *On the method of characteristics in rate-type viscoelasticity with non-monotone equilibrium curve*, ZAMM Z. Angew. Math. Mech., **72**, pp. 667–674, 1992.
15. I. MÜLLER and HUIBIN XU, *On the pseudoelastic hysteresis*, Acta Metall. Mater., **39**, pp. 263–271, 1991.
16. J.F. BELL, *The experimental foundations of solid mechanics*, Handbuch der Physik, Springer-Verlag, 1973.
17. M.K. DUSZEK-PERZYNA and P. PERZYNA, *Adiabatic shear band localization in elastic-plastic single crystals*, Int. J. Solids Structures, **30**, pp. 61–89, 1993.

18. R.C. BATRA and C.H. KIM, *Effect of thermal conductivity on the initiation, growth and bandwidth of adiabatic shear bands*, Int. J. Engng. Sci., **29**, pp. 949–960, 1991.
19. A. MOLINARI and R.J. CLIFTON, *Analytical characterization of shear localization in thermo-viscoplastic materials*, ASME J. Appl. Mech., **54**, pp. 806–812, 1987.
20. A. MARCHAND and J. DUFFY, *An experimental study of the formation process of adiabatic shear bands in a structural steel*, J. Mech. Phys. Solids, **36**, pp. 251–283, 1988.
21. I. VARDOULAKIS, *Potentials and limitations of softening models in geomechanics (The role of second order work)*, Eur. J. Mech., A/Solids, **13**, pp. 195–226, 1994.
22. N. CRISTESCU, *Dynamic plasticity*, North-Holland, Amsterdam 1967.

INSTITUTE OF MATHEMATICS OF THE ROMANIAN ACADEMY, BUCHAREST, ROMANIA.

Received November 4, 1994.

Arch. Mech., 47, 2, pp. 405–413, Warszawa 1995

Density jump variation in the initial stage of the gravity flow of granular materials (*)

J. ZAWIDZKI (WARSZAWA)

THE PAPER deals with some concepts of the density jump variation on the discontinuity surface separating the initial gravity flow region and the dead zone of granular materials. In the main paper dealing with the problem (S.C. COWIN and W.J. COMFORT III, [2]) this jump was assumed to be constant. Two new concepts are presented: the density jump as a linear function of the stress jump, and the density jump resulting from the assumption of a constant propagation speed of the discontinuity surface. It is shown that these two concepts lead to very close results being, however, qualitatively different from those of [2].

1. Introduction

IMMEDIATELY AFTER the opening of the outlet orifice in bins containing granular materials, a flow zone arises and propagates from the bottom of the bin towards the upper free surface of material. This is the first stage of the gravity emptying process. This phenomenon was investigated experimentally by KVAPIL, [1], and then described by means of some empirical formulae bounding the dimensions of the flow zone (assuming its ellipsoidal form) with the dimensions of grains.

COWIN and COMFORT, [2], considered a silo with a flat bottom that suddenly moves downwards. Starting from the conservation laws on an instantaneous horizontal discontinuity plane separating the free fall zone and the region at rest, and assuming a constant density jump, they established formulae for the propagation speed of the discontinuity surface and found a good agreement with the performed experiment. The assumption of the constant density jump was also made in author's paper [3] where an attempt of generalization of this approach on some 2D or 3D cases was done. This assumption has some advantages from the point of view of analytical solutions, however, it is hard to accept that the parts of material close to the upper free surface are subjected to the same density jump as those much more stressed at the bottom of the bin.

In the present paper the density jump is assumed to be variable in the propagation process of the flow zone. Two concepts of the density jump variation will be presented and illustrated on some one-dimensional examples like in [2].

2. Governing equations

Let $\mathbf{n}$ denote a unit vector normal to the discontinuity surface $\mathcal{F}$, $\mathbf{u}$ – the velocity vector of this surface and $\mathbf{v}$ – the velocity of material. The mass and

(*) Paper presented at 30th Polish Solid Mechanics Conference, Zakopane, September 5–9, 1994.

momentum conservation laws, (cf. [4]), are as follows:

$$[\rho(\mathbf{u}-\mathbf{v})]\cdot\mathbf{n}=0, \tag{2.1}$$

$$[\rho\,\mathbf{v}\otimes(\mathbf{u}-\mathbf{v})+\boldsymbol{\sigma}]\cdot\mathbf{n}=\mathbf{0}, \tag{2.2}$$

where ρ denotes the material density, $\boldsymbol{\sigma}$ – the stress tensor, and the square brackets mean jumps of the correspondent quantities. We use the index n to indicate the respective normal components of vectors or tensors, whereas the indices – and + distinguish quantities on the opposite sides of the discontinuity surface and refer to the zone at rest and to the flow zone, respectively.

Because in the region at rest holds $\mathbf{v}_-=\mathbf{0}$, the vectorial equation (2.2) yields the following relation between the particle velocity vector $\mathbf{v}_+$ and the stress vectors $\mathbf{t}^{(n)}$ on both sides of the discontinuity surface,

$$\rho_+\mathbf{v}_+(u^n-v_+^n)=\mathbf{t}_-^{(n)}-\mathbf{t}_+^{(n)}. \tag{2.3}$$

It means that on the boundary between the dead zone and the flow region, the particle velocity is collinear with the jump of the stress vector. In the one-dimensional problem presented below this relation will be satisfied automatically.

The modelling problem for the proposed concepts of the desity jump variation is, like in [2], a propagation process of the discontinuity plane $\mathcal{F}$ in a granular material of the density ρ_o under the gravity acceleration g, contained in a bin with a suddenly released flat bottom as in Fig. 1, where the introduced coordinate system is also shown.

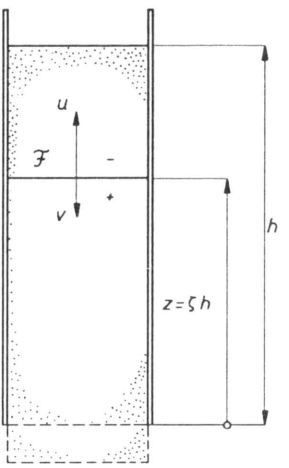

FIG. 1. One-dimensional model of the flow zone propagation process.

The Eqs. (2.1) and (2.2) can be written as:

$$\rho_-(u^z-v_-^z)=\rho_+(u^z-v_+^z), \tag{2.4}$$

$$\rho_-(u^z-v_-^z)v_-^z+\sigma_-^{zz}=\rho_+(u^z-v_+^z)v_+^z+\sigma_+^{zz}. \tag{2.5}$$

In the zone at rest (−) and in the flow region (+), where a jump rarefaction occurs, we have on both sides of the discontinuity surface $\mathcal{F}$ respectively:

$$\rho_- = \rho_o, \qquad v_-^z = 0, \qquad \sigma_-^{zz} \leq 0, \tag{2.6}$$

$$\rho_+ = \delta\rho_o, \qquad v_+^z \neq 0, \qquad \sigma_+^{zz} = 0, \tag{2.7}$$

where $\delta \in (0, 1]$ characterizes the density jump, and the compression stress is assumed to be negative.

We introduce the following dimensionless quantities:

$$\zeta \equiv z/h \qquad \text{(space coordinate)}, \tag{2.8}$$

$$\tau \equiv t\sqrt{g/h} \qquad \text{(time)}, \tag{2.9}$$

$$S_-^{zz} \equiv \sigma_-^{zz}/(\rho_o g h) \qquad \text{(stress)}, \tag{2.10}$$

$$U^z \equiv u^z/\sqrt{gh}\,, \qquad V^z \equiv v^z/\sqrt{gh} \qquad \text{(velocities)}. \tag{2.11}$$

With the above notations, in view of (2.4) and (2.5) we get (cf. [2]):

$$U^z = \sqrt{\frac{\delta}{1-\delta}}\sqrt{-S_-^{zz}}\,, \tag{2.12}$$

and

$$V^z = -\frac{1-\delta}{\delta}U^z\,. \tag{2.13}$$

Note that

$$\frac{d\zeta}{d\tau} = U^z\,. \tag{2.14}$$

$\zeta \in [0, 1]$ being the actual position of the discontinuity plane.

The above formulae for the propagation speed U^z and for the particle velocity V^z will next be discussed for some concepts of the δ parameter variations, with some typical distributions of the vertical stress S_-^{zz}.

3. Stress state in the granular material at rest

As it was emphasized in [2], the stress state in the material at rest determines the discontinuity propagation speed and the material velocity. Therefore we specify here the stress distributions most important from the practical point of view.

The granular material is assumed to be cohesionless and characterized by the angle of internal friction φ.

When the walls of the bin shown in Fig. 1 are perfectly smooth, then the vertical stress distribution is linear:

$$S_{-}^{zz} = -1 + \zeta . \tag{3.1}$$

However, if the granular material is restricted by some vertical rough walls closing the horizontal area A of the perimeter U, then the stress state is described by the silo theory (cf. [3])

$$S_{-}^{zz} = -\zeta_o [1 - \exp[(1 - \zeta)/\zeta_o]] , \tag{3.2}$$

where

$$\zeta_o \equiv \frac{A}{U h \lambda \mu} , \qquad \zeta_o \in (0, \infty). \tag{3.3}$$

In the above formulae $\lambda \in (0, 1]$ means the ratio of the horizontal stress to the vertical stress (with the Koenan assumption $\lambda = (1 - \sin\varphi)/(1 + \sin\varphi)$), and $\mu \in [0, \mathrm{tg}\varphi]$ denotes the friction coefficient between the granular material and the wall.

The limit case $\zeta = \infty$ corresponds to the linear stress distribution given by the formula (3.1). The remaining range of ζ_o describes the so-called "silo behaviour".

In Fig. 2 some stress distribution curves are shown for some range of the silo parameter ζ_o.

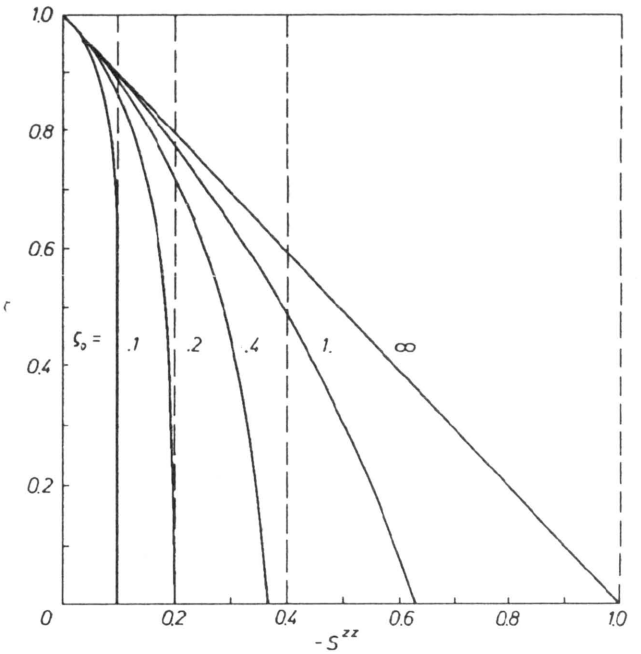

FIG. 2. Typical vertical stress distributions in granular materials.

4. The density jump variation concepts

4.1. Constant density jump (case "a")

For the uniform presentation of all discussed concepts we begin with the idea of COWIN and COMFORT, [2], where they assumed:

$$\delta = \delta_o = \text{const.} \tag{4.1}$$

This value should be put into the formulae (2.12) and (2.13) with the stress given by (3.1) or (3.2).

4.2. Density jump depending on the normal stress component jump (case "b")

Generally, this law can be written as:

$$[\rho] = \mathcal{G}([\sigma^{nn}]). \tag{4.2}$$

In the present subsection, a linear relation between the density jump and the stress jump is proposed:

$$\rho_o(1 - \delta) = C[\sigma^{nn}], \tag{4.3}$$

where C denotes a constant coefficient. It is easy to see that the zero stress jump leads to the incompressible behaviour.

In order to determine the constant C we bound a value of the density jump parameter δ_o with a certain stress jump value (practically with a certain value of the stress itself) that will be called the reference stress jump. It seems to be reasonable to choose the vertical stress $\sigma_-^{zz}\big|_{z=0}$ for granular materials at rest without silo effect as this reference value:

$$[\sigma^{nn}]_{\text{ref}} = \sigma_-^{zz}\Big|_{z=0} = -\rho_o g h. \tag{4.4}$$

Note, that the dimensionless reference stress jump is then

$$[S^{nn}]_{\text{ref}} = -1, \tag{4.5}$$

and represents a bound for all considered stress states (cf. Fig. 2).

Equation (4.3) with $\delta = \delta_o$ and $[\sigma^{nn}]$ given by (4.4) yields the value of the constant C:

$$C = (\delta_o - 1)/gh, \tag{4.6}$$

and the proposed law (4.3) can be written in the dimensionless form:

$$\delta = 1 - (\delta_o - 1)[S^{nn}]. \tag{4.7}$$

In the considered problem of the vertical propagation of the flow zone we have

$$[S^{nn}] = S_-^{zz} \tag{4.8}$$

and the Eq. (4.6) takes the form:

$$\delta = 1 - (\delta_o - 1)S_-^{zz} . \tag{4.9}$$

Note that for the dimensionless stress range $[-1, 0]$, the corresponding range of δ is $[\delta_o, 1]$.

The density ratio δ in the formulae (2.12) and (2.13) should be replaced now by the Eq. (4.9).

4.3. Concept of the constant propagation speed (case "c")

Let us assume that, at the beginning of the propagation process (time $\tau = 0$), the density jump ratio $\delta(0)$ is determined by the stress $S_-^{zz}\Big|_{z=0}$ according to the Eq. (4.9). The initial propagation speed $U_o = U^z_{\tau=0}$ can be calculated now from the Eq. (2.12) as:

$$U_o = \sqrt{\frac{\delta(0)}{1 - \delta(0)}} \sqrt{-S_-^{zz}(0)} . \tag{4.10}$$

Note that this value is the same as the initial value of U^z resulting from the concept "b".

The main feature of the present concept is the assumption that the propagation speed U^z is constant during the whole process,

$$U^z = U_o . \tag{4.11}$$

Such an assumption was made in [6] for the initial stage of a radial flow. However, no general density variation law resulting from this assumption was investigated.

The Eq. (2.12) becomes now the law for the evolution of the density jump ratio δ:

$$U_o = \sqrt{\frac{\delta}{1 - \delta}} \sqrt{-S_-^{zz}} , \tag{4.12}$$

from which we find the explicit expression:

$$\delta = \frac{U_o^2}{U_o^2 - S_-^{zz}} . \tag{4.13}$$

Note that this law is also of the type (4.2) but has the nonlinear form. It is easy to see that for the dimensionless stress range $[-1, 0]$ the corresponding range of δ is

as in the case "b" $[\delta_o, 1]$. The zero stress jump leads again to the incompressible behaviour.

The particle velocity V^z, (2.13), in view of (4.11) and (4.12), can be written as

$$V^z = \frac{S^{zz}}{U_o}. \tag{4.14}$$

5. Comparison of the presented concepts

All the discussed concepts of the density jump variation were tested on several stress distributions specified by the parameters ζ_o from the range $[0.1, \infty]$, (cf. Sec. 3). For the presentation of results the extreme values of this range are chosen: $\zeta_o = .1$ (this value is close to that of the example given in [2]), and $\zeta_o = \infty$ corresponding to the linear stress distribution.

In Fig. 3 the distributions of the density jump ratio δ are shown for some initial values of δ_o from the range [0.85, 0.99].

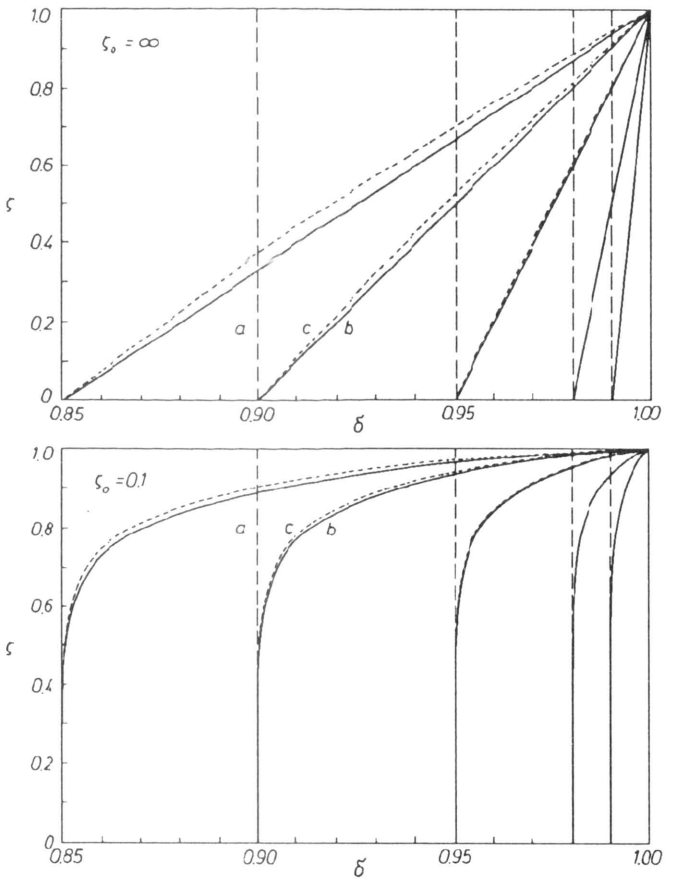

FIG. 3. Concepts of variation of the density jump ratio δ.

It is worth to note that the curves describing the "b" and "c" concepts almost coincide, and in the case $\zeta_o = .1$, in view of the nearly uniform stress distribution in the lower half of the bin, even all the three concepts give there very close results.

In Fig. 4 the distributions of the particle velocities V^z and of the discontinuity propagation speed U^z are shown for two stress state parameters $\zeta_o = .1$ and $\zeta_o = \infty$. For a better visualization of the results, a lowered initial density jump ratio $\delta_o = .8$ is assumed.

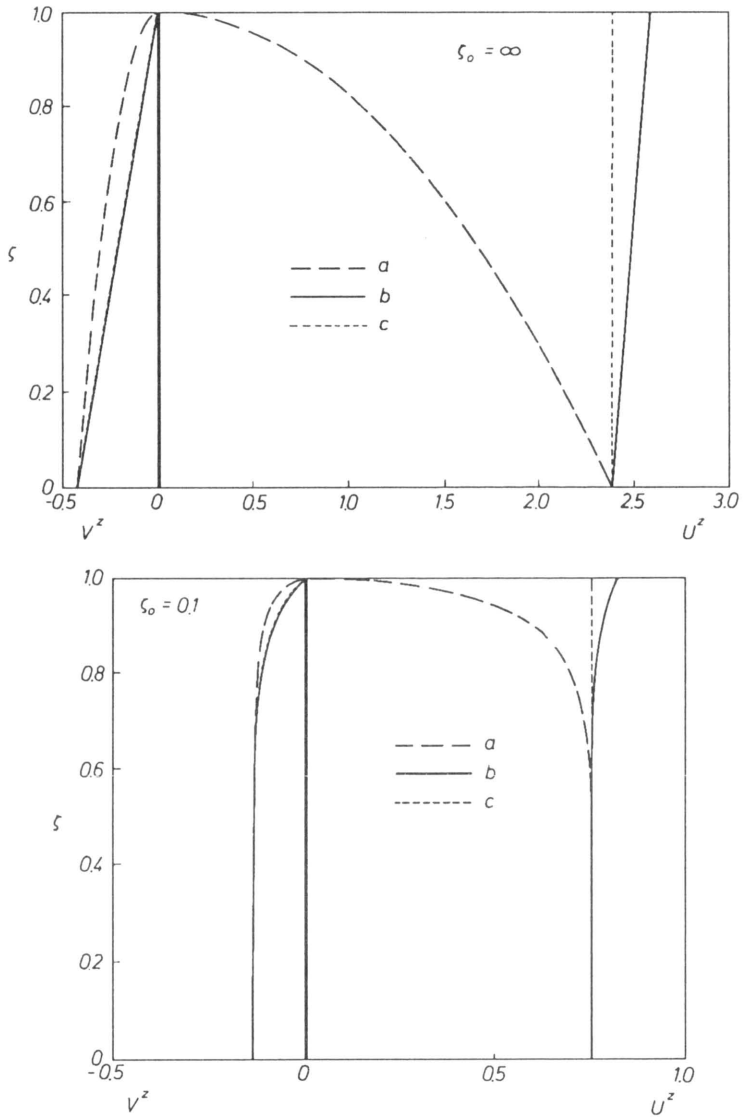

FIG. 4. Particle velocities V^z and the propagation speeds U^z for different concepts of the density jump variation.

As regards the particle velocity V_z distribution, the "b" and "c" concepts give again very close results and the difference in comparison with the "a" concept is quantitative only (the velocities are smaller than in the "a" case).

The propagation speed U^z distributions exhibit however essential qualitative differences. Only in the case "a", U^z together with V^z are zero on the upper free surface ($\zeta = 1$). In the case "b" the propagation speed U^z slightly increases with ζ, and in the case "c" it is constant according to the assumption (4.11). It is again worth to note that, in the case of the silo stress state ($\zeta = .1$), all the three concepts give results almost coinciding in the lower half of the bin.

6. Concluding remarks

The concept "b" of the density jump parameter δ variation being linear with the stress jump allows for a more realistic description of the propagation process of the flow zone in granular materials. It seems to have some advantages especially for discrete solutions of some more complex initial flow problems, where the constant δ assumption would be not justified in the vicinity of the free surface.

The constant propagation speed assumption "c", being very close to the "b" concept, can be successfully used for a quick estimation of the propagation process values.

For the small values of the stress distribution parameter ζ_o, all the three concepts give close results and the discrepancies increase first in the end stage of the propagation process. Hence, for the example considered in [2] the times of the whole propagation process differ insignificantly. However, in the case $\zeta_o = \infty$ (linear stress distribution) the differences between the concept "a" and the proposed concepts "b" and "c" arise already in the early stage of the propagation process.

References

1. R. KVAPIL, *Theorie der Schüttgutbewegung*, VEB Verlag Technik, Berlin 1959.
2. S.C. COWIN, W.J. COMFORT III, *Gravity-induced density waves in sand columns*, J. Appl. Mech., Trans. ASME, **49**, 497–500, 1982.
3. J. ZAWIDZKI, *Propagation of a flow zone in the gravity outflow of granular materials*, Studia Geotechnica et Mech., **16**, 1–4, 61–69, 1993.
4. E. BECKER, W. BÜRGER, *Kontinuumsmechanik*, B. G. Teubner Verlag, Stuttgart 1975.
5. S.C. COWIN, *The theory of static loads in bins*, J. Appl. Mech., Trans. ASME, **44**, 409–412, 1977.
6. J. HORABIK, *Description of the initial phase of gravitational discharge of granular material from a hopper*, Int. Agrophysics, **2**, 1, 31–43, 1986.

POLISH ACADEMY OF SCIENCES
INSTITUTE OF FUNDAMENTAL TECHNOLOGICAL RESEARCH, WARSZAWA.

Received November 18, 1994.

XXXIst Solid Mechanics Conference

XXXIst Solid Mechanics Conference **SolMec'96**, traditionally organized by Institute of Fundamental Technological Research PAS will be held on September 9–14, 1996, at Hotel KORMORAN in MIERKI near Olsztyn, approximately 200 km north of Warsaw.

Main topics of the Conference are: mechanics and thermodynamics of solids with microstructure, dynamics of solids and structures, computational solid mechanics, mathematical and computer methods in mechanics and engineering sciences, experimental methods in mechanics, contact and interface problems in mechanics, environmental mechanics.

Conference Chairman is Witold KOSIŃSKI.
Inquires can be made to the Organizing Committee
IFTR PAS, ul. Świętokrzyska 21,
00-049 Warszawa, POLAND;
Phone: ++4822-268802, Fax: ++4822-269815, e-mail solmec96@ipp.gov.pl

DIRECTIONS FOR THE AUTHORS

The journal *ARCHIVES OF MECHANICS (ARCHIWUM MECHANIKI STOSOWANEJ)* deals with the printing of original papers which should not appear in any other periodicals.

As a rule, the volume of a paper should not exceed 40 000 typographic signs, that is about 20 type-written pages, format: 210 × 297 mm, leaded. The papers should be submitted in two copies. They must be set in accordance with the norms established by the Editorial Office. Special importance is attached to the following directions:

1. The title of the paper should be as short as possible.

2. The text should be preceded by a brief introduction; it is also desirable that a list of notations used in the paper should be given.

3. The formula number consists of two figures: the first represents the section number and the other the formula number in that section. Thus the division into subsections does not influence the numbering of formulae. Only such formulae should be numbered to which the author refers throughout the paper, and also the resulting formulae. The formula number should be written on the left-hand side of the formula; round brackets are necessary to avoid any misunderstanding. For instance, if the author refers to the third formula of the set (2.1), a subscript should be added to denote the formula, viz. $(2.1)_3$.

4. All the notations should be written very distinctly. Special care must be taken to write small and capital letters as precisely as possible. Semi-bold type should be underlined in black pencil. Explanations should be given on the margin of the manuscript in case of special type face.

5. It has been established to denote vectors by semi-bold type. Trigonometric functions are denoted by sin, cos, tg and ctg, inverse functions – by arc sin, arc cos, arc tg and arc ctg; hyperbolic functions are denoted by sh, ch, th and cth, inverse functions – by Arsh, Arch, Arth and Arcth.

6. Figures in square brackets denote reference titles. Items appearing in the reference list should include the initials of the first name of the author and his surname, also the full title of the paper (in the language of the original paper); moreover;

a) In the case of books, the publisher's name, the place and year of publication should be given, e.g.,
5. S. Ziemba, *Vibration analysis*, PWN, Warszawa 1970;

b) In the case of a periodical, the full title of the periodical, consecutive volume number, current issue number, pp. from ... to ..., year of publication should be mentioned; the annual volume number must be marked in black pencil so as to distinguish it from the current issue number, e.g.,
6. M. Sokołowski, *A thermoelastic problem for a strip with discontinuous boundary conditions*, Arch. Mech., **13**, 3, 337–354, 1961.

7. The authors should enclose a summary of the paper. The volume of the summary is to be about 100 words.

8. The authors are kindly requested to enclose the figures prepared on diskettes (format PCX, BitMap or PostScript).

Upon receipt of the paper, the Editorial Office forwards it to the reviewer. His opinion is the basis for the Editorial Committee to determine whether the paper can be accepted for publication or not.

The printing of the paper completed, the author receives 25 copies of reprints free of charge. The authors wishing to get more copies should advise the Editorial Office accordingly, not later than the date of obtaining the galley proofs.

The papers submitted for publication in the journal should be written in English. No royalty is paid to the authors.

Please send us, in addition to the typescript, the same text prepared on a diskette (floppy disk) 3 1/2″ or 5 1/4″ as an ASCII file, in Dos or Unix format.

EDITORIAL COMMITTEE
ARCHIVES OF MECHANICS
(ARCHIWUM MECHANIKI STOSOWANEJ)